

Biomechanical Structure-Function Relationships of Collagen Tissues, B Cell Membranes, and Amyloid Fibers

by

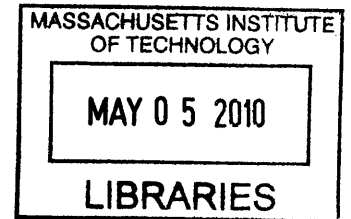
Carlos E. Castro

Submitted to the Department of Mechanical Engineering in
Partial Fulfillment of the Requirements for the Degree of

Doctor of Philosophy in Mechanical Engineering
at the
Massachusetts Institute of Technology
February 2010

© 2010 Massachusetts Institute of Technology
All rights reserved

ARCHIVES



Signature of Author.....
Department of Mechanical Engineering

Certified by
Matthew J. Lang
Associate Professor of Biological and Mechanical Engineering
Thesis Supervisor

Certified by
Mary C. Boyce
Gail E. Kendall Professor of Mechanical Engineering
Thesis Supervisor

Accepted by
David E. Hardt
Ralph E. and Eloise F. Cross Professor of Mechanical Engineering
Graduate Program Committee Chair

This Doctoral Thesis has been examined by the following Thesis Committee:



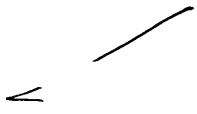
Mary C. Boyce, Ph.D. ✓
Thesis Supervisor and Committee Co-Chair
Gail E. Kendall Professor of Mechanical Engineering
Massachusetts Institute of Technology



Roger D. Kamm, Ph.D.
Germeshausen Professor of Mechanical and Biological Engineering
Massachusetts Institute of Technology



Matthew J. Lang, Ph.D.
Thesis Supervisor and Committee Co-Chair
Keck Assistant Professor of Biological and Mechanical Engineering
Massachusetts Institute of Technology



Hidde Ploegh, Ph.D. ✓
Professor of Biology
Member, Whitehead Institute for Biomedical Research
Massachusetts Institute of Technology

Biomechanical Structure-Function Relationships of Collagen Tissues, B Cell Membranes, and Amyloid Fibers

by

Carlos E. Castro

Submitted to the Department of Mechanical Engineering
on October 19, 2009 in Partial Fulfillment of the
Requirements for the Degree of
Doctor of Philosophy in Mechanical Engineering

ABSTRACT

Mechanical forces are critical to defining the physiological function of biological systems spanning length scales from 1 nm (single molecules) up to 1m (full mammalian systems). This work combines theoretical and experimental mechanics to gain insights into the physiological function of three biological systems at distinct length scales: collagen tissues comprised of wavy fibers (~ 1mm), B lymphocyte membranes (~ 1 μ m), and amyloid protein fibers (~ 1nm).

The initial portion of this thesis addresses the mechanics of fibrous collagen tissues such as ligaments, tendons, and pericardium that serve as load bearing components in biological systems. A novel micromechanical model describing the force-extension of wavy fibers comprising these tissues is integrated with bundle and network frameworks. The developed models accurately predict the mechanical behavior of bundled fiber tissues (i.e ligaments and tendon) and fibrous membranes (i.e. vessel walls and pericardium) and elucidate deformation mechanisms within these tissues.

Moving down in length scale, the second part of this thesis employs single cell experiments with optical tweezers to characterize the mechanical behavior of the B cell membrane, which is a critical component of its physiological functions including migration and antigen detection. Our results show that the mechanical properties of the membrane, specifically the effective viscosity of the membrane, evolve upon activation of B cell biochemical machinery. We further identify the presence of receptors in membrane nanotubes conferring B cells with the ability to sense antigen at remote locations.

Lastly, this thesis studies the aggregation and underlying structure of amyloid forming proteins by characterizing their physical properties at the fibril and single molecule level. Amyloid formation, which is associated with many diseases including Alzheimer's, results from the aggregation of misfolded proteins. This work combines optical trapping with fluorescence imaging to quantify the physical properties and molecular interactions of amyloid fibers formed from polymorphic variants of the yeast prion protein, Sup35. Our results show that Sup35 polymorphism leads to distinct physical properties of

amyloid aggregates. We further subject fibers to unfolding and rupture to elucidate structural details of misfolded Sup35.

Thesis Co-supervisor: Matthew J. Lang

Title: Associate Professor of Mechanical and Biological Engineering

Thesis Co-supervisor: Mary C. Boyce

Title: Gail E. Kendall Professor of Mechanical Engineering

To: My parents

Acknowledgements

When I decided to pursue my PhD at MIT, I didn't know what I was getting into. Five years later I can look back at my experience with a great appreciation for how much I have grown both as a scientist and as a person. I was very blessed to be surrounded by caring people who made the last four years some of the best years of my life. I can't convey how grateful I am to them, but I would like to mention how they impacted my life.

First I would like to thank DuPont, NIH, and SMART for funding my education and research throughout my PhD. The NIH Biomechanics Training Grant that funded two years of my PhD greatly contributed to my education in terms of linking me to other graduate students working in biomechanics to expand my knowledge of the field.

The impact of my thesis work was greatly enhanced due to the vision and forward thinking of my thesis committee. It was very valuable to have Roger Kamm, a leader in the field of biomechanics, supporting my work. His broad knowledge of the field was an important asset to make my work as novel as possible. I also appreciate Roger taking extra time to help me with my future career by giving helpful advice and writing several reference letters. Hidde Ploegh was an invaluable addition to my committee. I was very lucky to take his Immunology class in the semester when I was writing my thesis proposal. Our B cell collaboration stemmed from a conversation I had with Hidde after class one day. I am grateful to Hidde's foresight, which enabled our collaboration to make an important impact to the field of Immunology.

I could not have asked for more from my advisors, Mary Boyce and Matt Lang, both from an academic and a personal standpoint. The prospect of working with Mary, one of the foremost researchers in solid mechanics, was a big factor in my decision to attend MIT. I learned as much about mechanics through discussions in her office as I did from classes. Her guidance helped me develop into an independent thinker and effective researcher. Matt has been a great role model for me over the last four years. After four years of Matt's training I have learned how to build, troubleshoot, and optimize cutting edge biophysics instrumentation. Whether it was aligning a laser, setting up an experimental assay, or troubleshooting optics, Matt was always willing to spend time in the lab personally teaching me how to be an experimentalist. Both Matt and Mary also invested countless time into preparing me for a career in academia and gave me invaluable guidance during my job search process. Thanks to them, I feel well prepared to perform novel research in a biomechanics lab of my own.

Several other professors made important contributions to my life over my years at MIT. I was lucky to collaborate with Sue Lindquist on the amyloid project. After experiencing Sue's scientific guidance, it is easy to see how she has become a leader in the field of prion biology and protein conformation. Thanks to Gareth McKinley for convincing me to join the Program in Polymer Science and Technology. Gareth was a great teacher and mentor outside the classroom especially in my first year at MIT. I am grateful to Mark Bathe, Krystyn Van Vliet, and Jennifer McManus for spending many hours in advising

me on my career path and becoming good friends in the process. I also thank Alan Grodzinsky, Lalit Anand, John Hutchinson, and Bob Cohen for being positive influences on my academic career. I owe a big thanks to the MIT staff, Una Sheehan, Leslie Regan, Joan Kravit, Olga Parkin, Kristine Marzilli, Chris Connaire, Greg Sands, Tony Pulsone, and Annmarie Donovan, who were so helpful throughout my years here.

I am thankful to my collaborators who all also became good friends. Dr. Andrew Hu, a post-doc in the Ploegh Lab, was a huge help on the B cell project. He was a great mentor in the field of biology, and I always enjoyed our coffee breaks. I worked closely with Dr. Jijun Dong, a post-doc in the Lindquist lab, on the amyloid project. She taught me almost everything I know about prion biology. Countless hours at the trap were made much more enjoyable by having a great person like Jijun to get to know. I am also thankful to Dr. Alec Robertson and Dr. Sun Taek Kim who I was lucky to collaborate with on other projects and to Dave Quinn for his work on building the one of the trapping instruments. Thanks to Rajdeep, Nuo, Melis, Sai, Katia, Ethan, Meredith, Renaud, Tim, Juha, Lifeng, Chia-Ling, Damien, Brian, Ting-Ting, and Casey from the Boyce Lab and Mo, Yongdae, Hyungsuk, Marie Eve, Ricardo, Ted, Bill, Miriam, Mariya, Sangjin, Ben, Becky, Adrien, and Sergio from the Lang Lab who were a joy to work with. I owe a special thanks to Sharon Soong, Adam Mulliken, Mohit Garg, and Jeff Palmer from the Boyce lab and Jorge Ferrer, Ricardo Brau, Peter Tarsa, and David Appleyard from the Lang Lab. As senior members of the lab when I joined, they made me feel welcome and spent extra time helping me learn the ropes.

I would like to thank the lifelong friends I have made outside of lab who made an impact on my life as I hope I did on theirs. I am grateful to Rory, Frank, Barbara, Grinia, Sharon, Sungyon, Amit, Anjuli, Angela, Tony, Donny, Borjan, Andrej, and Dave who I shared so many good times with. I am especially grateful to Cathal, Conor, Al, and Bob, who were my roommates while at MIT, for always making me look forward to getting back to my apartment. I also am grateful to the unbelievables soccer team and MIT grad soccer club who were important parts of my time here. I owe a special thanks to my girlfriend, Gida Cotran, for helping me to stay sane through the mad rush to finish my thesis. She is one of the most amazing girls I have ever known. She has made me as happy as I have ever been, and I am very lucky to have her in my life.

Finally, and most importantly, I am thankful to my family: my parents Jose and Ana; my brother Jose; my two sisters Gina and Claudia; my sister-in-law Patty; my brothers-in-law Todd and Jeff; my nieces and nephews Alexia, Gabriel, Isabela, Colin, Conor, and Brady; and my extended family, especially my aunt Ruth. The hardest part of my PhD has been being away from my family for several years. There are always tough times in any graduate program, but their love and support always kept me going. I can proudly say that my best friends throughout my life have been my family, and I can't wait to get back to Ohio to share my life with them again. I am especially thankful to my mom and dad. Thanks to my mom for all her prayers and always being there to do the work behind the scenes. Thanks to my dad for his words of wisdom (i.e. parent talks), and showing me how wonderful a life in academia could be. I would consider it my greatest success in life to raise a family like they have.

Table of Contents

List of Figures.....	13
List of Tables.....	17
Chapter 1: Introduction and Background.....	19
1.1 Introduction.....	19
1.1.1 Crimped Collagen Fibers.....	21
1.1.2 Mechanics of B Lymphocyte Membranes.....	22
1.1.3 Physical Properties of Prion Amyloid Fibers.....	25
1.2 Optical Trapping Overview.....	27
1.2.1 Position Calibration of an Optical Trap.....	31
1.2.2 Stiffness Calibration of an Optical Trap.....	32
1.3 Optical Trapping Instrumentation.....	36
1.4 References.....	39
Chapter 2: An Elastica Approximate for Fibers and Fibrous Networks...	43
2.1 Introduction.....	43
2.2 The Elastica Approximate Model.....	46
2.2.1 Review of the Elastica Solution.....	47
2.2.2 Limit of Small Extension.....	53
2.2.3 Limit of Large Forces.....	54
2.2.4 Composite Small Extension and Large Force Limits.....	57
2.2.5 Incorporation of Axial Stretching.....	60
2.2.6 Cross-Sectional Geometry and Microstructural Heirarchy.....	62
2.2.7 Variation of Crimp Geometry.....	64
2.3 Application of EAM to Fit Collagen Fascicle Data.....	66
2.4 Incorporation Model into Networks.....	70
2.5 Conclusions.....	74
2.6 Appendix 2A: Extension to General Fiber Geometry.....	79
2.7 References.....	85
Chapter 3: Physiological Function of B Cell Membrane Mechanics.....	89
3.1 Introduction.....	89
3.2 Experimental Methods.....	96
3.3 Review of Membrane Tethering Mechanics.....	99
3.4 Membrane Tethering Experimental Results.....	103
3.4.1 Cell-bead Adhesion Results.....	103
3.4.2 Membrane Tethering Force-extension.....	103
3.4.3 Membrane Mechanical Properties.....	104
3.4.4 Tether Force Relaxation.....	107
3.4.5 1D Model for Radial Tether Growth.....	112

3.5 Conclusions.....	116
3.6 Appendix 3A: Mechanical Equilibrium of Liquid Tubes.....	120
3.7 Appendix 3B: Samples of Tether Force-extension Data.....	126
3.8 References.....	146
Chapter 4: B cell Biochemical and Biomechanical Machinery.....	149
4.1 Introduction.....	149
4.2 Experimental Methods.....	153
4.2.1 Experimental Methods.....	153
4.2.2 Combined Membrane Tethering and mlg Fluorescence.....	153
4.3 Experimental Results.....	155
4.3.1 XBP-1 ^{KO} Deficient B Cells.....	155
4.3.2 mlg Composition of B Cell Membrane Nanotubes.....	158
4.4 Discussion.....	164
4.5 References.....	170
Chapter 5: Physical Properties of Yeast Prion Amyloid Fibers.....	173
5.1 Introduction.....	173
5.2 Physical Properties of NM Fibers.....	177
5.2.1 NM Amyloid Fiber Equilibrium Morphologies.....	177
5.2.2 Fluorescence Imaging of Thermal Fluctuations.....	179
5.2.3 Force-extension Behavior of Homogeneous NM fibers.....	184
5.2.4 Force-extension Behavior of Kinked NM fibers.....	190
5.3 Molecular Interaction of Yeast Prion Proteins.....	193
5.4 Discussion.....	205
5.4.1 Physical Properties of NM fibers.....	205
5.4.2 Molecular Interactions of Yeast Prion Proteins.....	210
5.5 Appendix 5A: Experimental Methods.....	213
5.5.1 Protein Purification and Labeling.....	213
5.5.2 Fluorescence Imaging of Morphology.....	213
5.5.3 Fluorescence Imaging of Thermal Fluctuations.....	214
5.5.4 Force-extension with Fluorescence Imaging.....	215
5.5.5 Unfolding and Rupture of Prion Molecular Interactions.....	217
5.5.6 Imaging of Fibers after Rupture Events.....	219
5.5.7 Melting Curves of NM and RΔ2-5 Fibers.....	219
5.6 Appendix 5B: Sample Amyloid Fiber Data Curves.....	220
5.6.1 Force-extension Curves.....	220
5.6.2 High Force Unfolding and Rupture Curves.....	230
5.7 References.....	235

List of Figures

Figure 1.1 Mechanics at biology's length scales.....	20
Figure 1.2 Stress-strain behavior of crimped collagen fibers.....	22
Figure 1.3 Physical Interaction of B and T cells.....	23
Figure 1.4 Optical trapping forces.....	29
Figure 1.5 Optical traps behave like a linear spring.....	31
Figure 1.6 Position sensing device voltage response.....	32
Figure 1.7 Power spectrum of a trapped bead.....	33
Figure 1.8 Stokes drag experiment.....	35
Figure 1.9 Combined force-fluorescence trap layout.....	37
Figure 1.10 Large force trap layout.....	38
Figure 2.1 Fibers with wavy geometry.....	46
Figure 2.2 Geometry used to approximate wavy fibers.....	47
Figure 2.3 Numerical elastica solution for wavy fiber force-extension.....	51
Figure 2.4 Linear elastic wavy fiber small extension solution.....	54
Figure 2.5 Large force wavy fiber approximation.....	57
Figure 2.6 Elastica approximate model for wavy fiber force-extension.....	59
Figure 2.7 Elastica approximate model with axial extension included.....	62
Figure 2.8 Effect of cross-sectional geometry and structural hierarchy.....	64
Figure 2.9 Effect of random crimp geometry.....	66
Figure 2.10 Force-extension behavior of collagen fascicle.....	67
Figure 2.11 Schematic of 2D idealized 4-chain network.....	71

Figure 2.12 Simulation of simple shear in a 2D network.....	74
Figure 2.A1 Schematic of generalized geometry.....	79
Figure 2.A2 Small extension and large force limits for general geometry.....	81
Figure 2.A3 Elastica approximate model for general geometry with axial extension included.....	82
Figure 2.A4 Effect of varying generalized geometry.....	84
Figure 3.1 The B cell receptor.....	90
Figure 3.2 B cells stimulated with lipopolysaccharide.....	91
Figure 3.3 Leukocyte rolling and extravasation.....	92
Figure 3.4 B cell spreading during antigen detection.....	93
Figure 3.5 Biomechanical machinery of B cells.....	94
Figure 3.6 Membrane tethering experimental background.....	95
Figure 3.7 Membrane tethering experimental assay.....	98
Figure 3.8 Schematic of energetic contributions to membrane tethering.....	100
Figure 3.9 Cell-bead adhesion results.....	103
Figure 3.10 Representative data of force versus extension and time.....	104
Figure 3.11 Steady tether force results.....	105
Figure 3.12 Steady tether force versus velocity.....	106
Figure 3.13 Tether force relaxation data.....	107
Figure 3.14 Results for force relaxation fit to double exponential model.....	108
Figure 3.15 Static tether force versus radius.....	109
Figure 3.16 Schematic of radial growth during force relaxation.....	111
Figure 3.17 Experimental validation of radial growth.....	112
Figure 3.18 Effect of viscosity and tether length on radial growth.....	115

Figure 3.19 Prediction of tether force relaxation with radial growth model.....	116
Figure 3.A1 Mechanical equilibrium of membrane tubes.....	120
Figure 4.1 B cell capping upon antigen detection.....	150
Figure 4.2 XBP-1 deficiency leads to decreased mlg expression and changes in lipid composition.....	151
Figure 4.3 Membrane nanotubes physically connect T cells	153
Figure 4.4 Steady tether force results for XBP-1 ^{KO} cells.....	156
Figure 4.5 XBP-1 ^{KO} Plasmablasts have lower effective viscosity.....	157
Figure 4.6 Prediction of tether force relaxation behavior of XBP-1 ^{KO} B cells using radial growth model.....	158
Figure 4.7 BCR is not present in membrane tether pulled after a 30 minute incubation with fluorescent HEL.....	159
Figure 4.8 BCR is present in membrane tethers pulled prior to a 5 minute incubation with fluorescent HEL.....	159
Figure 4.9 Dependence of BCR mobility on B cell activation by HEL.....	161
Figure 4.10 Dependence of BCR mobility on B cell activation by HEL in XBP1- ^{KO} B cells.....	162
Figure 4.11 BCRs are pulled into membrane tethers during extension.....	163
Figure 4.12 BCR occasionally appears as discrete spots along the tether with spatial periodicity.....	164
Figure 5.1 Morphologies of NM fibers reconstituted at 4 °C and 37 °C.....	179
Figure 5.2 Determining persistence length from thermal fluctuations.....	182
Figure 5.3 Results of persistence length and kink torsional stiffness from NM fiber thermal fluctuations.....	183
Figure 5.4 Experimental tethered fiber assay.....	185
Figure 5.5 Experimental results of combined force-extension and fluorescence imaging.....	186

Figure 5.6 NM fiber mechanical properties from force-extension data.....	189
Figure 5.7 Force-extension model for kinked fibers.....	192
Figure 5.8 Loading and Unloading profiles for NM fibers with large force.....	194
Figure 5.9 Examples of unfolding and rupture of NM fibers.....	195
Figure 5.10 Multiple loading cycles on single NM fibers.....	196
Figure 5.11 Imaging of surface-bound fiber fragment after rupture.....	197
Figure 5.12 Examples of rare refolding events.....	198
Figure 5.13 Determination of length of unfolding domains.....	200
Figure 5.14 Distributions of unfolding lengths.....	201
Figure 5.15 Melting curves for wild-type NM and R Δ 2-5 fibers.....	202
Figure 5.16 Bond kinetics determined from lifetime versus rupture force.....	205
Figure 5.17 Trap force verification.....	218

List of Tables

Table 1.1 Summary of amyloid related diseases.....	26
Table 3.1 Membrane mechanical properties throughout differentiation.....	106

Chapter 1

Introduction and Background

1.1 INTRODUCTION:

Mechanical forces play an important role in defining the physiological function of biological systems that span lengths scales from 1 nm (proteins and single molecules) up to 1m (full mammalian systems). For example, conformational changes on the order of a few nanometers in ion channels which regulate intracellular concentration of ions such as Ca^{2+} can be driven by membrane stresses or strains [1-3]. At cellular length scales, endothelial cells (~ 10-100 μm) which line blood vessel walls align and form actin stress fibers in the direction of shear flow [4-6]; and some cells can upregulate collagen production in response to mechanical strains [7]. Furthermore, an entire field of research exists to study the biomechanics of human movement. This thesis studies representative structures at the molecular (~1nm), cellular, and tissue (~1mm) length scales where mechanics plays a critical role in defining physiological function.

The approach taken to understand and model the mechanical behavior of biological systems must be tailored to the length scale of interest. In general biological systems in themselves can span several length scales. For example, B cells have a diameter of ~ 5-15 μm ; however, the membrane protrusions of B cells we discuss in chapters 3 and 4

have a diameter of $\sim 10\text{-}100$ nm, and the immunoglobulins expressed on the B cell membrane that initiate signaling and activation have dimensions of ~ 1 nm. Often times, describing the mechanical behavior of these complex systems requires a combination of different modeling approaches. Similarly, probing the mechanical behavior of biological systems requires experimentation tailored to the length scale of interest to guide and validate models. In this thesis we use a combination of applied experimental and theoretical mechanics to understand the role of forces and mechanical properties in the physiological function of systems at three distinct length scales: collagen tissues (\sim mm), B lymphocytes ($\sim \mu\text{m}$), and prion amyloid fibers (\sim nm). Figure 1.1 shows how these systems fit into a spectrum of some of the applied mechanics approaches used to describe the mechanical behavior of biological systems at different length scales.

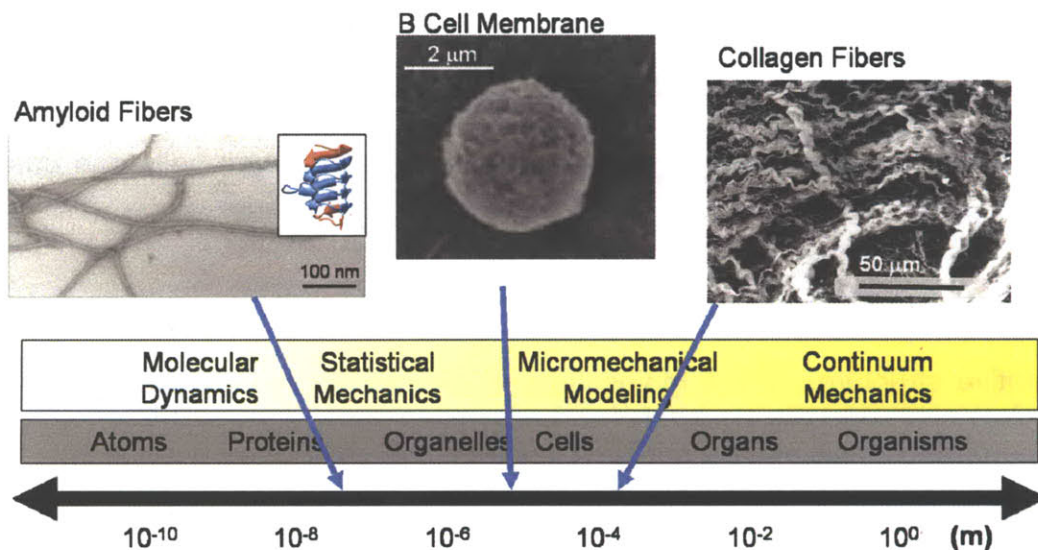


Figure 1.1 Mechanics at biological length scales. Biology spans length scales ranging from single proteins (\sim nm) to full organisms (\sim m). This thesis focuses on systems at three distinct length scales: (left) amyloid fibers [Images Courtesy of Dr. Jijun Dong], (middle) B cells [8], and (right) collagen fibers [9]. An abbreviated list of mechanical modeling approaches tailored to the length scale of interest is shown in yellow. The approaches are often complimentary since biological systems often span several length scales in themselves.

Our general research approach combines system manipulation by molecular and cell biology techniques, measurement by force spectroscopy with optical tweezers, and mechanical modeling using a combination of the approaches listed in figure 1.1. The main focus of this thesis is applying novel modeling and measurement techniques to answer relevant questions in biology. The system manipulation aspect of this research was done in collaboration with the Ploegh Lab for the B cell work and the Lindquist lab for the amyloid fiber work, both at the Whitehead Institute for Biomedical Research.

1.1.1 Crimped Collagen Fibers. Starting with the largest length scale, we first address the mechanical behavior of collagen tissues comprised of networks of wavy collagen fibers in Chapter 2. This work focuses on the development of a micromechanical model to understand the stress-strain response of collagen tissues including ligaments, tendons, pericardium, and vessel walls whose primary load bearing constituent is a fibrous collagen network where the fibers generally have a wavy geometry [10-13]. The main physiological function of these soft tissues is to bear and transfer mechanical loads. Figure 1.2(a) shows an image of a bovine pericardium where the light and dark regions illustrate the highly aligned crimped fibers [12]. The wavy geometry of similar collagen fibers in rat tail tendons gives the nonlinear stress-strain response shown in figure 1.2(b) [11]. The wavy geometry initially deforms with little resistance by unbending of the crimped geometry, then experiences nonlinear stiffening while crimps straighten, and finally reaches a constant large stiffness when fibers become straight.

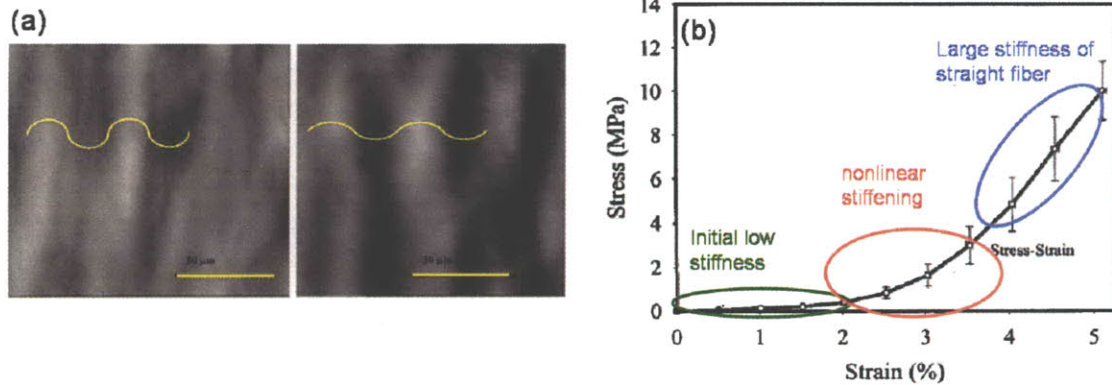


Figure 1.2 Stress-strain behavior of crimped collagen fibers. (a) shows crimped fibers of a bovine pericardium all aligned in the same direction under no load (left) and after 15% strain (right) when crimps have begun to straighten (scale bars indicate 50 μm) [12]. (b) The crimped fiber gives a nonlinear stress-strain response with initially low stiffness (unbending of crimps), nonlinear stiffening (straightening of crimps), and large stiffness response large strains (extension of straight fibers) [11].

During physiological processes, collagen tissues generally function in the nonlinear stiffening region of their stress-strain behavior [14]. Therefore, it is critical to accurately describe the nonlinear stiffening in order to describe the load bearing and transferring function of these tissues in physiological processes. In Chapter 2, we take a micromechanical modeling approach to develop a mechanical model for the force-extension behavior of wavy collagen fibers and bundles of fibers. This model accurately captures the full force-extension behavior of wavy fibers. Furthermore, our micromechanical model is useful to understand the deformation mechanisms of bundled fiber tissues such as tendons. We then integrate the wavy fiber model into a continuum mechanics model for fibrous networks to describe 2-dimensional tissues such as those found in vessel walls.

1.1.2 Mechanics of B lymphocyte Membranes. Working our way down in length scale, Chapter 3 addresses the importance of the mechanical behavior of the B cell

membrane during physiological functions. B cells are a critical component of the immune system that are responsible for detecting foreign antigens in mammals. During their lifetime, B lymphocytes must leave the bone marrow, circulate through the bloodstream, migrate into and through lymphoid organs where antigens are localized, probe lymphoid tissues for antigens, communicate with T lymphocytes, and migrate out of lymphoid tissues and re-enter the bloodstream. The lymphocyte membrane is a critical component for nearly all aspects of these functions, where its wrinkled topology facilitates easy expansion of the cell due to external stimuli and enables interaction and communication with surfaces, in particular the endothelial wall, lymphoid tissues, and T cells. For example, figures 1.3(a) and 1.3(b) shows a B cell interacting with a T cell. Contacts between B and T cells eventually form large areas of membrane contact. The excess B cell membrane that spreads out over the surface of the B cell is contained in the wrinkled geometry of the resting B cell membrane

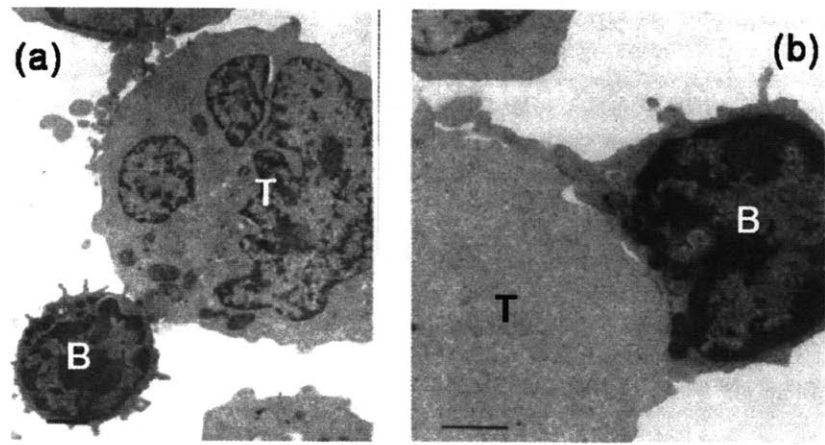


Figure 1.3 Physical interactions of B and T cells. During their physiological function B cells interact with T cells. (a) shows an EM micrograph of initial contact between a B and T cell [Sanders et al, J Immunology 1986]. (b) Eventually these interactions lead to a large area of contact where the B cell membrane spreads out over the surface of the T cell (Scale bars are 1 μm) [15].

Here we perform single cell experiments with optical tweezers to quantify the mechanical properties of B cell membranes and track the evolution of those properties after B cell activation and throughout differentiation into antibody secreting Plasma cells. We further examine the dynamic stress relaxation behavior of membrane flow in the formation of membrane tethers (membrane nanotubes extracted from the surface of the cell), a process that occurs physiologically for example during cell rolling. A micro mechanical model is developed to describe the flow of membrane into tethers in order to relieve stress. All experiments are done on primary B cells that were extracted from B Cell Receptor (BCR) transgenic mice enabling us to probe the B cell in an antigen specific manner.

Chapter 4 addresses the inter-dependence of the biochemical and biomechanical machinery of the B cell. First, we investigate whether changes in the biochemical machinery have consequences for the biomechanical machinery of the B cell. Specifically, we quantify the membrane mechanical properties of X-box protein 1 (XBP-1) deficient B cells from BCR transgenic mice. XBP-1 is a transcription factor that regulates lipid synthesis and is critical for the differentiation of B cells into antibody secreting Plasma cells. We ask if XBP-1 deficiency results in changes in the mechanical behavior of the membrane that might impact B cell physiological function. Secondly, we investigate a potential biochemical role of membrane nanotube protrusions of B cells during antigen detection by employing a combined force and fluorescence approach with optical tweezers. Specifically, we ask if the BCR, the primary sensing agent of B cells, is present in membrane nanotubes extending from the

cell. BCR presence in nanotubes would confer cells with the ability to sense antigen at remote locations and possibly transfer antigens via nanotubes that form intercellular connections. Our results give insights into the immune function of the transcription factor XBP-1 in B cells as well as illustrate the cooperative nature of the B cell biochemical and biomechanical machinery. Furthermore, we shed new light on B cell function demonstrating the potential of B cells to sense antigens at remote locations via membrane nanotubes that protrude from their surface.

1.1.3. Physical Properties of Prion Amyloid Fibers. Taking one more step down in length scale, Chapter 5 examines the physical properties of amyloid-forming prion proteins. Amyloid fiber formation, which is associated with more than 30 diseases including disorders such as Alzheimer's, Creutzfeldt-Jacob and Parkinson's (see table 1.1), result from protein conformational changes leading to non-native structures that are subject to aggregation. Amyloids also serve important functions in diverse organisms, from bacteria to mammals that include biofilm formation, scaffolding, environmental adaptation and long term memory. In fact, it is now recognized that a capacity to acquire an amyloid conformation (albeit generally under nonphysiological conditions) is an inherent property of most peptides and proteins [16]. Furthermore, the amyloid self-assembly process has also been stimulated in synthetic preparations [17, 18]. Amyloid fibers exhibit mechanical properties comparable to those of spider silk [19]. Their impressive mechanical properties combined with the ease of assembly make amyloid fibers particularly suited for nanomaterials applications, including as templates

for conducting nanowire formation[20], as scaffolds for cell growth [21], and as functionalized biosensors [22].

Function	Protein	Associated disease
Transport molecules	Serum amyloid protein A	Secondary systemic amyloidosis
	Apolipoprotein A-I	Familial amyloid polyneuropathy Type II
	Apolipoprotein A-II	Familial amyloid polyneuropathy Type III
	Transthyretin	Familial amyloid polyneuropathy Type I
Coagulation factors	Lactoferrin	Corneal amyloidosis
	Fibrinogen	Fibrinogen amyloidosis
Enzymes	Lysozyme	Lysozyme amyloidosis
Cytoskeletal proteins	Keratin	Cutaneous amyloidosis
	Tau	Alzheimer's disease, frontotemporal dementia
Hormones	Amylin	Type II diabetes
	Calcitonin	Medullary carcinoma of the thyroid
	Prolactin	Aging pituitary prolactinomas
	Insulin	Insulin-related amyloid
Regulatory proteins	Atrial natriuretic factor	Atrial amyloidosis
	Gelsolin	Finnish hereditary amyloidosis
Protease inhibitors	Cystatin C	Icelandic hereditary cerebral amyloid angiopathy
Immune system-related	Immunoglobulin light chains (κ and λ)	Primary systemic amyloidosis, amyloidosis associated with multiple myeloma
	Immunoglobulin heavy chain	Primary systemic amyloidosis
	β 2-Microglobulin	Hemodialysis-related amyloidosis
Cell-adhesion molecules	Kerato-epithelin	Corneal dystrophy
Unknown function	Lactadherin (Mec1)	Aortic medial amyloidosis
	Amyloid β	Alzheimer's disease, cerebral amyloid angiopathy
	Prion protein	Spongiform encephalopathies
	Amyloid British	British familial dementia
	Amyloid Danish	Danish familial dementia
	α -Synuclein	Parkinson's disease

Table 1.1 A summary of amyloid-related diseases is given along with the corresponding amyloid forming protein and its natural biological function [23].

Prion proteins are a special class of amyloid fiber forming proteins which are self-templating and thereby transmissible as disease vectors. Despite interest in amyloid fibers as novel materials and their importance in biology, little work has been done to quantify their physical and mechanical properties, and more specifically to relate these to protein structure and the self-assembly process. In this work, we employ a single molecule approach of combined force and fluorescence with optical trapping to quantify the physical properties of amyloid fibers formed from polymorphic variants (dissimilar structures from the same protein) of the yeast prion protein, Sup35. First, we employed fluorescence imaging to quantify the microstructure and thermal fluctuations of fibers in solution. The thermal fluctuations were used to identify the persistence length of two

subsets of fibers that are known to have different underlying prion structures [24]. We then developed a tethered fiber assay and performed single fiber force-extension experiments with optical tweezers to characterize the mechanical properties of prion fibers in bending and extension. Finally, we studied the molecular interactions that lead to misfolding and aggregation of prions by subjecting fibers to forces large enough to rupture those interactions. Our results have implications for the physical basis of strain diversity that results from polymorphic prion proteins. Furthermore, our unfolding and rupture experiments give insight into structural details of the prion conformation of Sup35.

1.2 OPTICAL TRAPPING OVERVIEW:

The primary experimental tool employed in this thesis is optical trapping. Optical traps function by the application of forces to micron scale particles through the application of laser light. The ability to apply forces to and trap particles using light was discovered by A. Ashkin 40 years ago [25]. Today optical force probes commonly referred to as optical traps or optical tweezers are widely applied in the fields of biophysics and biomechanics [26, 27]. Optical traps are capable of applying and measuring forces ranging from ~ 1-300 pN and measuring displacement with nm resolution making them ideal for the study of many biological systems. For example, the molecular motor kinesin, which transports intracellular cargo, is capable of applying forces of ~ 5 pN and achieve motion by systematic displacements ranging from ~1-10 nm [28]. Optical tweezers have been applied to study the mechanics of a wide range of systems including molecular motors [29-31], biopolymers [32-35], filamentous biological

networks [36], F-actin and actin binding proteins [37, 38], and cell membranes [39, 40]. Additionally optical traps have been employed to manipulate bacteria, organelles, and entire cells [41, 42].

Optical traps use radiation pressure and momentum transfer of a tightly focused laser beam to manipulate and apply forces to particles ranging from ~ 10 nm up to ~ 10 μ m. In general, spherical dielectric particles (i.e. glass or polystyrene beads) maximize the applied forces; however, optical traps can be used to manipulate any object on the appropriate length scale with some appreciable curvature such as a cell membrane [43]. Stable trapping is achieved using a high numerical aperture objective to focus a laser to a diffraction limited spot. Infrared lasers are often used to minimize the water absorption and hence sample heating [44]. Momentum is transferred to particles in the path of the laser due to reflection or refraction of the laser light. Figure 1.4 shows a schematic of a laser beam focused by a high numerical aperture objective passing through a spherical particle.

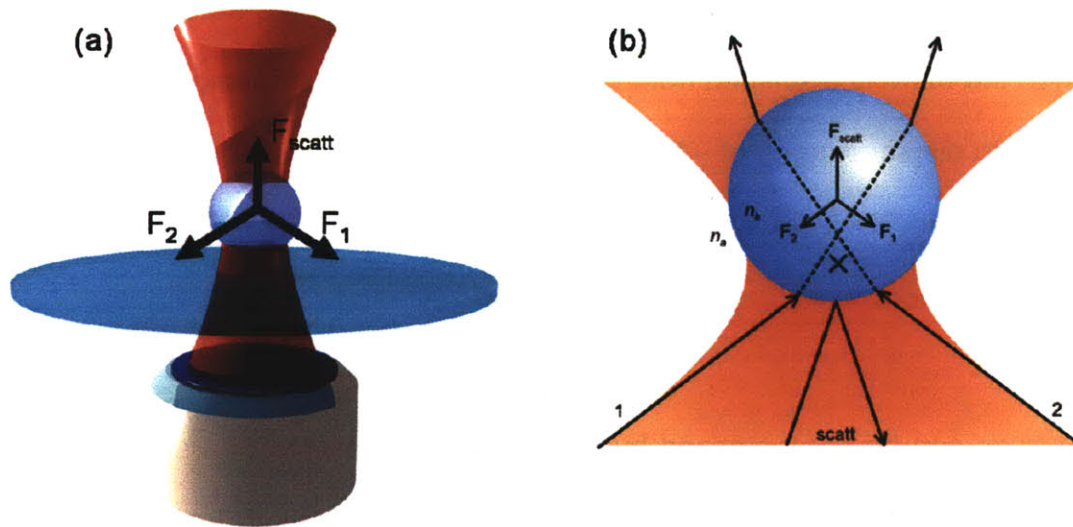


Figure 1.4 Optical trapping forces. (a) Optical traps utilize a high numerical aperture objective in order to focus an infrared laser to a diffraction limited spot (waist is ~ 500 nm). Forces are applied to particles (usually spherical beads) in the path of the laser through reflection (scattering forces) and refraction (momentum transfer). (b) Light bends when it enters the bead and when it leaves the bead due to the change in index of refraction. In order to conserve momentum, a force is applied to the bead in the direction opposite the momentum change of light (F_1 and F_2). Some of the light reflects directly off the bead, and results in a downstream force due to radiation pressure (F_{scatt}). These forces balance to provide an equilibrium position of the bead in the center of the laser just downstream of the focal point (i.e. waist).

Some of the light reflects off the bead resulting in a scattering force in the downstream direction, F_{scat} . The light passing through the particle changes direction when it enters and leaves the bead due to the change in index of refraction resulting in a change in momentum. In order to conserve momentum, a force opposite to the momentum change of the light is applied to the bead, F_1 and F_2 . These forces create a 3-dimensional potential energy well for the bead with the equilibrium position just downstream of the focal point of the laser. If the bead is displaced from its equilibrium position the Gaussian intensity profile of the trapping laser results in a restoring force pushing the bead back towards its equilibrium position. The forces experienced by the trapped particle are proportional to the derivative of the gradient of the light. Thus, when

the trapped particle is in the center of the trap, it experiences zero force on average, and when the bead is displaced from the center of the trap the restoring force increases linearly up to displacements of ~100-150 nm. Therefore, an optically trapped bead can be approximated as a linear spring up to ~ 100-150 nm of displacement from its equilibrium position.

Optical traps can be characterized by a single parameter, the trap stiffness, k_{trap} . The displacement of the bead from its equilibrium position can then be used to determine the force applied to the bead using the equation $F_{trap} = k_{trap} * x_{bead}$. If the bead is attached to a sample the trap can be used to apply a force to the sample. For example, figure 1.5(a) shows an optically trapped bead attached to a flexible polymer. The other end of the polymer is attached to a glass cover slip surface. If the sample is displaced relative to the trap as shown in figure 1.5(b), in this case by moving the coverslip, the bead will be pulled out of its equilibrium position. The restoring force, F_{trap} , is applied to the sample via the attachment to the bead. The deformation of the sample can be determined by the motion of the bead and the motion of the coverslip. Therefore, measuring the position of the bead can provide both the force applied to the sample, and the deformation of the sample. The resulting force versus deformation data can be used to determine relevant mechanical properties of the sample such as the bending stiffness in the case of polymers [28]. Alternatively, changes in force can be used to identify transitions of the sample such as folding or unfolding events of proteins [45-47].

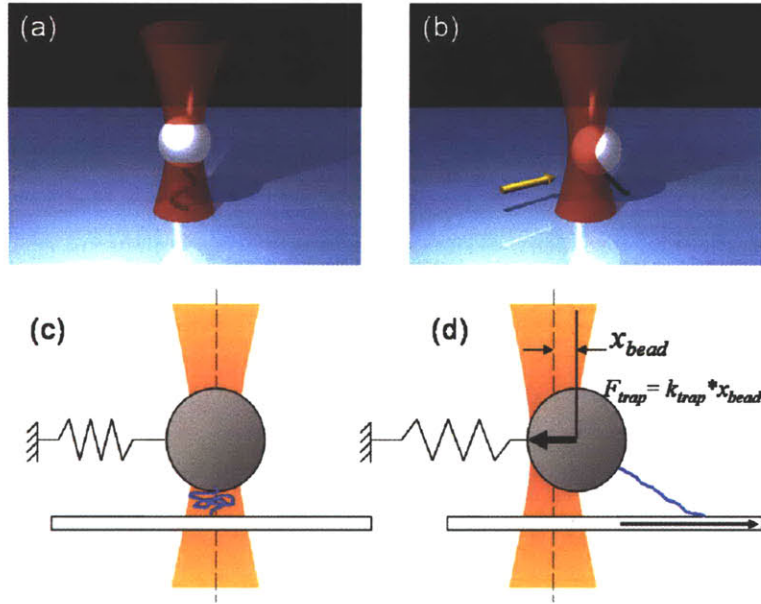


Figure 1.5 Optical traps behave like a linear spring. An example tethered polymer assay is depicted in a 3D rendering (a-b) and in a 2D schematic illustrating the trap as a linear spring (c-d). (a,c) The bead is centered above the tether attachment point where it experiences essentially zero force. On average, the bead is located at the equilibrium position in the center of the laser. (b,d) The cover surface attachment point of the tether is displaced (this is usually done using a piezo electric microscope stage) and applies a force to the bead resulting in a restoring force pulling the bead back to the center of the trap, F_{trap} . The trap can accurately be modeled as a linear spring up to displacements of $\sim 100\text{-}150$ nm.

1.2.1 Position Calibration of an Optical Trap. Quantifying optical trapping forces relies on measuring the position of the bead, x_{bead} , and knowledge of the trap stiffness, k_{stiff} . x_{bead} is generally measured either using video tracking or a position sensing device (PSD) to monitor scatter from the trap laser or a secondary detection laser after passing through the bead. Video tracking utilizes visual measurement of the pixel location of the bead throughout the experiment [44]. The bead displacement is calculated using the pixel size and knowing the pixel location of the bead equilibrium position. PSDs read out a voltage based on the location where light hits the sensor. The 2 dimensional voltage response of the PSD as a function of bead position is calibrated by raster

scanning the bead in known increments through the detection region. This data is then fit to a fifth order polynomial which serves as a calibration curve to convert PSD voltages into bead position. Figure 1.6 shows a typical voltage response for both axes of the PSD as a function of position. The position is shown in terms of the acousto-optic deflector (AOD) frequency. AODs steer the laser beam based on the frequency of an input signal. The AOD frequency can easily be converted to position in the sample plane using a calibration factor (has units of nm/MHz). Note that the AOD and PSD axes are oriented off axis by 45° . Our instruments employ PSD measurement of bead position.

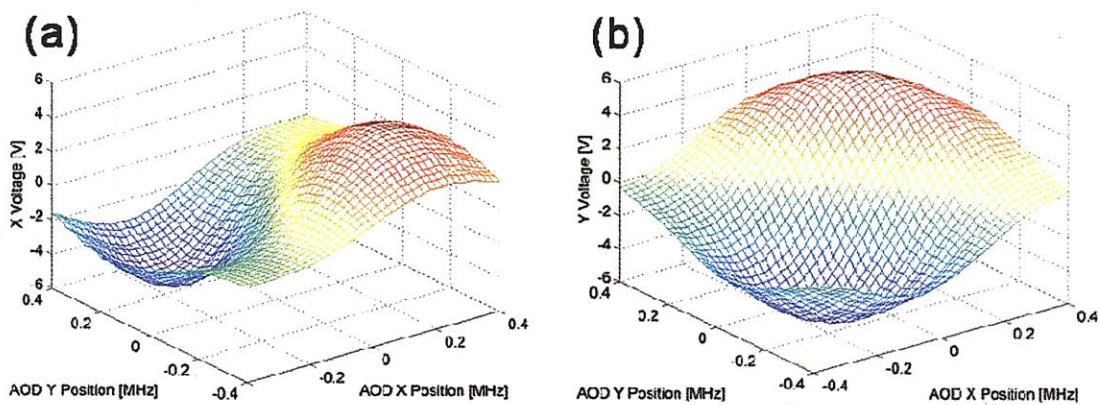


Figure 1.6 Position sensing device voltage response. (a) X and (b) Y voltage signals from a position sensitive device were recorded as a trapped bead was raster scanned across the detection zone. For small displacements, the dependence of voltage signal on position is linear, but at larger displacements, the dependence becomes highly nonlinear. The position is shown in terms of AOD frequency which is converted to position in the sample plane using a calibration factor (nm/MHz).

1.2.2 Stiffness Calibration of an Optical Trap. Once the relation between bead position and detector response is known, it can be used to calibrate the stiffness of the trap. In general the trap stiffness is a function of the laser power, the numerical aperture of the objective used, the diameter and index of refraction of the trapped bead, and the height of the bead of the coverslip surface [44]. Three methods are commonly

used to characterize the stiffness of the trap. The first and simplest method for stiffness calibration method relates the Brownian motion of the bead to the stiffness of the trap. Utilizing the linear spring approximation, the harmonic energy potential of the trap is $U_{trap} = \frac{1}{2}k_{trap}x^2$. This energy is related to the thermal energy of the medium, $k_B T$, (k_B is Boltzmann's constant and T is absolute temperature) using the theorem of equipartition of energy [48].

$$\frac{1}{2}k_B T = \frac{1}{2}k_{trap} \langle x^2 \rangle \quad (1.1)$$

The trap stiffness can then be determined by measuring the positional variance of the bead, $\langle x^2 \rangle$. This method is very quick, but noise sources that increase the variance of bead position can lead to an underestimation of the trap stiffness. The second stiffness calibration method takes the one-sided power spectral density of a bead position trace and fits it to a Lorentzian function as shown in figure 1.7.

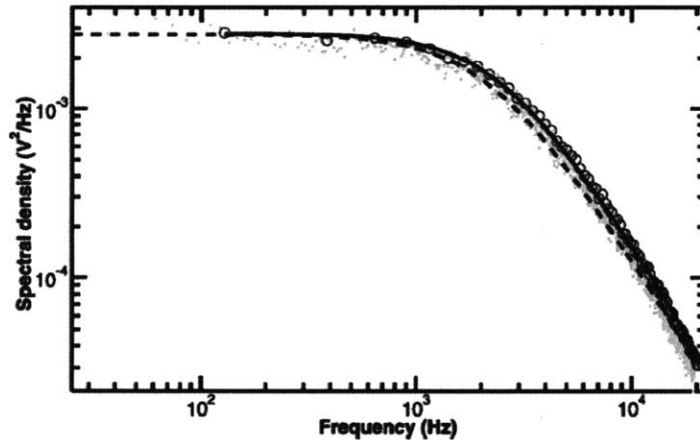


Figure 1.7 Power spectrum of a trapped bead [44]. The corner frequency can be related to the trap stiffness using equation 1.3.

The Lorentzian function gives the power spectrum as a function of frequency, $S(f)$.

$$S(f) = \frac{k_B T}{6\pi^3 \eta a (f_0^2 + f^2)} \quad (1.2)$$

The corner frequency, f_0 , is related to the trap stiffness using equation 1.3 [44].

$$f_0 = 12\pi^2 k_{\text{trap}} \eta a \quad (1.3)$$

This method can reveal the presence of noise invisible to the other methods, and can be used to monitor local heating by the trap [49, 50].

The third method (Stokes drag) relies on applying a frictional drag force to the bead by fluid flow as shown in figure 1.8 and measuring the corresponding bead displacement, x . Fluid flow is generally accomplished by moving the sample relative to the stationary trap using a piezoelectric microscope stage.

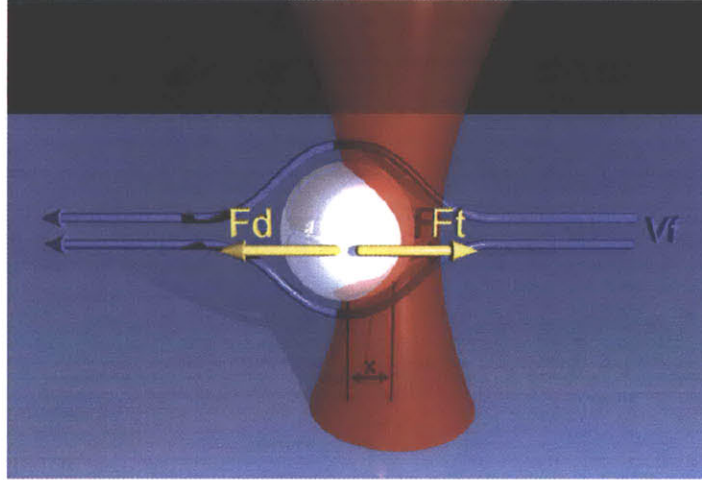


Figure 1.8 Stokes drag experiment. Fluid flow relative to the bead applied a frictional drag force, F_d , which is balance by the trap force, F_t . The trap stiffness can be determined by dividing F_d by the bead displacement, x .

The trap stiffness can then be determined using equation (1.4) where the drag force, $F_d = 6\pi\eta aV_f$ (Stokes drag equation for a sphere) is balanced by the trapping force, $F_t = k_{trap}x$, where η is the fluid viscosity, a is the bead radius, V_f is the fluid velocity, and k_{trap} is the trap stiffness.

$$6\pi\eta aV = k_{trap}x \tag{1.4}$$

Proximity to a surface, which is often the case in optical trapping experiments, alters the drag force according to Faxen's correction for flow parallel to the surface [44],

$$F_d = \frac{6\pi\eta aV_f}{\left[1 - \frac{9}{16}\left(\frac{a}{z_b}\right) + \frac{1}{8}\left(\frac{a}{z_b}\right)^3 - \frac{45}{256}\left(\frac{a}{z_b}\right)^4 - \frac{1}{16}\left(\frac{a}{z_b}\right)^5\right]} \tag{1.4}$$

where z_b is the distance from the center of the bead to the surface. This method is the slowest, but it allows for characterization of any nonlinearities in the trap stiffness as a function of bead displacement and the maximum force capacity of the instrument. A detailed review of these calibrations methods is provided elsewhere [44, 51].

1.3 OPTICAL TRAPPING INSTRUMENTATION:

The experiments in this thesis were performed on two different optical trapping instruments in the Lang Laboratory. These instruments were built around inverted microscope platforms (Nikon, Melville, NY) that were heavily modified to improve functionality and stability. One of the instruments was designed for combined force and fluorescence applications at a single molecule level. This device combines separate lasers for optical trapping (1064 nm 4W capacity; Coherent, Santa Clara, CA), position detection (975 nm; Corning Lasertron, Bedford, MA), and fluorescence excitation (532 nm and 488 nm; World Star Tech, Toronto, ON) through a base that has improved mechanical stability. In addition, the setup includes a pair of computer controlled acousto-optic deflectors (AODs; IntraAction, Bellwood, IL), which permit precise steering of the trapping beam in two dimensions, and remote-controlled flipper mirrors and shutters, which facilitate rapid switching between bright-field imaging (CCD camera; DAGE-MTI, Michigan City, IN) and fluorescence imaging (EMCCD camera; Andor Technology, South Windsor, CT), and a piezoelectric stage (Physik Instrumente, Auburn, MA). This instrument was used for the membrane tethering with fluorescence (Chapter 4) and the fluorescent amyloid fiber force-extension (Chapter 5) experiments.

Figure 1.9 shows a schematic layout of the instrument. Further details of the instrument design are given elsewhere [52].

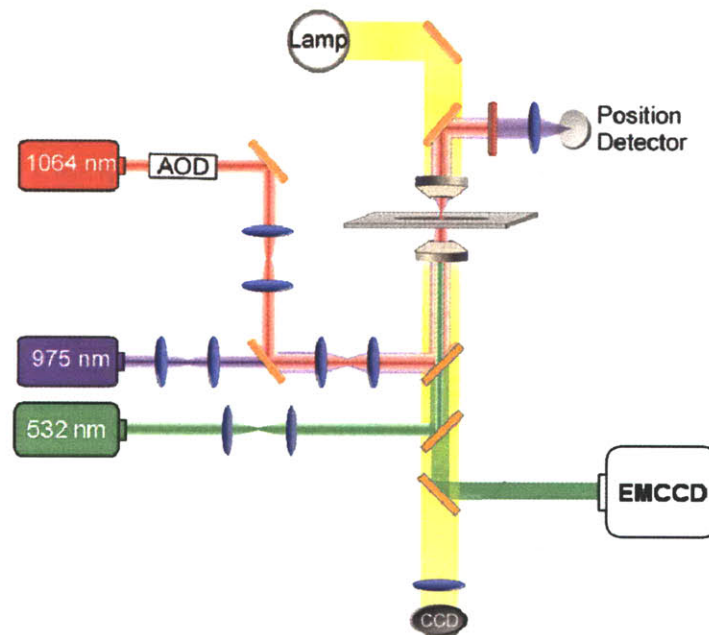


Figure 1.9 Schematic layout of optical trap instrument used for combined force and fluorescence imaging experiments

The second instrument was optimized for the application of large forces for experiments at the cellular length scale. This device utilizes a similar setup to the previously described instrument with a few key differences. First, the trapping laser (1064 nm 10W capacity; IPG Photonics, Oxford, MA) is split into two branches of approximately equal power using a cube polarizer (ThorLabs; Newton, NJ). One branch (primary branch) passes through AODs and was generally used for position calibration and trapping at forces up to ~ 100 pN. The second branch that does not pass through the AODs, avoiding the $\sim 50\%$ power loss, was used to achieve trapping forces up to ~ 250 pN. When employing the second branch, it was initially aligned with the primary branch (position of the second branch was independently using picomotors to move one of the

telescope lenses). Position calibrations were performed using the primary branch with AODs. The bead was then transferred to the secondary branch prior to performing a stiffness calibration, and the experiment was carried out with the secondary branch. Secondly, while fluorescence excitation was available on this instrument (532 nm), it was not utilized since the instrument lacked an EMCCD camera for highly sensitive fluorescence imaging. This instrument was used for the membrane tethering experiments which did not require fluorescence imaging (Chapters 3 and 4) and for the amyloid unfolding and rupture experiments at large forces (Chapter 5). Figure 1.10 shows a schematic layout of this optical trapping instrument.

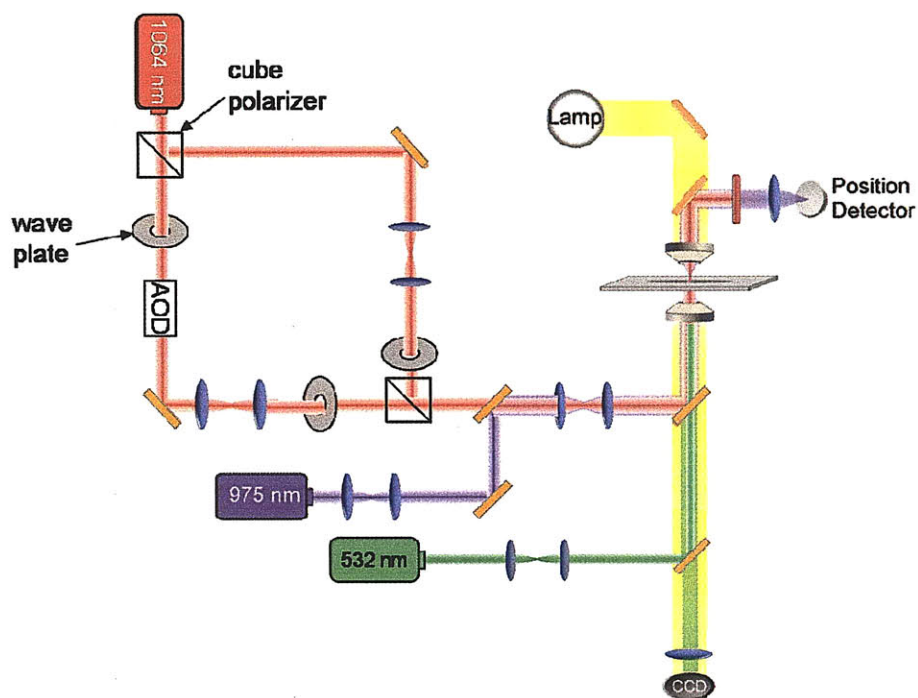


Figure 1.10 Schematic layout of the optical trap instrument used for large force applications.

1.4 REFERENCES

- [1] Martinac, B., 2004. "Mechanosensitive ion channels: molecules of mechanotransduction". *J Cell Sci.* **117**: p. 2449-2460.
- [2] Blount, P. and Moe, P. C., 1999. "Bacterial mechanosensitive channels: integrating physiology, structure and function". *Trends Microbiol.* **7**: p. 420-424.
- [3] Hamill, O. P. and Martinac, B., 2001. "Molecular basis of mechanotransduction in living cells". *Physiol Rev.* **81**: p. 685-740.
- [4] Barbee, K. A., Davies, P. F. and Lal, R., 1994. "Shear Stress-Induced Reorganization of the Surface-Topography of Living Endothelial-Cells Imaged by Atomic-Force Microscopy". *Circ Res.* **74**: p. 163-171.
- [5] McCue, S., Noria, S. and Langille, B. L., 2004. "Shear-induced reorganization of endothelial cell cytoskeleton and adhesion complexes". *Trends Cardiovas Med.* **14**: p. 143-151.
- [6] Ohashi, T. and Sato, M., 2005. "Remodeling of vascular endothelial cells exposed to fluid shear stress: experimental and numerical approach". *Fluid Dyn Res.* **37**: p. 40-59.
- [7] Ku, C. H., Johnson, P. H., Batten, P., Sarathchandra, P., Chambers, R. C., Taylor, P. M., Yacoub, M. H. and Chester, A. H., 2006. "Collagen synthesis by mesenchymal stem cells and aortic valve interstitial cells in response to mechanical stretch". *Cardiovasc Res.* **71**: p. 548-556.
- [8] Fleire, S. J., Goldman, J. P., Carrasco, Y. R., Weber, M., Bray, D. and Batista, F. D., 2006. "B cell ligand discrimination through a spreading and contraction response". *Science.* **312**: p. 738-741.
- [9] Ottani, V., Raspanti, M. and Ruggeri, A., 2001. "Collagen structure and functional implications". *Micron.* **32**: p. 251-260.
- [10] Gasser, T. C., Ogden, R. W. and Holzapfel, G. A., 2006. "Hyperelastic modelling of arterial layers with distributed collagen fibre orientations". *J Roy Soc Interface.* **3**: p. 15-35.
- [11] Hansen, K. A., Weiss, J. A. and Barton, J. K., 2002. "Recruitment of tendon crimp with applied tensile strain". *Journal of Biomechanical Engineering-Transactions of the Asme.* **124**: p. 72-77.
- [12] Sacks, M. S., 2003. "Incorporation of experimentally-derived fiber orientation into a structural constitutive model for planar-collagenous tissues". *Journal of Biomechanical Engineering-Transactions of the Asme.* **125**: p. 280-287.
- [13] De Vita, R. and Slaughter, W. S., 2007. "A constitutive law for the failure behavior of medial collateral ligaments". *Biomech Model Mechan.* **6**: p. 189-197.
- [14] Viidik, A., Danielsen, C. C. and Oxlund, H., 1982. "On Fundamental and Phenomenological Models, Structure and Mechanical-Properties of Collagen, Elastin and Glycosaminoglycan Complexes". *Biorheology.* **19**: p. 437-451.
- [15] Sanders, V. M., Snyder, J. M., Uhr, J. W. and Vitetta, E. S., 1986. "Characterization of the Physical Interaction between Antigen-Specific B-Cells and T-Cells". *J Immunol.* **137**: p. 2395-2404.
- [16] Dobson, C. M., 2003. "Protein folding and misfolding". *Nature.* **426**: p. 884-890.
- [17] Glover, J. R., Kowal, A. S., Schirmer, E. C., Patino, M. M., Liu, J. J. and Lindquist, S., 1997. "Self-seeded fibers formed by Sup35, the protein determinant of [PSI⁺], a heritable prion-like factor of *S-cerevisiae*". *Cell.* **89**: p. 811-819.

- [18] MacPhee, C. E. and Dobson, C. M., 2000. "Formation of mixed fibrils demonstrates the generic nature and potential utility of amyloid nanostructures". *Journal of the American Chemical Society*. **122**: p. 12707-12713.
- [19] Smith, J. F., Knowles, T. P. J., Dobson, C. M., MacPhee, C. E. and Welland, M. E., 2006. "Characterization of the nanoscale properties of individual amyloid fibrils". *Proceedings of the National Academy of Sciences of the United States of America*. **103**: p. 15806-15811.
- [20] Scheibel, T., Parthasarathy, R., Sawicki, G., Lin, X. M., Jaeger, H. and Lindquist, S. L., 2003. "Conducting nanowires built by controlled self-assembly of amyloid fibers and selective metal deposition". *Proceedings of the National Academy of Sciences of the United States of America*. **100**: p. 4527-4532.
- [21] Gras, S. L., Tickler, A. K., Squires, A. M., Devlin, G. L., Horton, M. A., Dobson, C. M. and MacPhee, C. E., 2008. "Functionalised amyloid fibrils for roles in cell adhesion". *Biomaterials*. **29**: p. 1553-1562.
- [22] Baxa, U., Speransky, V., Steven, A. C. and Wickner, R. B., 2002. "Mechanism of inactivation on prion conversion of the *Saccharomyces cerevisiae* Ure2 protein". *Proceedings of the National Academy of Sciences of the United States of America*. **99**: p. 5253-5260.
- [23] Sigurdsson, E. M., Wisniewski, T. and Frangione, B., 2002. "Infectivity of amyloid diseases". *Trends Mol Med*. **8**: p. 411-413.
- [24] Krishnan, R. and Lindquist, S. L., 2005. "Structural insights into a yeast prion illuminate nucleation and strain diversity". *Nature*. **435**: p. 765-772.
- [25] Ashkin, A., 1970. "Acceleration and Trapping of Particles by Radiation Pressure". *Phys Rev Lett*. **24**: p. 156-&.
- [26] Moffitt, J. R., Chemla, Y. R., Smith, S. B. and Bustamante, C., 2008. "Recent advances in optical tweezers". *Annu Rev Biochem*. **77**: p. 205-228.
- [27] Neuman, K. C. and Nagy, A., 2008. "Single-molecule force spectroscopy: optical tweezers, magnetic tweezers and atomic force microscopy". *Nat Methods*. **5**: p. 491-505.
- [28] Khalil, A. S., Appleyard, D. C., Labno, A. K., Georges, A., Karplus, M., Belcher, A. M., Hwang, W. and Lang, M. J., 2008. "Kinesin's cover-neck bundle folds forward to generate force". *P Natl Acad Sci USA*. **105**: p. 19247-19252.
- [29] Mehta, A. D., Rief, M., Spudich, J. A., Smith, D. A. and Simmons, R. M., 1999. "Single-molecule biomechanics with optical methods". *Science*. **283**: p. 1689-1695.
- [30] Abbondanzieri, E. A., Greenleaf, W. J., Shaevitz, J. W., Landick, R. and Block, S. M., 2005. "Direct observation of base-pair stepping by RNA polymerase". *Nature*. **438**: p. 460-465.
- [31] Asbury, C. L., Fehr, A. N. and Block, S. M., 2003. "Kinesin moves by an asymmetric hand-over-hand mechanism". *Science*. **302**: p. 2130-2134.
- [32] Khalil, A. S., Ferrer, J. M., Brau, R. R., Kottmann, S. T., Noren, C. J., Lang, M. J. and Belcher, A. M., 2007. "Single M13 bacteriophage tethering and stretching". *Proceedings of the National Academy of Sciences of the United States of America*. **104**: p. 4892-4897.
- [33] Wang, M. D., Yin, H., Landick, R., Gelles, J. and Block, S. M., 1996. "Stretching DNA with optical tweezers." *Biophysical Journal*. **70**: p. Sup63-Sup63.

- [34] Wen, J. D., Manosas, M., Li, P. T. X., Smith, S. B., Bustamante, C., Ritort, F. and Tinoco, I., 2007. "Force unfolding kinetics of RNA using optical tweezers. I. Effects of experimental variables on measured results". *Biophysical Journal*. **92**: p. 2996-3009.
- [35] Baumann, C. G., Smith, S. B., Bloomfield, V. A. and Bustamante, C., 1997. "Ionic effects on the elasticity of single DNA molecules". *Proceedings of the National Academy of Sciences of the United States of America*. **94**: p. 6185-6190.
- [36] Lee, H., Pelz, B., Ferrer, J. M., Kim, T., Lang, M. J. and Kamm, R. D., 2009. "Cytoskeletal Deformation at High Strains and the Role of Cross-link Unfolding or Unbinding". *Cellular and Molecular Bioengineering*. **2**: p. 28-38.
- [37] Ferrer, J. M., Lee, H. S., Chen, J., Kamm, R. D. and Lang, M. J., 2007. "Mapping the F-actin and actin binding proteins interactions: From macromechanics to single molecule biophysics". *Biophys J*: p. 303a-303a.
- [38] Ferrer, J. M., Lee, H., Chen, J., Pelz, B., Nakamura, F., Kamm, R. D. and Lang, M. J., 2008. "Measuring molecular rupture forces between single actin filaments and actin-binding proteins". *P Natl Acad Sci USA*. **105**: p. 9221-9226.
- [39] Raucher, D. and Sheetz, M. P., 1999. "Characteristics of a membrane reservoir buffering membrane tension". *Biophys J*. **77**: p. 1992-2002.
- [40] Li, Z. W., Anvari, B., Takashima, M., Brecht, P., Torres, J. H. and Brownell, W. E., 2002. "Membrane tether formation from outer hair cells with optical tweezers". *Biophys J*. **82**: p. 1386-1395.
- [41] Ashkin, A., Dziedzic, J. M. and Yamane, T., 1987. "Optical Trapping and Manipulation of Single Cells Using Infrared-Laser Beams". *Nature*. **330**: p. 769-771.
- [42] Ashkin, A. and Dziedzic, J. M., 1987. "Optical Trapping and Manipulation of Viruses and Bacteria". *Science*. **235**: p. 1517-1520.
- [43] Holm, A., Sundqvist, T., Oberg, A. and Magnusson, K. E., 1999. "Mechanical manipulation of polymorphonuclear leukocyte plasma membranes with optical tweezers causes influx of extracellular calcium through membrane channels". *Med Biol Eng Comput*. **37**: p. 410-412.
- [44] Neuman, K. C. and Block, S. M., 2004. "Optical trapping". *Rev Sci Instrum*. **75**: p. 2787-2809.
- [45] Kellermayer, M. S. Z., Smith, S. B., Granzier, H. L. and Bustamante, C., 1997. "Folding-unfolding transitions in single titin molecules characterized with laser tweezers". *Science*. **276**: p. 1112-1116.
- [46] Onoa, B., Dumont, S., Liphardt, J., Smith, S. B., Tinoco, I. and Bustamante, C., 2003. "Identifying kinetic barriers to mechanical unfolding of the T-thermophila ribozyme". *Science*. **299**: p. 1892-1895.
- [47] Woodside, M. T., Anthony, P. C., Behnke-Parks, W. M., Larizadeh, K., Herschlag, D. and Block, S. M., 2006. "Direct measurement of the full, sequence-dependent folding landscape of a nucleic acid". *Science*. **314**: p. 1001-1004.
- [48] Boltzmann, L., 1871. "Einige allgemeine Satze uber Warmegleichgewicht (Some general statements on thermal equilibrium)." *Wiener Berichte*. **63**: p. 679-711.
- [49] Peterman, E. J. G., Gittes, F. and Schmidt, C. F., 2003. "Laser-induced heating in optical traps". *Biophysical Journal*. **84**: p. 1308-1316.
- [50] Abbondanzieri, E. A., Shaevitz, J. W. and Block, S. M., 2005. "Picocalorimetry of transcription by RNA polymerase". *Biophysical Journal*. **89**: p. L61-L63.

- [51] Svoboda, K. and Block, S. M., 1994. "Biological applications of optical forces". *Annu Rev Biophys Biomol Struct.* **23**: p. 247-85.
- [52] Brau, R. R., Tarsa, P. B., Ferrer, J. M., Lee, P. and Lang, M. J., 2006. "Interlaced optical force-fluorescence measurements for single molecule biophysics". *Biophys J.* **91**: p. 1069-1077.

Chapter 2

An Elastica Approximate for Fibers and Fibrous Networks

2.1 INTRODUCTION:

Single fiber or chain mechanics play an important role in defining the mechanical response of biological molecules and networks, synthetic polymer networks, as well as woven and non-woven textiles. Single fiber mechanics has widely been approached by a consideration of the free energy of extension. In general, extension contributes to the free energy of the fiber in two ways: 1) a reduction in entropy due to a decrease in number of possible configurations a fiber may occupy with increasing extension, and 2) a change in enthalpy due to fiber deformation. The most commonly used models in molecular mechanics are the freely-jointed chain (FJC) model [53, 54] and the worm-like chain (WLC) model [55-57]; these models are based on entropic elasticity. Many biological and synthetic fibers have a limited configurational space and hence their mechanical behavior is dominated by changes in enthalpy; these fibers typically possess an initially wavy or crimped structure due to either growth or processing (figure 2.1). When force is applied to the fiber ends, the increase in fiber end-to-end distance is due to the unbending of the wavy structure. Hence, an Euler elastica model [58-65] is the physically appropriate representation of the force-extension behavior during fiber

straightening. However, the elastica solution is an integral formulation and is not easily incorporated into models of systems of fibers such as fibrous networks or assemblies. An analytical approximation to the elastica model would be useful to concisely describe the mechanical behavior of the fibers and fibrous networks of interest.

Previous work to develop simplified models of the straightening out of initially curved fibers has been focused on collagen and soft tissues such as tendon that contain crimped collagen fibers. The nature of the crimped geometry gives collagen the highly nonlinear mechanical response characteristic of an elastica. Initially the waves in the crimped structure are unbent with little resistance. As the fiber approaches a straight configuration, the response becomes much stiffer because the straightened fiber now exhibits a substantial resistance to direct axial stretching. This nonlinearity makes it difficult to provide a simple, non-integral expression for the force-extension behavior of collagen and other fibers of similar geometry. Diamant et al [66] and Comninou and Yannas [67] derived analytical solutions for fibers of specific planar geometries. Specifically, Diamant et al considered a fiber with a planar zigzag geometry, and Comninou and Yannas derived an analytical stress-strain relation for the case of a sinusoidal fiber with a small initial crimp allowing for extensibility. Lanir [68, 69] generalized the model to include the mechanical interactions between a surrounding matrix and the fiber and the role of elastin. Buckley et al [64] derived elastica-based numerical solutions for several geometries ranging from a planar zigzag to a fiber consisting of circular arcs (similar to figure 2). Stouffer et al [70] developed a model based on extensible links and torsional springs and applied this model to human patellar

tendon-bone units. However, with this approach, geometrical information about the fiber cannot be found from data fitting. More recently, Hurschler et al [71] developed a seven parameter constitutive model to describe tendon and ligament. Simplified versions of this model were fit to data to obtain both material properties and geometrical information. Cacho et al [72] derived a constitutive model for a general fiber geometry with a random crimp wavelength that includes fiber failure. However, the Cacho et al model cannot be solved analytically. Bertoldi and Boyce [73] recently presented a simplified analytical expression for the force-induced unbending of the biological filaments in mussel byssal threads which is then followed by direct axial stretching and the unfolding of folded domains. Garikipati et al [65] followed a similar approach to the force-induced unbending approximation in Bertoldi and Boyce, deriving an analytical strain energy function for crimped collagen fibers. Their model is subject to the constraint that the fiber is always circular or always sinusoidal during the unbending phase. Constitutive models have also been developed for helical geometries. Specifically, Beskos and Jenkins [74] developed a model based on a helical geometry for mammalian tendon, and Freed et al [75] derived an analytical strain energy function using Castigliano's theorem for a helical spring.

In this work we present an approximation to the elastica solution that provides a direct analytical axial force-extension relationship for the case of the unbending of wavy filaments such as those shown in figure 2.1. Our elastica approximate for fiber force-extension behavior is then extended to capture the important contributions of fiber elongation after fiber straightening. As an example application, our proposed elastica-

based force-extension relationship is compared to experimental data on a crimped collagen fascicle, enabling separate reduction of a fiber axial stiffness and bending stiffness, giving insights into the hierarchical microstructure of the fiber. Finally, the fiber force-extension relationship is used together with a network model to provide an expression for the stress-strain behavior of filamentous networks.

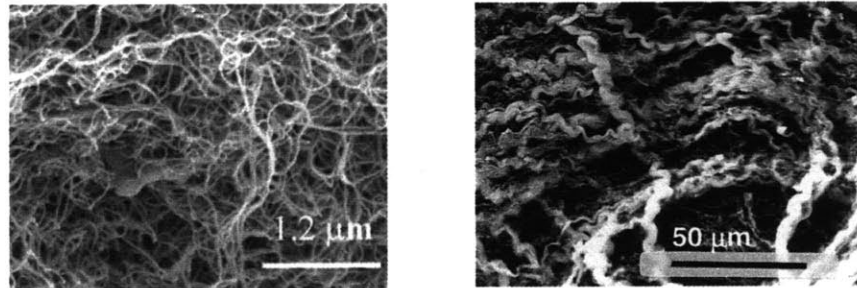


Figure 2.1 Fibers with wavy geometry. Fibers of interest include synthetic fibers such as (a) carbon nanotubes [76] or biological structures such as (b) the crimped collagen fibers found in the connectival stroma of the small intestine [9].

2.2 THE ELASTICA APPROXIMATE MODEL (EAM):

The wavy fibers of interest can be approximated by initially circular arcs which extend an angle 2α , each of radius ρ , and subjected to end forces as shown figure 2. Taking advantage of the symmetry of this wavy geometry, the force-extension behavior can be determined using the elastica solution for the case of an inextensible cantilevered arch of initial curvature $-1/\rho$ that is then unbent by application of end force $\pm F$. Our coordinate system is depicted in figure 2, where x is the horizontal position from the cantilevered end and y is the vertical distance from the point of load application (hence this position moves vertically as the beam deforms). A more general geometry is considered Appendix A where the circular arcs are connected by straight segments.

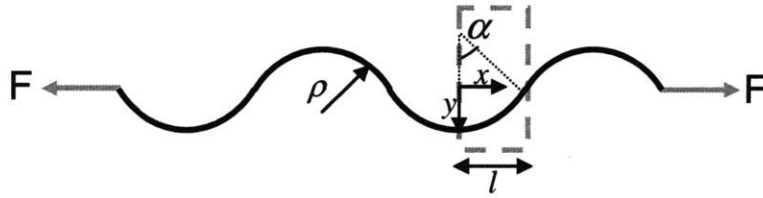


Figure 2.2 Geometry used to approximate the wavy fibers of interest.

2.2.1 Review of the Elastica Solution. The elastica solution for this problem as presented in [58] is reviewed here. Our coordinate system is depicted in figure 2.2, where x is the horizontal position from the cantilevered end and y is the vertical distance from the point of load application (hence this position moves vertically as the beam deforms). The sign convention used here results in a positive curvature when the beam is bent downward. The positive moment convention is taken to cause a positive curvature. The relationship between the change in curvature and the moment at any point along the beam is given by:

$$\frac{\partial^2 y}{\partial x^2} \left[1 + \left(\frac{\partial y}{\partial x} \right)^2 \right]^{\frac{3}{2}} + \frac{1}{\rho} = k^2 y \quad (2.1)$$

where $k^2 = \frac{F}{EI}$ and EI is the effective bending stiffness of the beam. Integrating

equation (2.1) and noting that $y = 0$ at the free end (end B) and calling $\frac{\partial y}{\partial x} = y'_B$ at end B,

gives

$$\left(1 + \left(\frac{\partial y}{\partial x}\right)^2\right)^{\frac{1}{2}} = -\frac{k^2}{2} \left(z^2 - \frac{1}{4k^4 \rho^2}\right) + C \quad (2.2)$$

where $C = \left(1 + (y'_B)^2\right)^{\frac{1}{2}}$ and $z = y - \frac{1}{k^2 \rho}$. A substitution of variables, calling

$$\frac{k^2}{2} \left(z^2 - \frac{1}{k^4 \rho^2}\right) - C = \cos(2\theta), \quad (2.3)$$

and substituting equation (2.3) into equation (2.2) gives:

$$\left(1 + \left(\frac{\partial y}{\partial x}\right)^2\right)^{\frac{1}{2}} = -\frac{1}{\cos(2\theta)} = \frac{1}{2\sin^2 \theta - 1} \quad (2.4)$$

At the cantilevered end (end A), $\frac{\partial y}{\partial x} = 0$ giving $\theta_A = \frac{\pi}{2}$. At end B, $\frac{\partial y}{\partial x} = y'_B$ which gives

$\theta_B = \frac{1}{2} \arccos(-C)$. Using a second substitution of variables, calling

$$\frac{2}{p^2} = 1 + C + \frac{1}{2k^2 \rho^2}, \quad (2.5)$$

Equation (2.3) then becomes:

$$z = -\frac{2}{pk} (1 - p^2 \sin^2 \theta)^{\frac{1}{2}} \quad (2.6)$$

The slope of the beam at any given point, determined from equation (2.4) is:

$$\frac{dy}{dx} = \frac{2 \sin \theta \cos \theta}{2 \sin^2 \theta - 1} \quad (2.7)$$

Taking the beam to be inextensible, its contour length, L_C , at any force can be described by the arc length formula:

$$L_C = \int_A^B ds = \int_{x_A}^{x_B} \left(1 + \left(\frac{dy}{dx} \right)^2 \right)^{\frac{1}{2}} dx \quad (2.8)$$

which after combination with equation (2.7) reduces to:

$$L_C = \frac{p}{k} \int_{\frac{\pi}{2}}^{\theta_B} (1 - p^2 \sin^2 \theta)^{\frac{1}{2}} d\theta \quad (2.9)$$

The end-to-end distance of the beam, l , is given by:

$$l = \int_{x_A}^{x_B} dx = \int_{\frac{\pi}{2}}^{\theta_B} \frac{dx}{dy} \frac{dy}{d\theta} d\theta \quad (2.10)$$

From the definition of z , we can see that $\frac{dy}{d\theta} = \frac{dz}{d\theta}$, and hence, $\frac{dy}{d\theta}$ is obtained from equation (2.6).

$$\frac{dy}{d\theta} = \frac{p}{k} 2 \sin \theta \cos \theta (1 - p^2 \sin^2 \theta)^{\frac{1}{2}} \quad (2.11)$$

Combining equations (2.7), (2.10), and (2.11) yields:

$$l = \int_{\frac{\pi}{2}}^{\theta_b} \frac{p}{k} (2 \sin^2 \theta - 1) (1 - p^2 \sin^2 \theta)^{\frac{1}{2}} d\theta \quad (2.12)$$

The substituted variable, p , which is a function of F , can be solved iteratively using equation (2.9) since the length of the beam is known. Once p is found, equation (2.12) can be numerically integrated to calculate l as a function of F (recall that k^2 is a normalized force ($k^2 = \frac{F}{EI}$)). Here the bisection method was used to solve for p from equation (2.9), and a trapezoidal method was used to integrate equation (2.12). In the following analyses the angle α was kept constant at 90° for simplicity. However, the model developed is general for $0 \leq \alpha \leq 90^\circ$. The effect of varying this angle is addressed in figure 2.7. Figure 2.3(a) shows the results for the fiber force normalized by dividing by $\frac{EI}{\rho^2}$ which collapses different geometries and material properties onto a single curve for the inextensible elastica solution. These results are compared to a finite element (FE) solution for the geometry of interest. Figure 2.3(b) explicitly

demonstrates the effects of varying the geometry. The geometry is defined in terms of the non-dimensional parameter $\tilde{\rho} = \frac{\rho}{\sqrt[4]{I}}$. For this analysis, I is left constant, and ρ is varied. This parameter can also be varied by changing the cross-sectional dimensions. The effects of varying cross-sectional shape are addressed in Section 2.2.6. All results are plotted versus the stretch, λ , which is the ratio of the current end-to-end distance, l , to the initial end-to-end distance, l_0 (in this case $l_0 = \rho$). Figure 2.3 (a) also shows the fiber geometry at different stages of stretch. Figure 2.3(b) shows the initial geometries drawn to scale with respect to each other, and the inset graph shows the error as the ratio of the force calculated from the elastica solution, $F_{elastica}$, to the force from the FE solution, F_{FE} .

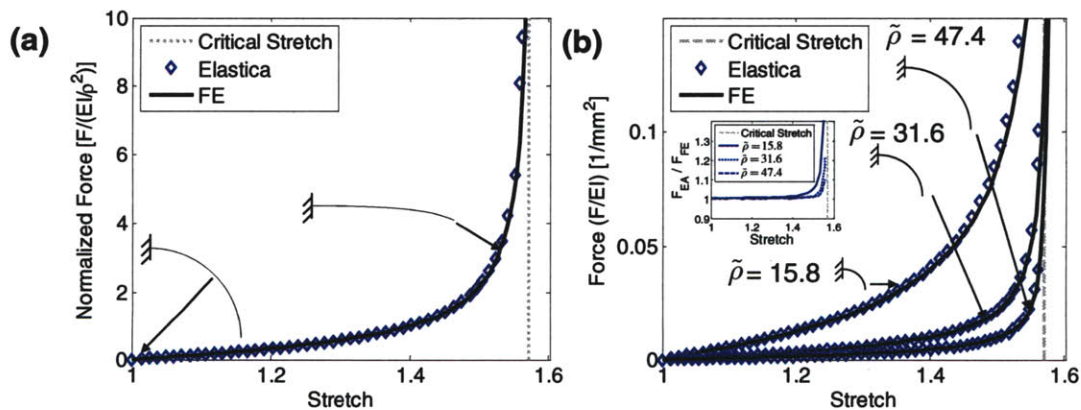


Figure 2.3 The numerical elastica solution is compared to the FE solution for the force of unbending a fiber. A1(a) shows a normalized force where all geometries collapse onto a single curve with the undeformed and a deformed geometry shown, and (b) shows the fiber force vs. extension behavior for three geometries: $\tilde{\rho} = 15.8$, $\tilde{\rho} = 31.6$, and $\tilde{\rho} = 47.4$ where $\tilde{\rho} = \frac{\rho}{\sqrt[4]{I}}$. A1(b) also shows the beam initial geometries to scale with respect to each other, and the inset shows the error between the elastica predicted force and the FE force.

The elastica and *FE* solutions are shown to be coincident for small and moderate extensions and begin to diverge when the beam approaches the critical stretch, λ_C , where λ_C is defined as $\frac{L_C}{l_0}$. This discrepancy occurs because the axial stretching of the beam is neglected in the elastica solution and is included in the *FE* solution. Axial stretching will be incorporated into the elastica-based model later in this paper. Nevertheless, the elastica solution accurately describes the force of unbending the wavy fiber up to large extensions. The inset plot of figure 2.3(b) shows the ratio of $F_{elastica}$ to F_{FE} for the three geometries considered, further highlighting the excellent agreement; for the worst case ($\rho = 5$), this ratio is less than 1.1 for 88% of its full extension, which we define to be when $\lambda = \lambda_C$ (in other words, up to a stretch of 1.50 where the fully extended stretch is 1.57). However, this elastica solution required numerical integration and is not convenient for simple data fitting to determine fiber mechanical properties. Additionally, the fact remains that fibers often exist as a part of a network in biological and synthetic structures, or as a part of a woven structure in textiles. It is impractical to incorporate the full elastica solution into a network model. A simple 1D direct analytical expression for the fiber force-extension constitutive relationship to approximate this elastica solution is desirable.

In order to simplify the analysis of such wavy fibers, it is desired to develop an analytical approximation for the force-extension behavior of wavy fibers based on the elastica solution. To develop the desired 1D equivalent model, two limiting cases are considered: first, the limit of small extension (*SE*) where the geometry is taken as fixed and the linear elastic solution is obtained; and second, the limit of large force (*LF*) when

l approaches the contour length L_C where $L_C = \rho\alpha$. An analytical solution is derived for each limiting case and a constitutive model that covers the entire range of deformation is established by combining the two limiting solutions. This model achieves an accurate estimate of the elastica solution. The axial stretching which occurs once the fiber is nearly straight is then incorporated.

2.2.2 Limit of Small Extension (SE). In the limit of small extension (SE), the linear elastic solution can be used to provide an expression for the Force-Stretch behavior of the wavy fiber. It can be shown that normal and shear section force contributions to the strain energy of the fiber are negligible compared to the bending moment contribution to the strain energy. The strain energy in the SE limit, U_{SE} , can thus be calculated by integrating the moment contribution over the arc length:

$$U_{SE} = \frac{1}{2EI} \int_0^{l_c} M^2 ds = \frac{1}{2EI} \int_{\frac{\pi}{2}-\alpha}^{\frac{\pi}{2}} [F\rho(\sin\phi - \cos\alpha)]^2 \rho d\phi \quad (2.13)$$

where s is the coordinate along the arc length. Integration gives:

$$U_{SE} = \frac{K_B}{2} l_0^2 (\lambda - 1)^2 \quad (2.14)$$

where the initial stiffness of the wavy configuration is:

$$K_B = \frac{EI}{\rho^3 \left[(\alpha) \left(1 + \frac{1}{2} \cos(2\alpha) \right) - \frac{3}{4} \sin(2\alpha) \right]} \quad (2.15)$$

Differentiation of the strain energy expression with respect to l gives the fiber force, F_{SE} , versus fiber stretch, λ , relationship for the small extension limit.

$$F_{SE} = K_B l_0 (\lambda - 1) \quad (2.16)$$

Figure 2.4 shows the SE solution for the fiber force-stretch behavior compared to the elastica solution for three different geometries with $\tilde{\rho} = 15.8$, $\tilde{\rho} = 31.6$, and $\tilde{\rho} = 47.4$ (α was kept constant at 90°).

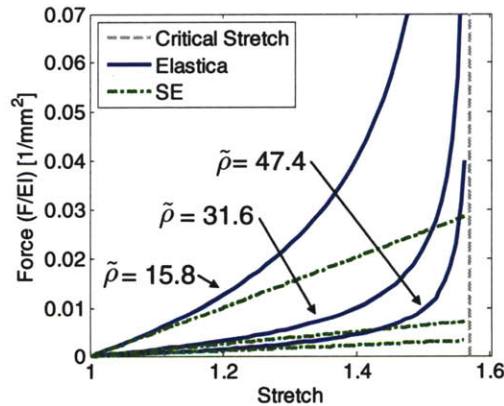


Figure 2.4 The linear elastic SE solution for the fiber force vs. stretch compared to the elastica solution for three different geometries: $\tilde{\rho} = 15.8$, $\tilde{\rho} = 31.6$, and $\tilde{\rho} = 47.4$ where

$$\tilde{\rho} = \frac{\rho}{\sqrt[4]{I}}.$$

2.2.3 Limit of Large Forces (LF). In order to evaluate the behavior of the fiber in the limit when l approaches L_C , we consider the limiting behavior of the elastica solution at

very large forces (LF). An analytical expression in this limit would be useful to simplify the use of the model for describing single fiber mechanics. From equation (2.5), we observe that as $F \rightarrow 0$, $\rho \rightarrow 0$, and as $F \rightarrow \infty$, $\rho \rightarrow 1$. At large forces, $\rho \rightarrow 1$ and equation (2.5) can be simplified and used together with the expression for θ_B to obtain a direct expression for $\sin \theta_B$.

$$\sin \theta_B = \left(1 - \frac{1}{4k^2 \rho^2}\right)^{\frac{1}{2}} \quad (2.17)$$

Equation (2.9) can also be simplified by taking the limit as $\rho \rightarrow 1$ and becomes:

$$L_C = \frac{1}{k} \int_{\frac{\pi}{2}}^{\theta_B} (\cos \theta)^{-1} d\theta \quad (2.18)$$

Additionally, equation (2.12) can be simplified by substituting $\rho = 1$. After some simplification, this substitution yields:

$$l = \frac{1}{k} \int_{\frac{\pi}{2}}^{\theta_B} [(\cos \theta)^{-1} - 2 \cos \theta] d\theta = L_C - \frac{2}{k} (1 - \sin \theta_B) \quad (2.19)$$

Combining equations (2.17) and (2.19) results in an expression for l as a function of EI , F , and ρ that approximates the exact elastica numerical solution at large forces.

$$l = L_c - \frac{2}{k} \left[1 - \left(1 - \frac{1}{4k^2 \rho^2} \right)^{\frac{1}{2}} \right] \quad (2.20)$$

Using a series expansion of the square root term and neglecting higher order terms with the assumption that $\frac{1}{4k^2 \rho^2} \ll 1$, gives:

$$l - L_c = -\frac{1}{4\rho^2} \left(\frac{EI}{F} \right)^{\frac{3}{2}} \quad (2.21)$$

Inverting equations (2.21) results in a direct expression for the force as a function of stretch valid in the *LF* limit where $\lambda_c = \frac{L_c}{l_0}$:

$$F_{LF} = EI \left[4\rho^2 l_0 (\lambda_c - \lambda) \right]^{\frac{2}{3}} \quad (2.22)$$

Figure 2.5 compares the results for the *LF* approximation (used over the entire range of extension) to the exact elastica solution for three different geometries with $\tilde{\rho} = 15.8$, $\tilde{\rho} = 31.6$, and $\tilde{\rho} = 47.4$ (α was kept constant at 90°). As expected, the *LF* limit expression fails to capture the behavior from small to moderate extensions, but converges to the exact elastica solution at large forces; in particular, in the regime where $\lambda > 0.9\lambda_c$.

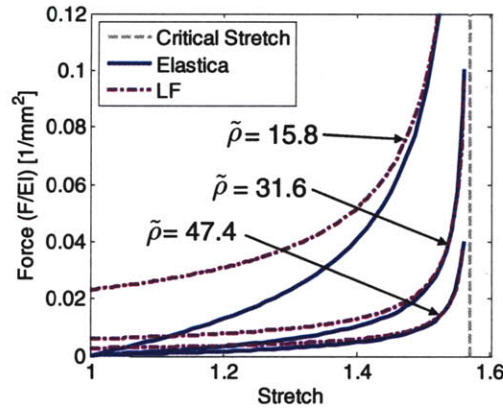


Figure 2.5 The *LF* approximation for the fiber force vs. stretch compared to the elastica solution for three different geometries: $\tilde{\rho} = 15.8$, $\tilde{\rho} = 31.6$, and $\tilde{\rho} = 47.4$ where $\tilde{\rho} = \frac{\rho}{\sqrt[4]{I}}$.

2.2.4 Composite Small Extension and Large Force Limits.

From the results in

figures 2.4 and 2.5 it is evident that the force-extension behavior for the unbending of a fiber could be obtained by constructing a composite function that is governed by the *SE* limit at small extensions and then dominated by the *LF* approximation as l approaches L_C . To achieve this end, we take the following approach:

$$F = F_{SE} + F_{LF}W(\lambda) \quad (2.23)$$

where $W(\lambda)$ is a weighting function that satisfies the following conditions:

$$W(\lambda) = \begin{cases} 0 & \lambda = 1 \\ 1 & \lambda = \lambda_c \end{cases} \quad (2.24)$$

Using these constraints we can find an appropriate solution for the force as a function of the fiber stretch.

$$F = F_{SE} + F_{LF} \left(\frac{\lambda - 1}{\lambda_c - 1} \right)^n \quad (2.25)$$

As $\lambda \rightarrow \lambda_c$, the *SE* solution becomes small compared to the *LF* approximation.

Therefore, the *SE* solution was not weighted to eliminate its contribution in this regime.

Substituting equations (2.16) and (2.22) into equation (2.25), we find the force-extension relationship:

$$F = K_B l_0 (\lambda - 1) + EI \left(4\rho^2 l_0 (\lambda_c - \lambda) \right)^{\frac{2}{3}} \left(\frac{\lambda - 1}{\lambda_c - 1} \right)^n \quad (2.26)$$

This model can accurately describe the mechanical behavior of the extension of the single fiber shown in figure 2.2. The exponent on the weight is left as a fitting parameter to be used in order to minimize the deviation between the model prediction and the exact elastica solution. A parameter to measure the deviation of the elastica approximate model (*EAM*) from the exact elastica solution was introduced for the purpose of optimizing n . This parameter is defined as:

$$\sigma = \frac{1}{N} \sum_{i=1}^N \left(\frac{F_{EAM,i}}{F_{elastica,i}} - 1 \right)^2 \quad (2.27)$$

where N is the total number of points used. If the *EAM* perfectly describes the elastica solution, then $\sigma = 0$. Figure 2.6(a) shows the normalized fiber force vs. stretch results of the *EAM* compared to the exact numerical elastica solution for $n = 1.0, 2.5,$ and 4.0 . The inset shows the ratio of $F_{EAM}/F_{elastica}$ for varying n . n was optimized by a simple trial and error method of varying n in increments of 0.25 to minimize σ . The optimal value of n was found to be 2.5 , where the ratio $F_{EAM}/F_{elastica}$ is between 0.9 and 1.1 over the entire extension. Figure 2.6(b) illustrates the effects of changing the crimp geometry on fiber force for the cases of $\tilde{\rho} = 15.8, \tilde{\rho} = 31.6,$ and $\tilde{\rho} = 47.4$ with $n = 2.5$ (α was kept constant at 90°) where $\tilde{\rho} = \frac{\rho}{\sqrt[4]{I}}$ is the non-dimensional radius. The *EAM* is successful in capturing the strong influence of ρ on both the initial stiffness and the nonlinear stiffening of the fiber force-extension behavior.

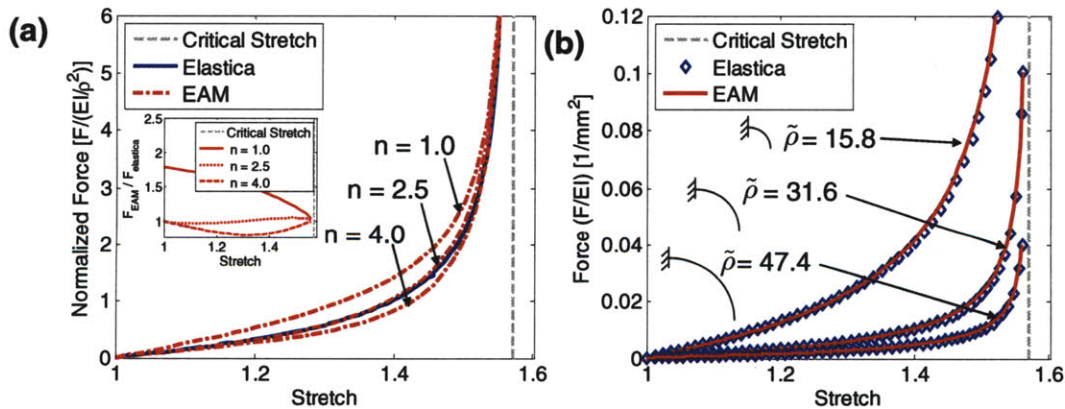


Figure 2.6 The *EAM* solution for the fiber force vs. stretch compared to the exact elastica solution. 4(a) shows the normalized force where the three geometries overlap and the effects of varying the fitting parameter, n . The inset shows the ratio of F_{EAM} to $F_{elastica}$. The optimal result for the fitting parameter is $n = 2.5$. 4(b) shows the fiber force vs. stretch with $n = 2.5$ for three different geometries, $\tilde{\rho} = 15.8, \tilde{\rho} = 31.6,$ and $\tilde{\rho} = 47.4$

where $\tilde{\rho} = \frac{\rho}{\sqrt[4]{I}}$, which are drawn to scale with respect to each other.

2.2.5 Incorporating Axial Stretching. The elastica approximation developed provides excellent agreement with the exact elastica solution. However, due to the assumption that the fiber is inextensible, the elastica solution asymptotically approaches infinite force as $\lambda \rightarrow \lambda_c$. A contribution to extension from direct axial stretching of the straightened fiber can be added to the extension from unbending following either an approach taking a multiplicative decomposition of the stretch (Bertoldi and Boyce [73]) or an approach taking an additive decomposition of the end-to-end displacement such as that used in the modified Wormlike Chain model [57] and the modified Freely Jointed Chain model [54]. Here, an additive decomposition is used, where equations of compatibility and equilibrium give:

$$\delta_{tot} = \delta_A + \delta_B \quad (2.28)$$

$$F_{tot} = F_A = F_B \quad (2.29)$$

where the subscript A indicates the axial stretching contribution and the subscript B indicates the bending contribution; δ_i and F_i are the change in length and the force, respectively. The resulting expression for the force of extending the fiber is then given by:

$$F = K_B l_0 \left(\lambda - 1 - \frac{F \lambda_c}{EA} \right) + EI \left[4 \rho^2 l_0 \left(\lambda_c - \lambda + \frac{F \lambda_c}{EA} \right) \right]^{\frac{2}{3}} \left(\frac{\lambda - 1 - \frac{F \lambda_c}{EA}}{\lambda_c - 1} \right)^n \quad (2.30)$$

where $\frac{EA}{L_c}$ is the effective axial stiffness of the straight fiber. Figure 2.7 shows results for the complete model compared to the corresponding finite element (*FE*) solution, for $\tilde{\rho} = 15.8$, $\tilde{\rho} = 31.6$, and $\tilde{\rho} = 47.4$ (α was kept constant at 90°). The *FE* solution was obtained using the software ABAQUS, where the beam was discretized with 39 three-node quadratic beam elements (ABAQUS type B22 elements).

Figure 2.7(a) shows the normalized fiber force versus stretch behavior. The optimal fitting parameter was $n = 2.5$. The inset in figure 2.7(a) shows the contributions of the unbending and axial stretching to the total fiber deformation. The fiber deforms through the nonlinear stiffening region (toe region) by unbending. The axial stretch is negligible until the fiber unbends to its contour length. Hence, the mechanical behavior in the toe region, which is the region of physiological function for many biological wavy fibers such as the collagen fibers in tendon [14], is dominated by the unbending mechanics of the crimp pattern. For the previous analyses, the angle α was set to be 90° . However, as seen in figure 2.1, this is not always the case for biological or synthetic fibers of interest. The described model is applicable for fibers with $0 < \alpha < 90^\circ$, where these limits correspond to a completely straight fiber and a fiber made of semicircular arcs respectively. Figure 2.7(b) shows the results for normalized fiber force for three geometries $\alpha = 60^\circ$, $\alpha = 45^\circ$, and $\alpha = 30^\circ$ with optimal values for n of 2.5, 2.5, and 2.25

respectively. The arc radius and cross-sectional dimensions were held constant such that $\tilde{\rho} = 31.6$. The results no longer collapse to a single curve for the normalized force because α affects both the critical stretch and the initial stiffness of the wavy configuration, K_B . These effects are accurately captured by the proposed model. For all three cases, the force ratio is between 0.9 and 1.1 over the entire extension for the three geometries examined.

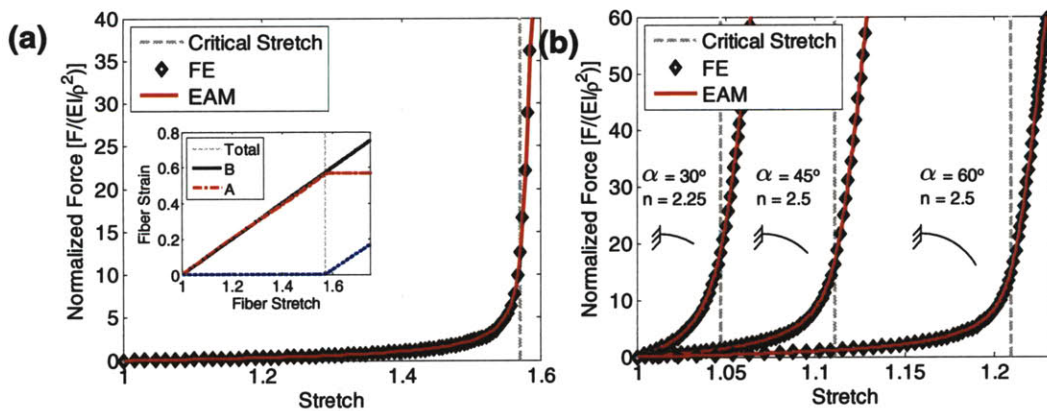


Figure 2.7 The *EAM* solution with axial stretching included for the fiber force vs. stretch compared to the *FE* solution. 5(a) shows the normalized force where the three geometries overlap. The optimal result for the fitting parameter is $n = 2.5$. The inset shows the contributions of the unbending (B) and axial stretching (A) to the total deformation of the fiber. 5(b) shows the fiber force vs. stretch for three geometries: $\alpha = 60^\circ$, $\alpha = 45^\circ$, and $\alpha = 30^\circ$. The arc radius and cross-section dimensions were kept constant ($\tilde{\rho} = 31.6$ where $\tilde{\rho} = \frac{\rho}{\sqrt[4]{I}}$), and the optimal n values are given.

2.2.6 Cross-sectional Geometry and Micro-Structural Hierarchy. As previously mentioned, the non-dimensional parameter, $\tilde{\rho}$, can be varied by changing the fiber arc radius, ρ , or by changing the cross-sectional dimensions. The cross-sectional dimensions affect both the effective bending stiffness, EI , and the effective axial stretching stiffness, EA . Natural and synthetic fibers have different cross-sectional shapes which govern I , and hence, affect the initial stiffness of the force-extension

curve; whereas the cross-sectional area governs the slope at large extensions. Furthermore, many fibers, specifically collagen fibers, contain structural hierarchy, and hence the macroscopic fiber cross-section may be divided into several substructures. The EAM is still useful to describe these bundled fibers. In order to illustrate the effects of fiber cross-sectional geometry and structural hierarchy, two parametric studies were performed. First, the fiber cross-sectional area, A , was held constant while the cross-section area moment of inertia, I , was varied by changing the cross-sectional shape. For this case, α was set to be 90° , ρ was held constant, and the fitting parameter was $n = 2.5$. The effects of varying I (cross-sectional shape) are shown in figure 2.8(a).

In the second case, the total fiber cross-sectional area was fixed and we compare the cases where the fiber was subdivided into rigidly coupled (RC) or uncoupled (UC) sub-fibers. The degree of coupling between fibers is determined by the bonded vs. non-bonded interactions of the sub-fibers. If the sub-fibers are RC then the force-extension behavior of the bundle is equivalent to that of a homogeneous fiber with the cross-sectional dimensions of the bundle. If the fibers are not bonded and free to slide past each other, the individual fiber deformation is decoupled from the others, and the bending stiffness of the bundle is simply the sum of the bending stiffness of the constituents – this will be dramatically lower than that of a homogeneous fiber with the cross-sectional dimensions of the bundle. For this parametric study, the cross-sectional moment of inertia of the homogeneous fiber $I_0 = b_0 h_0^3 / 12$, is 2.56 mm^4 . Dividing the fiber into a bundle of 4 UC equiaxed sub-fibers with cross-sectional dimensions $b = b_0 / \sqrt{N} = b_0 / 2$ and $h = h_0 / \sqrt{N} = h_0 / 2$, where N is the total number of fibers in the bundle,

results in a cross-sectional moment of inertia $I_{4UC} = I_0/N = 0.64 \text{ mm}^4$. In general, the EI of a bundle of UC fibers scales linearly with N , whereas the EI of RC fibers scales with N^2 . A bundle of 16 UC fibers results in $I_{16UC} = 0.16 \text{ mm}^4$. The force extension behavior of RC and UC bundles of 4 and 16 fibers with the same total cross-sectional area are shown in figure 2.8(b). All cases are compared to FE solutions. If the macroscopic force-extension behavior falls between the RC and UC cases, then there is some moderate resistance to shear sliding between fibers. It is obvious from these results that bundles can give vastly different force-extension behavior based on the degree of coupling even though they may have the same effective axial stretching stiffness, EA .

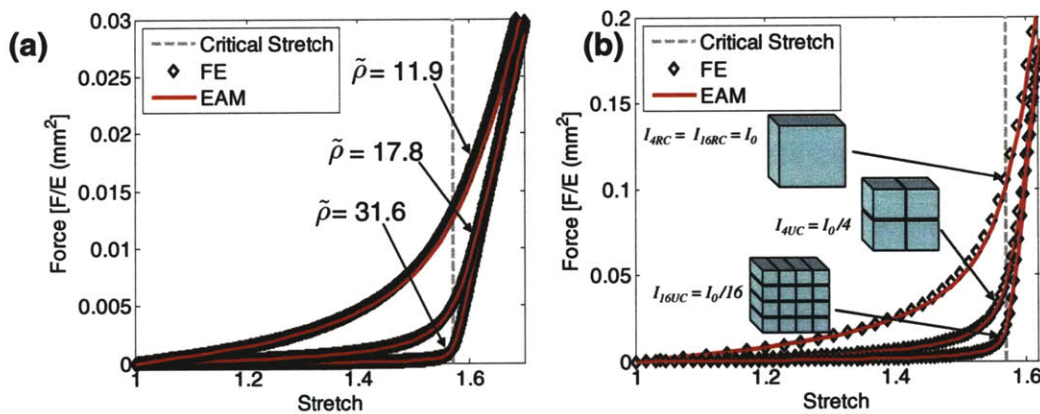


Figure 2.8 The EAM with axial stretching included for the fiber force vs. stretch compared to FE solutions. (a) the results of changing I by varying cross-sectional shape for $\tilde{\rho} = 11.9$, $\tilde{\rho} = 17.8$, and $\tilde{\rho} = 31.6$ where $\tilde{\rho} = \frac{\rho}{\sqrt[4]{I}}$ and ρ , α , and A were fixed. (b) shows the the force extension behavior of rigidly coupled (RC) and uncoupled (UC) bundles of 4 and 16 fibers with the same total cross-sectional area. Schematics of the fiber cross-section are shown, and the effective cross-sectional moment of inertia, I , is specified in terms of the homogeneous fiber cross-sectional moment of inertia, I_0 .

2.2.7 Variation of Crimp Geometry. Throughout the model development, we have assumed that the fiber geometry is periodic. However, in real biological and synthetic systems, the arc radius, ρ , is unlikely to be constant along the length of the fiber. To

test the capability of the *EAM* to capture less regular crimp geometries three fibers with a non-constant arc radius were simulated using FE analysis. The three fiber geometries all have the same cross-sectional geometry, and each has an average normalized arc radius of $\langle \tilde{\rho} \rangle = 20.0$. The fibers are shown in figure 2.9 in undeformed and deformed configurations and are denoted as 1, 2, and 3 having an α of 45° , 60° , and 90° which results in a λ_C of 1.11, 1.21, 1.57 respectively. The random fibers are drawn to scale with respect to the corresponding effective fiber, but not with respect to the other random fibers. Fitting the *EAM* with a constant arc radius to the force-extension behavior of these fibers results an effective fiber radii, $\tilde{\rho}_{eff}$, of 19.3, 20.0, and 19.3. The force-extension of the effective fibers with a constant arc radius is also shown in figure 2.9 compared to the corresponding *FE* solutions for the random fibers. The *EAM* is found to accurately predict the force-extension behavior of the fiber over the entire range of extension for different geometries, demonstrating the ability of the *EAM* to be used in an inverted manner to determine fiber properties and geometry. The inset in figure 2.9 shows the deformation of two individual crimps pointed out as a “large crimp” and “small crimp.” The less stiff large crimp deforms to a greater degree initially, and as the large crimp straightens and stiffens, the small crimp begins to extend more. In this manner, all of the crimps become flat at the same time instead of small crimps straightening first.

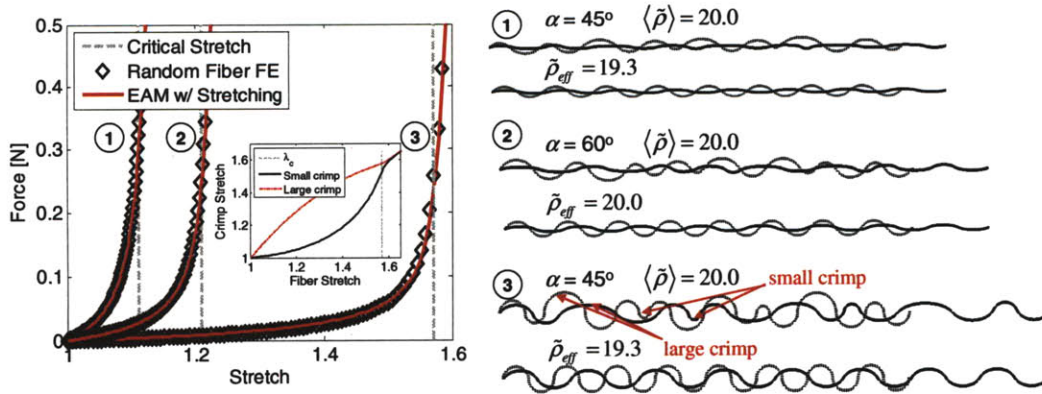


Figure 2.9 The results of fitting the *EAM* to a fiber geometry with a non-constant radius of curvature are shown compared to FE simulations of the force-extension of the “random” fibers. The “random” fibers are comprised of circular arcs with $\alpha = 45^\circ$, 60° , and 90° respectively and an average normalized arc radius of $\langle \tilde{\rho} \rangle = 20.0$ where $\tilde{\rho} = \frac{\rho}{\sqrt{4I}}$.

The random and effective fibers are shown in their initial and deformed configurations. Note that the “random” fibers are drawn to scale with respect to the corresponding effective fiber, but not with respect to other random fibers.

2.3 APPLICATION OF *EAM* TO FIT COLLAGEN FASCICLE DATA:

Hansen et al [11] reported stress-strain data for collagen fascicles from rat tail tendons. The fascicle was found to possess a crimped geometry when removed from the tendon (i.e. when in an unloaded state). Optical coherence tomography imaging and optical microscopy were used to image the collagen crimp at different stages of deformation. The proposed model was fit to the data presented by Hansen et al to determine material parameters and a geometrical description of the collagen fascicles. Initially the data was fit with $n = 1.0$ to obtain an approximate geometry of the fiber. The resulting parameters were then used to optimize n by comparing the model results to an “exact” *FE* solution obtained from ABAQUS on the approximate geometry. The optimal n value was 2.6. Finally, the *EAM* was fit to the data using the determined value of n . Figure 2.10(a) shows the results for the fiber force versus stretch behavior of collagen fascicles

with $n = 2.6$. Figure 2.10(b) shows the evolution of the crimp angle (see illustration in figure 2.10(b)) throughout the deformation. The crimp angle was obtained from FE simulation because the y-coordinates of the fiber are necessary along with the fiber end-to-end distance throughout the deformation. The crimp angle evolves in a nearly linear manner for $\lambda < \lambda_c$, and then asymptotically approaches zero for $\lambda > \lambda_c$

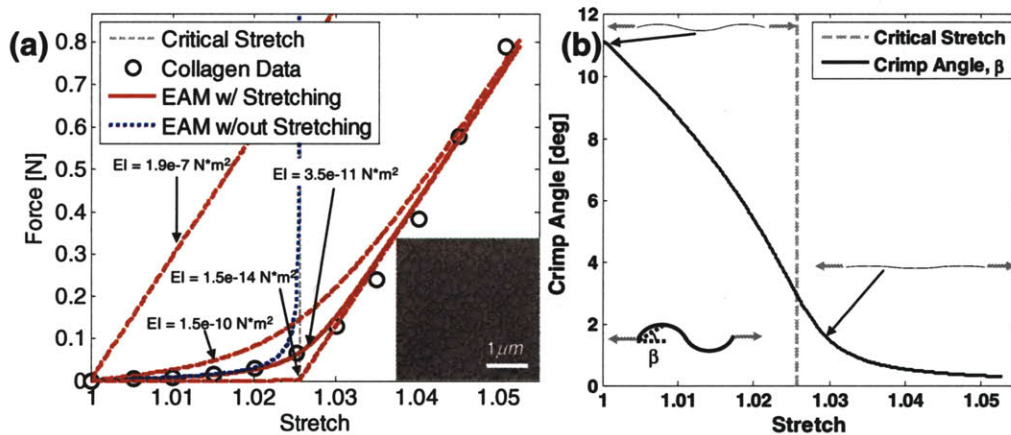


Figure 2.10 (a) Shows results of fitting the model to force vs. stretch behavior obtained by Hansen et al [11] for a collagen fascicle with an average cross-sectional area of 0.078 mm^2 . Also shown are force-extension behavior for a homogenous cross-section ($EI = 1.9e-7 \text{ N}\cdot\text{m}^2$), uncoupled $10 \mu\text{m}$ fibers ($1.5e-10 \text{ N}\cdot\text{m}^2$), and uncoupled $0.1 \mu\text{m}$ fibrils ($1.5e-14 \text{ N}\cdot\text{m}^2$). The inset is a TEM image of a wallaby tail tendon showing collagen fibrils [77]. (b) Shows the crimp angle as a function of stretch obtained from FE simulation using the parameters determined from data fitting. (b) also shows the undeformed and deformed fiber and a schematic to illustrate the crimp angle, β .

By fitting the model to the data, we can derive both geometrical parameters and material properties. The resulting geometrical parameters used to fit the data are $\rho = 150 \mu\text{m}$ and $\alpha = 22.3^\circ$. These geometrical parameters result in an initial crimp wavelength of $228 \mu\text{m}$ and a crimp angle of 11.15° . Hansen et al measured an average initial crimp wavelength of approximately $240 \mu\text{m}$. This shows that the model can accurately describe the fascicle wavelength. The values obtained for the effective

bending stiffness, EI , and the effective axial stretching stiffness, EA , are $3.5e-11 \text{ N}\cdot\text{m}^2$ and 30.0 N respectively. Using the reported average area of 0.078 mm^2 gives an elastic modulus for collagen of 384 MPa . Hansen et al do not report values for bending stiffness or axial stiffness; however, the calculated elastic modulus is consistent with the elastic modulus of collagen fibrils of approximately 430 MPa reported by Sasaki et al [78].

Neglecting the fascicle structural hierarchy and assuming a homogeneous equiaxed cross-section (this is equivalent to assuming that the fascicle substructures are rigidly coupled to each other during deformation) and a linear elastic material with area $A = 0.078 \text{ mm}^2$ and the reduced $E = 384 \text{ MPa}$ results in an effective bending modulus of $1.9e-7 \text{ N}\cdot\text{m}^2$, which is 4 orders of magnitude larger than the effective $EI = 3.5e-11 \text{ N}\cdot\text{m}^2$ reduced from the data. These results indicate that the fascicle is not a homogeneous linear elastic material. This discrepancy is likely due to the hierarchical microstructure of the fascicle, which consists of assemblies of smaller fibrils which may bend independently as described by Ker et al [77]. The consequence of this poor bonding is a much lower apparent macroscopic EI . The hierarchical structure of a fascicle consists of fibers ($\sim 10 \mu\text{m}$ in diameter [79]) which are composed of fibrils ($\sim 0.1 \mu\text{m}$ in diameter [79]) which are bonded by weak secondary hydrogen bonds and some intermolecular cross-links. The influence of this structural hierarchy on tensile behavior of collagen fibers has recently been simulated by Buehler [80].

We can then treat the fascicle as a collection of fibers that are loosely held together, and we assume that the individual fibers at the lower levels of structural hierarchy behave as a linear elastic material. These loosely bound fibers can unbend independently during deformation and hence result in a lower apparent EI at the macroscopic level of the fascicle. For an equiaxed cross-section, the ratio of bending stiffness of completely coupled fibers and/or fibrils (i.e. perfect rigid bonding) versus uncoupled fibers (i.e. zero shear stiffness between fibers) is approximately equal to the number of fibers. Assuming the fascicle is made up of completely uncoupled $\sim 10 \mu\text{m}$ diameter collagen fibers (no shear resistance between fibers) results in an effective EI of $1.5\text{e-}10 \text{ N}\cdot\text{m}^2$. Further assuming uncoupled $0.1 \mu\text{m}$ diameter collagen fibrils results in an effective EI of $1.5\text{e-}14 \text{ N}\cdot\text{m}^2$. These two values bound the reduced effective EI and suggest that the fascicle acts as a bundle of wavy collagen fibrils which are only loosely coupled to each other. This is consistent with the observations of Ker et al [77] that the fibrous microstructure of tendon is loosely bound from the fibril level and upwards. A framework for integrating shear stiffness between fibers into a mechanical bending model has been developed by Bathe et al. [81] for the case of actin bundles. A similar approach could be integrated with the EAM to describe cross-linked wavy fibers. Here we have demonstrated how application of the EAM model alone identifies the difference in bending and axial stretching mechanics of the fiber which cannot be distinguished by fitting only the large stiffness axial stretching regime, and further gives insight into the mechanisms of fiber deformation.

2.4 INCORPORATING MODEL INTO NETWORKS:

The wavy fibers described by the proposed mechanical model are often found in network structures. These networks occur naturally in some cases such as mammalian tendon or artificially in the case of electrospun fiber or carbon nanotube mats. In such networks, crimped fibers will be bonded, cross-linked and/or entangled in either random networks (see figure 2.1) or preferentially aligned networks. When loaded, the more compliant regions of the network will deform to accommodate the macroscopic deformation. Fibers will accommodate deformation by rotating towards the loading direction and by straightening (uncrimping); the fiber straightening and alignment in these regions leads to stiffening of these regions and the stiffening of the overall material response. In general, these networks are 3D; however, in some cases, such as membrane structures, the fibers are primarily aligned within a 2D membrane. In this case, we can simplify the mechanical treatment to 2D. Here we give an example of incorporating the inextensible *EAM* constitutive equations into a 2D isotropic network model developed by Qi et al [82] which is a 2D version of the 3D 8-chain network developed by Arruda and Boyce [83]. The fibers in the collagen network of figure 2.1(b) are randomly oriented and hence we will assume a transversely isotropic membrane network. Any preferred orientation of fibers can be incorporated using an approach similar to that used by Bischoff et al [84] used for 3D networks. The schematic representation of this model given by Qi et al is shown in figure 2.11 in an undeformed state and after deformation. In this model, the behavior of a 2D network of randomly oriented fibers is approximated by the four fibers taken to be at the average initial orientation of all fibers. The initial orientation is taken with respect to the maximum

principal stretch. The fiber elastica approximation (sans axial extension) is used here to describe the force-stretch behavior of the constituent fibers; the model captures the behavior for λ up to $\sim 0.9\lambda_C$, and hence this method is accurate until the fibers in the network are nearly straight.

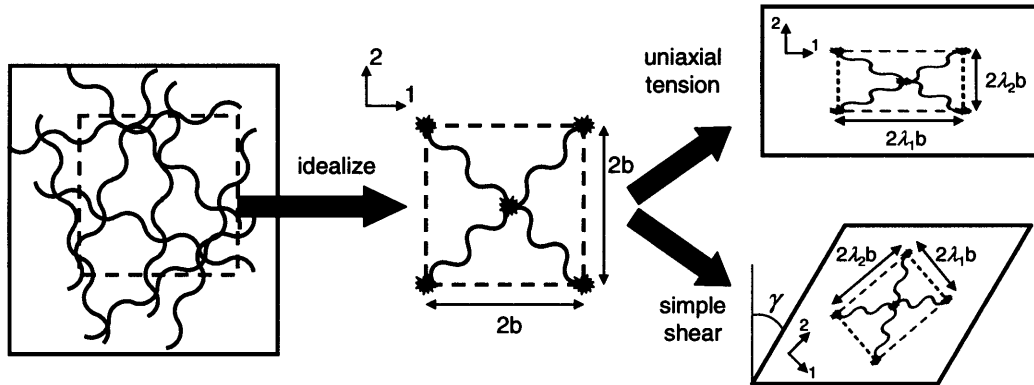


Figure 2.11 Schematic of the 2D idealized 4-chain network. The randomly oriented isotropic network is idealized by four fibers which form a unit cell. The axes of this unit cell are oriented with the directions of principal stretch throughout the deformation.

The network model of Qi et al is convenient because the network deformation can be described by the first invariant of the 2D left Cauchy-Green tensor, $\mathbf{B}_{2D} = \mathbf{F}_{2D}\mathbf{F}_{2D}^T$, where \mathbf{F}_{2D} is the 2D deformation gradient. This invariant, defined as $I_{1,2D}$, is given by:

$$I_{1,2D} = \lambda_1^2 + \lambda_2^2 \quad (2.31)$$

where λ_1 and λ_2 are the principal membrane stretches. The stretch of each fiber in the network can be written in terms of $I_{1,2D}$.

$$\lambda_f = \left[\frac{1}{2} I_{1,2D} \right]^{1/2} = \left[\frac{1}{2} (\lambda_1^2 + \lambda_2^2) \right]^{1/2} \quad (2.32)$$

Furthermore, for purposes of this example, we introduce the assumption of a constant membrane surface area imposed by the surrounding substance and/or fluid which is mathematically expressed as:

$$\lambda_1 \lambda_2 = 1 \quad (2.33)$$

The strain energy per chain in the network can be found by integrating equation (2.26) with respect to l and noting that the fiber stretch in the network is λ_f . For the case of $n = 1.0$, the strain energy density is then given by:

$$\tilde{U}_{tot} = \frac{\nu K_B (l_0)^2 (\lambda_f - 1)^2}{2} + \frac{3\nu EI (l_0)^{1/3}}{4^{5/3} \rho^{4/3} (\lambda_c - 1)} \left[(\lambda_c - 1)^{1/3} (3\lambda_c - 3) - (\lambda_c - \lambda_f)^{1/3} (\lambda_f + 3\lambda_c - 4) \right] \quad (2.34)$$

where ν is the areal chain density (number of chains per unit membrane area). This chain density can be determined from images such as that shown in Figures 2.1(a) and 2.1(b) or can be used as an additional fitting parameter. The Cauchy stress, which in this case is a “membrane stress” (force per unit length), is found by proper differentiation of the strain energy density.

$$\mathbf{T}_{2D} = 2 \frac{\partial \tilde{U}_{tot}}{\partial I_{1,2D}} \mathbf{B}_{2D} + h \mathbf{1} \quad (2.35)$$

where h is an additional equibiaxial stress obtained by satisfying equilibrium through the traction boundary conditions. Combining equations (2.34) and (2.35) yields:

$$\mathbf{T}_{2D} = \frac{\nu l_0}{2\lambda_f} \left[K_B l_0 (\lambda_f - 1) + EI (4\rho^2 l_0 (\lambda_c - \lambda_f))^{\frac{2}{3}} \left(\frac{\lambda_f - 1}{\lambda_c - 1} \right) \right] \mathbf{B}_{2D} + h\mathbf{1} \quad (2.36)$$

For the case of simple shear, equations (2.36) reduces to the shear stress-strain relationship:

$$\sigma_{12} = \frac{\nu l_0}{2\lambda_f} \left[K_B l_0 (\lambda_f - 1) + EI (4\rho^2 l_0 (\lambda_c - \lambda_f))^{\frac{2}{3}} \left(\frac{\lambda_f - 1}{\lambda_c - 1} \right) \right] \tan \gamma \quad (2.37)$$

where the fiber stretch for simple shear is $\lambda_f = \left[\frac{1}{2} (\tan^2 \gamma + 2) \right]^{1/2}$.

Figure 2.12(a) shows the results for simple shear (see figure 2.11) of the 4-chain network model, depicting the membrane shear stress-strain behavior as well as the constituent fiber force as a function of shear strain. The effective bending stiffness used is $EI = 3.5e-11 \text{ N}\cdot\text{m}^2$ which was the result obtained from fitting a single collagen fascicle. Typical geometrical parameters were estimated from the image in figure 2.1(b) as $\rho = 10 \text{ }\mu\text{m}$, $\alpha = 90^\circ$, and $\nu = 1(10^9) \text{ chains/m}^2$. Figure 2.12(b) shows the fiber crimp angle as the network is stretched. The nonlinearity in crimp angle at small macroscopic stretches is due to the nonlinear fiber stretch since the fibers can also rotate to accommodate macroscopic deformation. The fiber rotation is given by the combination

of the rotation of the principal stretch direction and the rotation of the fiber angle with respect to the principal stretch direction; the model is seen to capture the alignment of the fibers with the shear direction as the imposed shear strain is increased. λ_f remains below 1.5 up to a macroscopic shear strain of 1 corresponding to a $\sim 60^\circ$ shear deformation. Figure 2.9 shows that for fibers with $\alpha = 90^\circ$, the force-extension behavior is dominated by the unbending up to $\lambda = \lambda_x$. Hence, to accurately describe the stress-strain behavior of such networks in physiological deformations, it is necessary to explicitly treat the unbending of the crimp pattern.

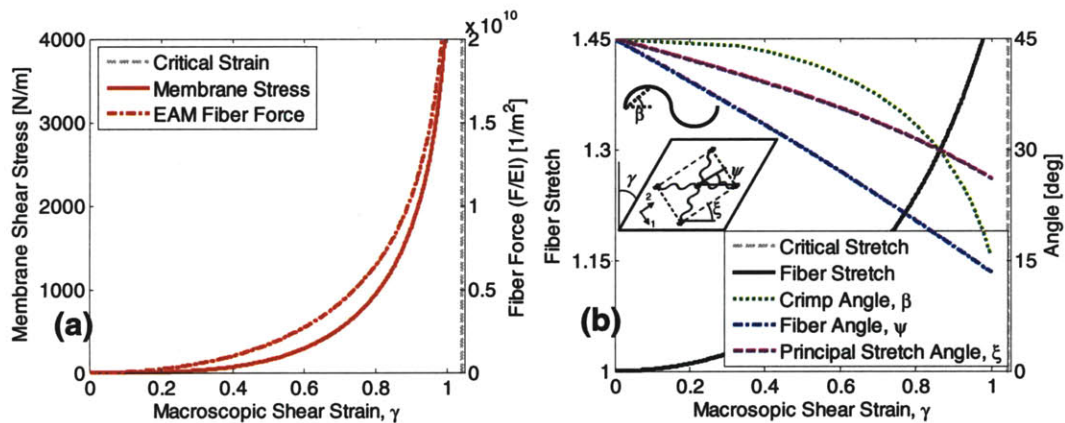


Figure 2.12 Simulation of simple shear in a 2D network. (a) shows the results of simulating simple shear on the 4 chain network model for membrane stress and fiber force using the parameters $EI=3.5e-11 \text{ N}\cdot\text{m}^2$, $\rho = 10 \mu\text{m}$, and $\alpha = 90^\circ$, and $\nu = 1(10^9)$ chains/ m^2 . The dotted line shows where the fibers reach their critical stretch. (b) shows the evolution of the fiber stretch and crimp angle along with the rotation of the fibers which is given by combined rotation of the principal direction and rotation of the fibers with respect to the principal direction.

2.5 CONCLUSIONS:

An analytical expression for the force-extension behavior of a wavy fiber was developed based on the integral elastica solution utilizing two limiting cases: 1) a linear elastic solution in the limit of small extension (*SE*) (equation (2.16)), and 2) an approximation to the numerical elastica solution in the limit of large forces (*LF*) (equation (2.22)). The two

limiting solutions were additively combined applying a weighting function to the *LF* solution to achieve the mechanical behavior over the entire range of deformation. Axial stretching was incorporated into the model by considering a summation of bending and axial extension contributions to the overall deformation. The full analytical *EAM* model presented in equation (2.30) was shown in parametric studies to accurately capture the enthalpic unbending plus the direct axial stretch behavior of a wide range of fiber geometries. The optimal fitting parameter, n , was determined for several geometries. For the case of a fiber made up of circular arcs, $n = 2.5$ provides accurate results. For the more general geometry considered in Appendix A, optimal fitting parameters are given for several geometries.

Two applications of this model were demonstrated. First, it was used to fit force-extension data for single collagen fascicles obtained from rat tail tendons, where these fascicles were observed to have a crimped configuration in the unloaded state. The *EAM* accurately describes the initial stiffness, nonlinear stiffening, and axial stretching behavior of the collagen fascicle. The radius of curvature of the collagen fascicles, ρ , the crimp angle, β , the effective axial stretching stiffness, EA , and the effective bending stiffness, EI , were reduced from force-extension data. The crimp wavelength reduced from the data gave good agreement with physical measurements of fascicle geometry [11], and the elastic modulus reduced agrees with previous measurements of the elastic modulus of collagen [78].

In the second application, the analytical expression for the fiber force-extension behavior enabled incorporation into a 2D model of fibrous membrane networks. The results of a simulation of a 2D network comprised of wavy collagen fibers were shown (figure 2.12).

In dealing with biological systems and networks, it is worth examining the assumptions of the EAM. A strength of the EAM is that data reduction enables separate identification of a bending stiffness and an axial stiffness. These values can be compared and used to infer deformation mechanisms within the fiber. In the case presented in section 2.3, the reduced bending stiffness indicates that the collagen fascicle does not behave as a homogenous linear elastic material. The low apparent EI is due to the poorly bonded uncoupled substructure of the collagen fascicle resulting in an apparent bending stiffness that was much lower than that expected for a well-bonded homogenous material. The fascicle acts as a collection of loosely bound collagen fibrils where the fibrils can bend independently which is consistent with previous observations. This poor bonding between collagen fibrils has been found to play an important role in the macroscopic tensile behavior of collagen fibers [80]. A more detailed treatment of the bending stiffness could combine the proposed model with an explicit treatment of fiber cross-linkers using the methodology developed by Bathe et al [81] for actin bundles.

Furthermore, in the network model it was assumed that the wavy fibers are randomly oriented and cross-linked. In the random configuration, the network will accommodate macroscopic deformation by the rotation and straightening of compliant initially crimped

fibers. However, more ordered structures containing highly aligned arrangements of short (stiff) and long wavy (compliant) fibers will exhibit a stress-strain behavior that sequentially stiffens as each fiber is stretched to its contour length and stiffens. The macroscopic behavior is then dominated by progressively sampling the axial stretching behavior of these fibers as they straighten. In these cases a statistical treatment of fiber waviness, contour lengths, and/or orientation is appropriate. Hurschler et al [85] use this approach to describe tendon and ligaments with nearly parallel fibers assuming statistical distribution of fiber orientation and a simple linear force-extension behavior of the fibers once they are straightened and begin to bear a load. Cacho et al [72] use the same linear approximation for fiber force-extension behavior but instead consider a statistical distribution of fiber contour lengths. Sacks [12] uses a similar approach, but applied fiber orientation data from SALS experiments instead of assuming a statistical distribution of fiber orientation. Liao et al [86] considered fibers with a normal distribution of contour length and integrated a stretch based failure criteria. Qi et al [82] similarly used normally distributed contour lengths to examine multi-chain strands made of flexible modular chains subject to thermal fluctuations and unfolding.

The network model results presented herein had taken the crimped state of the network fibers to be an unloaded state. In some material systems, the fiber crimp may be a result of, or amplified by loads imposed on the fiber by other tissue constituents. Effects of internally balanced prestresses, i.e. the presence of initial internal loads creating the initial crimped configuration, could be included following the approach of Arslan et al [87] and Palmer et al [88].

In general, the proposed *EAM* model can be utilized to describe the force-extension behavior of individual wavy fibers. Application of this model leads to identification of both geometrical and material parameters of the fibers of interest. Specifically, the model is applicable to initially wavy fibers which have limited configurational space, and hence their free energy is dominated by enthalpic effects of unbending and axial stretching. The model can capture fiber geometries consisting of regions of non-zero curvature connected end-to-end or bridged by straight segments (the addition of straight segments is considered in Appendix A). Such geometry is found in biological molecules such as collagen fibers and in synthetic fibers such as carbon nanotubes (see figure 2.1) and steel, copper, or other synthetic wools. Previous models have been developed for similar fiber geometries; however, several of these models required a numerical solution, and those which developed an analytical solution were subject to limiting assumptions about the fiber geometry. The *EAM* model has the advantage of providing an analytical solution with the capability to approximate a wide range of wavy fiber geometries.

2.6 APPENDIX 2A: EXTENSION TO GENERAL FIBER GEOMETRY

As shown in figure 2.A1, a more general fiber geometry can be used which consists of a straight segment tangentially extending from a portion of a circular arc. This straight segment can be oriented at any angle α such that $0^\circ \leq \alpha \leq 90^\circ$ which then corresponds to an arc angle between 0° and 180° . The methodology for deriving this model is similar to that already described for the prior circular arc geometry.

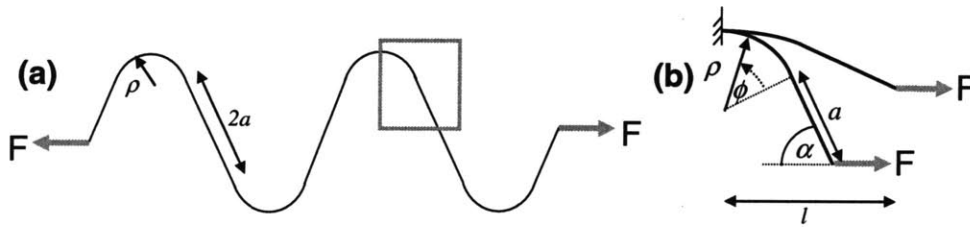


Figure 2.A1 Due to its symmetry, the generalized model geometry shown in (a) can be simplified into cantilevered beam geometry shown in (b).

The *SE* limit expression is generalized for the more general fiber waviness geometry, taking into account the moment distribution along the arc and straight segment portion which gives:

$$F_{SE} = K'_B l_0 (\lambda - 1) \quad (2.38)$$

$$U_{SE} = \frac{K'_B}{2} l_0^2 (\lambda - 1)^2 \quad (2.39)$$

where the stiffness of the wavy configuration is:

$$K'_B = \frac{3EI}{a^3 \sin^2 \alpha + 3\rho^3 \beta} \quad (2.40)$$

$$\beta = \cos 2\alpha \left(1 - \frac{a^2}{\rho^2}\right) \left(\frac{\alpha}{2}\right) - \sin 2\alpha \left[\frac{3}{4} + 2\frac{a}{\rho} \left(\frac{\alpha}{2}\right)\right] + 2\frac{a}{\rho} \sin^2 \alpha + \left(\frac{\alpha}{2}\right) \left(\frac{a^2}{\rho^2} + 2\right) \quad (2.41)$$

The large deformation solution is similarly based on the elastica solution for unbending a curved beam. Generalizing the geometry for the elastica solution makes an adjusted analytical approximation difficult. However, we can use the equation previously derived for the *LF* approximation and adjust the contour length (critical stretch) accordingly to account for the additional length of the straight segments. The *SE* and *LF* limits are compared to the corresponding *FE* solution in Figure 2.A2 with the axial stretching removed for a case where $\alpha = 45^\circ$, $\tilde{\rho} = 31.6$, and $\tilde{a} = 31.6$, where $\tilde{\rho} = \frac{\rho}{\sqrt[4]{I}}$ and $\tilde{a} = \frac{a}{\sqrt[4]{I}}$.

The initial behavior of the fiber is well described by the *SE* solution. The inset in the graph shows the error ratios for both the *SE* and *LF* approximations. This *SE* error ratio is above 0.9 for approximately 15% of the extension (up to a stretch of 1.04 when the fully extended stretch is 1.26). The *LF* error ratio reaches a minimum of 1.72 at $\lambda = 0.99\lambda_C$. The fitting parameter, n , will be used to improve the accuracy of the model in the large force regime.

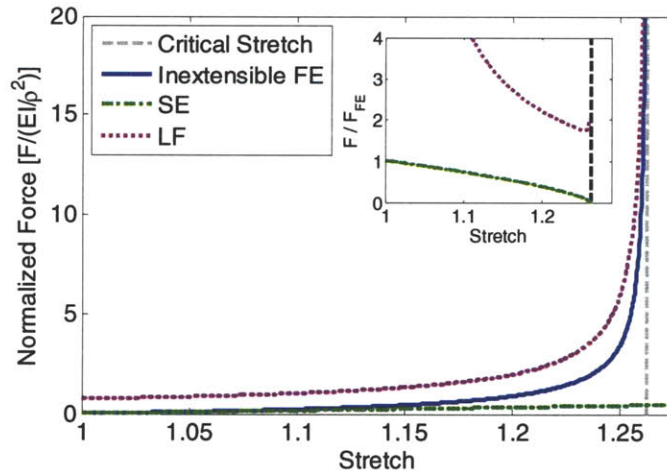


Figure 2.A2 The *SE* and *LF* solutions compared to the *FE* solution with the axial stretching removed for the generalized fiber geometry with $\alpha = 45^\circ$, $\tilde{\rho} = 31.6$, and $\tilde{a} = 31.6$ where $\tilde{\rho} = \frac{\rho}{\sqrt[4]{I}}$ and $\tilde{a} = \frac{a}{\sqrt[4]{I}}$. The inset shows the ratio of the *SE* and *LF* solutions to the *FE* solution.

In order to be able to describe the full mechanical behavior of the fiber, the same approach is taken of combining these two limiting cases with a weighting function applied to the *LF* approximation. Since the boundary conditions of the weighting function are the same as previously described in equation (2.24), the same functional form is used for the generalized geometry. The resulting constitutive model is:

$$F = K'_B l_0 (\lambda - 1) + EI \left[4\rho^2 l_0 (\lambda_c - \lambda) \right]^{\frac{2}{3}} \left(\frac{\lambda - 1}{\lambda_c - 1} \right)^n \quad (2.42)$$

Stretching is incorporated in the same manner as previously described, and the final constitutive model for the general fiber shown in figure 2.A1(a) is given by:

$$F = K'_B l_0 \left(\lambda - 1 - \frac{F \lambda_c}{EA} \right) + EI \left[4 \rho^2 l_0 \left(\lambda_c - \lambda + \frac{F \lambda_c}{EA} \right) \right]^{\frac{2}{3}} \left(\frac{\lambda - 1 - \frac{F \lambda_c}{EA}}{\lambda_c - 1} \right)^n \quad (2.43)$$

Figure 2.A3 shows the results for a fiber with $\alpha = 45^\circ$, $\tilde{\rho} = 31.6$, $\tilde{a} = 31.6$, and $n = 4.25$. For this case the fitting parameter, n , was determined as previously described. For simplicity, n was varied in increments of 0.25. For this geometry, the ratio of the force predicted by the *EAM* to the force from the *FE* results is between 0.9 and 1.1 for ~37% of the examined extension with the maximum and minimum values being 1.43 and 0.82 respectively.

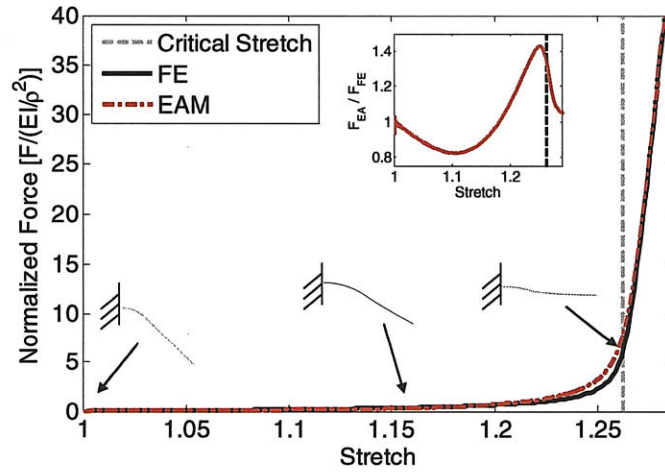


Figure 2.A3 Results of the complete model presented in equation (2.43) for the fiber force vs. extension applied to a geometry of $\alpha = 45^\circ$, $\tilde{\rho} = 31.6$, and $\tilde{a} = 31.6$ compared to an *FE* solution where $\tilde{\rho} = \frac{\rho}{\sqrt[4]{I}}$ and $\tilde{a} = \frac{a}{\sqrt[4]{I}}$. The inset shows the ratio of the *EAM* predicted force to the *FE* solution. The undeformed and two deformed states of the cantilevered beam are also shown.

The model shown in Fig. 2.A1(a) can describe a wide range of wavy fiber geometries. In order to evaluate the robustness of the proposed model, we considered different

geometries. Specifically, two cases were considered: 1) keeping α constant and varying the ratio a/ρ , and 2) keeping a and ρ constant and varying α . For the first case α was kept constant at 90° . This case considered a fiber where the straight segments are parallel to each other. For each case, the fitting parameter, n , was optimized as previously described; for simplicity, it was varied in increments of 0.25. Figure 2.A4(a) shows the results of optimizing n for case 1. From these results we can see that as a/ρ increases, the large force approximation becomes less accurate. This is accounted for by the increasing value of n .

The second case considered modeling fibers with different values of the angle α . This angle can vary from 0° to 90° with the extremes being a hairpin-like fiber with the straight segments parallel to each other and a straight fiber respectively. Since we had previously considered $\alpha = 90^\circ$, and the straight fiber case is trivial, we evaluated three fiber geometries, $\alpha = 30^\circ$, 45° and 60° , leaving $\tilde{\rho} = 31.6$, $\tilde{a} = 31.6$ constant. Figure 2.A4(b) shows the results of this case study. The optimal values for n which were determined as previously described are shown in the figure.

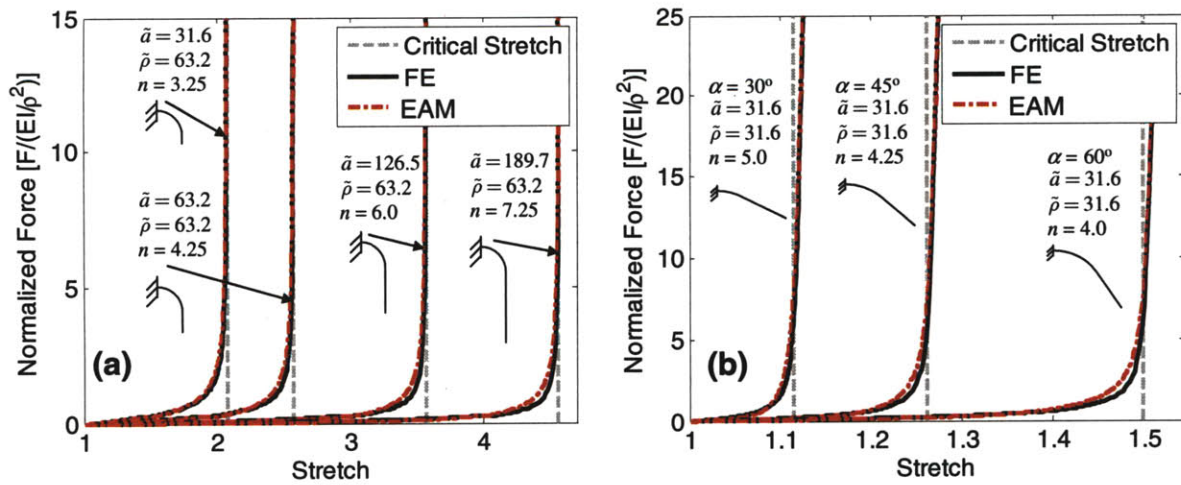


Figure 2.A4 Results of the *EAM* model for fiber force vs. stretch behavior varying the ratio of a/ρ in (a) and the angle α in (b) are compared to *FE* solutions. The original geometries are shown to scale with respect to each other in (a) and (b).

The extension behavior of the general fiber geometry in figure A1 is well approximated by the model presented in equation (2.43). The fiber in figure 2.2 is a special case of the generalized model where $a = 0$. In summary, when the fiber consists of only circular arcs connected end to end, the model presented provides an excellent approximation. As a increases the *LF* approximation becomes worse. However, this error can be counteracted by the fitting parameter n as shown in figure 2.A4. In the limiting case where a/ρ is large and the α is close to 0° , the approach taken by Bertoldi and Boyce [73] provides an appropriate description of fiber extension.

2.7 REFERENCES:

- [1] Beuche, F., 1962, *Physical Properties of Polymers*, Interscience, New York.
- [2] Smith, S., Cui, Y., Bustamante, C., 1996. "Overstretching B-DNA: The Elastic Response of Individual Double-Stranded and Single-Stranded DNA Molecules". *Science*. **271**: p. 795-799.
- [3] Flory, P. J., 1989, *Statistical Mechanics of Chain Molecules*, Hanser, New York.
- [4] Marko, J. F. and Siggia, E. D., 1995. "Stretching DNA". *Macromolecules*. **28**: p. 8759-8770.
- [5] Wang, M. D., Yin, H., Landick, R., Gelles, J. and Block, S. M., 1997. "Stretching DNA with optical tweezers". *Biophys J*. **72**: p. 1335-1346.
- [6] Frisch-Fay, R., 1962, *Flexible Bars*, Butterworths, Washington, D.C.
- [7] Magnusson, A., Ristinmaa, M. and Ljung, C., 2001. "Behaviour of the extensible elastica solution". *Int J Solids Struct*. **38**: p. 8441-8457.
- [8] Vaz, M. A. and Solano, R. F., 2003. "Postbuckling analysis of slender elastic rods subjected to uniform thermal loads". *J Therm Stresses*. **26**: p. 847-860.
- [9] Glassmaker, N. J. and Hui, C. Y., 2004. "Elastica solution for a nanotube formed by self-adhesion of a folded thin film". *J Appl Phys*. **96**: p. 3429-3434.
- [10] Mikata, Y., 2007. "Complete solution of elastica for a clamped-hinged beam, and its applications to a carbon nanotube". *Acta Mech*. **190**: p. 133-150.
- [11] Zhang, Y., Suhir, E. and Xu, Y., 2006. "Effective Young's modulus of carbon nanofiber array". *J Mater Res*. **21**: p. 2948-2954.
- [12] Buckley, C. P., Lloyd, D. W. and Konopasek, M., 1980. "On the Deformation of Slender Filaments with Planar Crimp - Theory, Numerical-Solution and Applications to Tendon Collagen and Textile Materials". *P Roy Soc Lond a Mat*. **372**: p. 33-64.
- [13] Garikipati, K., Gökçe, S. and Miehe, C., 2007. "Elastica-based Strain Energy Functions for Soft Biological Tissue". *J Mech Phys Solids*.
- [14] Diamant, J., Keller, A., Baer, E., Litt, M. and Arridge, R. G. C., 1972. "Collagen; Ultrastructure and Its Relation to Mechanical Properties as a Function of Ageing". *Proceedings of the Royal Society of London Series b-Biological Sciences*. **180**: p. 293-315.
- [15] Comninou, M. and Yannas, I. V., 1976. "Dependence of Stress-Strain Nonlinearity of Connective Tissues on Geometry of Collagen-Fibers". *J Biomech*. **9**: p. 427-433.
- [16] Lanir, Y., 1978. "Structure-Strength Relations in Mammalian Tendon". *Biophys J*. **24**: p. 541-554.
- [17] Lanir, Y., 1983. "Constitutive-Equations for Fibrous Connective Tissues". *J Biomech*. **16**: p. 1-12.
- [18] Stouffer, D. C., Butler, D. L. and Hosny, D., 1985. "The Relationship between Crimp Pattern and Mechanical Response of Human Patellar Tendon-Bone Units". *J Biomech Eng-T Asme*. **107**: p. 158-165.
- [19] Hurschler, C., Provenzano, P. P. and Vanderby, R., 2003. "Application of a probabilistic microstructural model to determine reference length and toe-to-linear region transition in fibrous connective tissue". *J Biomech Eng-T Asme*. **125**: p. 415-422.
- [20] Cacho, F., Elbischger, P. J., Rodriguez, J. F., Doblare, M. and Holzapfel, G. A., 2007. "A constitutive model for fibrous tissues considering collagen fiber crimp". *Int J Nonlinear Mech*. **42**: p. 391-402.

- [21] Bertoldi, K. and Boyce, M. C., 2007. "Mechanics of the hysteretic large strain behavior of mussel byssus threads". *J Mater Sci.* **42**: p. 8943-8956.
- [22] Beskos, D. E. and Jenkins, J. T., 1975. "Mechanical Model for Mammalian Tendon". *J Appl Mech-T Asme.* **42**: p. 755-758.
- [23] Freed, A. D. and Doehring, T. C., 2005. "Elastic model for crimped collagen fibrils". *J Biomech Eng-T Asme.* **127**: p. 587-593.
- [24] Poquillon, D., Viguier, B. and Andrieu, E., 2005. "Experimental data about mechanical behaviour during compression tests for various matted fibres". *J Mater Sci.* **40**: p. 5963-5970.
- [25] Ottani, V., Raspanti, M. and Ruggeri, A., 2001. "Collagen structure and functional implications". *Micron.* **32**: p. 251-260.
- [26] Viidik, A., Danielsen, C. C. and Oxlund, H., 1982. "On Fundamental and Phenomenological Models, Structure and Mechanical-Properties of Collagen, Elastin and Glycosaminoglycan Complexes". *Biorheology.* **19**: p. 437-451.
- [27] Hansen, K. A., Weiss, J. A. and Barton, J. K., 2002. "Recruitment of tendon crimp with applied tensile strain". *J Biomech Eng-T Asme.* **124**: p. 72-77.
- [28] Ker, R. F., 2007. "Mechanics of tendon, from an engineering perspective". *Int J Fatigue.* **29**: p. 1001-1009.
- [29] Sasaki, N. and Odajima, S., 1996. "Elongation mechanism of collagen fibrils and force-strain relations of tendon at each level of structural hierarchy". *J Biomech.* **29**: p. 1131-1136.
- [30] Kastelic, J., Galeski, A. and Baer, E., 1978. "Multicomposite Structure of Tendon". *Connect Tissue Res.* **6**: p. 11-23.
- [31] Buehler, M. J., 2006. "Nature designs tough collagen: Explaining the nanostructure of collagen fibrils". *P Natl Acad Sci USA.* **103**: p. 12285-12290.
- [32] Bathe, M., Heussinger, C., Claessens, M. M. A. E., Bausch, A. R. and Frey, E., 2008. "Cytoskeletal bundle mechanics". *Biophys J.* **94**: p. 2955-2964.
- [33] Qi, H. J., Ortiz, C. and Boyce, M. C., 2006. "Mechanics of biomacromolecular networks containing folded domains". *J Eng Mater-T Asme.* **128**: p. 509-518.
- [34] Arruda, E. M. and Boyce, M. C., 1993. "A 3-Dimensional Constitutive Model for the Large Stretch Behavior of Rubber Elastic-Materials". *J Mech Phys Solids.* **41**: p. 389-412.
- [35] Bischoff, J. E., Arruda, E. M. and Grosh, K., 2002. "A microstructurally based orthotropic hyperelastic constitutive law". *J Appl Mech-T Asme.* **69**: p. 570-579.
- [36] Hurschler, C., LoitzRamage, B. and Vanderby, R., 1997. "A structurally based stress-stretch relationship for tendon and ligament". *J Biomech Eng-T Asme.* **119**: p. 392-399.
- [37] Sacks, M. S., 2003. "Incorporation of experimentally-derived fiber orientation into a structural constitutive model for planar-collagenous tissues". *J Biomech Eng-T Asme.* **125**: p. 280-287.
- [38] Liao, H. Y. and Belkoff, S. M., 1999. "A failure model for ligaments". *J Biomech.* **32**: p. 183-188.
- [39] Arslan, M. and Boyce, M. C., 2006. "Constitutive modeling of the finite deformation behavior of membranes possessing a triangulated network microstructure". *J Appl Mech-T Asme.* **73**: p. 536-543.

[40] Palmer, J. S. and Boyce, M. C., 2008. "Constitutive modeling of the stress-strain behavior of F-actin filament networks". *Acta Biomater.* 4: p. 597-612.

Chapter 3

Physiological Function of B Cell

Membrane Mechanics

3.1 INTRODUCTION:

B lymphocytes are a critical component of the immune system, which undergo a broad array of important mechanical-biochemical events such as cell rolling, adhesion, spreading, migration, endocytosis, differentiation and proliferation during physiological function. This array of mechanical responses acts at multiple levels, from single cells to coordinated multicellular microarchitectures. B lymphocyte development originates in the bone marrow where a cell matures through several stages of differentiation eventually becoming a Naïve B Cell which expresses a single type of antibody, the B cell receptor (BCR), as an integral membrane protein. The BCR is a membrane bound antibody, also referred to as an immunoglobulin (Ig), comprised of two identical copies of a heavy chain and a light chain as shown in figure 3.1. Once a B cell is activated, it can differentiate into an antibody secreting Plasma Cell.

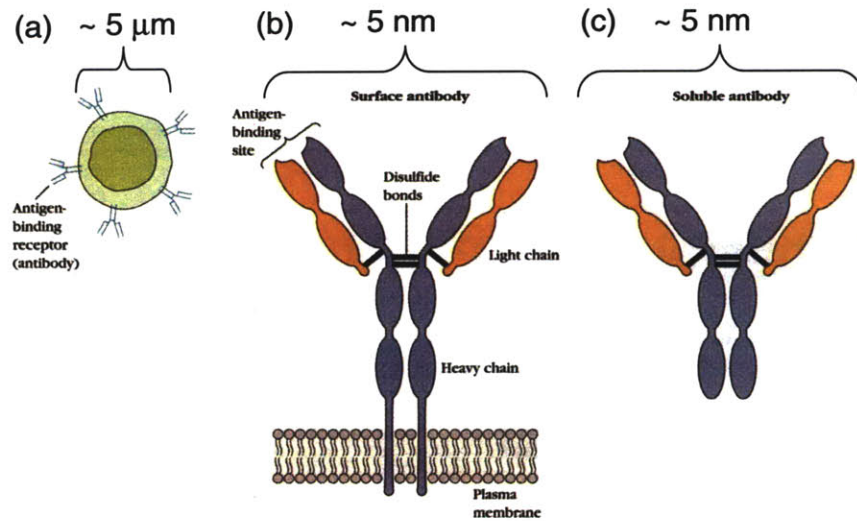


Figure 3.1 The B cell receptor is a membrane bound antibody as shown in (a) and that is comprised of two identical copies of a light change and heavy chain as shown in (b). The structures are bound together by disulfide bonds. Once the B cell is activated it can produce distinct heavy chains that result in secreted antibodies (c) [89].

During their lifetime, B lymphocytes must leave the bone marrow, circulate through the bloodstream, migrate into and through lymphoid organs where antigens are localized, probe lymphoid tissues for antigens, communicate with T lymphocytes, and migrate out of lymphoid tissues and re-enter the bloodstream. When a B lymphocyte detects an antigen and receives the proper assistance from T lymphocytes, it will then differentiate into an antibody secreting Plasma Cell. This differentiation process involves chemical and structural reorganizations that lead to changes in physical properties and enhanced signaling characteristics of the antigen detecting BCR. Specifically, initial activation of B cells leads to a signaling cascade that results in clonal expansion during which the gene encoding the BCR mutates to achieve antigen affinity maturation along with altered heavy chains that result in secreted antibodies. Furthermore, structural rearrangements during differentiation include a ~ 4-9 fold expansion in volume in addition to membrane protein, in particular BCR, clustering and cytoskeletal reorganization. Figure 3.2 shows

the size and membrane structure of a B cell prior to antigen stimulation (Naïve B Cell) and after completely differentiating into a Plasma Cell.

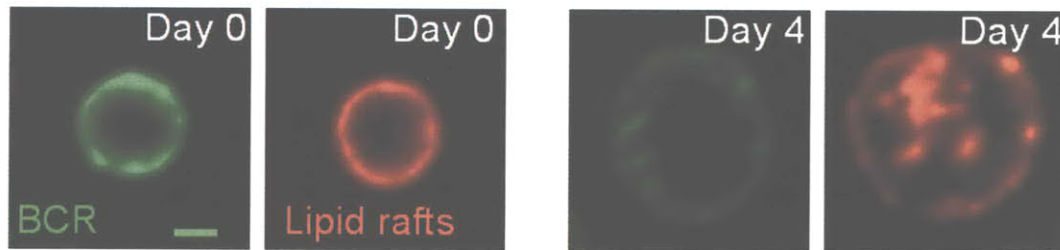


Figure 3.2 B cells were stimulated with lipopolysaccharide on Day 0 and undergo complete differentiation into a Plasma Cell by Day 4. Structural changes during differentiation include a 4-9 fold increase in volume and clustering of membrane proteins. These images show clustering of the BCR and clustering of lipid rafts. Scale bar is 2 μm . [Images courtesy of Dr. Andrew Hu, Ploegh Lab].

The lymphocyte membrane is a critical component for nearly all aspects of these functions, where its wrinkled topology facilitates easy expansion of the cell due to external stimuli and enables interaction and communication with surfaces, in particular the endothelial wall, lymphoid tissues, and T cells. In particular, lymphocytes take advantage of their membrane mechanical properties in the process of extravasation whereby cells migrate out of the bloodstream. In the initial stages of extravasation lymphocytes attach to the vessel wall via connections mediated by the intercellular adhesion molecules selectins [90]. These attachments, formed by E-selectin in the case of B cells [91], extract membrane tubes from the surface of the cell as shown in figure 3.3 for neutrophils [92].

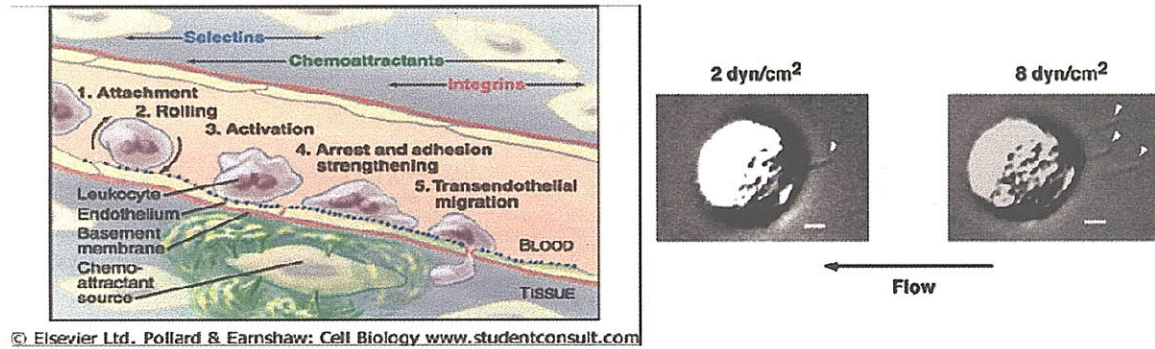


Figure 3.3 (a) Leukocytes use the process of extravasation, that initiates with attachment and rolling via selectin-mediated adhesion and culminates with transendothelial migration, to leave the bloodstream [93]. (b) During rolling membrane tethers extruded from the cell surface serve to slow the cell down and maintain contact with the vessel wall (scale bar is $2\mu\text{m}$) [92].

Membrane tether formation during rolling serves to slow the cell down and maintain contact with the vessel wall enabling endothelial cells to activate integrins on rolling cells. Tethering during cell rolling represents a passive reorganization of the B cell membrane to achieve a physiological function. Lymphocytes eventually stop, form an integrin mediated firm adhesion, and finally migrate into the surrounding tissue to perform their physiological function. B cells, in particular, extravasate into lymphoid organs, primarily lymph nodes, where they seek out antigens via their membrane bound Ig (mIg), the B cell receptor (BCR).

B cells also utilize their membrane in the process of probing the surfaces of lymph nodes for their corresponding antigen. Figure 3.4 shows a B cell resting on an antigen presenting surface [8].

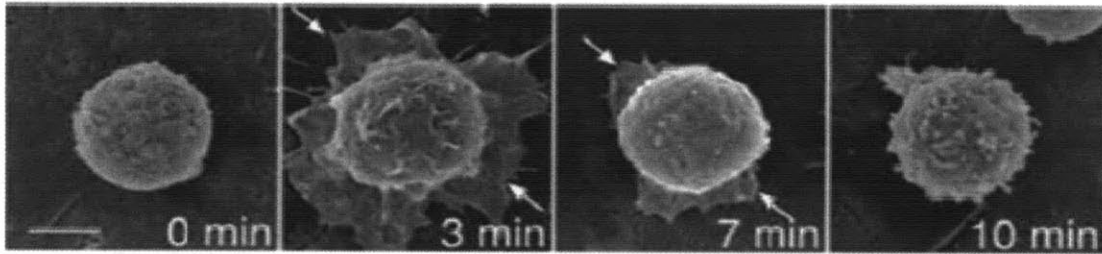


Figure 3.4 B cells resting on an antigen presenting surface use their membrane to probe for antigens on the time scale of 5 minutes (scale bar is $2\ \mu\text{m}$) [8]. The main cell body does not change shape or volume indicating that the cell takes advantage of excess surface area contained in the membrane to achieve these large displacements.

The membrane crawls along the substrate achieving large displacements to bind, collect, and localize antigens effectively amplifying BCR signaling. This process represents an active reorganization of the cell membrane that enables physiological function. In both processes, membrane tethering and antigen collection, the main cell body does not change shape or volume indicating that the B cell must contain a reservoir of cell membrane (i.e. excess surface area) that it can draw membrane from to achieve large displacements. In fact, B cells and other leukocytes, such as T cells and neutrophils, contain a wrinkled membrane topology as revealed by a close look at figure 2-3. In a similar manner to the wavy collagen fibers discussed in the previous chapter, the B cell membrane can achieve large displacements even though the areal strain to rupture is only $\sim 5\%$ [94] because it primarily deforms by unbending wrinkles instead of stretching the lipid bilayer.

Here we aim to characterize the physical machinery of the B cell membrane using membrane tethering as a means to probe its mechanical behavior. Figure 2-5 shows a schematic of the important mechanical components of the B cell membrane.

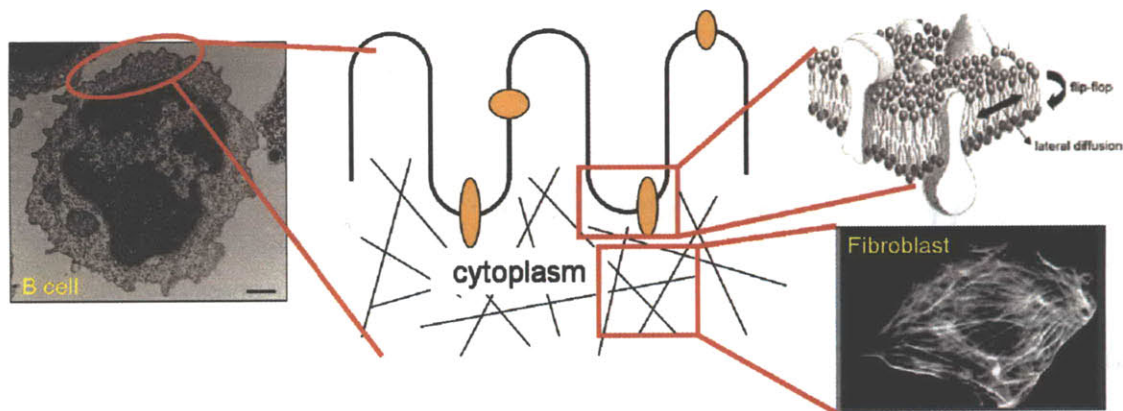


Figure 3.5 The biomechanical machinery of B cells. (left) B cells have a wrinkled membrane topology (scale bar is 500 nm) [95]. The components that define the mechanical behavior of the membrane, specifically the wrinkled lipid bilayer, membrane proteins, and the cytoplasm are shown schematically (middle). Also shown are a blown up schematic of a lipid bilayer with transmembrane proteins (top right) [96] and a fluorescent image of the actin cytoskeleton of a fibroblast (bottom right) [97].

Prior experimental studies have been conducted to probe cell membrane mechanics of other types of cells including neutrophils [98], red blood cells [99], fibroblasts [39], and outer hair cells [40] by simulating the membrane deformation that occurs during tethering and rolling through the use of optical tweezers [39, 40, 100, 101], micropipette aspiration [98, 102, 103], and atomic force microscopy [104]. One such experiment using optical tweezers to extract membrane tether from fibroblasts is shown in figure 3.6(a) [39]. These experimental approaches have identified three stages to tether formation and extension which are evident in the force trace shown in figure 3.6(b). 1) The probe initially feels the local cell stiffness until the membrane locally disassociates from the underlying cytoskeleton and a tether is formed. 2) The tether can then be drawn out at a relatively constant force as a result of a membrane reservoir that buffers membrane tension. This constant force may vary from ~ 10 pN to ~ 100 pN depending on the cell type. 3) When the membrane reservoir is depleted, the tether extraction

force increases until the tether breaks, detaches from the probe, or in the case of optical tweezers the tether force may exceed the maximum trapping force and the bead escapes the laser trap. Li et al. [40] showed that, if the tether extension is halted during the constant force stage and the length is held constant, there is exponential force relaxation as shown in figure 3.6(c).

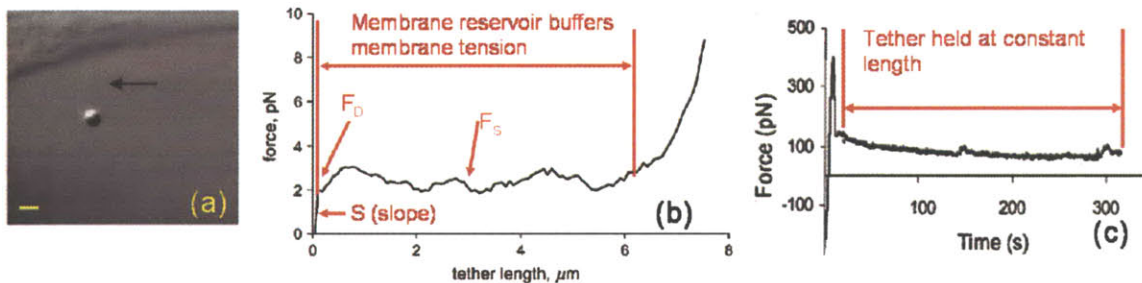


Figure 3.6 (a) shows a membrane tether extracted from a fibroblast using an optically trapped bead (scale bar is 2 μm) [39]. (b) The force of membrane tether extension is characterized by three stages: 1) a linearly increasing response indicative of the local stiffness; 2) a constant force region where lipids are drawn from a membrane reservoir; and 3) a nonlinear stiffening region upon depletion of the membrane reservoir [39]. (c) The force required to maintain a constant tether length relaxes over time which is indicative of dynamic membrane behavior [40].

Previous work to establish models to describe the tethering process and relate experimental results to mechanical properties of the cell membrane have considered the tether and the local cell membrane as a thermodynamic control volume. Hochmuth and Sheetz [101] and Hochmuth and Marcus [105] developed expressions for the static tether force and an effective viscosity by considering thermodynamic equilibrium on a membrane tether. Yu-Qiang et al [106] also consider thermodynamic equilibrium, and they account for the membrane reservoir with a parameter defined as the ratio of available area to the apparent area. However, no physical model exists to describe the dynamic behavior of the cell membrane that results in the force relaxation behavior

illustrated in figure 2-6(b). Such a model would be useful to understand large deformation behavior of the membrane that occurs during biological processes such as antigen detection and more specifically shed light on the physiological function of membrane nanotubes. Furthermore, understanding the dynamic behavior of the membrane can also enlighten how the membrane mechanical properties can impact processes such as cell migration, division, or antigen detection in the case of the B Cell.

We seek to understand the mechanical behavior of the cell membrane that enables large deformations at a constant membrane stress. Specifically we ask two questions:

- 1) How does the mechanical behavior of the B cell membrane impact B cell physiological functions?
- 2) What is the physical impact of the structural evolution of the B cell membrane that occurs throughout differentiation?

We address these questions using a combination of single cell experiments with optical tweezers and micromechanical modeling. First, an experimental assay was developed for implementation with optical tweezers to simulate the membrane tethering that occurs during cell rolling via specific attachment to the BCR. Second, a micromechanical model was developed to describe the dynamic rearrangement of the cell membrane that occurs during tether formation.

3.2 EXPERIMENTAL METHODS:

All experiments were done in an antigen specific manner using primary B cells obtained from MD4 mice in the Ploegh lab which produce B cells with BCRs specific for hen egg

lysozyme (HEL) [107] and HEL-coated beads. These cells were activated on Day 0 by adding lipopolysaccharide (LPS) to the cell culture media. Cells were fully differentiated into antibody secreting Plasma Cells over a course of 5 days. Membrane tethering experiments were carried out on each day (Day0 – Day4) to track the evolution of physical properties.

Experiments were carried out in a flow chamber made of a polylysine coated cover slip attached to a glass microscope slide via two pieces of double-sided sticky tape to create a flow channel of approximately 10-15 μl in volume. Primary B cells were flown into the channel at a concentration of 1×10^6 cells/ml in cell culture media and incubated for 10 minutes to allow B cells to adhere to the polylysine coated surface. A solution of 1 mg/ml casein in RPMI (Invitrogen) was then flown into the channel and incubated for 5 minutes to prevent subsequent bead binding to the cover slip surface. Streptavidin coated beads (1.2 μm – Spherotech) were pre-coated with biotinylated HEL. These beads were resuspended in RPMI and then flown into flow chamber for optical trap manipulation. Figure 2-7 shows a schematic and a DIC image of the experimental assay. A piezoelectric microscope stage was used to manipulate the sample.

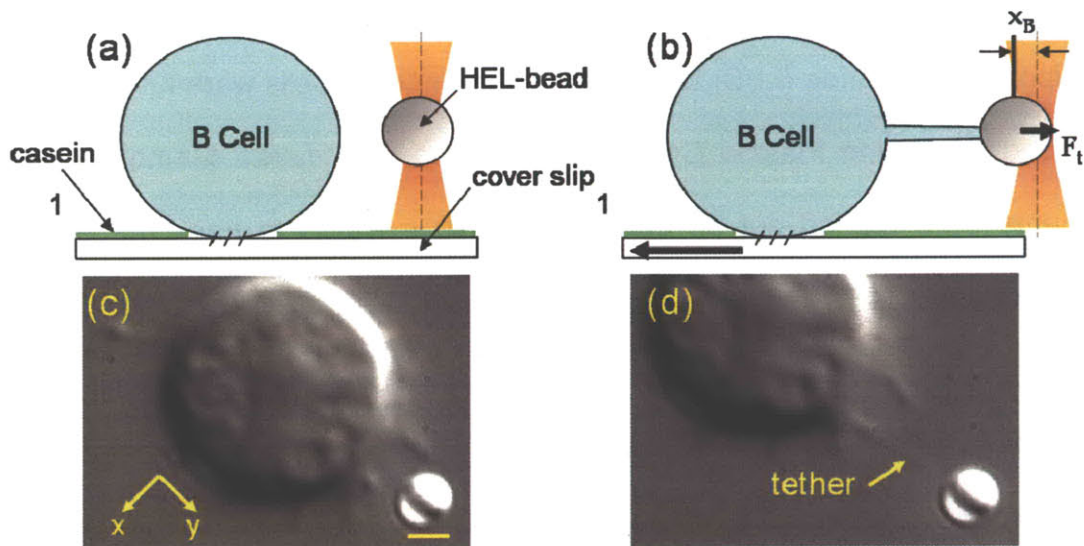


Figure 3.7 The experimental assay is shown schematically (a-b) and in a DIC images (c-d). B cells are immobilized on a polylysine coated cover slip. Then casein is used to coat the surface to prevent subsequent beads binding. Then HEL coated beads (1.2 μm) are flown into the chamber for optical trap manipulation. (a,c) Beads are trapped, aligned with B cells, and subjected to position and stiffness calibrations. Cells are brought into contact with the trapped bead using a piezoelectric stage to facilitate cell-bead binding. (c,d) The cell is pulled away from the bead and a membrane tether is extracted from the surface of the cell.

Beads were trapped with a 1064 nm trapping laser (CVI) then subjected to position and trap stiffness calibrations as described in Chapter 1. Two types of experiments were carried out. A “deft touch” protocol was used to test the adhesion of beads to the cells, and membrane tethering experiments were performed to characterize the mechanical properties of the cell membrane. In this experiment beads were trapped, and a single cell was visually aligned with the beads on either the x or y axis of the piezostage (45° from the vertical/horizontal axis in figure 2-6). The focal height of the bead was adjusted with the microscope focus to align the height of the bead with the equator of the cell in the z -axis prior to performing position and stiffness calibrations. The piezostage was moved to bring the cell towards the bead while monitoring the bead

position. When a bead displacement was detected, the stage was quickly moved in the opposite direction at a velocity of 5.0 $\mu\text{m/s}$ to pull the cell and bead apart. Adhesion between the cell and the bead was identified simply if the cell applied a force on the bead. This method was used to ensure the antigen specific nature of the cell-bead attachment. Measurements were carried out on single cells on Days 0-4 (~ 30 cells for each Day). Membrane tethering experiments were carried out using a similar assay and attachment protocol with the HEL-coated beads. However, beads were held in contact with cells for a slightly longer time (~0.5s), and then the cell was moved away from the bead at a constant velocity to a length of 5-20 μm . After reaching the preset maximum tether length, data was collected until the force reached a steady state value.

3.3 REVIEW OF MEMBRANE TETHERING MECHANICS:

Hochmuth and Marcus developed a framework to describe the constant region of the tether extension force profile [105]. Their derivation is reviewed here to provide the basis for quantifying membrane mechanical properties from the tether force data. Consider a tube of lipids that is extracted from the surface of a cell with excess surface area (i.e. a wrinkled bilayer topology). The incremental work, dW , done to extract the membrane tether an additional length, dL_t , is simply equal to:

$$dW = f_0 dL_t \quad (3.1)$$

where f_0 is the static tether force. Since the lipids in the membrane bilayer are very mobile, the tether is extended by adding new membrane material into the tube instead

of stretching the hydrophobic interactions between lipids. The major contributions to the change in free energy of the cell are then: 1) the bending energy needed to deform a relatively flat surface into a highly curved tube of radius R_t ; 2) the energy necessary to de-adhere the membrane from the cytoskeleton; and 3) the osmotic effect of mobile proteins that cannot diffuse into the tether and accumulate at the base of the tether. Figure 2-8 shows a schematic of the membrane tether and the contributions to the energy required to extend the tether.

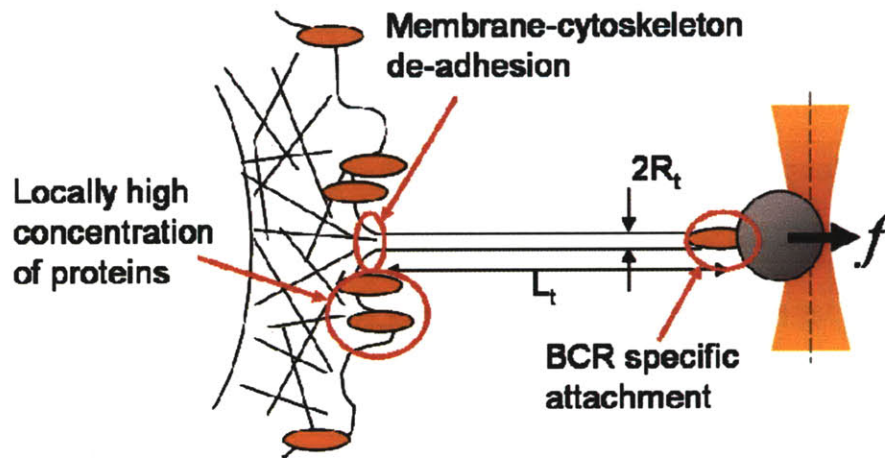


Figure 3.8 A schematic of the membrane tethering experiment via a specific attachment to the BCR is shown depicting the energetic contributions to extending the membrane including the bending energy to move lipids from a relatively flat surface to the high curvature ($1/R_t$) tether, the energy to de-adhere the lipid bilayer from the cytoskeleton, and the energy due to the osmotic potential of the locally high concentration of proteins at the base of the tether.

Taking these components into account, the total change in free energy per unit area,

$d\tilde{G}$, can be written as:

$$d\tilde{G} = \left[\frac{\kappa_B}{2} \left(\frac{1}{R_t^2} \right) \right] + \gamma + \Pi \quad (3.2)$$

where R_t is the tether radius, κ_B is the bending stiffness of the membrane, γ is the adhesion energy, and Π is a membrane osmotic pressure difference created by accumulation of membrane proteins at the base of the tether. Equating the work done to the total work gives the static tether force.

$$f_0 dL_t = \left[\frac{\kappa_B}{2} \left(\frac{1}{R_t^2} \right) \right] (2\pi R_t dL_t) + \gamma (2\pi R_t dL_t) + \Pi (2\pi R_t dL_t) \quad (3.3)$$

The osmotic effects are experimentally difficult to verify and quantify. Therefore, it is grouped together with the γ term to give an effective adhesion energy, γ_e . Reducing equation (3.3) gives the static tether force as a function of R_t .

$$f_0 = \frac{\pi \kappa_B}{R_t} + 2\pi R_t \gamma_e \quad (3.4)$$

Waugh and Hochmuth gave an independent relation for the static tether force based on mechanical equilibrium of membrane tubes [108].

$$f_0 = \frac{2\pi \kappa_B}{R_t} \quad (3.5)$$

A detailed derivation of this equation is provided in Appendix 3A. Combining equations (3.4) and (3.5) provides a simple means of relating the static tether force to the membrane adhesion energy provided the membrane bending stiffness is known.

$$\gamma_t = \frac{f_0^2}{8\pi^2\kappa_B} \quad (3.6)$$

These equations assume an infinitely slow pulling velocity. At a finite pulling velocity, viscous effects become important. In general the rate dependence of the tether force may be a result of a number of contributions including friction between the membrane and underlying cytoplasm, friction between the inner and outer leaflet of the lipid bilayer, rate dependence of the bonds that anchor the membrane to the cytoskeleton, and viscous flow of the cytosol into the membrane tube. Hochmuth et al [105] described all of these contributions by a single effective membrane viscosity, η_{eff} . The tether force was experimentally observed to vary linearly with pulling velocities ranging from 1-8 $\mu\text{m/s}$ [39, 98], and so the total tether force is given by:

$$f_t = f_0 + \eta_{eff} 2\pi U_t = \frac{\pi\kappa_B}{R_t} + 2\pi R_t \gamma_t + \eta_{eff} 2\pi U_t \quad (3.7)$$

where U_t is the pulling velocity. The 2π is present because the effective viscosity is a membrane viscosity, meaning it depends on the frictional resistance to the flow of membrane area into the tether. This mechanical framework provides a convenient means to identify both the static and viscous properties of the cell membrane.

3.4 MEMBRANE TETHERING EXPERIMENTAL RESULTS:

3.4.1 Cell-bead Adhesion Results. “Deft touch” experiments were performed to measure the adhesions of HEL-coated beads and non-specific (streptavidin-coated) beads to MD4 B cells. The adhesion results of HEL coated beads vs. a non-specific interaction (streptavidin coated beads) are shown in figure 3.9 illustrating that the beads indeed attached specifically to the BCR in an antigen-specific manner.

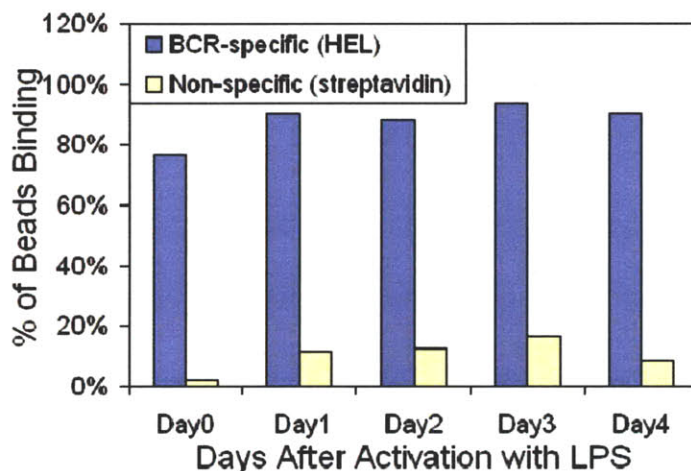


Figure 3.9 Deft-touch experiments to test the cell-bead adhesion confirm that the interaction is antigen-specific.

3.4.2 Membrane Tethering Force-extension. Membrane tethering experiments were carried out with HEL-coated beads on MD4 B Cells ranging from Naïve Cells (Day 0) to fully differentiated Plasma cells. Representative force versus tether length and force versus time curves are shown in figure 3.10. Appendix 3B contains a larger sampling of representative data traces.

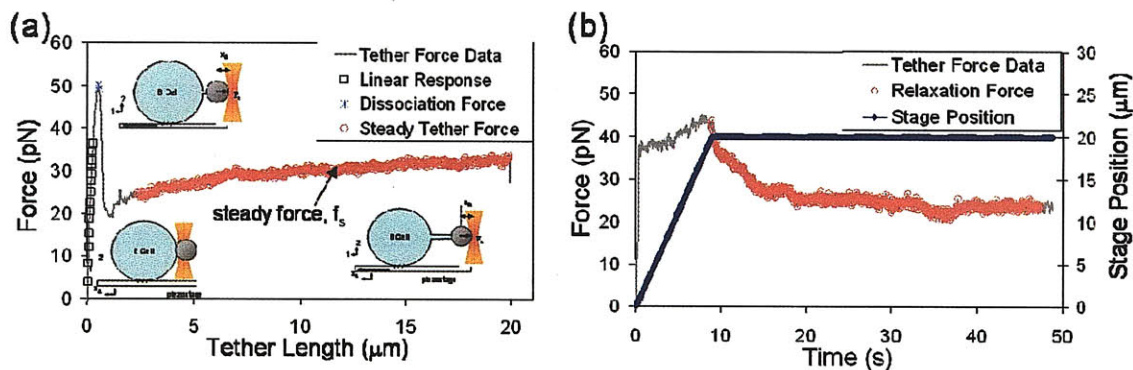


Figure 3.10 Representative force versus extension (a) and force versus time (b) curves are shown for a membrane tethering experiment with a pulling velocity of 2.25 $\mu\text{m/s}$. The insets in (a) show schematics of the experimental assay at different stages of the experiment.

In order to address the dynamic force relaxation behavior of the B cell membrane, tether extension was halted before reaching the nonlinear stiffening region of the tether force profile. In fact, tethers could be extended up to several cell diameters (20-50 μm) without depletion of the membrane reservoir. In general, the force of tether extension initially exhibited a linear response while the bead was deforming the local structure of the membrane and underlying cytoskeleton. At some critical force, f_d , the membrane locally dissociated from the underlying cytoskeleton, and a membrane tether was formed. The membrane tether was then extended at a relatively constant force to a length ranging from 10-20 μm by moving the piezostage a constant velocity ranging from 0.5 – 5.0 $\mu\text{m/s}$. After reaching the maximum tether length, the force exponentially relaxed to a constant value.

3.4.3 Membrane Mechanical Properties. Figure 3.11 shows f_t for two pulling velocities on MD4 B cells ranging from zero days after activation with LPS (Day0) up to 4 days

after activation (Day4) when cells should be fully differentiated into antibody secreting Plasma Cells. The graph shows the average value and the error bars indicate ± 1 standard deviation. The variation in the experiments is large due to the inhomogeneous nature of the B cell membrane. However, there are still two noticeable trends in the data. First, the larger pulling velocity results in a larger f_t due to the rate dependent viscous effects. Additionally, f_t increases on Days 3 and 4 for the 5.0 $\mu\text{m/s}$ pulling velocity while f_t for the slower pulling velocity stays nearly constant throughout differentiation.

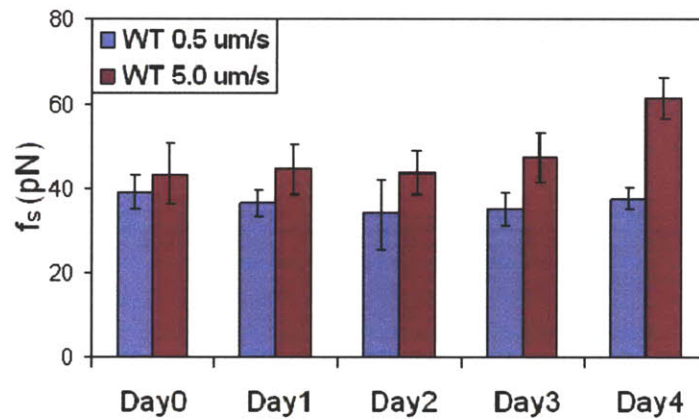


Figure 3.11 The steady tether force for MD4 B cells is shown as a function of the number days after activation. The columns and error bars indicate the average $\pm 95\%$ confidence interval. Day0 indicates Naïve cells, and Day4 cells are fully differentiated into antibody secreting Plasma Cells

Figure 3.12 shows the steady tether force versus pulling velocity for Day0 and Day4 cells in addition to a linear fit to each dataset. Membrane tethering experiments were performed at an intermediate velocity on Day4 to confirm the linear trend. Days 1, 2, and 3 are omitted from the graph for clarity.

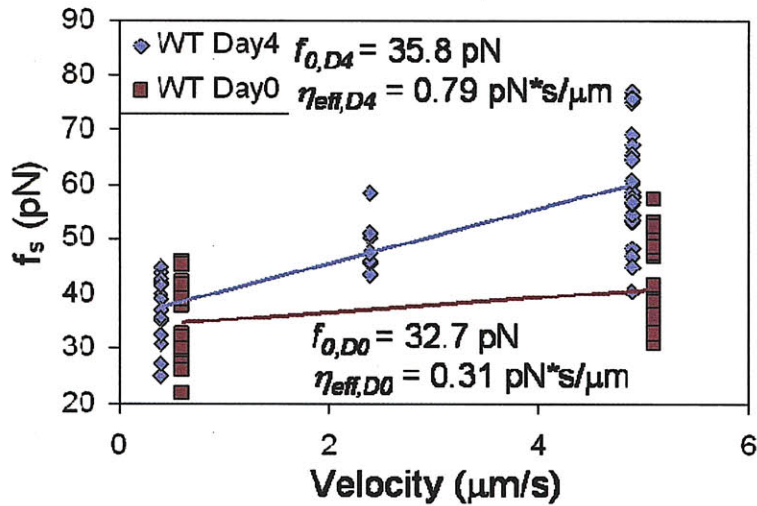


Figure 3.12 The steady tether force for MD4 B cells is shown as a function of the number days after activation. Day0 indicates Naïve cells, and Day4 cells are fully differentiated into antibody secreting Plasma Cells

The effective viscosity can be determined from the tether force dependence on velocity (i.e. the slope of the linear fit), and the y-intercept gives the static tether force. Table 3.1 shows the MD4 B cell membrane mechanical properties as determined from the force versus velocity curves. κ_B was assumed to be 0.2 pN/ μm which is a typical value for a lipid bilayer [99].

Day	η_{eff} (pN*s/ μm)	f_0 (pN)	γ_T (pN/ μm)
0	0.31	32.7	67.8
1	0.41	31.6	63.1
2	0.35	33.7	71.8
3	0.75	33.0	69.0
4	0.79	35.8	81.4

Table 3.1 The steady tether force for MD4 B cells is shown as a function of the number days after activation. Day0 indicates Naïve cells, and Day4 cells are fully differentiated into antibody secreting Plasma Cells

3.4.4 Tether Force Relaxation. Figure 3.13 shows the time-dependent relaxation of the tether force which occurs after halting the tether pulling in the steady force region and then holding the tether length constant at 20 μm .

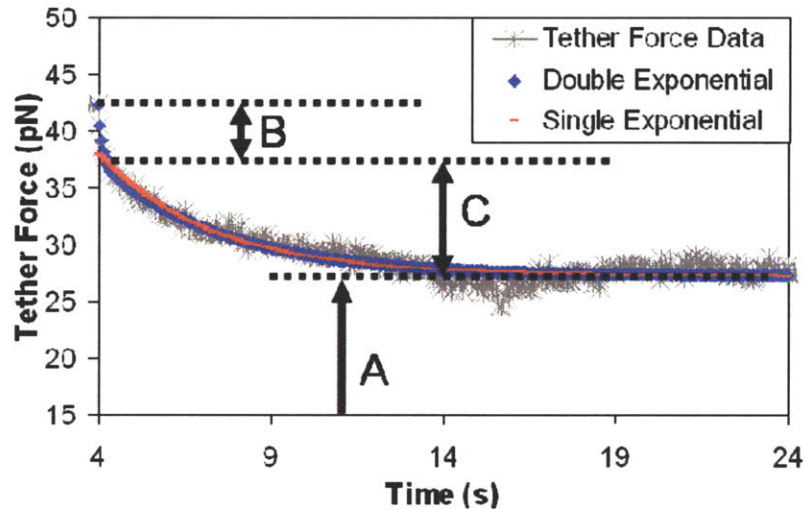


Figure 3.13 The steady tether force for MD4 B cells is shown as a function of the number days after activation. Day0 indicates Naïve cells, and Day4 cells are fully differentiated into antibody secreting Plasma Cells

The force relaxation data was initially fit to the following exponential force decay model.

$$f_i(t) = A + B \exp\left(\frac{-t}{\tau_1}\right) + C \exp\left(\frac{-t}{\tau_2}\right) \quad (3.8)$$

where B and C are the magnitude of the short and long time scale relaxations respectively, A is the equilibrium value of the tether force, and τ_1 and τ_2 are the respective time constants. As shown in figure 3.13, a single exponential model does not accurately capture the initial short time scale relaxation. Figure 3.14 shows the results of fitting force relaxation data on Day4 MD4 B cells to equation (3.8) where

membrane tethers were pulled to a length of 20 μm at three different velocities (0.5 $\mu\text{m/s}$, 2.5 $\mu\text{m/s}$, and 5.0 $\mu\text{m/s}$).

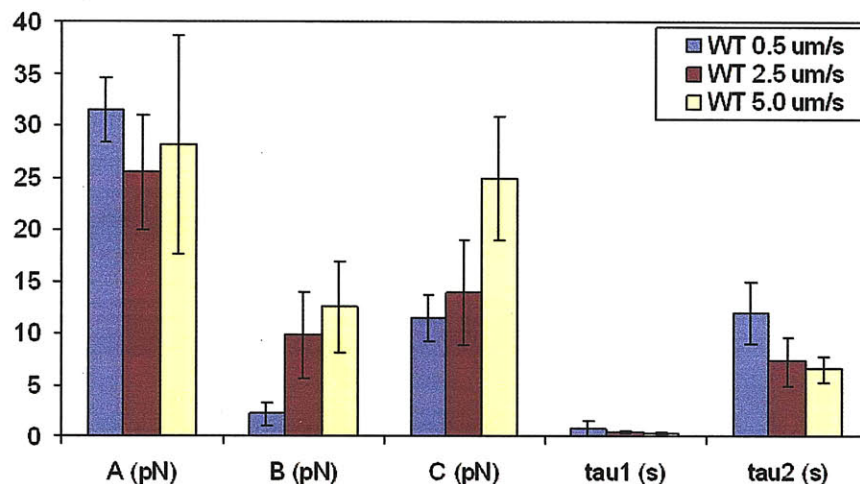


Figure 3.14 Results of fitting tether force relaxation data to the double exponential model of equation (3.8) where tethers were pulled to a length of 20 μm at three different velocities. The columns and error bars indicate the average \pm standard deviation.

The parameters in figure 3.14 can be related to the tether force model of equation (3.7) in order to identify the relevant relaxation mechanisms. The rate dependence of the steady tether force is contained in the last term of equation (3.7) which is linearly proportional to the pulling velocity, U_t . When the piezostage stops moving U_t becomes zero, and therefore, the last term of equation (3.7) should disappear on a short time scale. This is consistent with the results shown in figure 3.14 where the magnitude of the short time scale relaxation, B , is indeed proportional to the pulling velocity. The short time scale relaxation mechanism is then the effective rate dependence of the membrane vanishing after the pulling velocity becomes zero.

After the last term of equation (3.7) (i.e. the rate dependence) vanishes, only the static tether force, f_0 , given in equation (3.4) remains. Figure 3.15 shows a plot of the static tether force as a function of radius assuming $\kappa_B = 0.2 \text{ pN}/\mu\text{m}$ and $\gamma = 81.4 \text{ pN}$ which is the value obtained for Day 4 wild-type MD4 B cells.

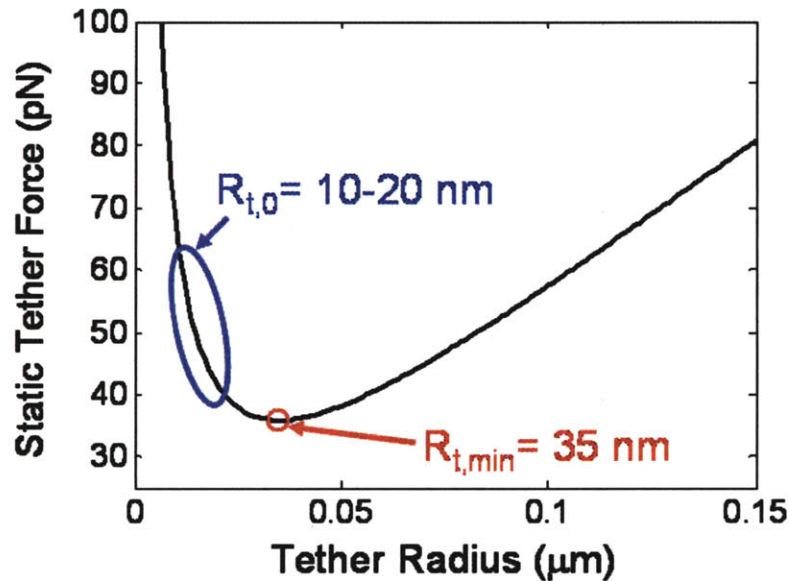


Figure 3.15 The static tether force is shown as a function of radius revealing a minimum in the tether force, f_{min} (red circle). The radius where f_{min} occurs, $R_{t,min}$, is typically larger than the typical radius of membrane tethers during extension, $R_{t,0}$ (blue oval).

There is a minimum in the tether force, $f_{t,min}$, of 36 pN which in this case occurs at a tether radius of, $R_{t,min} = 35 \text{ nm}$. If lipids can flow into the tether very quickly (or equivalently the tube is extended infinitely slowly), then the tube radius will remain constant at $R_t = R_{t,min}$, and the flow rate of membrane surface area into the tether would be:

$$\dot{A}_{t,min} = 2\pi R_{t,min} U_t \quad (3.9)$$

Rearranging this equation and assuming the membrane flows into the tether at a rate,

$\dot{A}_t^* \neq \dot{A}_{t,min}$, the tube radius is given as:

$$R_t = \frac{\dot{A}_t^*}{2\pi U_t} \quad (3.10)$$

Therefore, if the pulling velocity is constant and the flow rate of membrane surface area into the tether is constant, then R_t will also be constant. This is consistent with the experimental observation that the force indeed remains constant during tether extension. Furthermore, if we assume that the membrane flow into the tether is retarded due to the effective membrane viscosity, then $\dot{A}_t^* < \dot{A}_{t,min}$ and from equation (3.10), $R_t < R_{t,min}$. In this case there will be a driving force to increase the tube radius in order to minimize the force or equivalently the energy of the tether. In the case of pulling a membrane tether infinitely slowly, lipids have ample time to flow into the membrane tube to maintain equilibrium such that $R_t = R_{t,min}$. However, at finite pulling velocities, due to the large viscosity of the cell membrane because of the high concentration of membrane proteins, lipids cannot flow into the tube fast enough to maintain equilibrium resulting in $R_t < R_{t,min}$. Once the tether extension stops, lipids continue to diffuse into the tether in order to increase the tube radius and minimize the energy of the tether as shown in figure 3.16(a). Lipid flow into the tube reduces the elastic energy stored in the tether as shown schematically in figure 3.16(b).

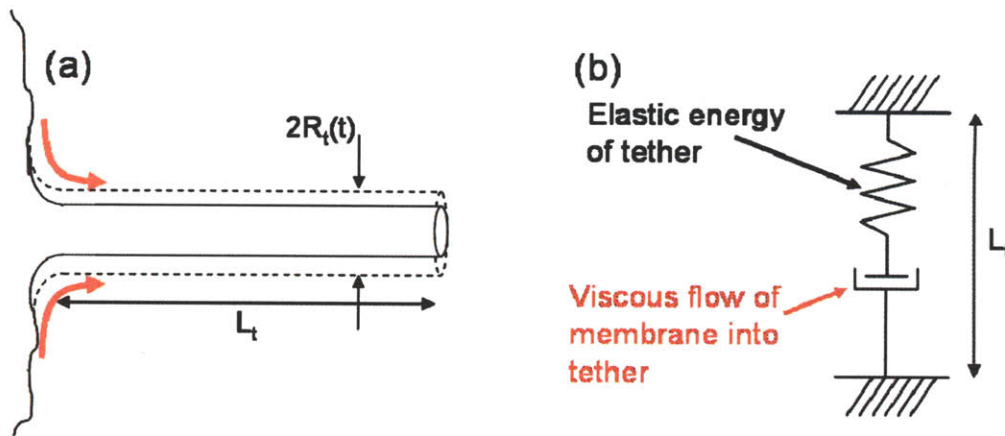


Figure 3.16 (a) After tether extension is halted, lipids continue to flow into the tube resulting in an increase in tether radius. (b) Viscous flow of lipids into the tether reduces the stored elastic energy.

This radial growth was experimentally validated. Figure 3.18(a) shows a DIC image of a membrane tether. Figure 3.17(b) shows the normalized intensity profile across the membrane tether (intensity is shown across the red-line depicted in figure 3.17(a)) both at the instant the tether extension is halted (red) and after 5 seconds of monitoring the force relaxation (blue). The tether cross-section is characterized by a light then dark region (going from top right to bottom left) as indicated by the increase then decrease in intensity. The width of the intensity pattern is indicative of the tether radius. As shown the tether radius increases over a time scale of 5 seconds which is consistent with the time constant of the second relaxation mechanism. Therefore, the longer timescale relaxation mechanism is due to the radial growth of the tether which decreases the force required to maintain a constant tether length. The final equilibrium force is simply the minimum value of the tether force versus tether radius curve. The final equilibrium force is only dependent on the membrane material properties, γ_t and κ_B . This is consistent with the experimental results shown in figure 3.12 where the equilibrium force, A , is independent of pulling velocity.

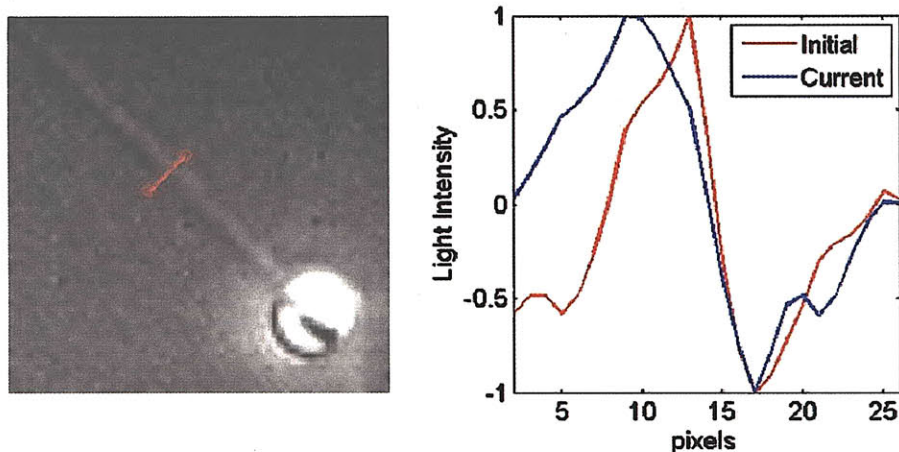


Figure 3.17 (a) shows a DIC image of a membrane tether extracted from a Day 4 wild-type MD4 B cell. (b) The normalized intensity profile of the tether cross-section (along red line in (a)) is shown both immediately and 5 seconds after halting the tether extension. The combined width of the light and dark peaks are indicative of the tether width which grows over time.

3.4.5 1D Model for Radial Tether Growth. A mechanical model was developed to describe the dynamic process of radial growth in the membrane tether. This model is based on equation (3.7) where the “driving force” for membrane flow into the tether during the steady force tether extension is the viscous force, f_v , where $f_v = 2\pi\eta_{eff}U_t = f_t - f_0$. Rearranging equation (3.7) yields:

$$U_t = \frac{f_t - f_0}{2\pi\eta_{eff}} \quad (3.11)$$

The surface area flow rate of membrane into the tether, \dot{A}_t^s , assuming a constant tube radius as previously discussed is:

$$\dot{A}_t^s = 2\pi R_t \frac{dL_t}{dt} = 2\pi R_t U_t \quad (3.12)$$

Combining equations (3.11) and (3.12) gives:

$$\dot{A}_t^s = \frac{R_t (f_t - f_0)}{\eta_{eff}} \quad (3.13)$$

Once the tether length is held constant, the tether surface area increases by increasing the radius. Therefore, equation (3.12) can be rewritten as:

$$\dot{A}_t^s = 2\pi \frac{dR_t}{dt} L_t = 2\pi \dot{R}_t(t) L_t \quad (3.14)$$

The radius can be additively decomposed into the initial tether radius at the moment when the tether extension is stopped, and a growth component, R_g , which is initially equal to zero and increases over time.

$$R_t(t) = R_{t,0} + R_g(t) = R_{t,0} + \int_{t_0}^{t-t_0} \dot{R}_g(t) dt \quad (3.15)$$

t_0 is the time at which the tether extension stops. The initial radius does not change with time and can be determined from value of the steady tether force using equation (3.7). Equation (3.14) can then be rewritten as:

$$\dot{A}_t^s(t) = 2\pi \dot{R}_g(t) L_t \quad (3.16)$$

Recall that \dot{A}_t^s is related to the “driving force” by equation (3.13). Here we assume that the relationship between the “driving force” and membrane area flow rate into the tether does not change after the tether extension is halted. However, once the pulling velocity stops, the “driving force” for membrane flow into the tether becomes the difference between the current tether force, and the minimum tether force shown in figure 3.13. Combining equations (3.16) and (3.13) and modifying the driving force gives the tether radial growth rate.

$$\dot{R}_g(t) = \frac{R_t(t)}{2\pi L_t \eta_{eff}} (f_t(t) - f_{t,min}) \quad (3.17)$$

Equations (3.4), (3.15), and (3.17) evolve with time and describe the radial tether growth, and the force relaxation as a function of time. When the “driving force”, $f_t(t) - f_{t,min}$, is large, the radius grows quickly and the force decays quickly. When the “driving force” approaches zero, the growth slows down resulting in force relaxation that resembles an exponential decay. Figure 3.18 illustrates the dependence of the increase in tether radius on the tether length and effective membrane viscosity based on our time-dependent growth model.

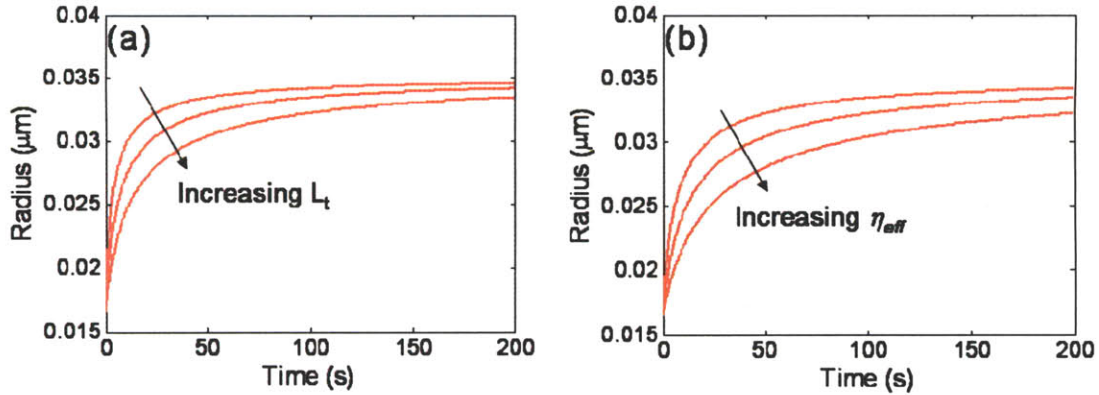


Figure 3.18 (a) shows the radial growth over time for the case of $\eta_{eff} = 0.79$ pN*s/ μm and $L_t = 5, 10,$ and 20 μm . (b) shows the radial growth for $L_t = 20$ μm and $\eta_{eff} = 0.40, 0.79,$ and 1.58 pN*s/ μm .

This model is useful to predict the force relaxation behavior of membrane tethers. Figure 3.19 shows predictions of the rate dependence and length dependence of the force relaxation. For these predictions the short time scale relaxation was fit with a single exponential model, and the longer time scale relaxation was predicted with the developed growth model. The value of the initial tether radius was determined from the initial force value (steady force during tether extension) using equation (3.7) where the viscous term was replaced by the experimentally measured magnitude of the short timescale relaxation, and γ_t was adjusted to fit the equilibrium force value. κ_B was left as 0.2 pN/ μm , and η_{eff} was taken from table 3.1 for Day 4 cells. Representative force relaxation traces were chosen such that the parameters reduced from equation (3.8) were close to the average values.

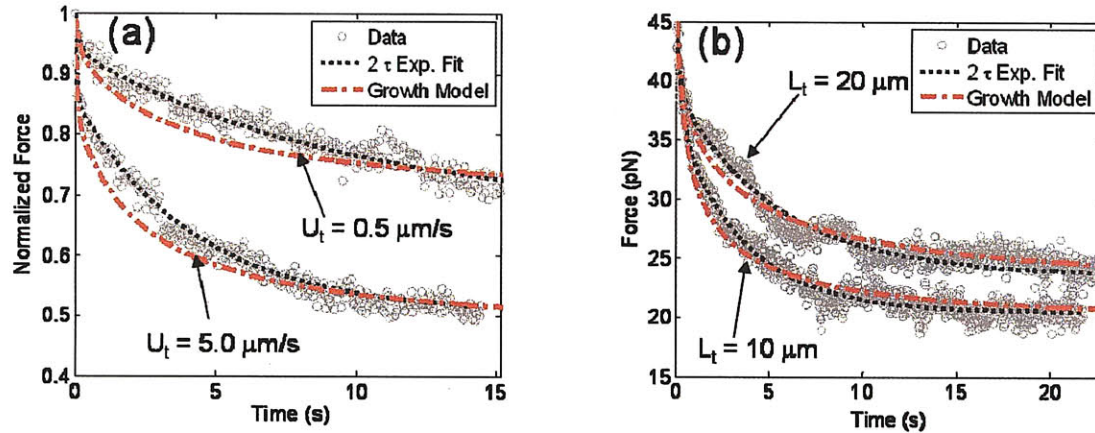


Figure 3.19 (a) shows the normalized force relaxation predictions of the 1-D growth model for two different pulling velocities. The force is normalized by the initial maximum value for each case. (b) shows the force relaxation predictions for two different tether lengths.

This model is also useful to further understand experimental force relaxation results. For example, the average time constants of the longer timescale relaxation for Day 0 and Day 4 cells were 3.43 s and 6.54 s respectively. These results suggest that Day 0 cells have a lower effective membrane viscosity which confirms the previous results for the steady tether force.

3.5 CONCLUSIONS:

This research combines state-of-the-art single cell mechanical experiments with powerful cell biology and biochemistry techniques to study the role of membrane mechanics in the physiological function of the B lymphocyte. The cell membrane was characterized utilizing membrane tethering experiments with optical tweezers. This approach was applied to primary B cells harvested from the spleen of BCR transgenic mice [107], allowing specific engagement of the BCR by an antigen coated bead. Experiments were carried out on naïve cells and throughout the Plasma Cell

differentiation process on cells that were activated with LPS. Naïve cells were found to have an effective membrane viscosity of $0.31 \text{ pN}\cdot\text{s}/\mu\text{m}$ and a total adhesion energy of $67.8 \text{ pN}\cdot\mu\text{m}/\mu\text{m}^2$. Effective viscosity can vary greatly in distinct cell types. Neuronal growth cones [101], outer hair cells [40], and red blood cells [105] have effective viscosities of 0.14, 2.4, and 27 $\text{pN}\cdot\text{s}/\mu\text{m}$ respectively. In these cells with a smooth cell membrane, the contribution of adhesion energy is difficult to isolate from the contribution of the cortical tension. This vast discrepancy in membrane properties are reflective of the unique functions of these cell types. Perhaps a more relevant comparison is to the results of Marcus and Hochmuth who found an adhesion energy of $150 \text{ pN}\cdot\mu\text{m}/\mu\text{m}^2$ and an effective viscosity of $1.1 \text{ pN}\cdot\text{s}/\mu\text{m}$ for human neutrophils [98], another type of leukocyte, placing the mechanical properties of a murine B cell slightly lower than those a human Neutrophil membrane.

Activation induces a series of biochemical changes in cells including upregulation of the BCR and cytoskeletal proteins that leads to global structural evolutions of the differentiating B Cell. Our experiments revealed that the physical changes occurring upon activation lead to an approximately two-fold increase in membrane viscosity. These results are consistent with Marcus and Hochmuth [98] who found a slight increase in membrane viscosity in human Neutrophils activated with fMLP. The source of the membrane's rate-dependent behavior is difficult to single out as it may involve contributions from several components of the B cell's physical machinery including frictional resistance between the membrane and cytoskeleton, slip between the leaflets of the membrane, viscous flow of cytosol, as well as rate-dependent behavior of bonds

connecting the membrane and cytoskeleton. Regardless of the source of rate-dependent behavior, the effective behavior of the cell membrane is critical to the physiological function of the B cell. The change in effective membrane viscosity is most evident after complete differentiation into a Plasma Cell when the cell is migrating through lymphoid tissues and is primed to secrete antibodies *in vivo*. Our 1-D growth model shows that the increased membrane viscosity results in slower tether force relaxation due to slower membrane flow into the tether. The membrane is integrally involved in antibody secretion, cell migration, and communication with the extracellular environment including other cells. The effective membrane viscosity, and more specifically dynamic flow of membrane to achieve large deformations, is likely an important factor in achieving these functions.

Finally, our results have shown that the lipid bilayer can passively rearrange in order to relieve stresses in the cell membrane. This passive rearrangement plays an important role in physiological function of B cells; specifically, it was identified and experimentally validated that the radius of the membrane tube grows over time which serves as a force relaxation mechanism. This rearrangement has implications for the physiological function of membrane tethers and likely also plays a role in other processes where the cell membrane achieves large deformations such as spreading during antigen detection. A mechanical model was developed to describe the radial growth and force relaxation based on a 1D growth framework where the radius is decomposed into an initial component and a growth component. Our simple framework describes the dependence of growth dynamics on tether length and tether extension velocity. Specifically the

characteristic time of membrane flow is inversely proportional to the membrane viscosity and the characteristic length over which the lipids flow (in this case L_t) and is directly proportional to the circumference, or radius of the membrane structure they are flowing into. The dynamic behavior of these membrane tubes likely plays an important role during cell rolling. Furthermore, several cell types, for example T cells [109], use these membrane tubes for intercellular communication. Understanding the physical properties of these membrane tubes is important for enlightening their role in intercellular signaling. For example, cytosol must flow into the tether to support radial growth. If membrane tubes connect different cells, this cytosolic flow may transport signaling proteins or ions that can be used for efficient and specific intercellular communication. The ability to dynamically describe the physical characteristics of membrane tubes is useful in understanding their physiological function as well as the mechanical role of membrane flow in B cell biological processes.

Here we have developed a novel approach of combining system manipulation by cell biology and biochemistry techniques with single cell experiments employing optical tweezers and micromechanical modeling of the cell membrane. Our results have characterized the mechanical properties of the B cell membrane in Naïve cells and shown evolution of physical properties upon B cell activation. This evolution affects the force relaxation behavior of the B cell membrane which likely plays a major role in the large deformations achieved by the membrane during physiological functions such as cell rolling and antigen detection. This indicates that, as expected, the physical machinery of the B cell is intertwined with the biochemical machinery of the B cell.

These experiments were done in a highly immunologically relevant system in an antigen specific manner. In the following chapter we further investigate the inter-dependence of the physical and biochemical machinery of the B cell.

3.6 Appendix 3A: Mechanical Equilibrium of Membrane Tubes

Equation 3.5 was originally obtained by Waugh and Hochmuth [108] through satisfying mechanical equilibrium in membrane tubes. Their derivation is summarized here. The constitutive relations are based on the assumptions that areal strains are very small and the shear stiffness is very low (i.e. no resistance to in-plane shear deformations), which reliably describe the mechanical behavior of a lipid bilayer. The surface isotropic stress, $\bar{\sigma}$, and the surface shear stress, σ_s , are defined as:

$$\bar{\sigma} = (\sigma_z + \sigma_\phi) / 2 \quad (3.18)$$

$$\sigma_s = (\sigma_z - \sigma_\phi) / 2 \quad (3.19)$$

where the coordinate system is depicted in figure 3.A1(a).

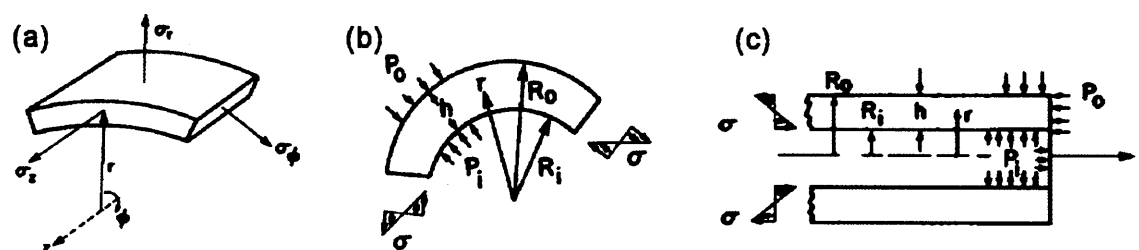


Figure 3.A1 Mechanical equilibrium of membrane tubes. (a) shows the stresses acting on a material element in the membrane tube and the coordinate system. (b) shows the force acting in the radial direction on a portion of the tube cross-section. (c) shows a

cross-sectional view along the axis of the tether denoting force acting in both the radial and axial directions[108].

The condition of zero resistance to in-plane shear deformations requires that $\sigma_s = 0$.

Combining this condition with equations 3.18 and 3.19 gives:

$$\sigma_z = \sigma_\phi = \bar{\sigma} \quad (3.20)$$

Since the in plane area changes are very small, the linear relationship between the internal stresses and the fractional area change, α , given in equation (3.21) is used to describe the membrane behavior.

$$\bar{\sigma} - \sigma_r = E\alpha(r) \quad (3.21)$$

E is the elastic modulus of the membrane (it is assumed that the membrane is homogeneous and isotropic in the plane of the membrane). The fractional area is defined as:

$$\alpha(r) = \frac{A(r)}{A_0} - 1 \quad (3.22)$$

where A_0 is the area under no applied loads which is assumed to be a flat configuration.

The area change, $\alpha(r)$, can be written with respect to the in terms of the area change of the mid-surface, α_{av} , using equation (3.22).

$$\alpha(r) - \alpha_{av} = (1 + \alpha_{av})[A(r)/A_{av} - 1] \quad (3.23)$$

The ratio, $A(r)/A_{av}$, is:

$$\frac{A(r)}{A_{av}} = \frac{2\pi r L_t}{2\pi R_{av} L_t} = \frac{r}{R_{av}} \quad (3.24)$$

where L_t is the length of the tube. Combining equations (3.23) and (3.24) yields:

$$\alpha(r) = \alpha_{av} + (1 + \alpha_{av})(r/R_{av} - 1) \quad (3.25)$$

Substituting equation (3.25) into equation (3.21) gives a constitutive relation between the stress difference, $\bar{\sigma} - \sigma_r$, and the tube radius.

$$\bar{\sigma} - \sigma_r = E\alpha_{av} + E(1 + \alpha_{av})(r/R_{av} - 1) \quad (3.26)$$

3.6.1 Radial Force Balance. The radial forces acting on the tube are shown in figure 3.A1(b). Equilibrium in the radial direction requires that:

$$\frac{d\sigma_r}{dr} = \frac{\bar{\sigma} - \sigma_r}{r} \quad (3.27)$$

This equation can be combined with equation (3.26) and integrated using the boundary condition $\sigma_r|_{r=R_i} = -P_i$ to give the radial dependence of σ_r .

$$\sigma_r(r) = -P_i + E \left[\frac{\alpha_i + 1}{R_i} (r - R_i) - \ln \left(\frac{r}{R_i} \right) \right] \quad (3.28)$$

Applying the boundary condition at the outer edge, $\sigma_r|_{r=R_o} = -P_o$, results in a relation between tube geometry, membrane properties, and the pressure difference.

$$P_i - P_o = E \left[\frac{\alpha_{av} + 1}{R_{av}} h - \ln \left(\frac{R_o}{R_i} \right) \right] \quad (3.29)$$

where h is the thickness of the tube, $R_{av} = (R_o + R_i)/2$. The logarithmic term in this equation can be approximated using the series expansion:

$$\ln(1+x) = x - \frac{x^2}{2} + \frac{x^3}{3} - \frac{x^4}{4} + \dots \quad (3.30)$$

Using this expansion in equation (3.28) yields the constitutive equation for a cylindrical pressure vessel:

$$\Delta P R_{av} = K_a \alpha_{av} - \frac{K_a}{12} \left(\frac{h}{R_{av}} \right)^2 + O \left(\frac{h}{R_{av}} \right)^4 + \dots \quad (3.31)$$

where $K_a = Eh$ is the area expansion modulus. The first term give the well-known relation for a thin-walled pressure vessel. The higher order terms give a correction for the case when the wall thickness becomes large compared to the tube radius.

3.6.2 Axial Force Balance. A force balance in the axial direction (see figure 3.A1(c)) yields:

$$\int_{R_i}^{R_o} \bar{\sigma} 2\pi r dr = P_i \pi R_i^2 - P_o \pi R_o^2 + f \quad (3.32)$$

Substituting equations (3.26), (3.28) into (3.31) and integrating gives:

$$\frac{f}{\pi R_{av}} = K_a \alpha_{av} \left(1 + \frac{h^2}{12 R_{av}^2} \right) + \frac{K_a h^2}{12 R_{av}^2} \quad (3.33)$$

In the case of membrane tethers, $\frac{h^2}{12 R_{av}^2} \ll 1$. Hence equation 3.31 can be reduced to:

$$\frac{f}{\pi R_{av}} = K_a \alpha_{av} + \frac{K_a h^2}{12 R_{av}^2} \quad (3.34)$$

Equation (3.34) can be combined with equation (3.31) (eliminating terms higher than order 2) to eliminate the second term giving a constitutive relation for the tether force.

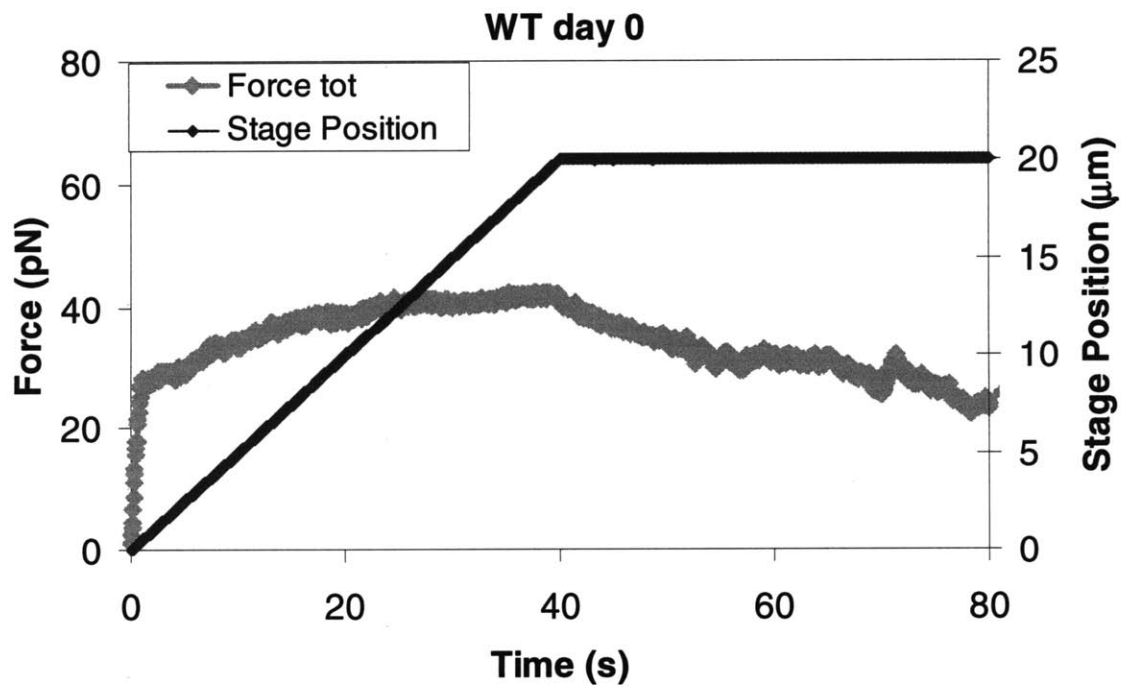
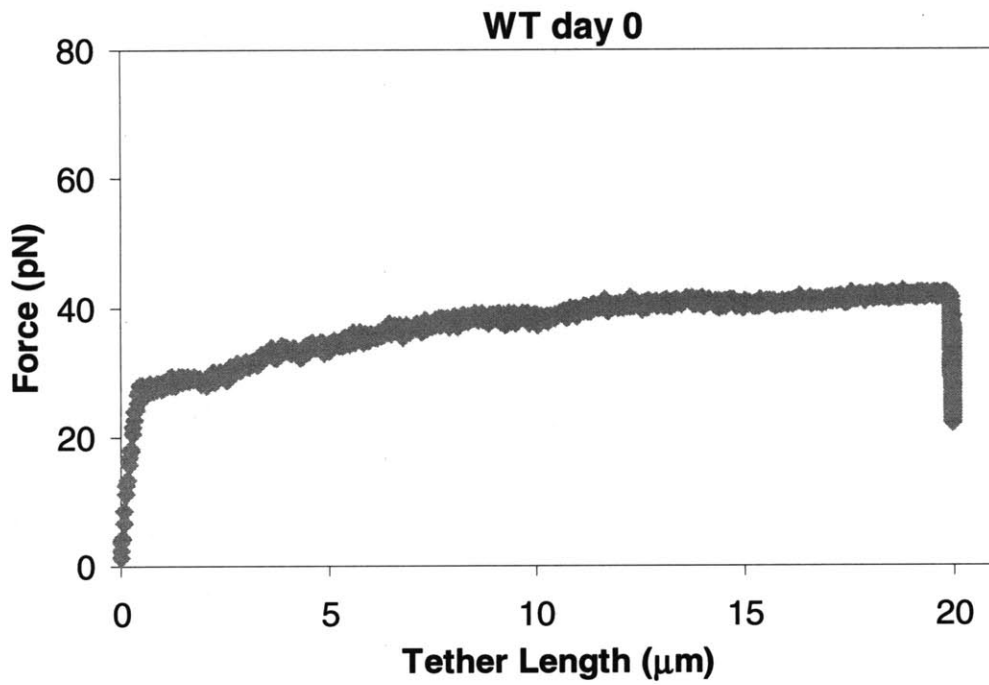
$$\frac{f}{\pi} - \Delta P R_{av}^2 = \frac{K_a h^2}{6 R_{av}} \quad (3.35)$$

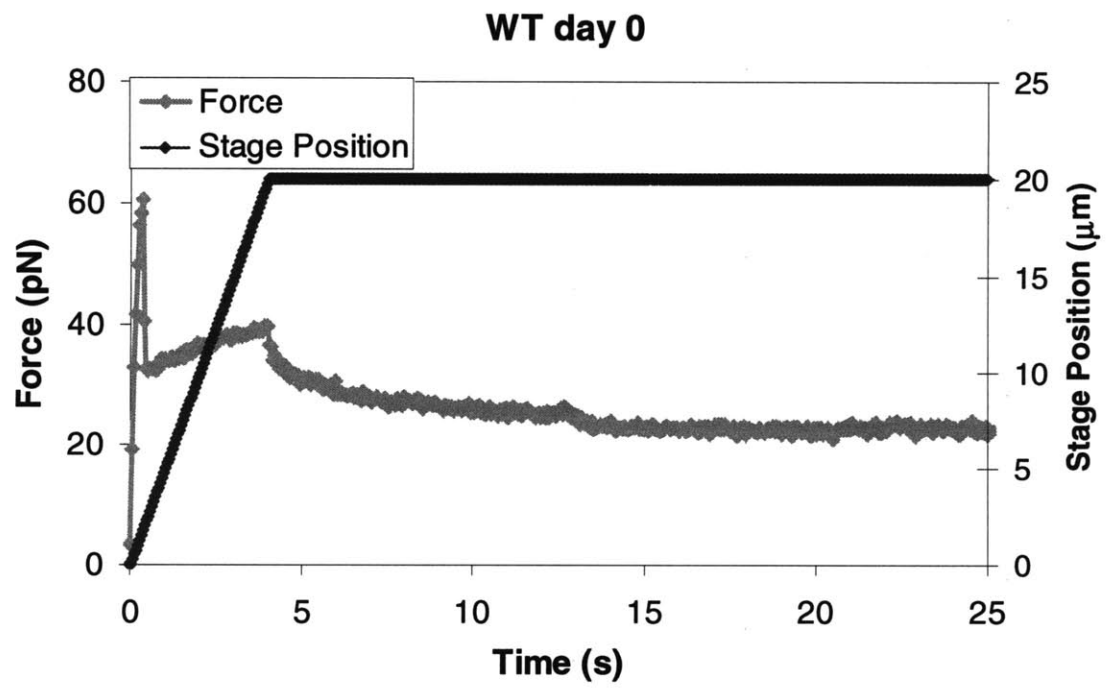
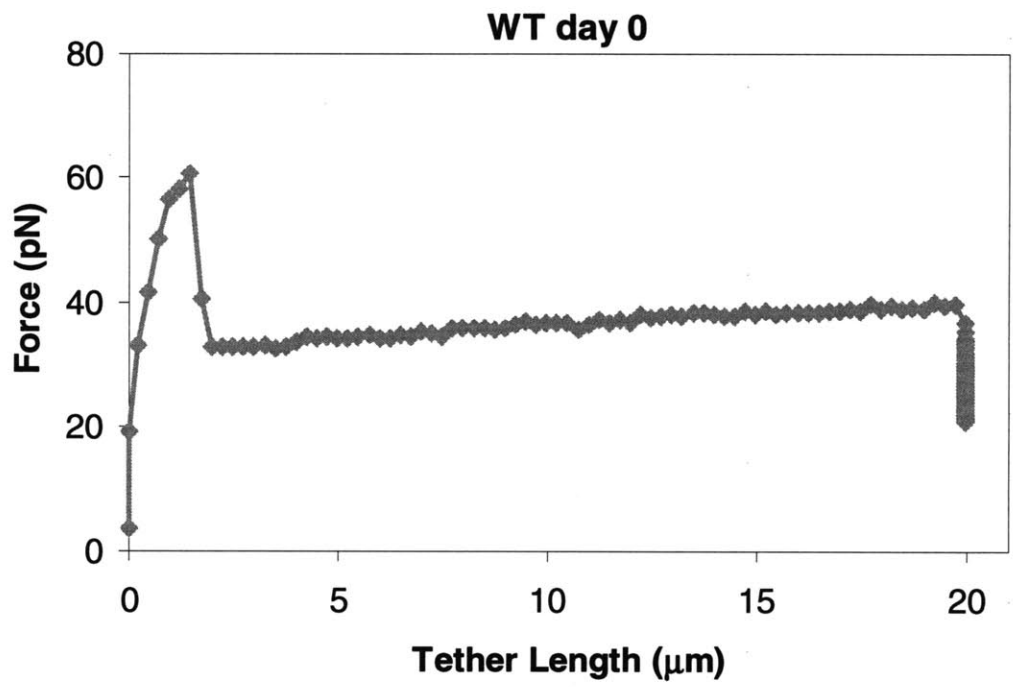
Typical values for $\Delta P R_{av}^2$ are on the order of 0.1 pN which is two order of magnitude smaller than force required to pull membrane tethers from biological cells. Therefore, the pressure difference can be neglected, and the relation given in equation (3.5) is obtained, relating the tether force, f , to material properties and the tube radius, R_{av} . The

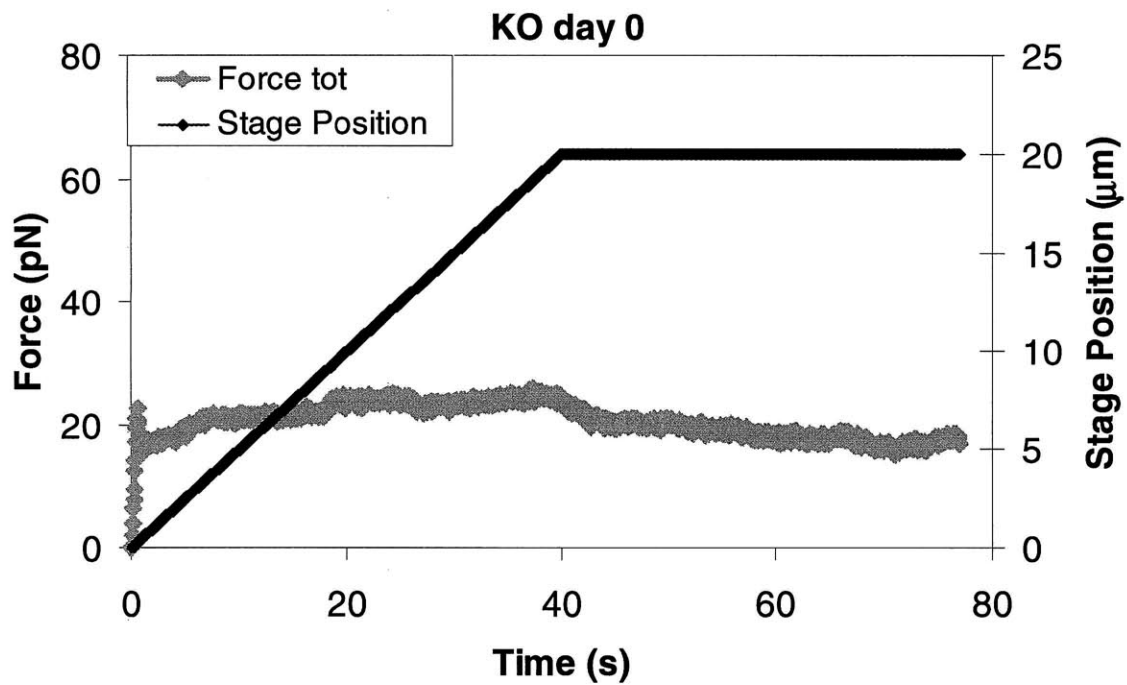
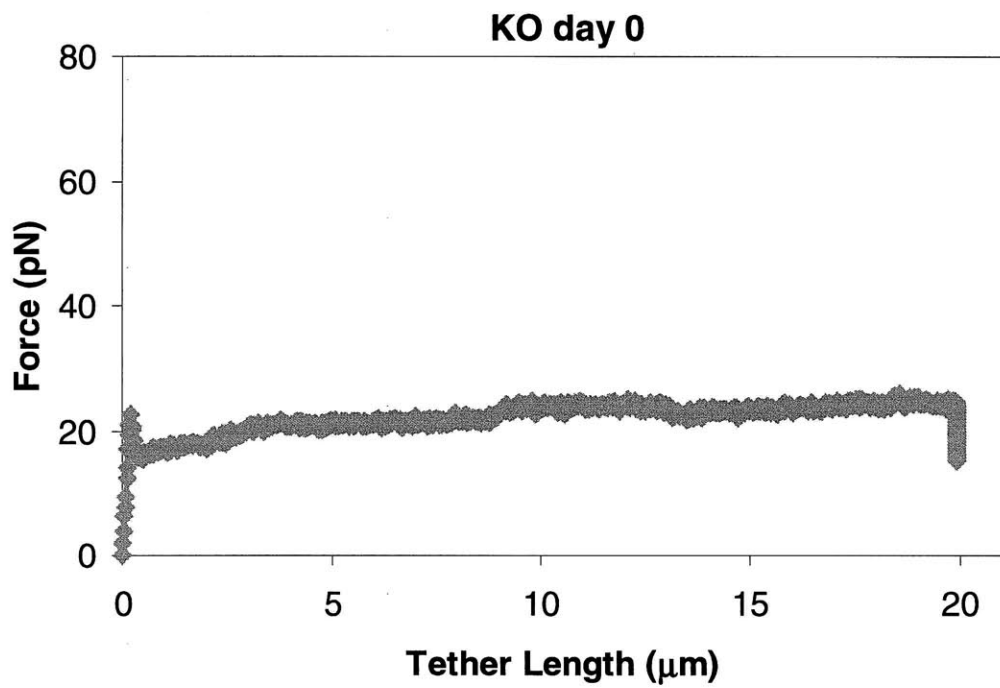
membrane bending stiffness is defined as $\kappa_B = \frac{Eh^3}{12}$. In this derivation it was assumed

that the membrane is made from a uniform material. However, in reality, the cell membrane is comprised of two lipid monolayers that can slip past each other. Waugh and Hochmuth [108] took an identical approach to show that equation (3.5) still holds in the case of a lipid bilayer.

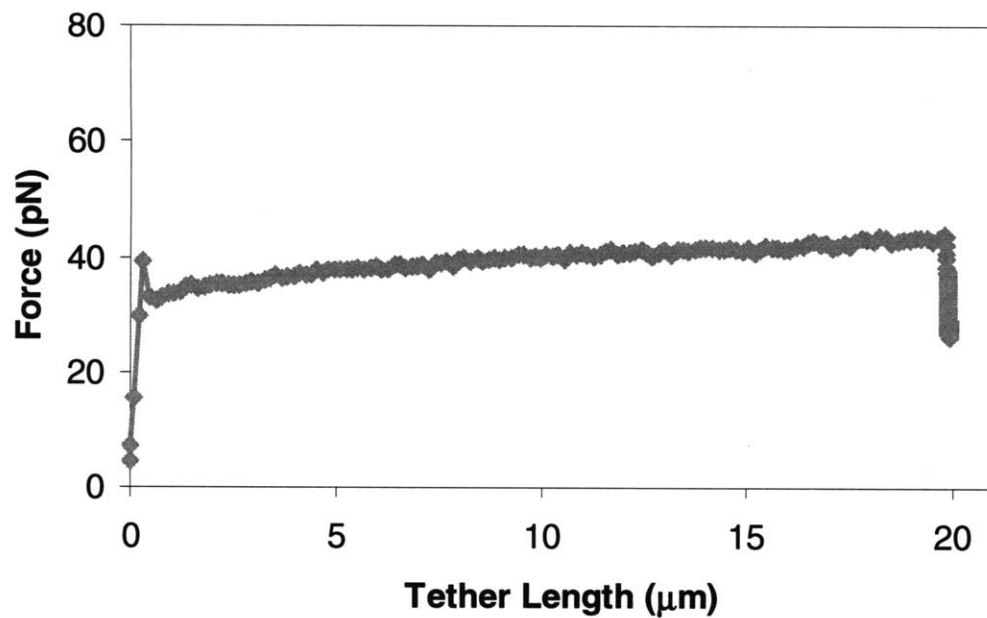
3.7 Appendix 3B: Samples of Tether Force-extension Data



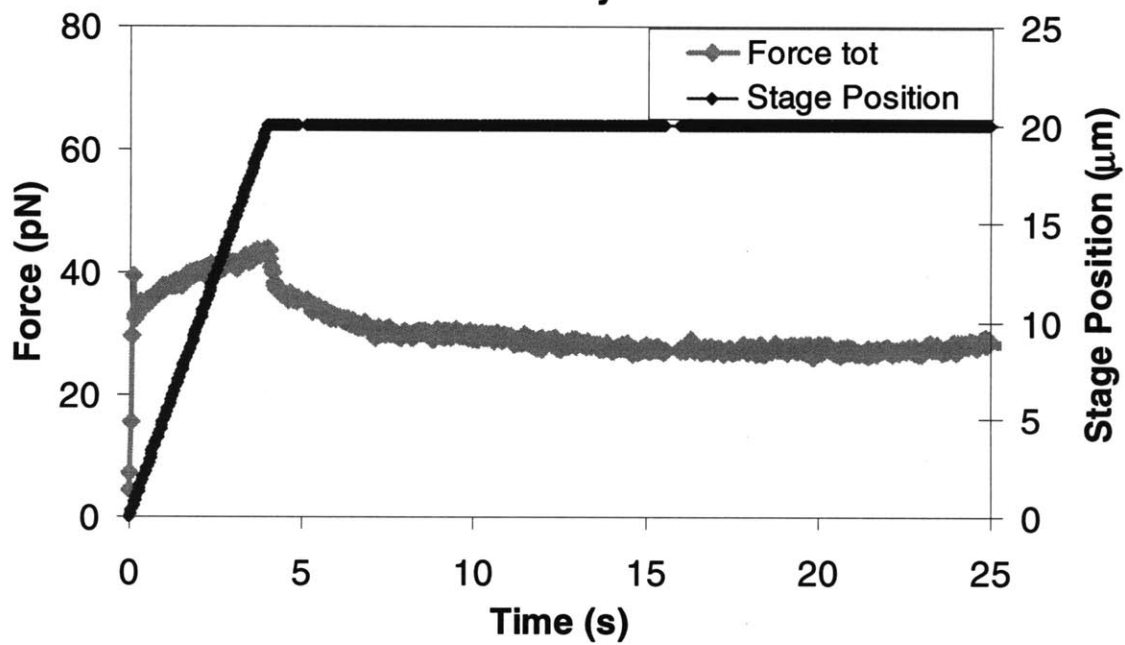


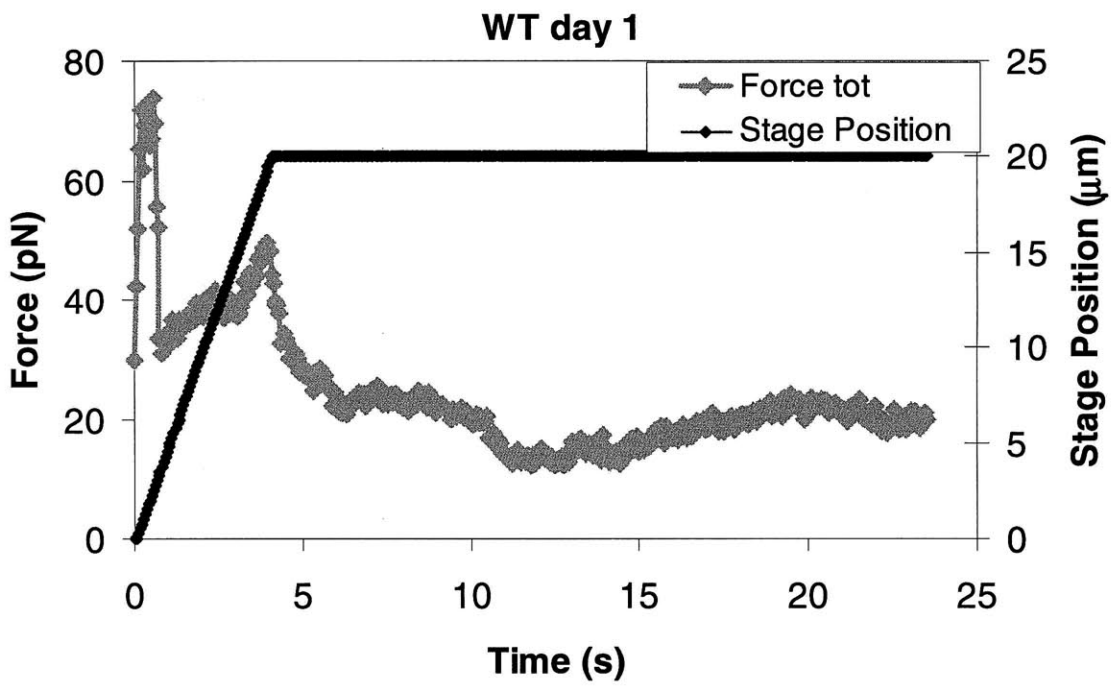
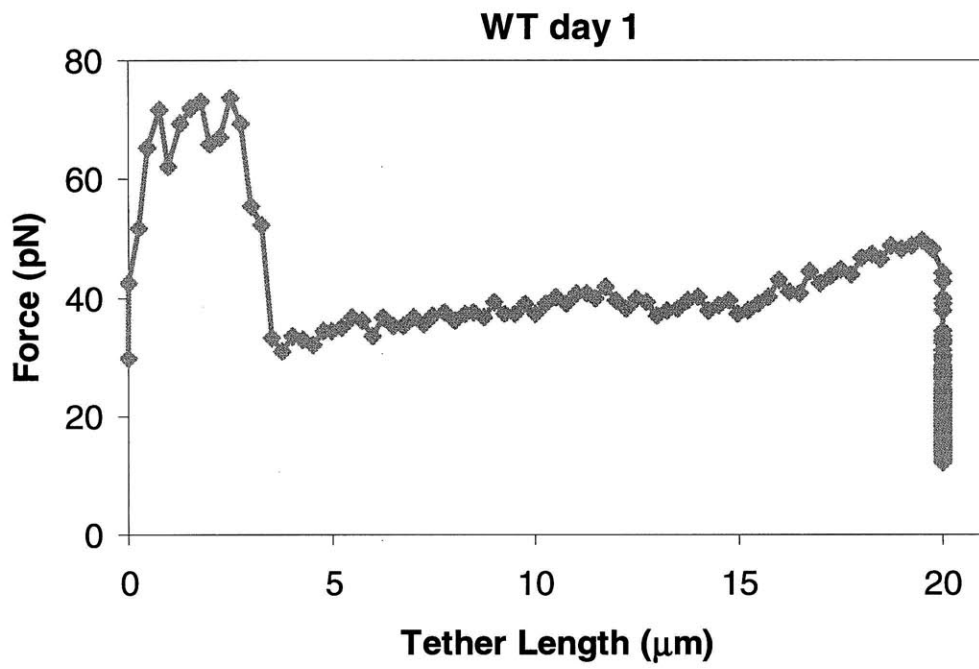


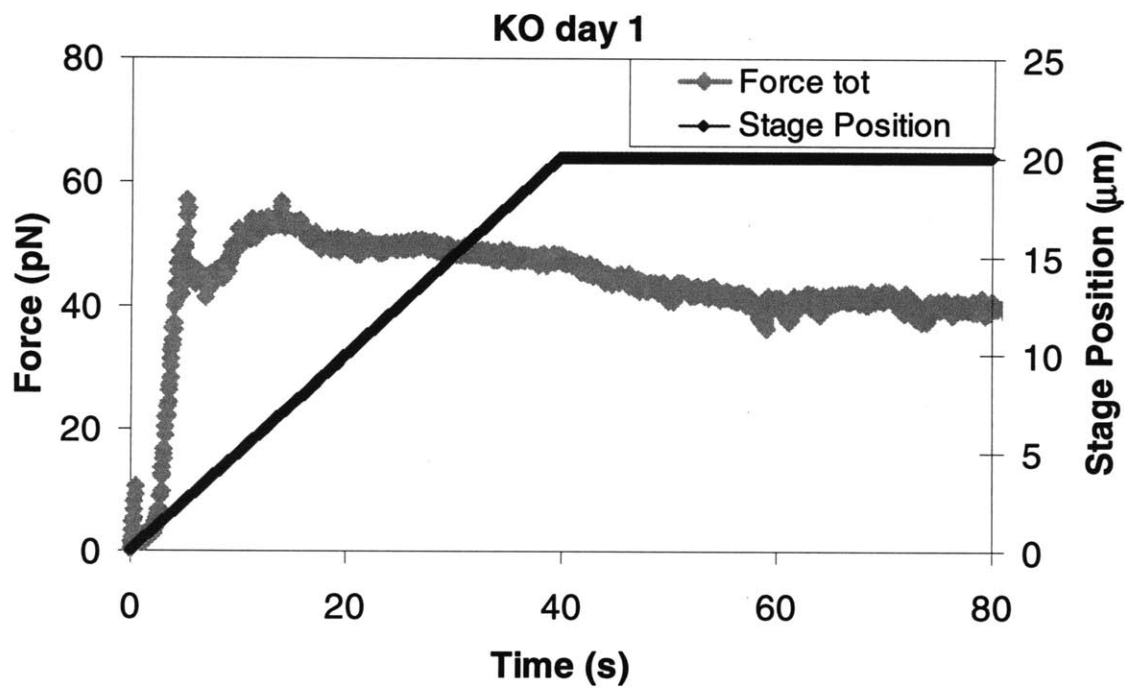
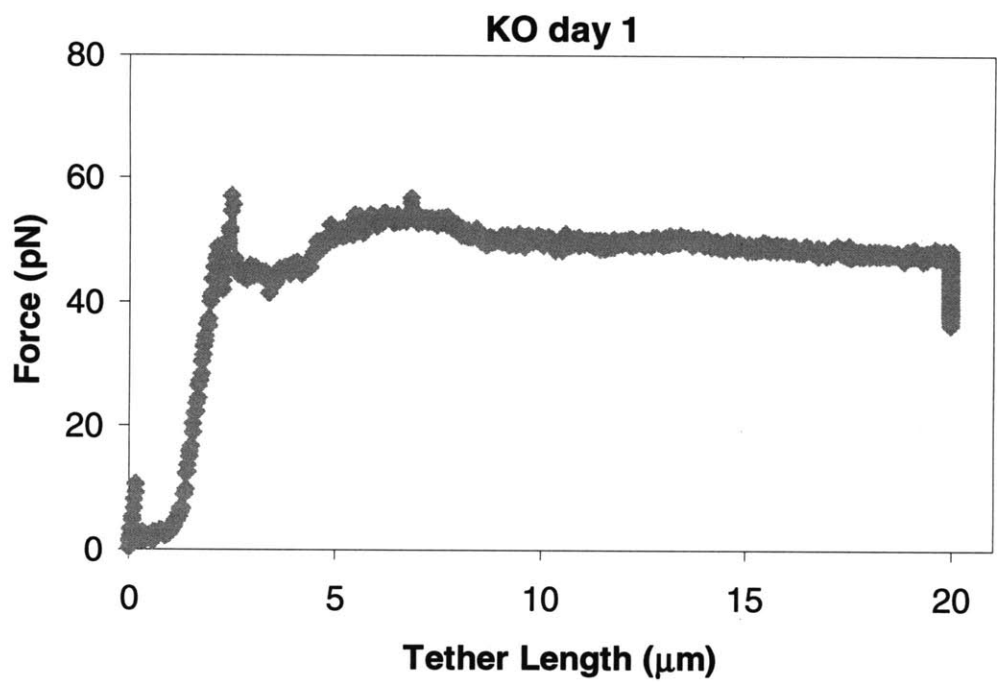
KO day 0

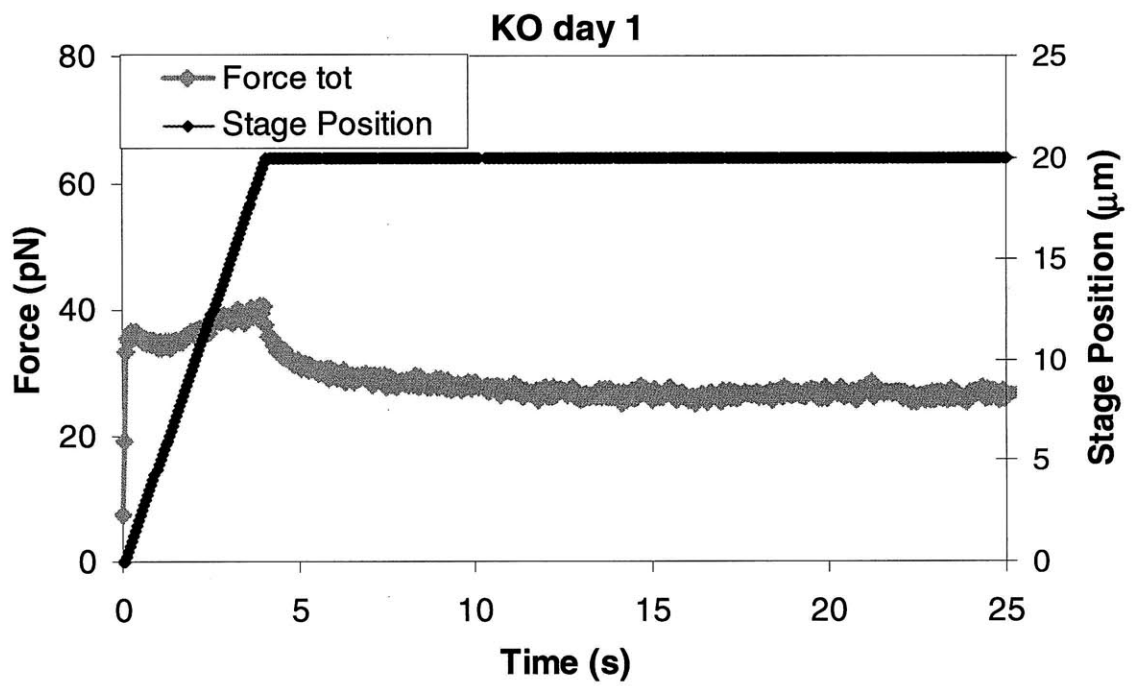
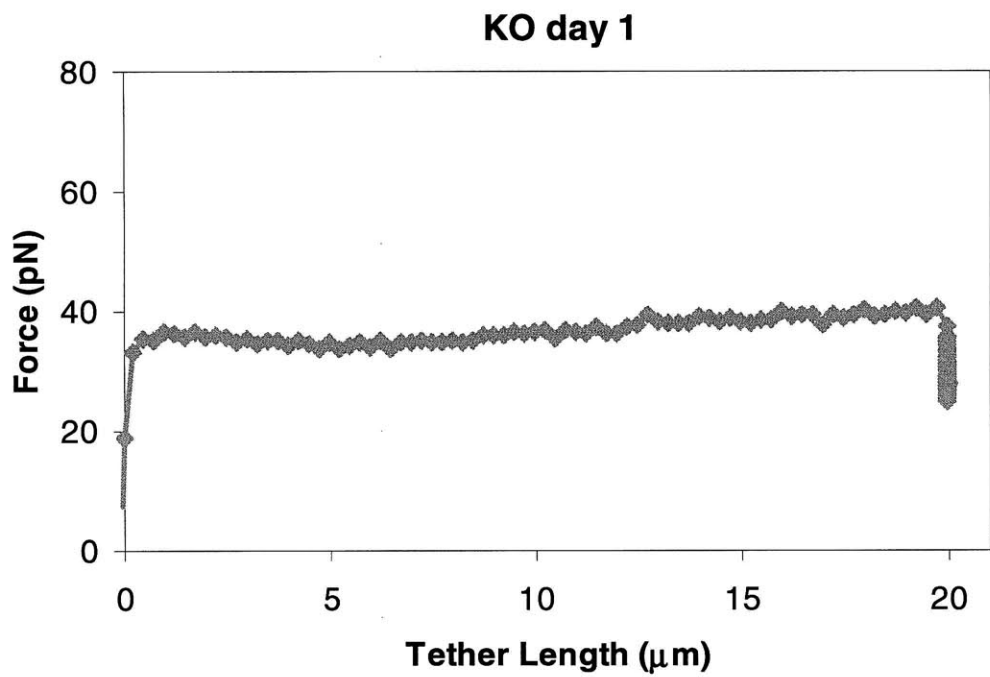


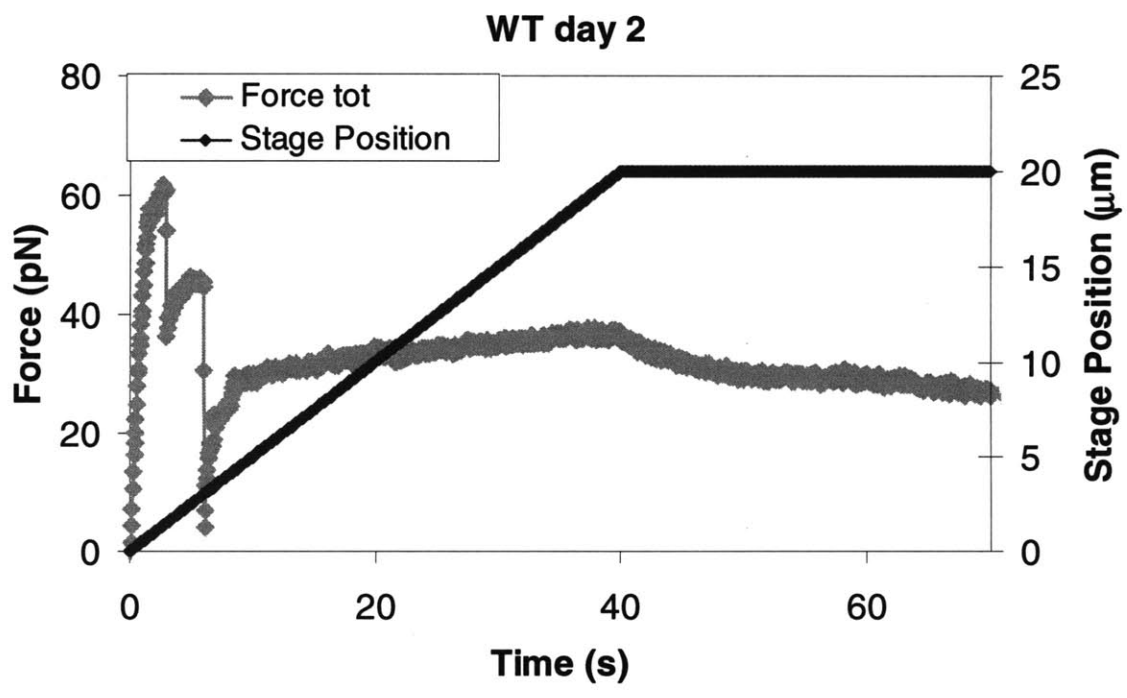
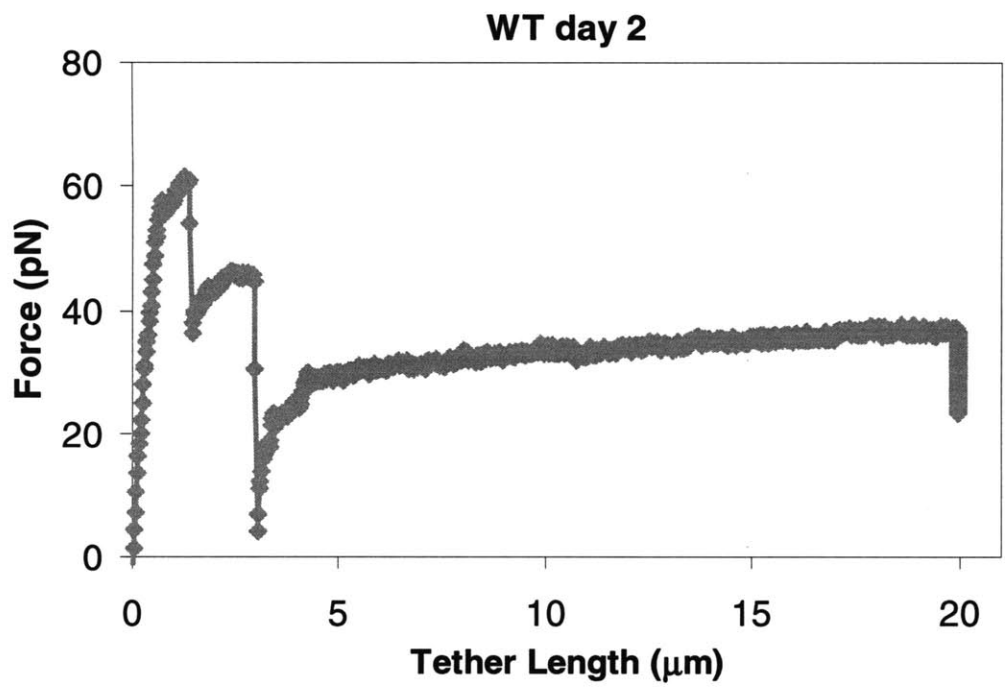
KO day 0

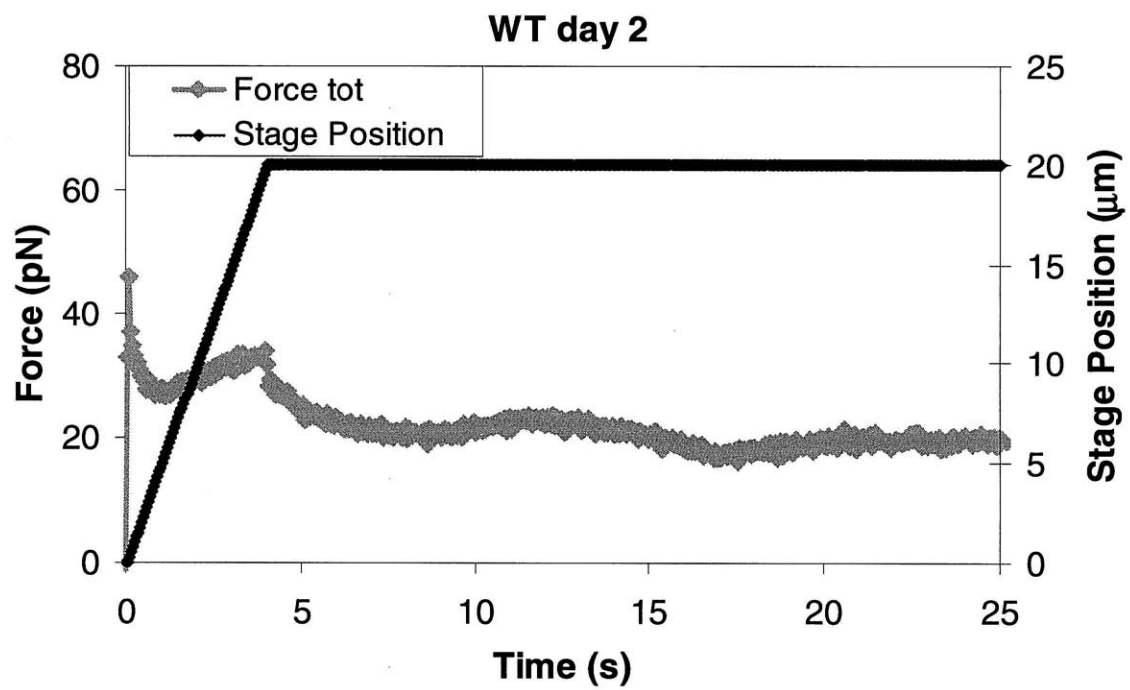
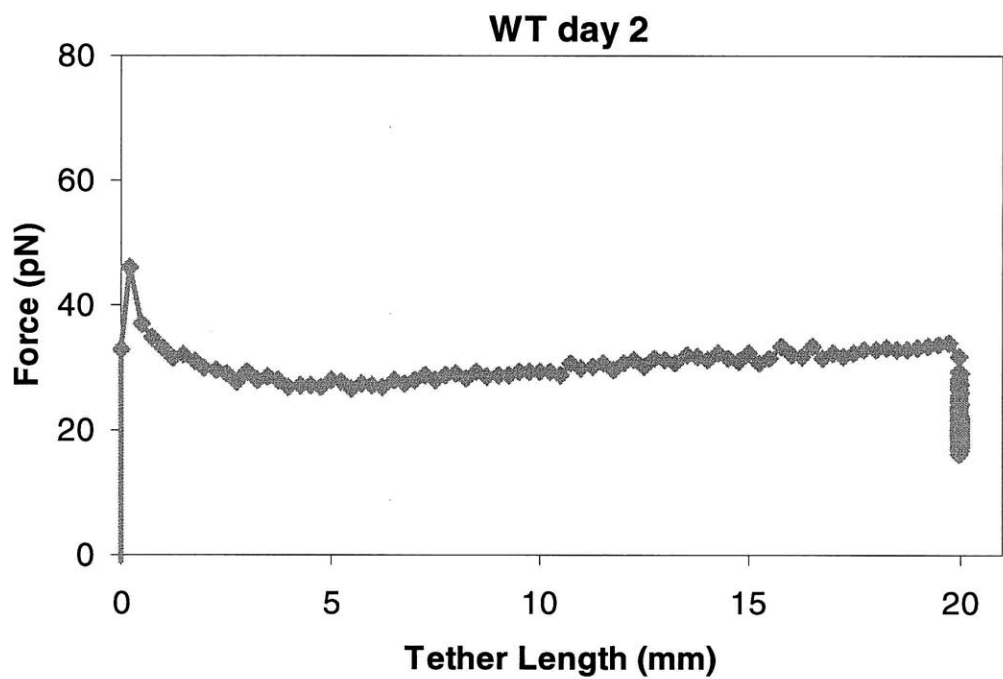


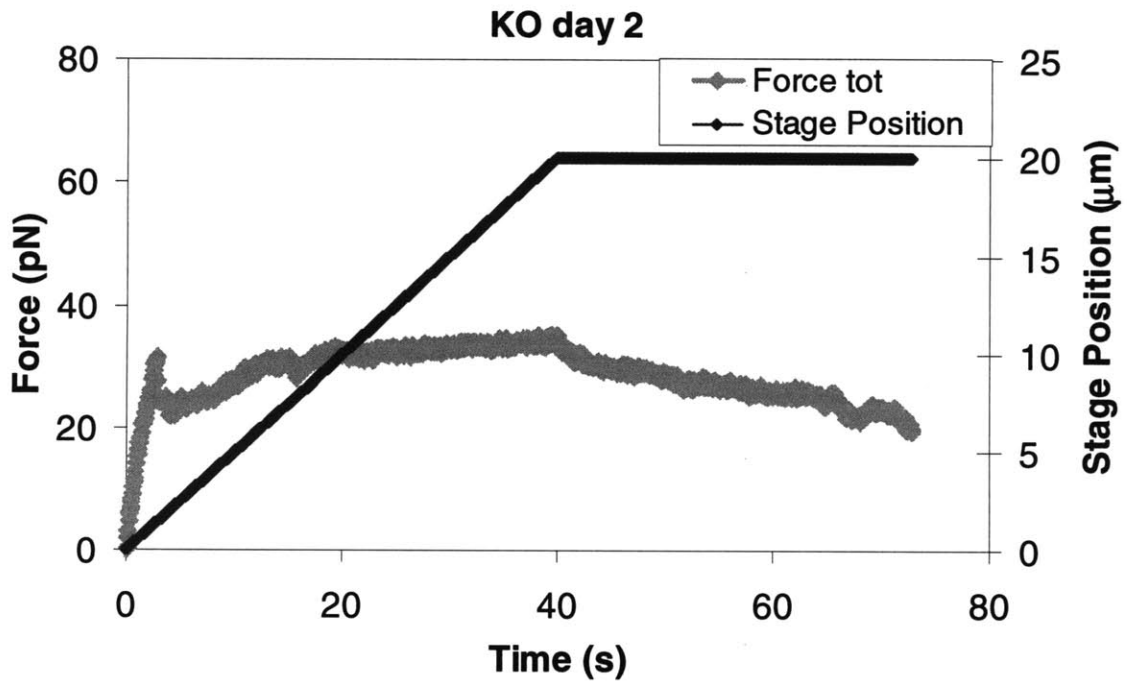
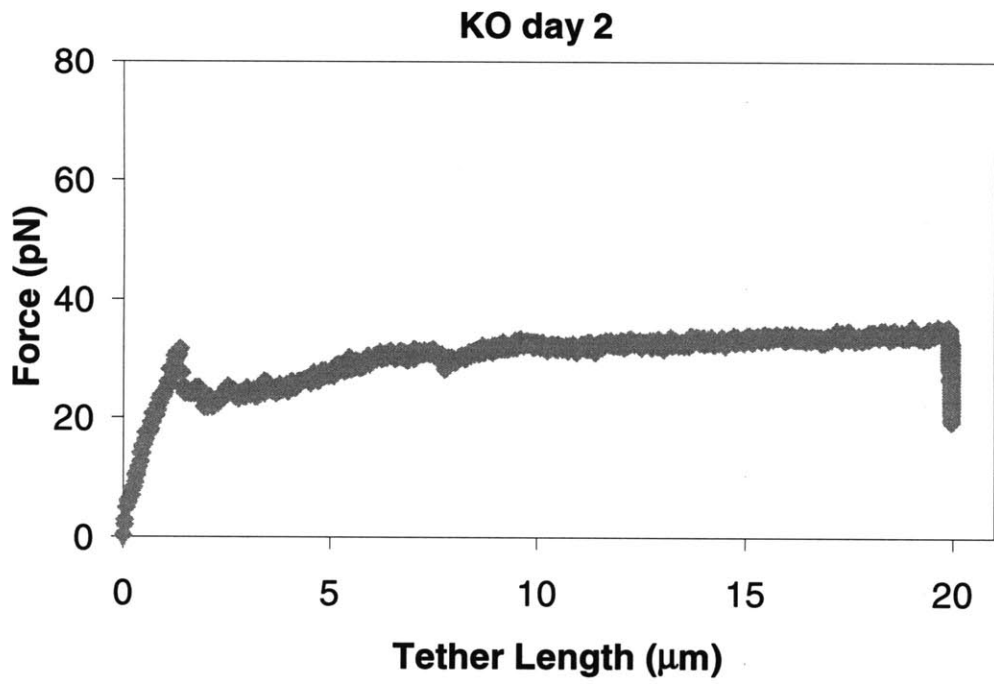


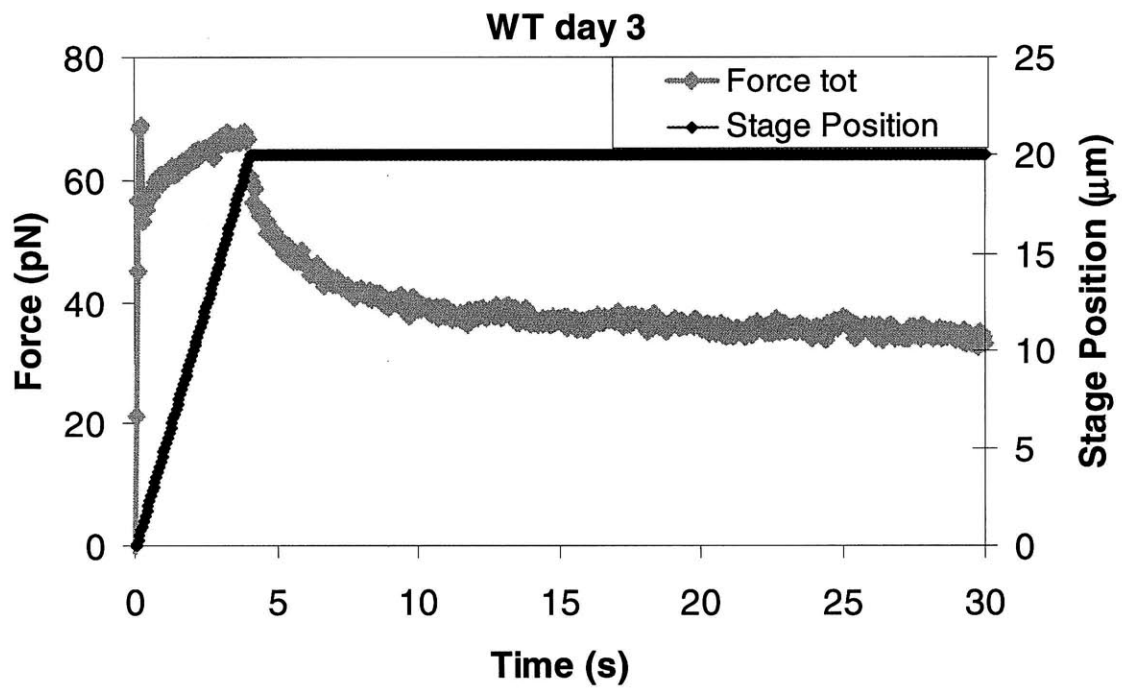
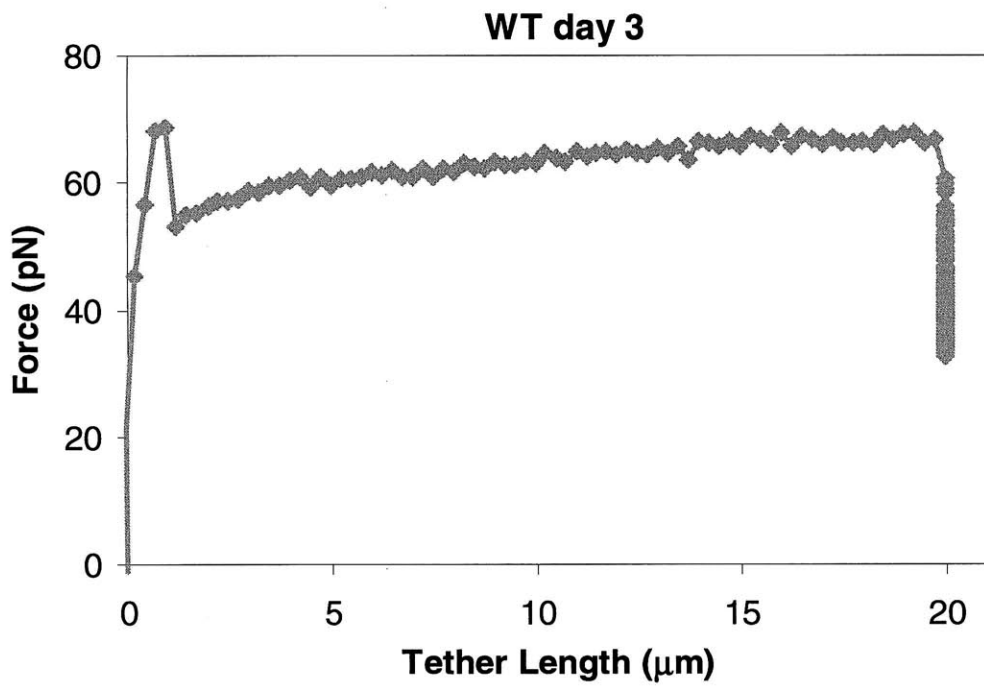


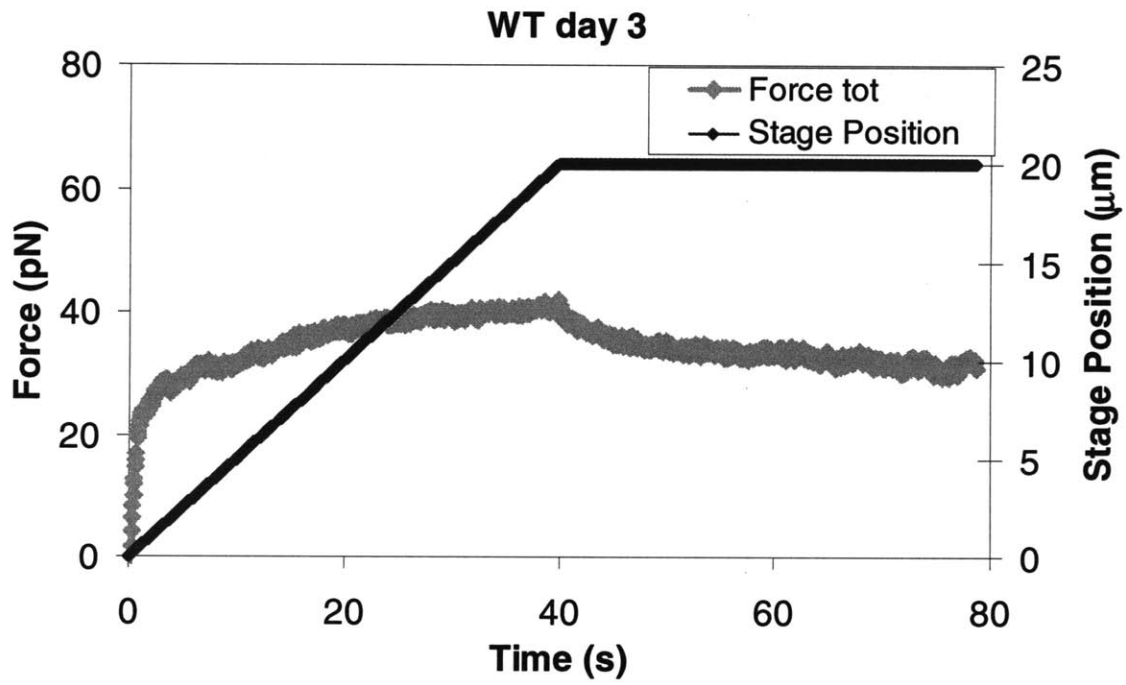
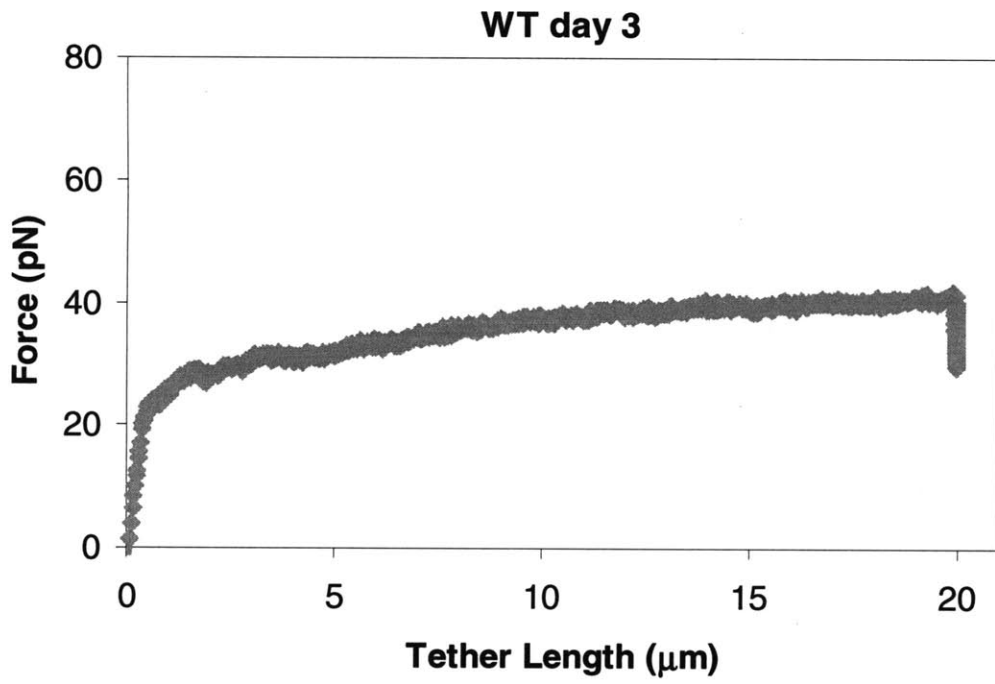


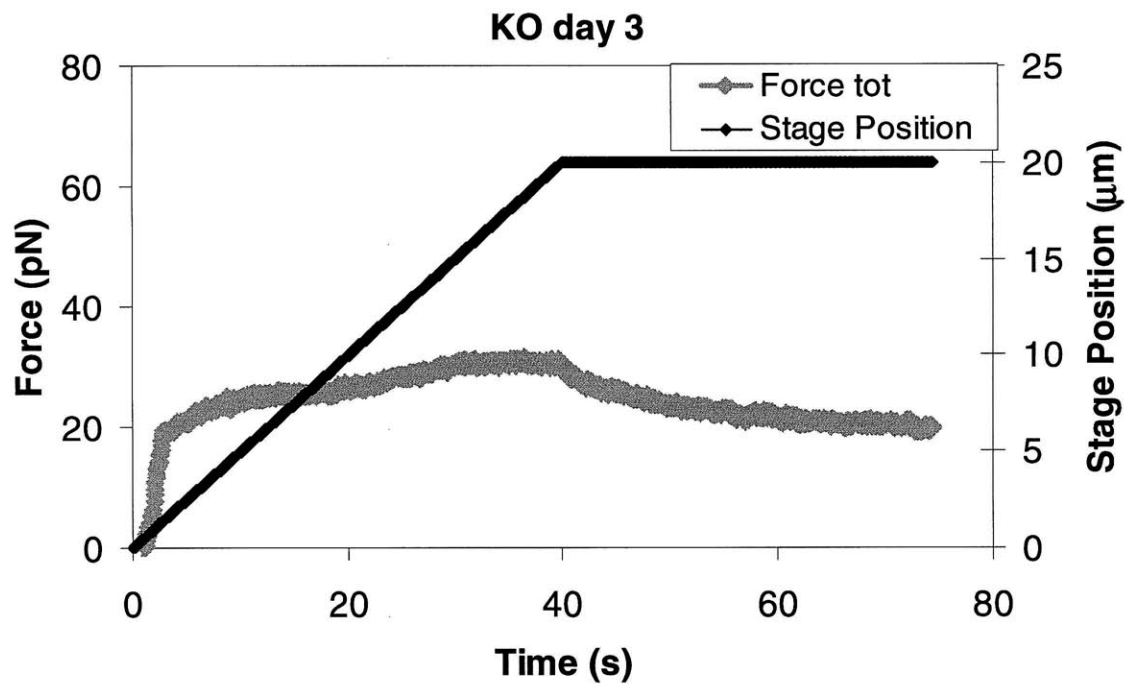
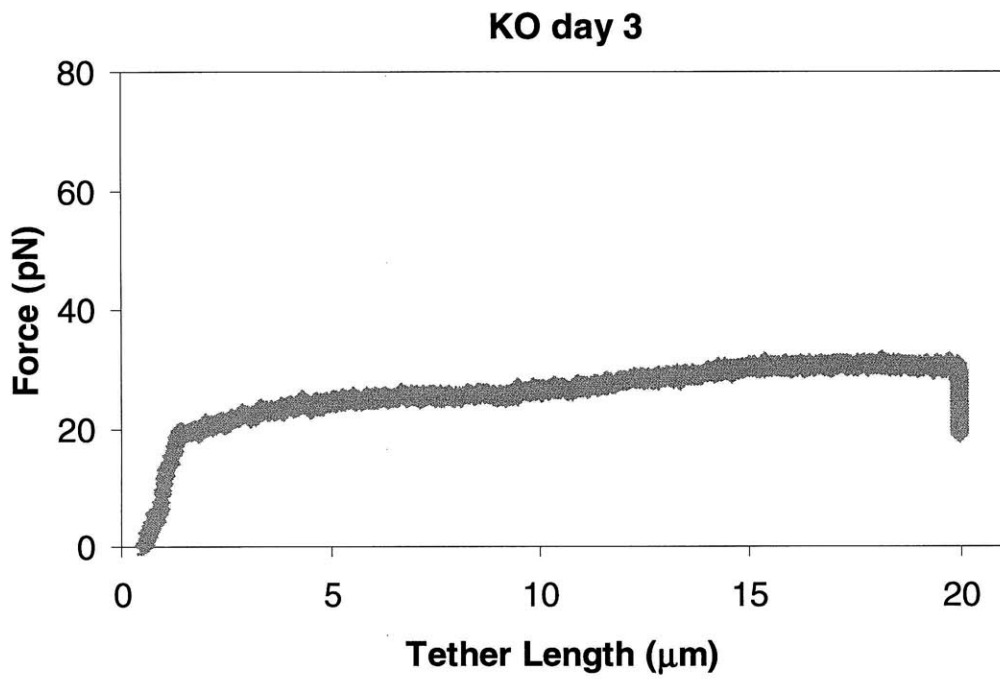


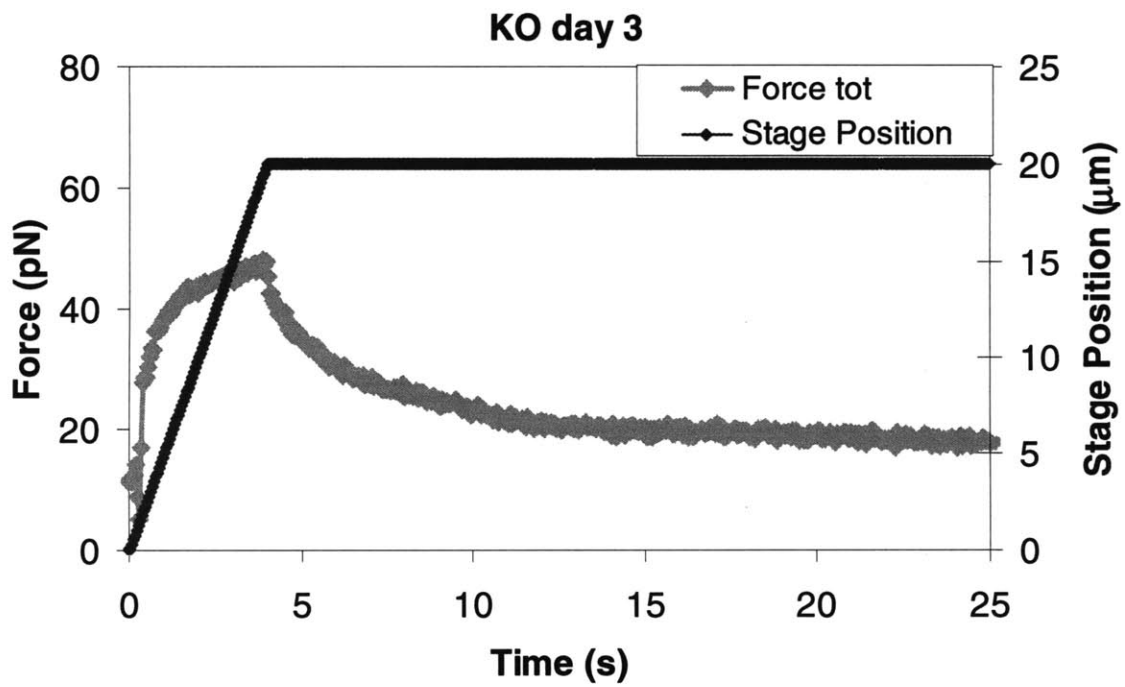
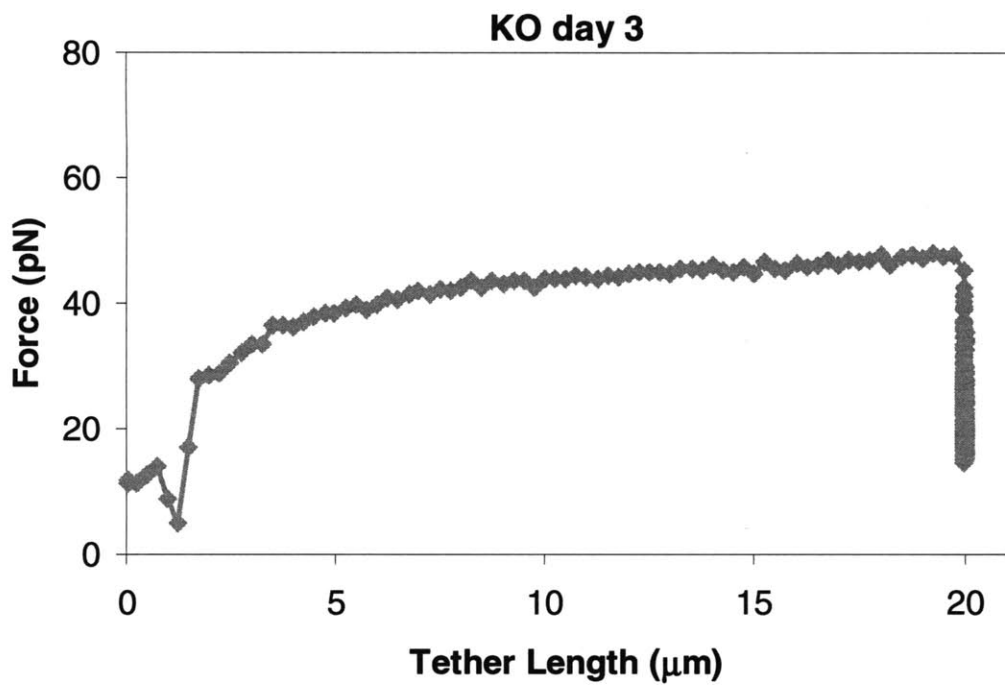


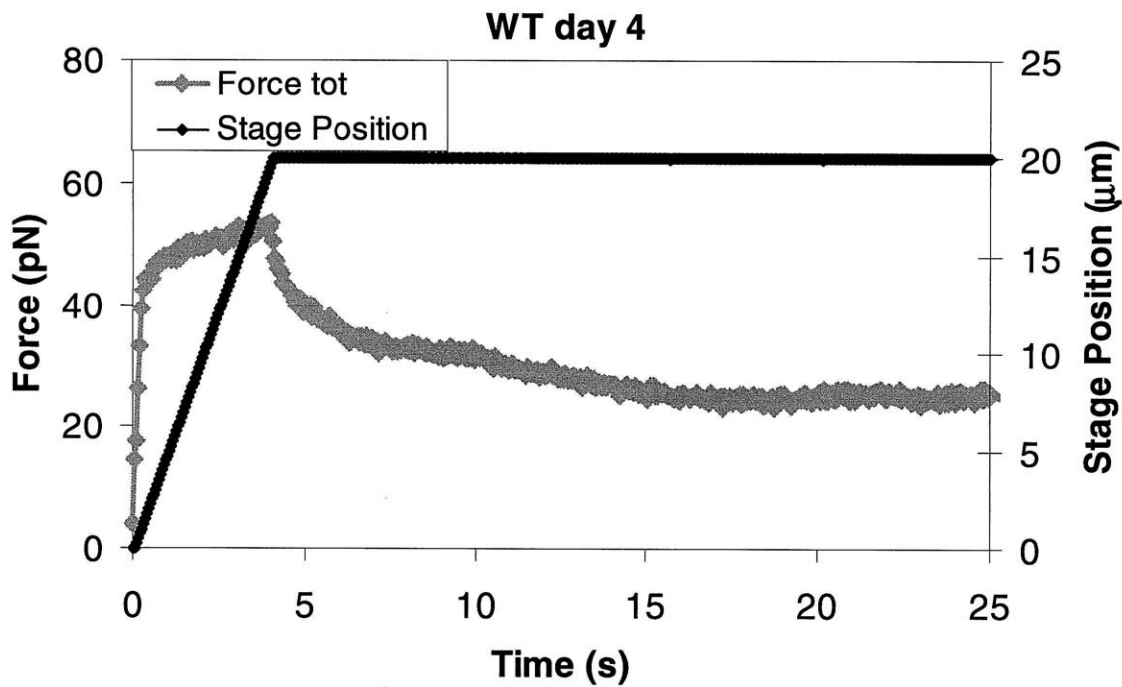
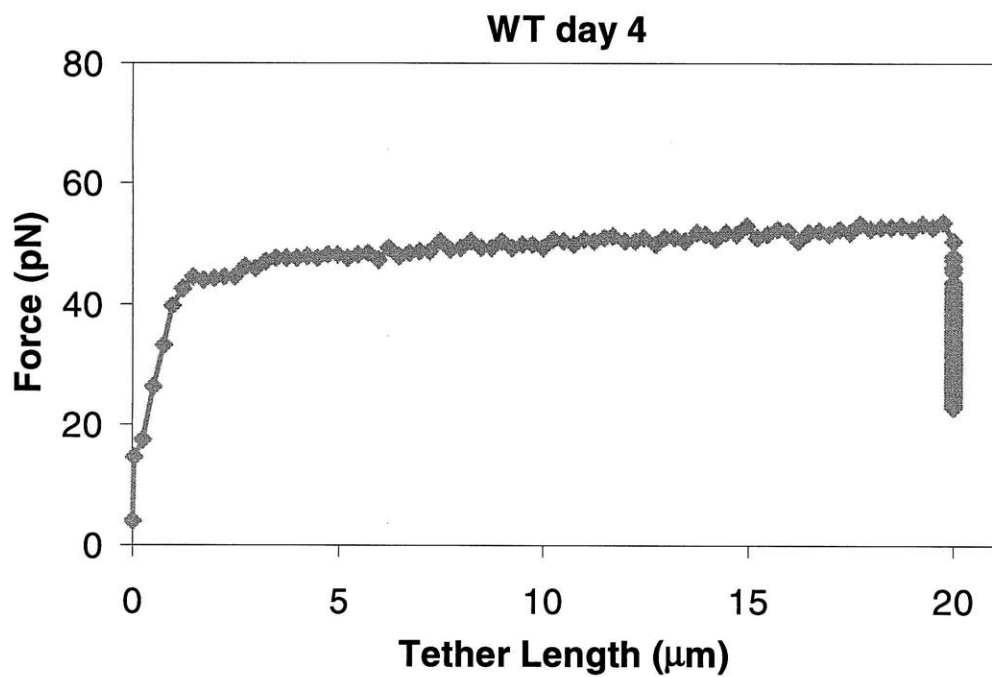


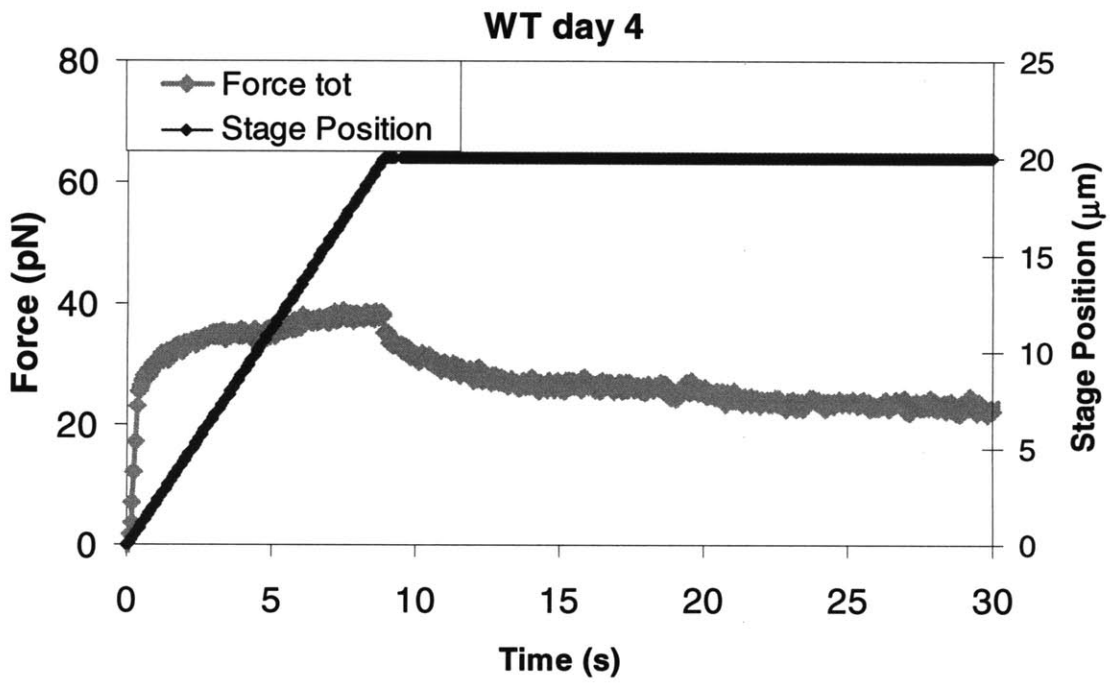
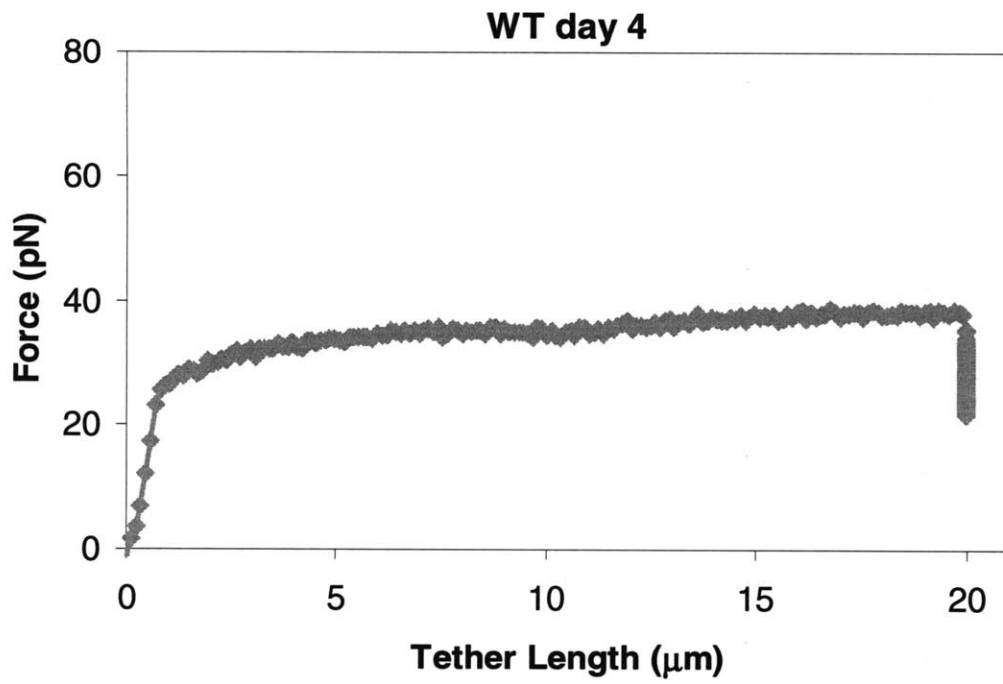


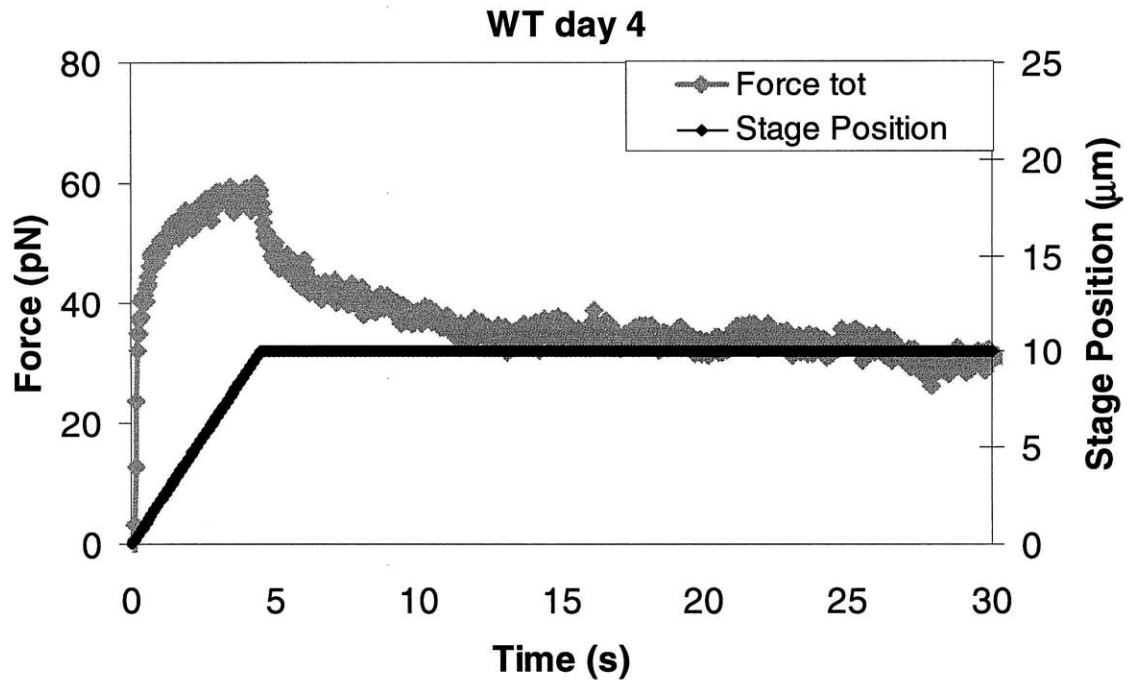
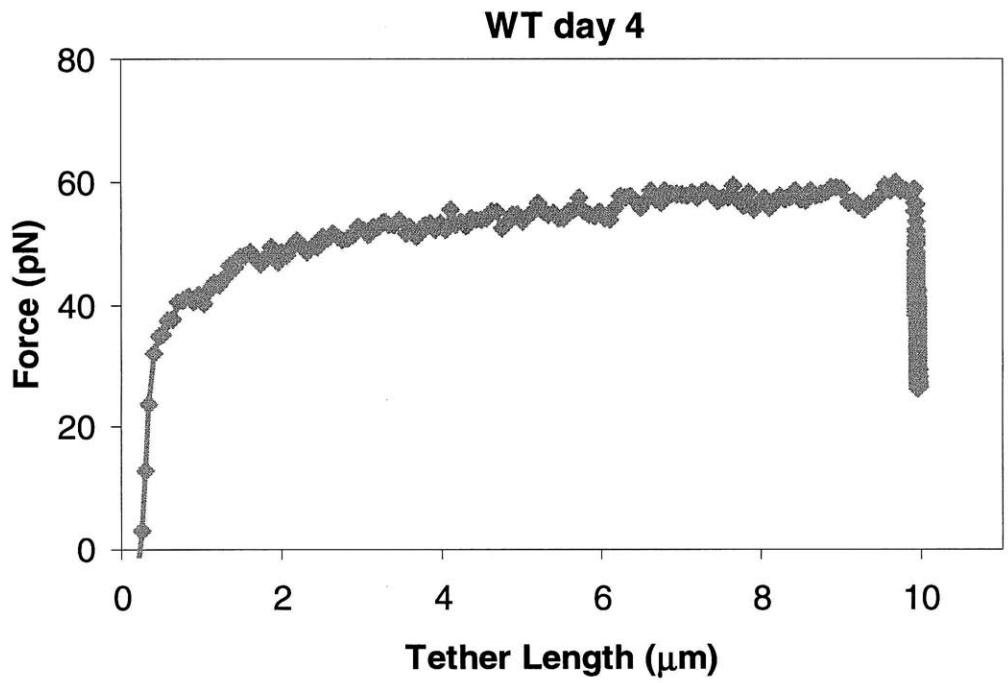


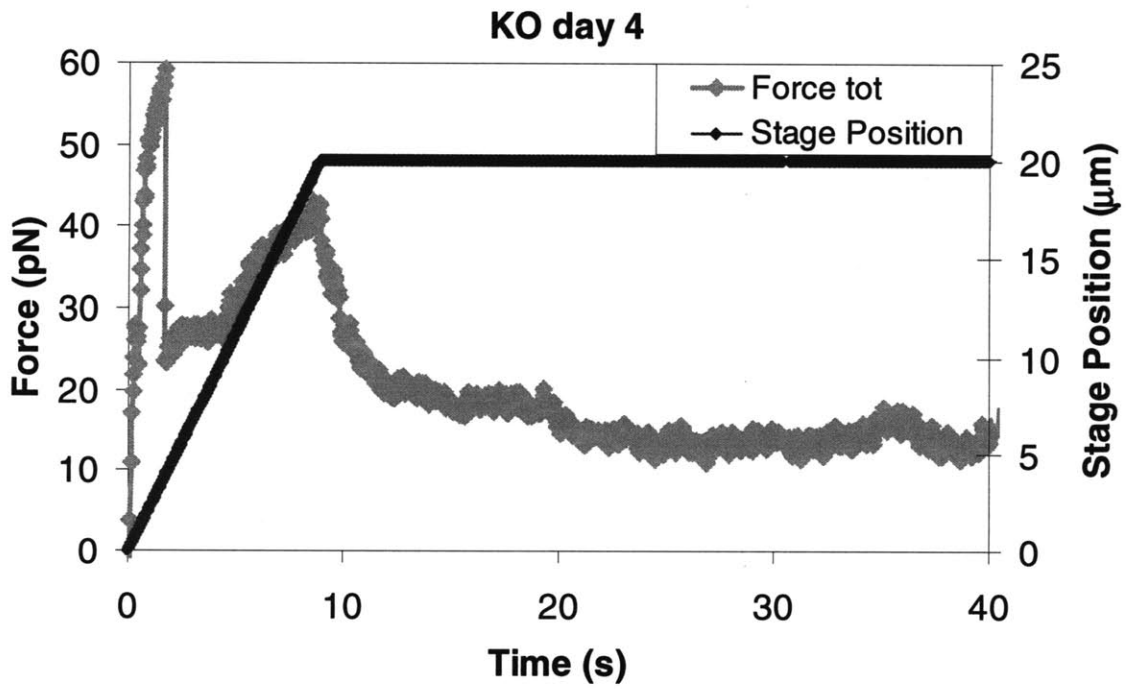
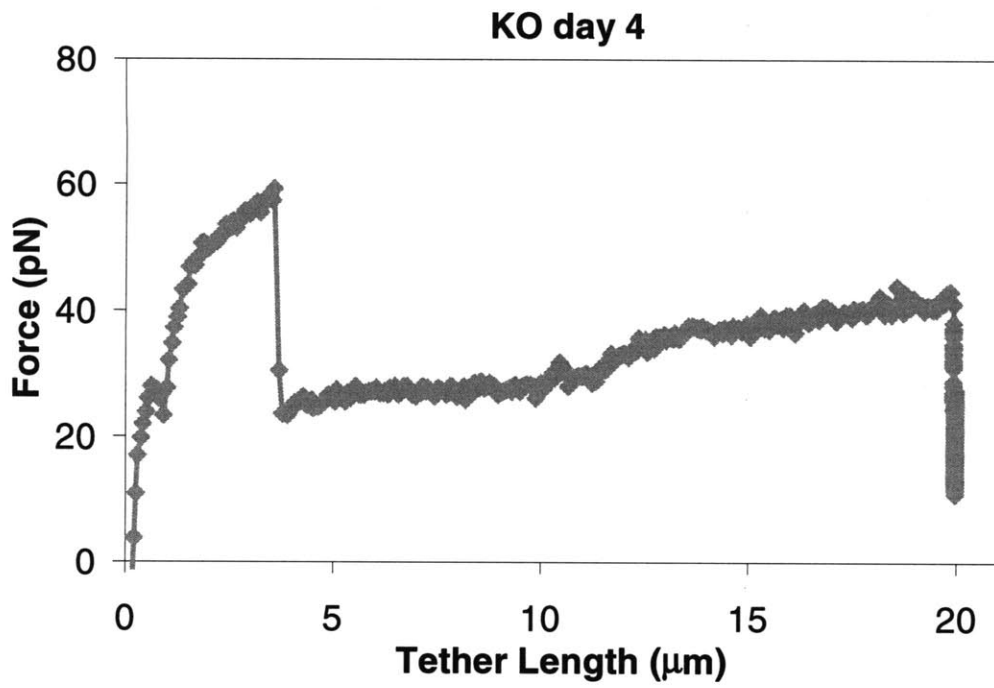


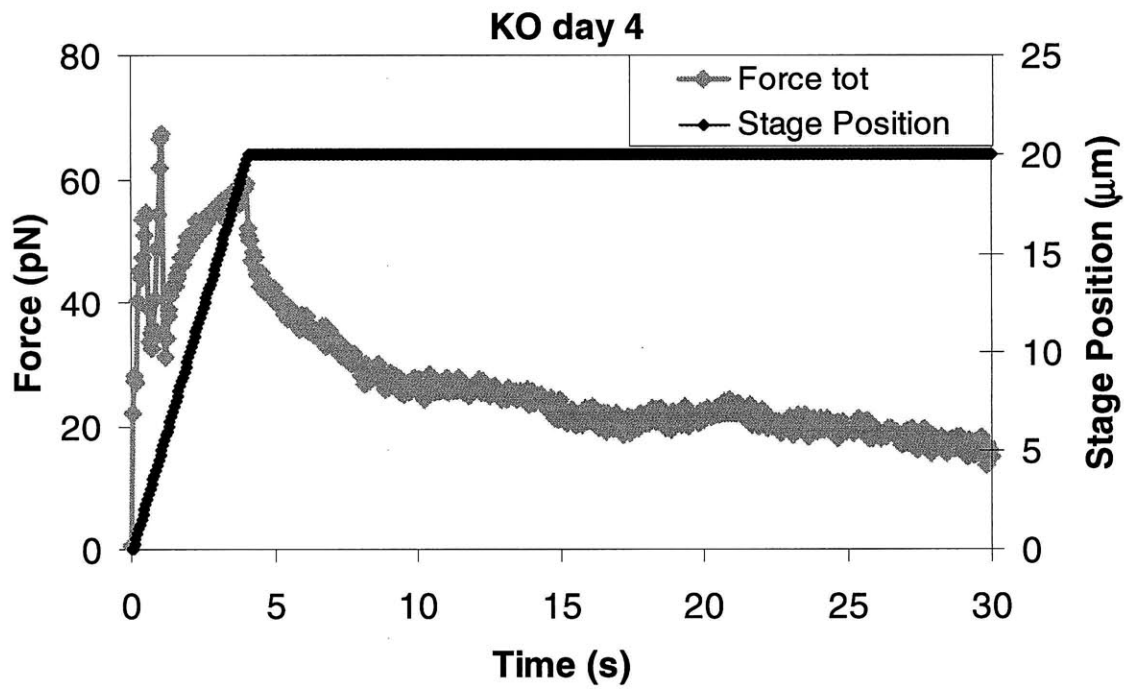
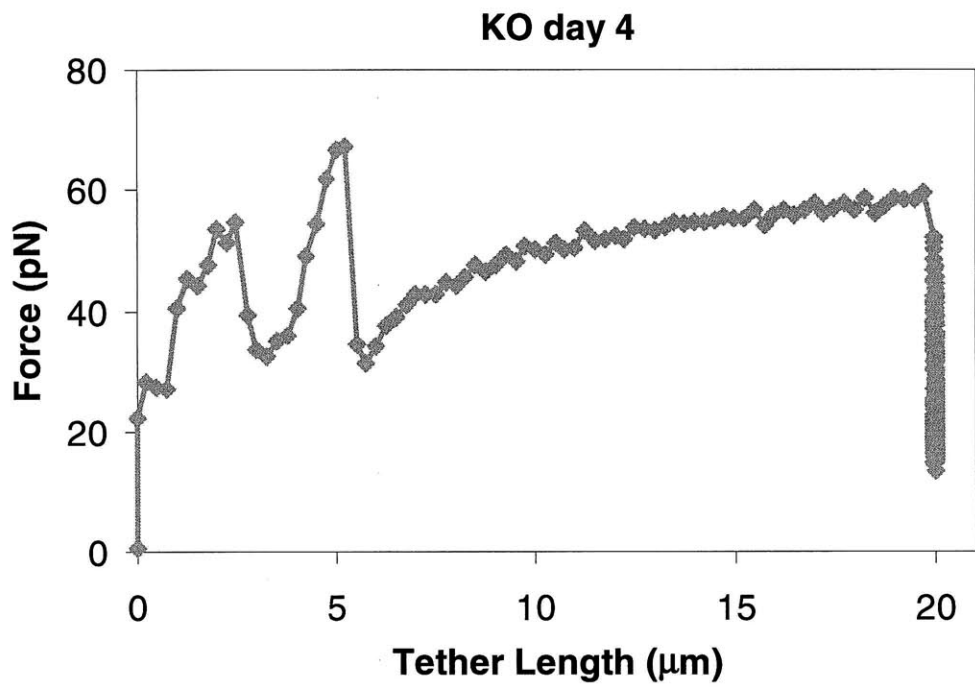


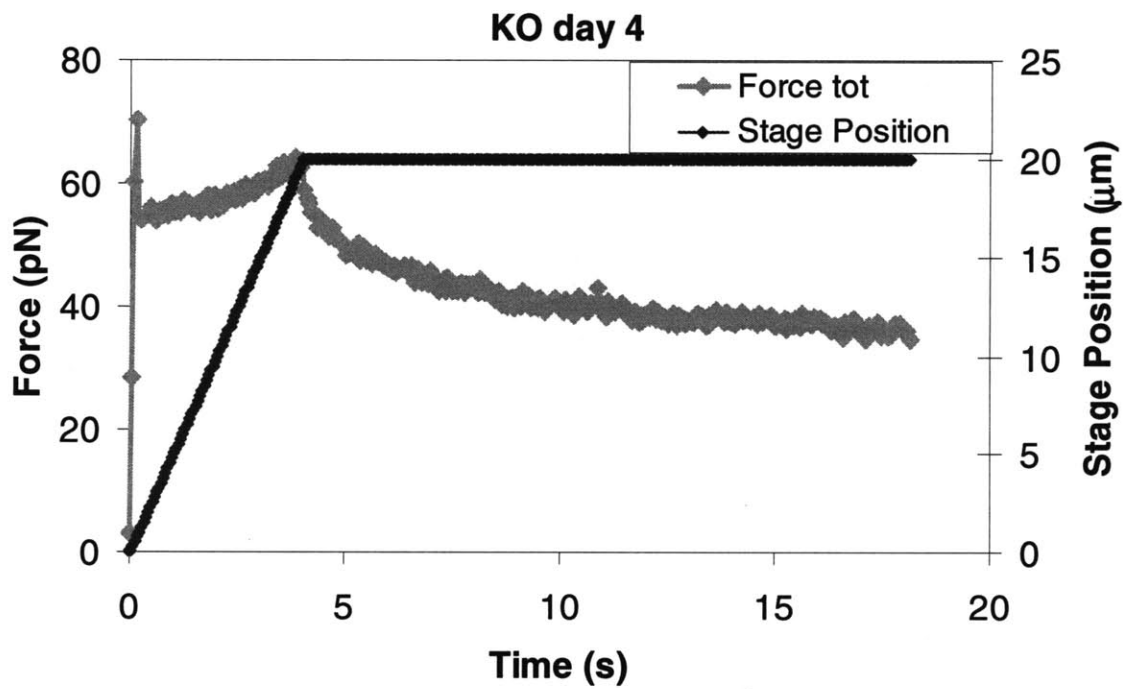
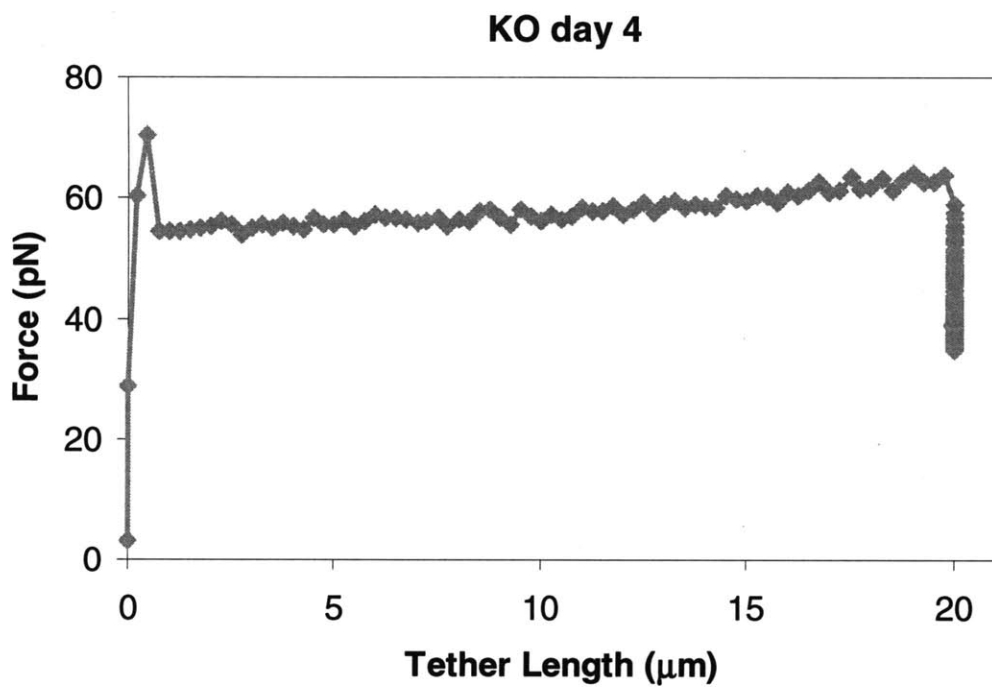












3.8 REFERENCES:

- [1] Kindt, T. J., Goldsby, R. A. and Osborne, B. A., 2007, *Kuby Immunology*, W.H. Freeman and Company, New York, NY.
- [2] Sarangapani, K. K., Yago, T., Klopocki, A. G., Lawrence, M. B., Fieger, C. B., Rosen, S. D., McEver, R. P. and Zhu, C., 2004. "Low force decelerates L-selectin dissociation from P-selectin glycoprotein ligand-1 and endoglycan". *J Biol Chem.* **279**: p. 2291-2298.
- [3] Montoya, M. C., Holtmann, K., Snapp, K. R., Borges, E., Sanchez-Madrid, F., Lusinskas, F. W., Kansas, G., Vestweber, D. and de Landazuri, M. O., 1999. "Memory B lymphocytes from secondary lymphoid organs interact with E-selectin through a novel glycoprotein ligand". *J Clin Invest.* **103**: p. 1317-1327.
- [4] Ramachandran, V., Williams, M., Yago, T., Schmidtke, D. W. and McEver, R. P., 2004. "Dynamic alterations of membrane tethers stabilize leukocyte rolling on P-selectin". *P Natl Acad Sci USA.* **101**: p. 13519-13524.
- [5] Pollard, T. and Earnshaw, W., 2007, *Cell Biology*, Elsevier, Philadelphia, PA.
- [6] Fleire, S. J., Goldman, J. P., Carrasco, Y. R., Weber, M., Bray, D. and Batista, F. D., 2006. "B cell ligand discrimination through a spreading and contraction response". *Science.* **312**: p. 738-741.
- [7] Evans, E. A. and Skalak, R., 1979, *Mechanics and Thermodynamics of Biomembranes*, CRC Press, Boca Raton, FL.
- [8] McGehee, A. M., Dougan, S. K., Klemm, E. J., Shui, G., Park, B., Kim, Y. M., Watson, N., Wenk, M., Ploegh, H. L. and Hu, C. C. A., 2009. "XBP-1-deficient plasmablasts show normal protein folding but altered glycosylation and lipid synthesis". *The Journal of Immunology.* **183**: p. 3690-3699.
- [9] Binder, W. H., Barragan, V. and Menger, F. M., 2003. "Domains and rafts in lipid membranes". *Angew Chem Int Edit.* **42**: p. 5802-5827.
- [10] Fuseler, J. W., Millette, C. F., Davis, J. M. and Carver, W., 2007. "Fractal and image analysis of morphological changes in the actin cytoskeleton of neonatal cardiac fibroblasts in response to mechanical stretch". *Microsc Microanal.* **13**: p. 133-143.
- [11] Marcus, W. D. and Hochmuth, R. M., 2002. "Experimental studies of membrane tethers formed from human neutrophils". *Ann Biomed Eng.* **30**: p. 1273-1280.
- [12] Hwang, W. C. and Waugh, R. E., 1997. "Energy of dissociation of lipid bilayer from the membrane skeleton of red blood cells". *Biophys J.* **72**: p. 2669-2678.
- [13] Raucher, D. and Sheetz, M. P., 1999. "Characteristics of a membrane reservoir buffering membrane tension". *Biophys J.* **77**: p. 1992-2002.
- [14] Li, Z. W., Anvari, B., Takashima, M., Brecht, P., Torres, J. H. and Brownell, W. E., 2002. "Membrane tether formation from outer hair cells with optical tweezers". *Biophys J.* **82**: p. 1386-1395.
- [15] Titushkin, I. and Cho, M., 2006. "Distinct membrane mechanical properties of human mesenchymal stem cells determined using laser optical tweezers". *Biophys J.* **90**: p. 2582-2591.
- [16] Hochmuth, R. M., Shao, J. Y., Dai, J. W. and Sheetz, M. P., 1996. "Deformation and flow of membrane into tethers extracted from neuronal growth cones". *Biophys J.* **70**: p. 358-369.

- [17] Girdhar, G. and Shao, J. Y., 2004. "Membrane tether extraction from human umbilical vein endothelial cells and its implication in leukocyte rolling". *Biophys J.* **87**: p. 3561-3568.
- [18] Xu, G. and Shao, J. Y., 2005. "Double tether extraction from human neutrophils and its comparison with CD4(+) T-lymphocytes". *Biophys J.* **88**: p. 661-669.
- [19] Sun, M. Z., Graham, J. S., Hegedus, B., Marga, F., Zhang, Y., Forgacs, G. and Grandbois, M., 2005. "Multiple membrane tethers probed by atomic force microscopy". *Biophys J.* **89**: p. 4320-4329.
- [20] Hochmuth, R. M. and Marcus, W. D., 2002. "Membrane tethers formed from blood cells with available area and determination of their adhesion energy". *Biophys J.* **82**: p. 2964-2969.
- [21] Jiang, Y. Q., Guo, H. L., Liu, C. X., Li, Z. L., Cheng, B. Y., Zhang, D. Z. and Jia, S. T., 2004. "Membrane tether formation on a cell surface with reservoir". *Chinese Phys Lett.* **21**: p. 1659-1662.
- [22] Hu, C. C. A., Dougan, S. K., McGehee, A. M., Love, J. C. and Ploegh, H. L., 2009. "XBP-1 regulates signal transduction, transcription factors and bone marrow colonization in B cells". *Embo J.* **28**: p. 1624-1636.
- [23] Waugh, R. E. and Hochmuth, R. M., 1987. "Mechanical Equilibrium of Thick, Hollow, Liquid Membrane Cylinders". *Biophys J.* **52**: p. 391-400.
- [24] Sowinski, S., Jolly, C., Berninghausen, O., Purbhoo, M. A., Chauveau, A., Kohler, K., Oddos, S., Eissmann, P., Brodsky, F. M., Hopkins, C., Onfelt, B., Sattentau, Q. and Davis, D. M., 2008. "Membrane nanotubes physically connect T cells over long distances presenting a novel route for HIV-1 transmission". *Nat Cell Biol.* **10**: p. 211-219.

Chapter 4

B Cell Biomechanical and Biochemical Machinery

4.1 INTRODUCTION:

A complex array of biochemical and biomechanical machinery (see figure 3.5) cooperatively enable B cells to achieve their physiological functions. One example of the inter-dependence of B cell biomechanical and biochemical machinery occurs during antigen recognition. The initial stage of B cell antigen detection is a biochemical response starting with BCR antigen recognition. Antigen detection triggers a complex signaling cascade that culminates with changes in gene expression leading to functional changes in the cell and ultimately, differentiation into an antibody secreting Plasma Cell or a Memory B Cell. Memory B Cells are responsible for the memory of mammalian immune systems, and Plasma Cells secrete up to hundreds or thousands of antibody molecules per second which are critical for an effective immune response. Upon being activated with antigen, B cells rearrange their cytoskeleton and membrane proteins to form dense local clusters of membrane bound Ig (mIg). Aggregation of mIg drives the onset of B cell signaling. As shown in figure 4.1(a), in mouse splenic B cells activated by goat-anti-mouse Ig antibodies, BCRs initially form small aggregates referred to as

patches on the timescale of 5 minutes which eventually form larger aggregates called caps on a timescale of 10-15 minutes [110]. Caps recruit signaling proteins and aid in the initial activation of the B cell immune response. Figure 4.1(b) shows the increase in the percentage of mouse splenic B cells forming caps over time after activation with sheep-anti-mouse Ig antibodies [111].

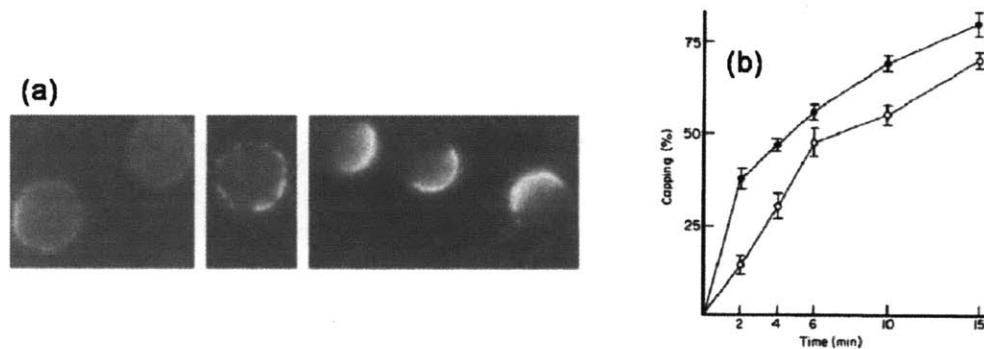


Figure 4.1 Upon activation with BCR specific antigen, BCRs cluster to form larger aggregates. (a) Prior to activation BCR is evenly distributed around the membrane (left). 5 minutes after activation with goat-anti-mouse Ig antibodies, small aggregates referred to as patches form (middle). After 15 minutes patches cluster to form large aggregates referred to as caps (right) [110]. (b) shows the kinetics of cap formation in terms of the percent of B cells forming caps after activation with sheep-anti-mouse Ig antibodies [111].

Here we address the inter-dependence of the biochemical and biomechanical machinery of B cells for two specific cases. First, we quantify the effect of alterations in the biochemical machinery, specifically the elimination of the transcription factor x-box protein 1 (XBP-1), on the biomechanical properties of B cells. XBP-1 is a vital component of the B cell biochemical machinery that is essential for differentiation [112, 113]. It is involved in the unfolded protein response (UPR) where it triggers the expansion the endoplasmic reticulum (ER) in response to excess accumulation of unfolded proteins [114]. The role of XBP-1 in differentiation, and specifically, the mechanism by which XBP-1 deficiency deters B Cell differentiation is not understood.

When a B cell differentiates it greatly increases production of antibodies, and hence it has been proposed that the increased demand on the ER results in accumulation of unfolded proteins and the UPR does not progress in the absence of XBP-1 and B cells are overwhelmed with unfolded protein [112, 113]. However, Hu and coworkers recently showed that activation of XBP-1 occurs normally even in B cells whose capacity to produce antibodies has been eliminated [107]. Therefore, XBP-1 is likely triggered directly by activation and not in response to accumulation of unfolded proteins in the ER. XBP-1 deficiency does cause biochemical differences which are most apparent in activated Day 4 B cells including a decreased mlg concentration and altered lipid synthesis which leads to a distinct membrane composition [95]. Figure 4.2 shows the mlg concentration (a) and composition of several lipids (b) in XBP-1 deficient cells and wild-type B cells on Day 0 and Day 4 [95].

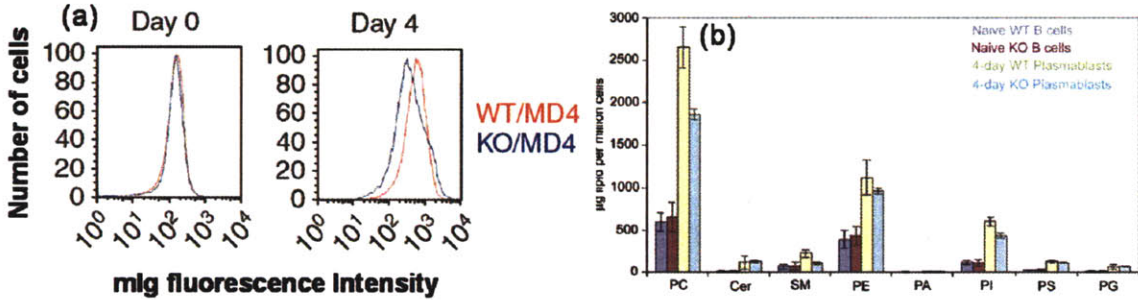


Figure 4.2 XBP-1 deficiency causes biochemical differences in B cells which are most apparent on Day 4 [107]. (a) shows a decreased concentration of mlg, and (b) shows differences in membrane composition for several lipids [95].

We characterize physical changes in the B cell membrane caused by XBP-1 deficiency. In doing so, we illustrate that alterations in the B cell biochemical machinery are manifested in the biomechanical machinery of the B cell. These physical changes must

also be taken into account when considering the immunodeficiency of biochemically manipulated immune cells.

We additionally ask if the membrane nanotubes, previously used to probe the mechanical properties of the B cell membrane, can potentially serve a biochemical immune function. These membrane nanotubes have previously been shown to enhance inter-cellular communication in cells including T cells [109], macrophages [115], neurons [116], and myeloid cells [117]. The characteristics and function of these tubes vary among different cell types including their structural composition. In many cell types, long range cell-cell attachments have beneficial functions such as intercellular vesicular cargo transport as was shown for neuronal and kidney cells [116]; however, in T cells, an immune cell similar in nature to the B cell, intercellular nanotubes are exploited by viruses such as HIV-1 to greatly enhance the viral transmission [109]. Figure 4.3 shows a fluorescence image of membrane tubes connecting T cells. Here we quantify the mlg composition of B cell membrane nanotubes by combining fluorescence imaging with membrane tethering following a recently used in Baumgart et al. [118] which probed the membrane curvature-dependent sorting of lipids and a cholera toxin protein. Our results reveal a potential biochemical function of B cell membrane protrusions and further illustrate the cooperativity of biochemical and physical machinery in immune cells.

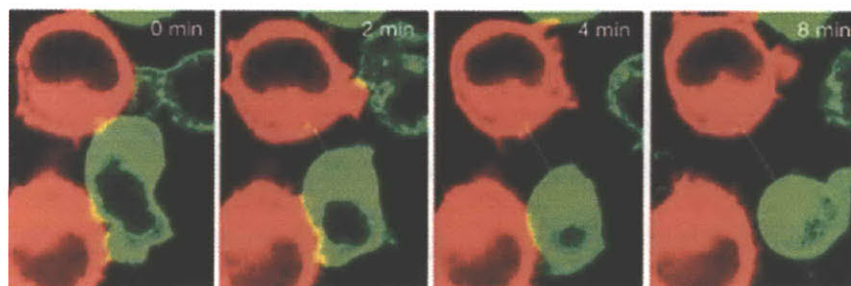


Figure 4.3 Sowinski et al showed that the HIV-1 virus exploits membrane nanotubes for efficient and specific transmission between T cells. Membrane nanotubes are formed when cells form an attachment (left) and then migrate away from each other on a time scale of several minutes. T cells are labeled with the fluorescent membrane dyes DiO (green) and DiD (red) [109].

4.2 EXPERIMENTAL METHODS:

4.2.1 *XBP-1 Deficient Experiments.* MD4 mice with a B cell specific XBP-1 deficiency were prepared in the Ploegh lab by Dr. Andrew Hu as described in [107]. B cells were isolated from the spleen of XBP-1 deficient MD4 mice (XBP-1^{KO}). XBP-1^{KO} were activated with LPS and membrane tethers were pulled from Day0 to Day4 B cells using an identical assay preparation and experimental setup to that described in the previous chapter. Membrane tethers were pulled using stage velocities of 0.5, 2.5 and 5.0 $\mu\text{m/s}$ to a length of 20 μm .

4.2.2 *Combined Membrane Tethering and mlg Fluorescence.* HEL was fluorescently labeled with Alexa 488 using an Alexa488 protein labeling kit (Invitrogen; Carlsbad, California). B cells were activated with LPS as previously described. B cells were either incubated with fluorescent HEL either 0, 5, or 30 minutes prior to tether pulling. In the case of 0 minutes, membrane tethers were pulled prior to incubation with HEL. Fluorescent HEL was then flown into the channel and incubated for 5 minutes

while leaving the trap on to maintain the membrane tether at a constant length. The unbound fluorescent HEL in solution was removed by washing 30 μ l of PBS through the channel. Membrane tethers were then imaged under fluorescence excitation with a 488 nm laser with a back thinned EMCCD camera (Andor) for 150-200 frames at a frequency of 2 Hz. To prolong fluorescence lifetime, a shutter in line with the excitation laser was synchronized with camera to avoid continuous excitation of fluorophores. For the 5 minute incubation, B cells were directly immobilized in the flow channel. 30 μ l of 1 mg/ml casein were flown through the channel to prevent non-specific binding of beads. Prior to the introduction of HEL beads in the sample, fluorescent HEL was flown into the channel and incubated for 5 minutes. Membrane tethering experiments were performed after removing excess HEL in solution by washing through 30 μ l of casein solution. Finally in the case of a 30 minute incubation, cells were incubated in culture with fluorescent HEL prior to the sample prep. After 30 minutes, B cells were immobilized in a flow channel, and the sample preparation described in chapter 2 was followed.

The membrane tether pulling protocol was altered in order to improve fluorescence imaging. The stage was left fixed, and the bead was moved by displacing the trap using acousto-optic deflectors. This was done to keep the cell and membrane tether fixed relative to the fluorescence excitation region which was in general placed over the tether to exclude the extremely bright fluorescence of the main cell body. This approach of moving the trap excluded the possibility of measuring the position of the bead, and hence we could not use the “deft touch” protocol to sense when the cell and bead came into contact. Instead, the direction of motion of the laser trap was reversed

upon visual confirmation of cell-bead contact. While this approach resulted in a lower success rate for tether formation, the process was repeated until either a tether was formed or the cell-bead interaction was too strong to be broken. Single membrane tethers were visually confirmed prior to fluorescence imaging.

4.3 EXPERIMENTAL RESULTS:

4.3.1 *XBP-1^{KO}* deficient B cells. Membrane tethering experiments were carried out on Day0 thru Day4 *XBP-1^{KO}* B cells at different pulling velocities to quantify their membrane mechanical properties. The binding characteristics and tether formation of HEL coated beads on *XBP-1^{KO}* B cells were similar to the wild-type MD4 cells. Figure 4.4(a) shows the steady tether force for Day0 thru Day4 B cells from *XBP-1^{KO}* mice (KO) compared to wild type MD4 mice (WT) at two different pulling velocities. Extending tethers at the higher velocity on Day 4 required lower forces than wild-type MD4 B cells. Figure 4.4(b) shows the distribution of tether forces at a pulling rate of 5.0 $\mu\text{m/s}$ for Day4. A t-test with a 99% confidence level confirmed that the two distributions shown in figure 4.4(b) are statistically distinct. However, there was no difference in the force required to pull a tether at 0.5 $\mu\text{m/s}$ on Day 4.

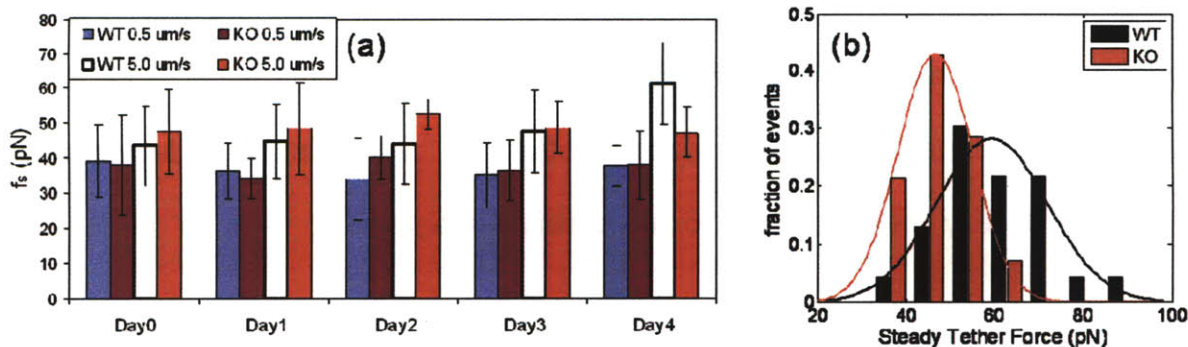


Figure 4.4 (a) shows the force required to extend membrane tethers from wild-type MD4 (WT) and XBP-1KO (KO) B cells for pulling velocities of 0.5 and 5.0 $\mu\text{m/s}$. No significant differences are seen between WT and KO except on Day 4 at a pulling velocity of 5.0 $\mu\text{m/s}$. (b) shows the distribution of tether forces on for Day 4 cells at 5.0 $\mu\text{m/s}$. A t-test with a 99% confidence level confirms that the distributions are statistically distinct.

Figure 4.5 shows the difference between XBP-1^{KO} and wild-type MD4 cells on Day 4 on a force versus velocity curve along with linear fits to each dataset. Experiments were done at an intermediate pulling velocity, 2.5 $\mu\text{m/s}$, to confirm the linear trend. These results show that the static tether force is similar for XBP-1^{KO} cells and wild-type MD4 cells however, the distinct rate dependent behavior reveals a different effective membrane viscosity. The difference in effective membrane viscosity is likely due to the biochemical differences (i.e. lipid composition and mlg expression) occurring in Day 4 cells shown in figure 4.2.

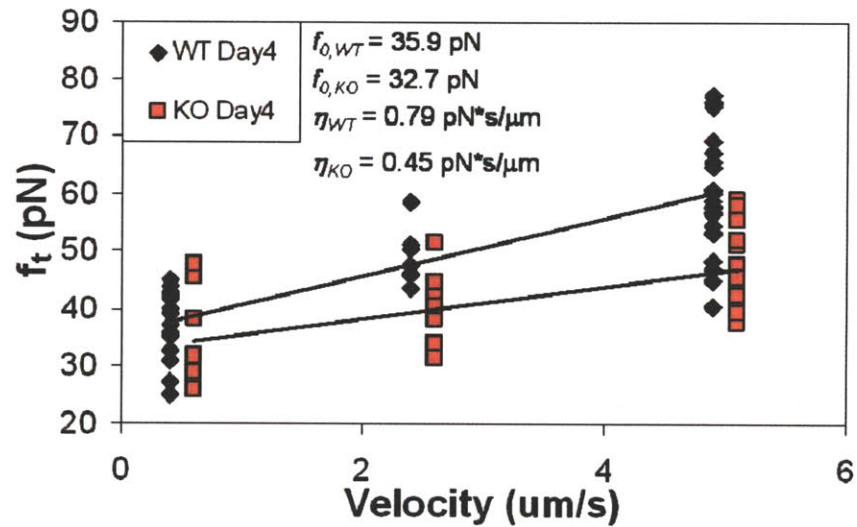


Figure 4.5 The force of tether extension is shown as a function of pulling velocity of wild-type MD4 (WT) and XBP-1^{KO} (KO) for Day 4 B cells (Plasmablasts). The static tether force, f_0 , is determined from an extrapolation to zero velocity, and the effective membrane viscosity, η , is determined from the slope of the curve.

The force relaxation behavior of the XBP-1^{KO} cells is consistent with the steady force behavior. The average time constants for the longer timescale relaxation of the XBP-1^{KO} B cells and the wild-type MD4 B cells were 4.77 and 6.54 seconds respectively. As predicted by the dynamic growth model developed in the previous chapter, a lower viscosity membrane results in faster force relaxation. Figure 4.6 shows a prediction of the force relaxation behavior using the growth model derived in section 3.4.5.

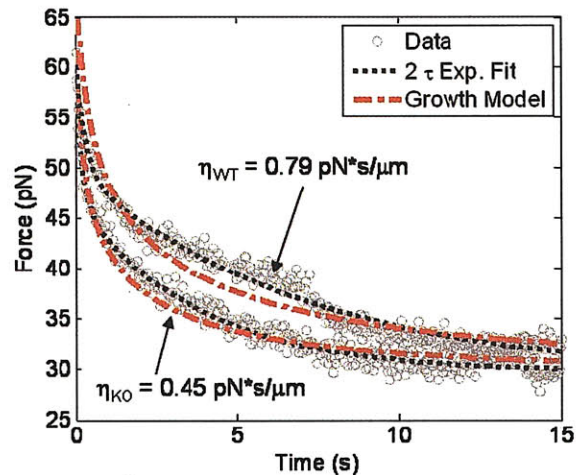


Figure 4.6 The dynamic growth model derived in chapter 2 is applied to predict the force relaxation behavior of membrane tethers from wild-type MD4 (WT) and XBP-1^{KO} (KO) B cells. Also shown are double exponential fits to the force relaxation data. The lower viscosity KO membrane results in faster force relaxation.

4.3.2 mlg composition of B cell membrane nanotubes. In all experiments, membrane tethers were formed by specifically attaching to a mlg (i.e. the B cell receptor). Hence, mlg was involved in the tether formation process at least at the bead attachment site. To examine the extent to which mlg was present in the tether, we utilized fluorescently labeled HEL to track the location of mlg. MD4 B cells were incubated for 0, 5, or 30 min with fluorescent HEL prior to membrane tethering. A zero minute incubation indicates that membrane tethers were pulled prior to incubation with HEL. If B cells were incubated with HEL for 30 min prior to tether pulling, no mlg was ever present in the membrane tethers. During these experiments, the fluorescence excitation region was placed over the membrane tether in order to exclude the extremely bright fluorescence emitted from the main cell body shown in figure 4.7(a). Figure 4.7 (b) and (c) show DIC and fluorescence images of a representative membrane tether pulled from a wild-type MD4 Day 4 B cell after a 30 minute incubation

with fluorescent HEL. The cell and bead are weakly illuminated at the edge of the excitation region which is highlighted in figure 4.7(c).

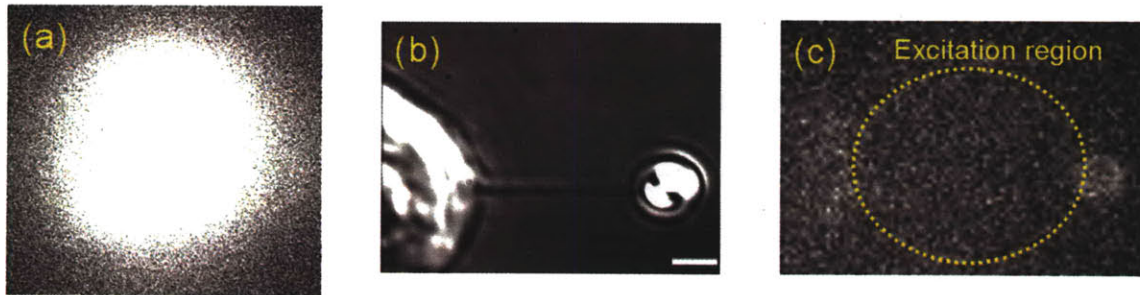


Figure 4.7 MD4 BCRs were labeled by incubating with fluorescent HEL for 30 minutes. (a) A wild-type MD4 B cell glows brightly due to the high concentration of BCR on the surface. (b) Membrane tethers were pulled using an optically trapped HEL-coated bead. (c) No BCR was present in membrane tethers after the 30 minute HEL incubation.

If membrane tethers were pulled prior to HEL incubation, mlg was often readily visible in the membrane tether. Figure 4.8(a) shows a membrane tether that was pulled from a wild-type Day 4 MD4 B cell prior to a 5 minute incubation with fluorescent HEL. After the 5 minute incubation the main cell body glows very brightly suggesting that a high density of fluorescent HEL binds to the surface of the cell (Figure 4.8(b). Placing the fluorescence excitation over the tether reveals the presence of mlg throughout the full length of the tether as shown in figure 4.8(c).

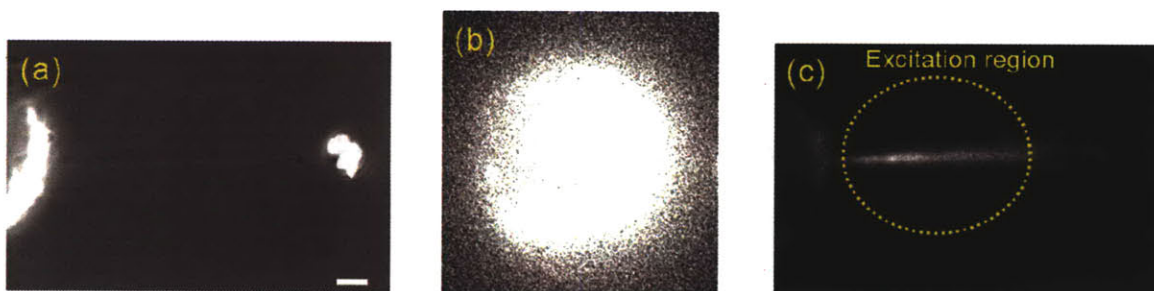


Figure 4.8 (a) Membrane tethers were pulled from wild-type MD4 B cells using an optically trapped HEL-coated bead. (b) Fluorescent HEL was then introduced into the flow channel readily binds on the surface of the main cell body. (c) Fluorescently labeled BCR was seen in the tether when the excitation region was focused over the tether.

These results indicate that on some timescale less than 30 minutes, the mobility of mlg becomes limited such that they can no longer diffuse into membrane tubes extending from the cell. To further investigate the time-dependent reduction of mlg mobility, similar membrane tethering experiments were performed after a 5 minute incubation with fluorescent HEL. In this case, mlg was still found in the tether, but not as often as in the 0 minute incubation. Figure 4.9(a-d) shows examples of Day 0 and Day 4 membrane tethers pulled after 0 and 5 minute incubations. In the case of the 0 minute incubation the tether had to be maintained over a time scale of 10 minutes which included two steps involving fluid flow through the channel. In most cases the membrane tether either ruptured during fluid flow, or the bead was pushed out of the trap due to the fluid drag force and subsequently stuck to the cell. Due to these difficulties, the mlg imaging experiments were only done on Day 0 and Day 4 cells. Generally, the Day 4 cells appeared to have more mlg in the tether as indicated by brighter fluorescence intensity; similarly more mlg was present in the tether in the case of a 0 minute incubation compared to a 5 minute incubation. Figure 4.9 (e) shows the percentage of cells where mlg was found in the tether as a function of incubation time for Day 0 and Day 4 cells.

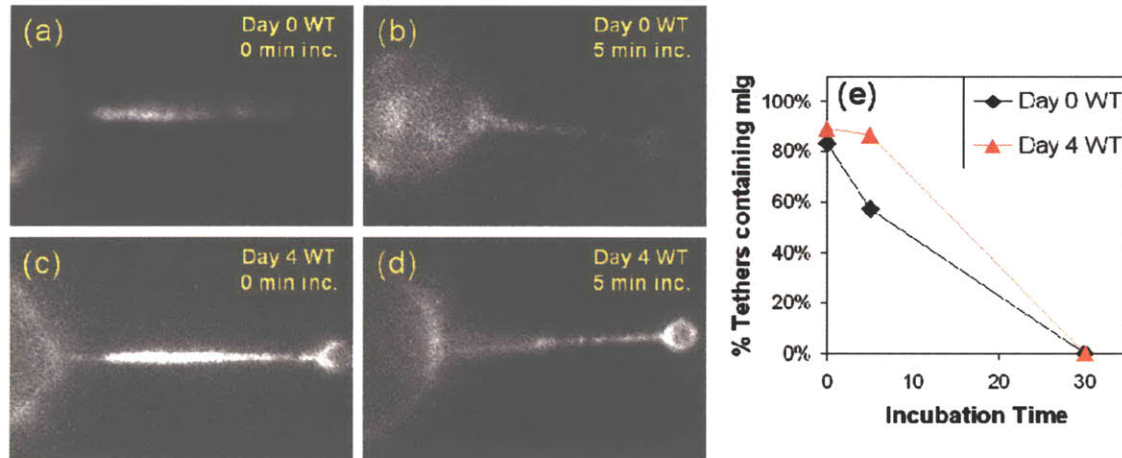


Figure 4.9 (a-d) Membrane tethers were pulled from wild-type MD4 B cells using an optically trapped HEL-coated bead either prior to or after a 5 minute incubation with HEL. mlg was found in the tether for Day 0 and Day 4 cells after 0 and 5 minute incubations but not after a 30 minute incubation. (e) shows the percentage of cells where mlg was found in the tether as a function of HEL incubation time.

The percentages are based on a total of 6 (0 minutes), 14 (5 minutes), and 10 (30 minutes) cells for Day 0 and 9 (0 minutes), 15 (5 minutes), and 10 (30 minutes) cells for Day 4. Both Day 0 and Day 4 B cells show a similar decrease in mlg presence in the tether over time. The discrepancy between Day 0 and Day 4 tethers after a 5 minute incubation could likely be due to the much larger density of mlg expression on the surface of Day 4 cells [107].

Similar experiments were carried out for XBP-1^{KO} B cells. Figure 4.10 (a-b) shows examples XBP-1^{KO} membrane tethers containing mlg for Day 0 and Day 4 with a 0 minute incubation. Figure 4.10 (c) shows the percentage of XBP-1^{KO} cells containing mlg as a function of HEL incubation time based on 7 (0 minutes), 12 (5 minutes), and 10 (30 minutes) cells for Day 0, and 9 (0 minutes), 17 (5 minutes), and 10 (30 minutes) cells for Day 4. The wild-type MD4 results are also shown for reference.

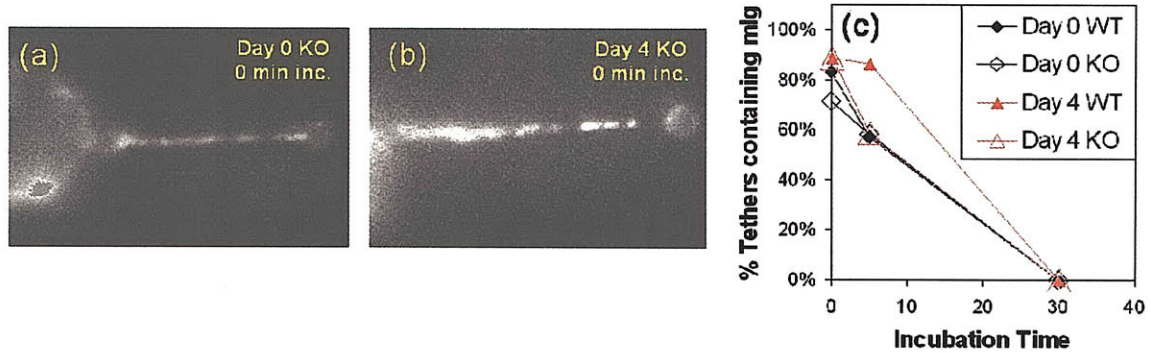


Figure 4.10 mlg was found in membrane tethers pulled from XBP-1^{KO} (KO) cells on Day 0 (a) and Day 4 (b). (c) shows the percentage of KO B cells where mlg was present in the tether compared to wild-type MD4 (WT).

The XBP-1^{KO} B cells show similar trends to the wild-type MD4 cells. There is a small discrepancy on Day 4 with a 5 minute incubation. This again could be due to a lower mlg concentration on the surface of XBP-1^{KO} B cells or the dynamics which limit the mobility of mlg may occur faster in XBP-1^{KO} cells. However, due to the small number of cells, this result is not statistically significant.

mlg may end up in the tether by two means: 1) it might be pulled into the tether immediately along with the cell membrane, or 2) it may initially be precluded from the tether and then diffuse in after some short timescale. In order to differentiate between these possibilities, membrane tethers were pulled while simultaneously imaging mlg fluorescence. Figure 4.11 shows 4 frames of a fluorescence image sequence taken while pulling a membrane tether from a wild-type MD4 B cell.

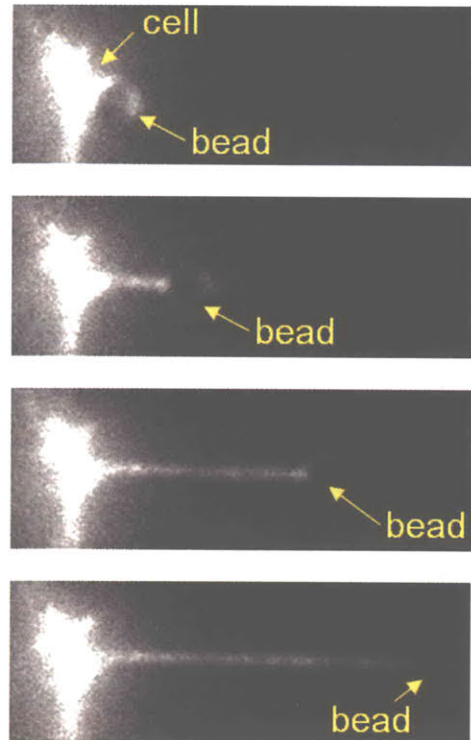


Figure 4.11 A membrane tether was pulled from wild-type MD4 B cells while simultaneously imaging fluorescent mIg. The first frame shows the bead attached to the cell membrane. The bead is subsequently pulled away from the cell at a constant velocity, and a membrane tube was extracted. mIg is immediately drawn out along the entire length of the membrane tether.

mIg appears to be pulled into the tether immediately along with the lipid bilayer. In experiment videos, mIg appeared to be mobile along the axis of the tether, suggesting that mIg might also be exchanged between the tether and the main cell body.

Interestingly, in some cases the fluorescence was not continuous along the tether, but instead was concentrated in discrete spots along the length of the tether. Figure 4.12 shows two examples where the mIg appears as bright spots in tether which seem to be periodically spaced apart. The corresponding brightfield images of tethers (figure 4.12 (c,d)) did not show any periodic features.

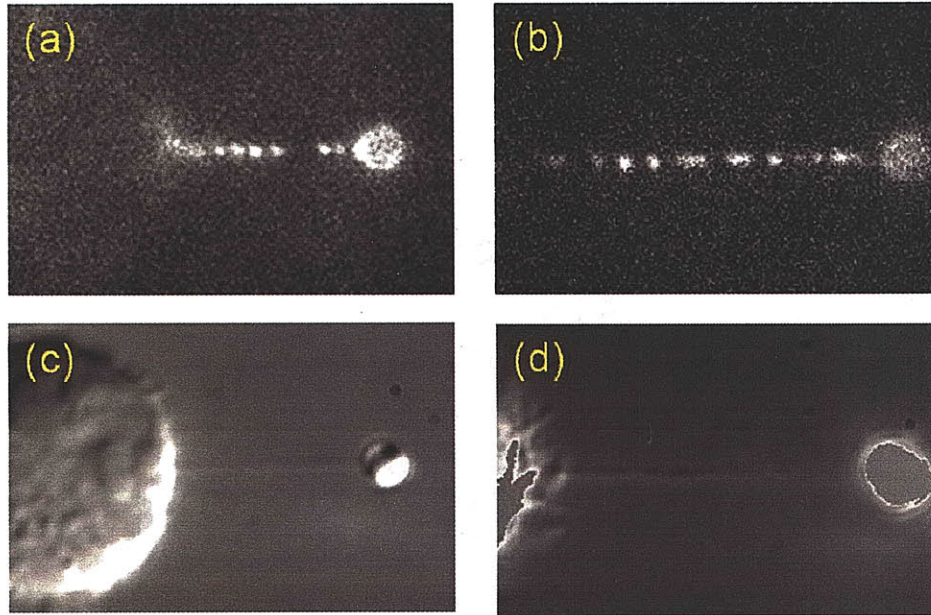


Figure 4.12 (a-b) Two examples are shown where mlg appeared as bright spots along the length of the tether. The spots appeared to have a periodic spacing on the order of 600 – 900 nm. (c-d) No periodic features were visible in the brightfield images of membrane tethers.

Due to their bright intensity, these spots are likely clusters of mlg instead of regularly spaced single molecules. When spots had periodic spacing they were separated by ~600 – 900 nm. However, the periodicity was generally transient and short-lived since clusters of mlg and possibly individual mlg molecules appeared to be mobile in the tether. In videos taken of the fluorescent tethers, individual spots appeared to move indicating that the mlg in the tether is mobile.

4.4 DISCUSSION:

Here we have applied the state-of-the-art biophysics tools of combined optical trapping and fluorescence imaging to examine the biomechanical and biochemical machinery of BCR transgenic B cells in addition to B cells from a knock-out mouse model. This work demonstrates a novel approach to the study of immunology. First, we determined that

the elimination of a particular transcription factor, XBP-1, results in a decrease in the membrane viscosity of B cells. Specifically, wild-type MD4 and XBP-1^{KO} Plasmablasts have effective membrane viscosities of 0.79 and 0.45 pN*s/ μ m respectively on Day 4. Interestingly, the membrane viscosity follows the same trend as the biochemical composition caused by XBP-1 deficiency where a reduced mlg concentration and altered B cell lipid composition are only apparent on Day 4. The reduced effective membrane viscosity results in lower forces required for membrane tether extension and faster membrane dynamics in tether force relaxation experiments. The exact mechanism of the membrane viscosity is difficult to isolate as discussed in chapter 2. The difference in effective mechanical response of the membrane (i.e. lower deformation forces and faster stress relaxation behavior) might impact functions such as antibody secretion, migration, and as specifically shown here, formation of membrane protrusions. For example, many membrane ion channels are regulated by or induce membrane stresses [1]. Changes in forces exerted on the membrane or in membrane stress relaxation characteristics may alter the activation or function of these mechanosensitive ion channels.

We combined membrane tethering experiments with fluorescence imaging to identify mlg presence in membrane nanotubes. mlg was readily visible in membrane tubes on B cells that had either not encountered BCR specific antigen, or had only encountered it for five minutes. These results show that membrane nanotubes may serve as a biochemically active extension of the B cell. BCR presence in membrane protrusions may impart the ability to sense antigen at remote locations. A BCR-antigen binding

event in the tether may lead to a signaling event in one of two ways: 1) the accessory molecules required for BCR signaling may also be present in the tether, or 2) a BCR could bind antigen at a location in the tether and then diffuse to the main cell body where it initiates BCR signaling.

While we have not experimentally tested the first scenario, the 0 minute incubation time illustrates the second scenario where BCR is likely present in the tether prior to binding antigen. BCRs present in the tether appeared to be mobile in image sequences taken which would enable antigen bound at a remote location to be transmitted back to the main cell body. The ability to utilize membrane protrusions as functional sensors could greatly expand the antigen detection capabilities of B cells. Furthermore, since these membrane nanotubes often connect immune cells [109, 117], B cells might employ membrane tubes to transfer BCR bound antigen from one cell to another. Similar membrane tubes in T cells were previously shown to transmit viruses such as HIV-1 virus, even though the same membrane nanotubes could not transfer internal calcium signals because the adjoining tubes have closed ends [109]. In light of our results, it is possible that immune cells transfer information across membrane tubes via ligand bound to membrane proteins. In immune cells this may be an efficient means to transfer activation signals over long distances to specific cells.

Interestingly, if B cells were incubated with BCR specific antigen for 30 minutes, no BCR was ever present in the membrane tethers indicating that the biochemical composition of membrane nanotubes is dependent on the activation state of the B cell.

These results are consistent with the BCR clustering behavior of activated B cells. On a time scale of 5 minutes, BCRs form small aggregates referred to as patches (See figure 4.1(a)). On a longer time scale of 15 minutes, these patches form larger aggregates referred to as a cap (See figure 4.1(b)). Our results indicate that initially BCRs are mobile and in general are capable of diffusing into membrane tethers. After small aggregations are formed (5 minutes), BCRs are still capable of diffusing into the membrane tether, although to a lesser degree. The BCR identified in the tether may either be clusters that are small enough to enter the tube, or single BCRs that have not yet aggregated into a cluster. Eventually the formation of larger aggregates on a longer time scale (30 minutes) limits the mobility of the BCR such that they are precluded from membrane nanotubes. Reduced mobility of the BCR would not impact the remote sensing function of membrane nanotubes since cells are already activated; however, precluding BCRs and other proteins that are sequestered in BCR aggregates from membrane tubes might inhibit the inter-cellular communication function of membrane tubes.

Similar experiments were carried out on XBP-1^{KO} B cells. It was found that XBP-1 deficiency may accelerate the dynamic membrane process which decreases the mobility of BCRs on Day 4. The Day 4 results are consistent with our previous results that showed XBP-1^{KO} B cells show faster membrane dynamics due to a lower effective membrane viscosity which may result in faster clustering of BCRs. The inability of BCRs to diffuse into the tether on Day 4 may also be due to the decreased BCR concentration shown in figure 4.2.

In some cases, clusters of BCRs appeared to be spaced periodically along the length of the tether separated by ~600-900 nm. This phenomenon could be due to several reasons. The spots found in the tether might be indicative of the spacing between BCRs in the local region where the membrane tether was pulled. Although considering the brightness of the spots, they likely consist of several BCR molecules. Assuming the spots are clusters of BCRs, the spacing may indicate the length scale over which clustering occurs. BCRs within a radius of 300-500 nm may form a single cluster which could result in an apparently periodic spacing in the tether. Finally, this could be a pearling instability [119]. Pearling occurs when larger spherical features form in a liquid tube giving the appearance of beads on a string. Previous research has shown that focused laser excitation can induce pearling in membrane nanotubes [120, 121]. Alternatively, the BCRs themselves might induce membrane curvature along the axis of the tether which could result in a “self-pearling.” Chaieb et al. showed that pearling could be induced by spontaneous curvature in tubular membranes [122]. No periodic features were visible in the brightfield images; however, any features below ~10-20 nm would fall below the resolution of the imaging system.

In summary, we have applied novel the experimental techniques of optical trapping and combined force-fluorescence microscopy to the field of immunology to illustrate the inter-dependence of the biomechanical and biochemical machinery of the B cell. This approach was useful to enlighten the impact of XBP-1^{KO} on B cell differentiation and BCR mobility. Our results show that alterations in the biochemical machinery of the B

cell are manifested in the physical properties of the cell, specifically the cell membrane, which might impact cellular functions such as antibody secretion, migration and extracellular communication. We further found that physical protrusions of the membrane, membrane nanotubes, generally contain BCR which potentially gives B cells the ability to detect antigen at remote locations. Our findings suggest that ligand bound membrane proteins might play a role in inter-cellular communication via membrane nanotubes in immune cells. Additionally, the biochemical composition of membrane nanotubes was dependent on the activation state of the cell. Hence, membrane nanotubes may provide a useful way to study the mobility of membrane proteins under different cellular conditions. The experimental methods developed here are robust and can be applied to the study of other immune cells.

4.5 REFERENCES:

- [1] Graziadei, L., Riabowol, K. and Barsagi, D., 1990. "Co-Capping of Ras Proteins with Surface Immunoglobulins in Lymphocytes-B". *Nature*. **347**: p. 396-400.
- [2] Mosbachozmen, L., Humez, S., Koponen, M., Fonteneau, P. and Loor, F., 1986. "Cyclosporine Facilitates B-Cell Membrane Immunoglobulin Capping". *Immunology*. **57**: p. 573-577.
- [3] Iwakoshi, N. N., Lee, A. H., Vallabhajosyula, P., Otipoby, K. L., Rajewsky, K. and Glimcher, L. H., 2003. "Plasma cell differentiation and the unfolded protein response intersect at the transcription factor XBP-1". *Nat Immunol*. **4**: p. 321-329.
- [4] Iwakoshi, N. N., Lee, A. H. and Glimcher, L. H., 2003. "The X-box binding protein-1 transcription factor is required for plasma cell differentiation and the unfolded protein response". *Immunol Rev*. **194**: p. 29-38.
- [5] Sriburi, R., Jackowski, S., Mori, K. and Brewer, J. W., 2004. "XBP1: a link between the unfolded protein response, lipid biosynthesis, and biogenesis of the endoplasmic reticulum". *J Cell Biol*. **167**: p. 35-41.
- [6] Hu, C. C. A., Dougan, S. K., McGehee, A. M., Love, J. C. and Ploegh, H. L., 2009. "XBP-1 regulates signal transduction, transcription factors and bone marrow colonization in B cells". *Embo J*. **28**: p. 1624-1636.
- [7] McGehee, A. M., Dougan, S. K., Klemm, E. J., Shui, G., Park, B., Kim, Y. M., Watson, N., Wenk, M., Ploegh, H. L. and Hu, C. C. A., 2009. "XBP-1-deficient plasmablasts show normal protein folding but altered glycosylation and lipid synthesis". *The Journal of Immunology*. **183**: p. 3690-3699.
- [8] Sowinski, S., Jolly, C., Berninghausen, O., Purbhoo, M. A., Chauveau, A., Kohler, K., Oddos, S., Eissmann, P., Brodsky, F. M., Hopkins, C., Onfelt, B., Sattentau, Q. and Davis, D. M., 2008. "Membrane nanotubes physically connect T cells over long distances presenting a novel route for HIV-1 transmission". *Nature Cell Biology*. **10**: p. 211-219.
- [9] Onfelt, B., Nedvetzki, S., Benninger, R. K. P., Purbhoo, M. A., Sowinski, S., Hume, A. N., Seabra, M. C., Neil, M. A. A., French, P. M. W. and Davis, D. M., 2006. "Structurally distinct membrane nanotubes between human macrophages support long-distance vesicular traffic or surfing of bacteria". *J Immunol*. **177**: p. 8476-8483.
- [10] Rustom, A., Saffrich, R., Markovic, I., Walther, P. and Gerdes, H. H., 2004. "Nanotubular highways for intercellular organelle transport". *Science*. **303**: p. 1007-1010.
- [11] Watkins, S. C. and Salter, R. D., 2005. "Functional connectivity between immune cells mediated by tunneling nanotubules". *Immunity*. **23**: p. 309-318.
- [12] Tian, A. and Baumgart, T., 2009. "Sorting of Lipids and Proteins in Membrane Curvature Gradients". *Biophys J*. **96**: p. 2676-2688.
- [13] Martinac, B., 2004. "Mechanosensitive ion channels: molecules of mechanotransduction". *J Cell Sci*. **117**: p. 2449-2460.
- [14] Nelson, P., Powers, T. and Seifert, U., 1995. "Dynamical Theory of the Pearling Instability in Cylindrical Vesicles". *Phys Rev Lett*. **74**: p. 3384-3387.
- [15] Bar-Ziv, R., Moses, E. and Nelson, P., 1998. "Dynamic excitations in membranes induced by optical tweezers". *Biophys J*. **75**: p. 294-320.

- [16] Barziv, R. and Moses, E., 1994. "Instability and Pearling States Produced in Tubular Membranes by Competition of Curvature and Tension". *Phys Rev Lett.* **73**: p. 1392-1395.
- [17] Chaieb, S. and Rica, S., 1998. "Spontaneous curvature-induced pearling instability". *Phys Rev E.* **58**: p. 7733-7737.

Chapter 5

Physical Properties of Yeast Prion Amyloid Fibers

5.1 INTRODUCTION:

Amyloid fibers are highly ordered self-assembled protein aggregates. Formation of amyloid fibers plays a vital role in both natural biological processes [1] and neurodegenerative disease[2]. Recently, amyloid formation has been shown to be a general property of proteins and peptides [3, 4]. The amyloid self-assembly process has also been stimulated in synthetic preparations [5, 6]. Amyloid fibers exhibit mechanical properties comparable to that of spider silk [7]. Their impressive mechanical properties combined with the ease of assembly make amyloid fibers particularly suited for nanomaterials applications, including as templates for conducting nanowire formation[8], as scaffolds for cell growth [9], and as functionalized biosensors [10].

Amyloid fibrils are morphologically very similar, with diameters between 5-15nm and over a micrometer in length. Different amyloid fibrils are also structurally related, with beta strands as the main structural component running perpendicular to the axis of the fibril. However, the detailed structural properties of amyloids and the forces that govern them have been

difficult to elucidate because the very nature of their assembly prevents the utilization of many standard structural and kinetic techniques.

Prion proteins are a special class of amyloid fiber forming proteins which are self-templating and thereby transmissible as disease vectors. Prion formation is linked to a variety of severe human and animal disorders such as bovine spongiform encephalopathy (Mad Cow Disease)[11]; however, these same transitions can lead to beneficial biological functions in bacteria and mammals such as biofilm formation, environmental adaptation, and long term memory [12-15]. In this work, we study amyloid fibers formed from a 253 amino acid N-terminal fragment (NM) of the yeast strain *saccharomyces cerevisiae* prion protein Sup35. The conformational change and amyloid formation of Sup35 inhibits stop codon recognition resulting in extended translation and novel yeast prion phenotypes [12, 13, 16]. Sup35 is a 685 amino acid long protein consisting of 3 domains: the C terminal domain (C - amino acids 254-685) containing the stop codon recognition function; the middle domain (M - amino acids 124-253), a highly charged region which imparts solubility; and the N terminal domain (N – amino acids 1-123) containing 5.5 imperfect repeats rich in glutamine, asparagines, glycine and tyrosine that are highly susceptible to amyloidogenesis. The N and M domains form amyloid fibers in vitro. Moreover, NM fibers reconstituted at different temperatures have unique underlying misfolded structures leading to distinct prion strains. Fibers assembled at 4 °C sufficiently induce “strong” [*PSI*+] when transformed into wild-type *saccharomyces cerevisiae* ([*psi*-]), while fibers assembled at 37 °C induce “weak” [*PSI*+] [17]. “Strong” and “weak” refer to the degree of change from the wild-type yeast. Tanaka et al showed that the fragmentation properties of 4 °C and

37 °C NM fibers are significantly different [18]. Phenotypically stronger strains are produced by fibrils that are chemically and mechanically weaker, because easier fragmentation generates more ends for polymerization, which in turn further reduces the concentration of soluble Sup35. Thus prion fibers are unique in that the same protein can form functionally distinct fibers by adopting different folded geometries, whereas biopolymers such as F-actin are made from a highly conserved population of monomers and functional diversity is conferred by accessory proteins leading to bundles, cross-links, and meshes.

Despite interest in amyloid fibers as novel materials and the importance of amyloid fibers in prion biology, little work has been done to experimentally quantify their physical and mechanical properties, and more specifically quantify the physical impact of prion polymorphism. Previous experimental measurements of the physical properties of other related classes of amyloid fibers have primarily focused on determination of fiber bending stiffness, κ_B , or equivalently, their persistence length, l_p [7, 19]. Smith et al. [7] used AFM imaging to quantify the mechanical properties of insulin amyloid fibers by measuring the tangent angle correlations of fibers deposited on a surface to extract persistence length and then by bending fibers partially suspended over grooves. Knowles et al. [19], measured the bending stiffness of a variety of amyloid fibers formed from peptide sequences approximately 5-50 amino acids in length using AFM imaging. They found that the elastic properties were primarily conferred by intermolecular hydrogen bonding, and the bending stiffness of the amyloid fibers followed the scaling of classical beam mechanics, $\kappa_B \sim I$ where I is the cross-sectional moment of inertia

(they assumed a circular cross-section). In the case of NM fibrils [18], a single protein may form fiber structures with different configurations and mechanical stabilities which play a vital role in prion biology since prion fiber growth is a seeded polymerization process. The molecular polymorphism of the Sup35 protein, whereby Sup35 can adopt different misfolded configurations, governs the difference mechanical stability between the configurations. Molecular polymorphism has previously been observed in Alzheimer's β -amyloid and leads to distinct fiber morphologies [20]. To further understand the physical basis of prion strain diversity and its relation to molecular polymorphism, and to guide the potential use of amyloid fibers as nanomaterials, we quantified the mechanical behavior and microstructure of NM fibers from two distinct prion strains with unique underlying folded geometries.

To that end, we have developed experimental methods to rigorously quantify the microstructure and mechanical properties of amyloid fibers through combined fluorescence imaging and force spectroscopy with optical tweezers. Optical tweezers are a powerful biophysics tool ideal for application and measurement of forces on the order of 1-100 pN with pN resolution and displacement measurement with a resolution of ~ 1 nm. Optical tweezers have been widely used to characterize the mechanics of biopolymers including DNA [21, 22], RNA [23], M13 bacteriophage [24], and actin and actin bundles [25, 26]. Our lab has recently combined optical tweezers with optimized single molecule fluorescence capabilities [27, 28], enabling measurement of the structure-function relationship of biopolymers. We develop assays to quantify the bending stiffness, extensional stiffness, and microstructure of both 4 °C and 37 °C

prion-amyloid fibers in solution which misfold to give different underlying structures [17]. In addition, the amyloid self-assembly process results in large variations in physical properties within a fiber sample set and molecular-scale defects within single fibers lead to kinks and self-crosslinking which likely indicate an inhomogeneous monomer population for self-assembly. We identify assembly temperature as a potential means to tune fiber properties, and we quantify physical differences resulting from molecular polymorphism that may contribute to the phenotypic diversity of Sup35 amyloidogenic yeast.

5.2 PHYSICAL PROPERTIES OF NM FIBERS:

5.2.1 NM amyloid fiber equilibrium morphologies. The initial goal of this work was to characterize the equilibrium microstructure of Sup35 amyloid fibers in solution. Fluorescence imaging of isolated fibers in solution revealed complex equilibrium structures that varied from nearly straight, apparently homogeneous fibers, to fibers with static curvatures on the order of the contour length, L_C . Additional complex features observed in the equilibrium structures included fibers with one or more local regions of static curvature (radii of static curvature ranged from $\sim 0.1 \mu\text{m}$ to $\sim 5 \mu\text{m}$), and fibers with point inhomogeneities resulting in static kinks. L_C varied from $\sim 1 \mu\text{m}$ up to $\sim 20 \mu\text{m}$ for both the 4°C and 37°C fibers. Representative images of the common morphologies are shown in figure 1 for the 4°C (a-g) and the 37°C (h-n) fibers. 53 % of the 4°C fibers (total of 75) had apparently straight homogeneous morphologies, while 41 % contained regions of static curvature, and 8 % contained single kinks. Two fibers contained both a kink and static curvature.

37 °C fibers (total of 53) exhibited a similar percentage of straight fibers, 51%; however, only 15% of the fibers contained regions of static curvature, and 34 % contained kinks. Closer inspection of the 37 °C kinks showed that many differed in nature from the 4 °C kinks. As seen in the intensity contour plot of the kinked 4 °C fiber shown in figure 1(g), the fluorescence varies smoothly along the fiber suggesting that the kink forms from a structural inhomogeneity and is not a result of overlapped NM monomers. The intensity contour plot of the 37 °C fiber in figure 1(n) reveals a similar kink (top) and, in contrast, two kinks which emit higher fluorescence intensity suggesting an overlap of NM monomers at these kinks. The overlapping kink on the left forms a branching cross-link between two fibers. The bright kinks likely originate from inter-fiber association formed during or post polymerization. Approximately 80 % of the 37 °C kinks contained overlapping monomers compared to none in the 4 °C fibers. Of that 80%, three quarters formed branching cross-links between fibers as in figure 1(l) and the left kink of figure 1(n). All quantitative measurements and analysis focused on fibers with L_c ranging from 3 μm to 10 μm .

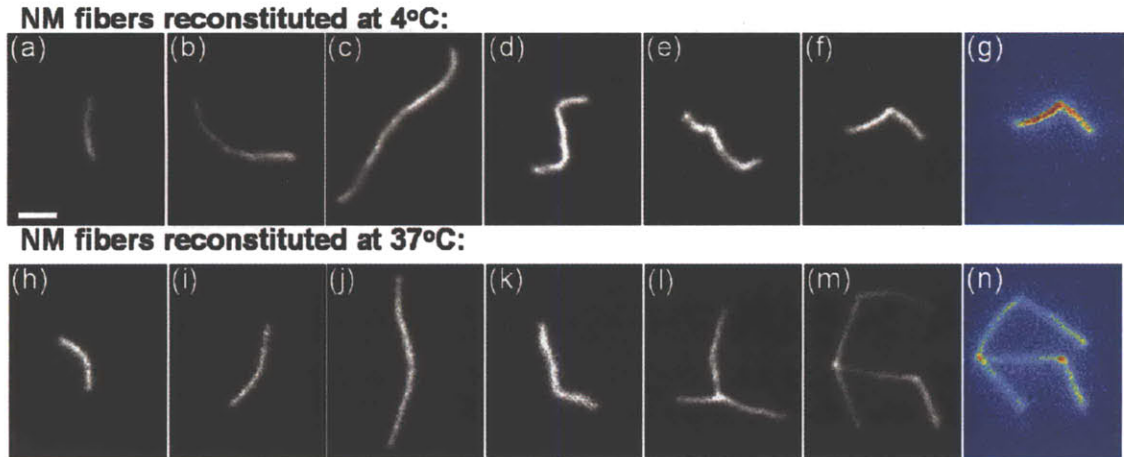


Figure 5.1 Fluorescently labeled NM fibers reconstituted in vitro exhibit complex morphologies in solution (scale bar is 2 μm). Fibers reconstituted at 4 $^{\circ}\text{C}$ show different degrees of bending (a-c), and some fibers have a stress-free configuration containing regions of high static curvature (d-e) or local static sharp turns (hinge-like regions) in the fiber, “kinks” (e-f). These kinks do not result in any overlapping monomers as indicated by the uniform fluorescence intensity (g). Fibers reconstituted at 37 $^{\circ}\text{C}$ result in similar geometries of homogeneous fibers in solution (h-j), and some fibers still contain local regions of high curvature (k) and kinks (m). However, some of the kinks in 37 $^{\circ}\text{C}$ fibers are formed by overlapping monomers as indicated by the higher fluorescence intensity (n). Some of the overlapping kinks seem to form branches as in (l) and the left side of (n), whereas others apparently occur within a fiber as in the right side of (n).

5.2.2 Fluorescence Imaging of Thermal Fluctuations. When suspended in solution at 22 $^{\circ}\text{C}$, fibers experienced thermal fluctuation. The magnitude of the shape fluctuations due to thermal energy can be directly correlated to fiber bending stiffness or persistence length [29, 30] through bending mode or cosine correlation analysis. A sequence of at least 200 frames of thermal shape fluctuations of fluorescent fibers were imaged and skeletonized to determine fiber shape, figure 2(a). Here, a bending mode analysis [29] was used to determine the persistence length, l_p , of fibers thermally fluctuating in solution. The bending energy, E_b , per unit arc length, s , of a fluctuating fiber can be written as:

$$\frac{\partial E_b}{\partial s} = \frac{1}{2} \kappa_B \left[\frac{d\theta}{ds} - \left(\frac{d\theta}{ds} \right)_0 \right]^2 \quad (5.1)$$

where κ_B is the bending stiffness of the fiber, and $\left(\frac{d\theta}{ds} \right)_0$ is the equilibrium or static curvature. The total energy is obtained by integrating equation (5.1) along the length of the fiber giving equation (2) assuming that κ_b is constant over the entire length of the fiber.

$$E_b = \frac{1}{2} \kappa_B \int_0^L \left[\frac{d\theta}{ds} - \left(\frac{d\theta}{ds} \right)_0 \right]^2 ds \quad (5.2)$$

The angle θ can be expressed by the following fourier series.

$$\theta(s) = \sum_{n=0}^{\infty} \theta_n(s) = \sum_{n=0}^{\infty} a_n \cos\left(\frac{n\pi s}{L_C}\right) \quad (5.3)$$

Combining equations (5.2) and (5.3) and integrating gives E_b in terms of the coefficients of the fourier modes.

$$E_b = \frac{1}{2} \kappa_B \sum_{n=1}^{\infty} \left(\frac{n\pi}{L_C} \right)^2 (a_n - a_n^0)^2 \quad (5.4)$$

The theorem of equipartition of energy states that each term in the series in equation (5.4) contributes on average $\frac{1}{2}k_bT$ of energy. Therefore, for each bending mode can be described by:

$$\left\langle (a_n - a_n^o)^2 \right\rangle = \frac{k_bT}{\kappa_B} \left(\frac{L_C}{n\pi} \right)^2 = \frac{1}{l_p} \left(\frac{L_C}{n\pi} \right)^2 \quad (5.5)$$

Note that the static curvature is included in this equation through coefficients a_n^o which in our case is necessary since many of the NM fibers studied here contained static curvature. We determine l_p by fitting equation (5.5) to the modes that appear to follow a slope of negative 2 on a log-log plot of the fourier coefficient variance, $\left\langle (a_n - a_n^o)^2 \right\rangle$, versus the wave number, $k_w = n\pi/L_C$. Figure 5.2(a) shows a skeletonized fiber (inset) reduced to a fourier series of modes 1 through 9 for the $s-\theta$ waveform. Figure 5.2(b) shows a fit of equation (5.5) to determine the persistence length l_p .

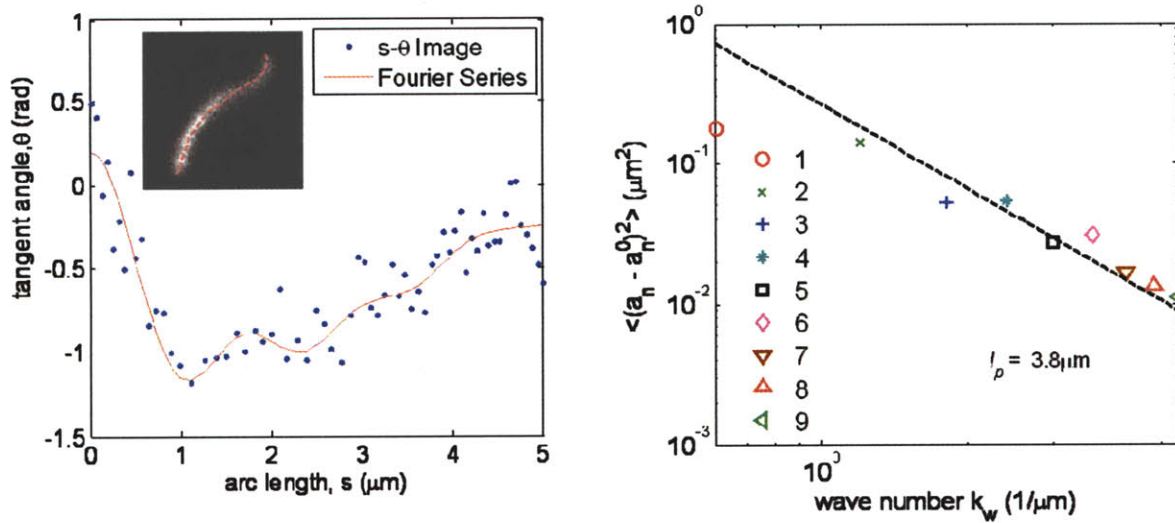


Figure 5.2 (a) shows an s - θ waveform for a skeletonized 4 oC fiber for one image of a sequence shown in the inset. (b) shows the variation in the fourier coefficients for modes 1 through 9 and a fit for l_p using equation (5.5).

Cosine correlation methods, which track the length over which fiber tangent angles are correlated to determine persistence length [30], were inappropriate because the inherent equilibrium curvature of some of the fibers (see figure 1) would yield an apparently lower persistence length. The results of the bending mode analyses of 21 fibers are shown in figure 5.3 (b). The persistence lengths were found to be $3.6 \pm 1.1 \mu\text{m}$ and $7.0 \pm 2.4 \mu\text{m}$ (average \pm standard deviation) for the 4 °C and 37 °C NM fibers, respectively. Fibers with regions of static curvature and apparently straight fibers were indistinguishable in terms of the reduced l_p . Fibers with kinks were not used for any bending mode analysis.

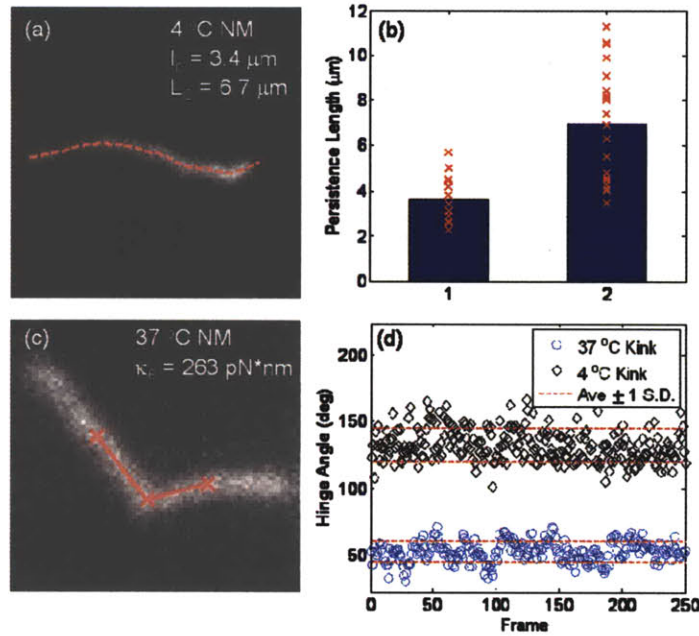


Figure 5.3 Fluorescence imaging was used to track the variations in shape of NM fibers subject to thermal fluctuations. A bending mode analysis of these shape fluctuations was used to determine persistence length. (a,c) show skeletons of the fiber shape for one of a sequence of images used in the bending mode analysis and the hinge angle analysis respectively. A summary of the results of the bending mode analysis is shown in (b). The average l_p s as determined from a bending mode analysis were $3.6 \mu\text{m}$ and $7.0 \mu\text{m}$ for the $4 \text{ }^\circ\text{C}$ and $37 \text{ }^\circ\text{C}$ fibers respectively. The thermal fluctuations of both $4 \text{ }^\circ\text{C}$ and $37 \text{ }^\circ\text{C}$ kinks are shown in (d).

Torsional stiffness of the kink regions was determined by measuring the thermal fluctuations in the kink angle, θ [31, 32] using a similar assay. The kink angle was fit manually over a series of skeletonized images by selecting three points to define the angle as shown in figure 5.3 (c). Figure 5.3(d) shows the thermal fluctuations of a $37 \text{ }^\circ\text{C}$ kink. The torsional stiffness, κ_θ , is extracted from the angle θ using the equation:

$$k_b T = \kappa_\theta \langle \theta^2 \rangle \quad (5.6)$$

4 °C kinks (N=4 measurements) exhibited an average torsional stiffness of 0.96×10^{-19} N*m/rad while the 37 °C kinks with no overlapping monomers were slightly stiffer with an average κ_{θ} of 1.72×10^{-19} N*m/rad (N=3). The 37 °C kinks with overlapping monomers were slightly stiffer with an average κ_{θ} of 2.08×10^{-19} N*m/rad (N=3) and the cross-linking kinks were more compliant with an average κ_{θ} of 1.48×10^{-19} N*m/rad (N=6). θ_0 varied over similar ranges for both 4 °C (angles spanning 59° to 131°) and 37 °C (angles spanning 54° to 115°) fibers.

5.2.3 Force-extension Behavior of Homogeneous NM fibers. Due to different morphologies of the amyloid fibers, it was important to identify the microstructure of each particular fiber subjected to mechanical deformation in order to extract mechanical properties. Here we developed an assay to simultaneously image structure while measuring persistence length and extensional stiffness. Fibers were tethered between a glass cover slip surface and a 0.8 μm bead. Force-extension experiments were carried out by holding the bead in a stationary laser trap while scanning the surface tether point using a piezoelectric stage. The experimental assay and loading protocol are detailed in figure 5.4.

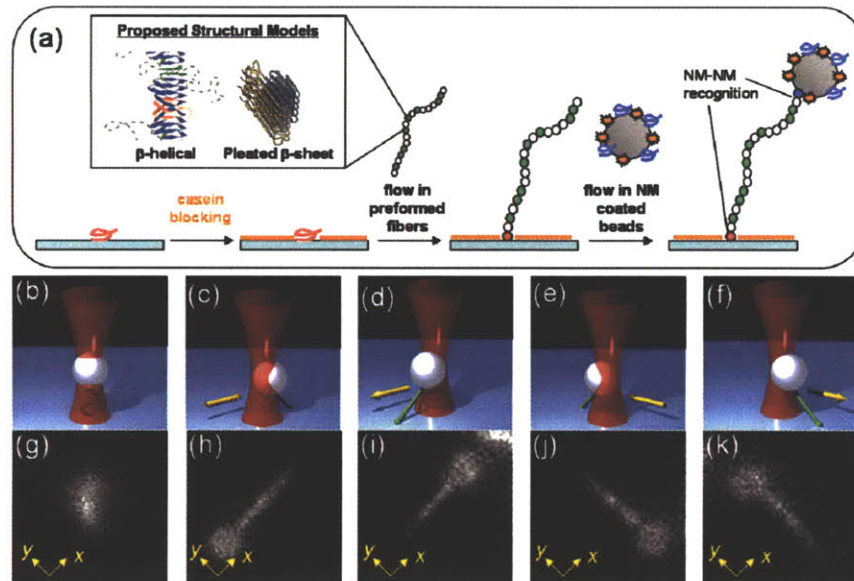


Figure 5.4 Schematics and fluorescent images of the experimental assay. (a) His-tagged NM monomers are non-specifically adhered to a glass coverslip surface. The remaining exposed glass is coated with Casein blocking protein to prevent pre-formed fibers and beads from non-specifically sticking to the glass. NM fibers preformed with 50% fluorescently labeled monomer (green) are then flown and attach to the His-NM on the surface. The inset shows two proposed structural models, β -helical [17] and pleated β -sheet [33]. Finally fluorescently labeled streptavidin beads pre-coated with biotinylated NM monomers (blue) and Alexa488 (orange) are flown into the sample and attach to the free end of the fiber via. Both the surface and bead attachment rely on the self recognition properties of the NM protein. Using the bead and the coverslip which sits on a piezoelectric stage serve the fiber is extended in the x-direction and the y-direction as shown schematically (b-f) and from an experiment in (g-k) resulting in 8 force-extension curves for the fiber, 4 loading and 4 unloading.

An interlaced optical force and fluorescence (IOFF) method, developed in our lab, allows for simultaneous force and fluorescence measurements [27]. This method prolongs the bead and fiber fluorescence signals by avoiding trap induced photobleaching to enable imaging of the fiber morphology throughout the force-extension experiment and proper determination of boundary conditions. When IOFF is not used, fiber and bead fluorescence in the vicinity of the trap bleach very quickly. Figure 5.5(a) shows images prior to (red), during (green), and after (cyan) an unloading

and loading pass without the IOFF. With IOFF the entire fiber and bead are easily visible throughout the complete experiment as seen in figure 5.5(b).

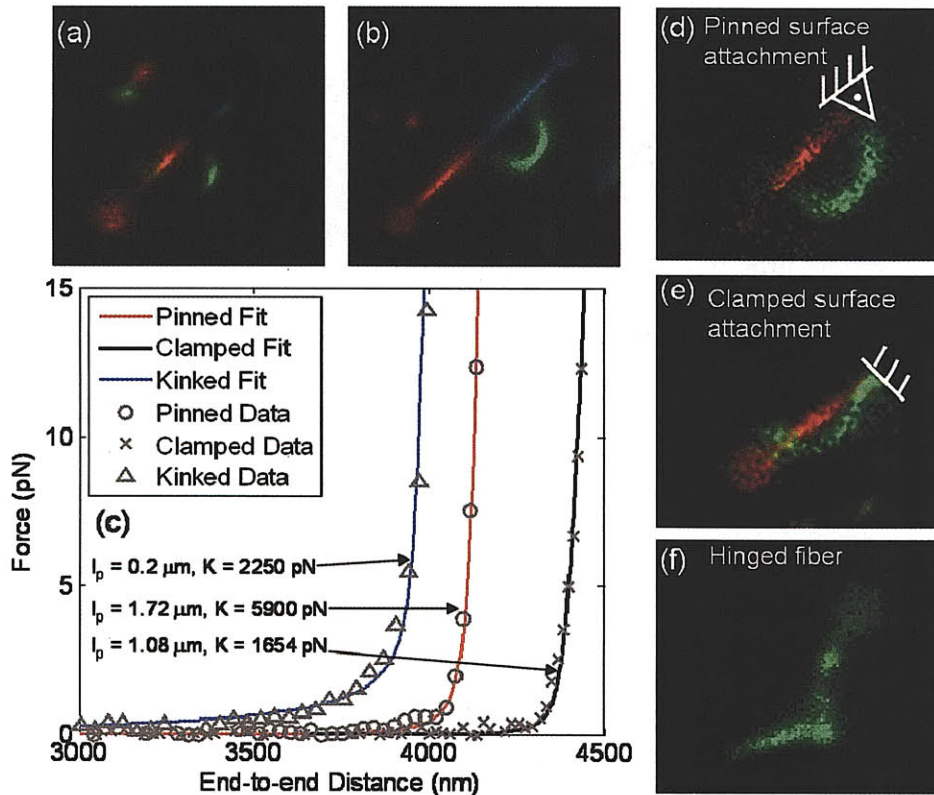


Figure 5.5 (a) overlaid images of the fiber prior to (red), during (green) and after (cyan) an unloading and loading experiment without the interlaced method. Details of the fiber structure especially near the bead are lost because of trap accelerated photobleaching. (b) Our IOFF method prolongs the fluorescence lifetime allowing for imaging of the fiber throughout the experiment. (c) Force extension data from experiments were fit to wormlike chain (WLC) models with appropriate boundary conditions to determine l_p , L_C , and K . Kinked fibers were modeled using equation (5.17) to determine κ_θ . (d) Some fibers were attached to the surface such that they could easily rotate about the attachment point (green) when r was decreased from the fully extended position (red) (symbol indicates freely rotating, pinned, boundary condition). (e) Some were attached more rigidly such that the fiber could not rotate at the attachment point and adopted a bimodal shape (green) when r was decreased from the fully extended position (red) (symbol indicates rigidly attached boundary condition prohibiting fiber rotation – clamped). (f) Kinked fibers were identified by fluorescent imaging.

The cross-linked nature of the 37 °C fibers made it difficult to identify isolated fibers for force-extension. Beads also readily stuck to the side of 37 °C NM fibers which made

force-extension data unreliable. Therefore, force-extension measurements were only conducted on the 4°C NM fibers. The resulting force-extension data for the 4 °C fibers, shown in figure 4(c), are characteristic of an extensible wormlike chain (WLC). The force is zero at a non-zero end-to-end distance, r , which is a significant fraction of L_C , indicating l_p is on the order of L_C . This is consistent with the equilibrium morphologies obtained previously which showed that the unloaded end-to-end distance is on the order of L_C . Hence, we use a WLC force-extension approximation consistent with $l_p \sim L_C$. Palmer et al [34] provided a convenient approximation to the Mackintosh et al [35] analytical solution for the force-extension behavior of a WLC with $l_p \sim L_C$ and extended the model to account for direct axial stretching which occurs as $r \rightarrow L_C$ [36]. The Palmer-Boyce adaptation, given by equations (5.7)-(5.9), was used to identify l_p , L_C , and the axial stiffness, K , from the force-extension data.

$$f = \frac{k_b T}{l_p} \left(\frac{1}{4(1 - \lambda_u r_0 / L_C)^2} \right) \left(\frac{L_C / l_p - 6(1 - \lambda_u r_0 / L_C)}{L_C / l_p - 2(1 - \lambda_u r_0 / L_C)} \right) \quad (5.7)$$

$$\lambda_e = \frac{L_C}{r_0} \frac{f}{K} + 1 \quad (5.8)$$

$$\lambda = \lambda_e \lambda_u = r / r_0 \quad (5.9)$$

In these equations, f is the force acting on the fiber; λ is the total fiber stretch which is decomposed into λ_u , the stretch due to the reduction in thermal fluctuations of the fiber

due to f , and λ_s , the stretch due to direct axial extension. r is the current end-to-end distance, and r_0 is the initial end-to-end distance which is derived from equation (5.7) as

$$r_0 = L_C \left(1 - \frac{L_C}{6l_p} \right).$$

In this model, both ends of the fiber are assumed to freely rotate about their respective attachment points (i.e. pinned boundary conditions). Any rotation constraint imposed by the boundaries will constrain the lateral motion of the fiber over a distance of order l_p . Therefore, boundary conditions have a negligible effect for a fiber with $l_p \ll L_C$. However, in the case where $l_p \sim L_C$, the boundary conditions become significant and must be taken into account. Careful examination of the fiber deformation revealed that some surface attachments were freely rotating (i.e. pinned - see figure 5.5(d)), and their force-extension follows equation (5.7); whereas some surface attachments were rigidly constrained against rotation due to surface binding at more than a single point (i.e. clamped - see figure 5.5(e)). The force-extension relationship for the clamped condition was determined in Palmer et al. [37] and is given by equation (5.7a).

$$f = \frac{k_b T}{l_p} \left(\frac{1}{16(1 - \lambda_u r_0 / L_C)^2} \right) \left(\frac{L_C / l_p - 24(1 - \lambda_u r_0 / L_C)}{L_C / l_p - 8(1 - \lambda_u r_0 / L_C)} \right) \quad (5.7a)$$

Representative results of fitting the pinned and clamped models to corresponding fibers are shown in figure 5.5(c). Fitting the clamped data in figure 5.5(c) with pinned boundary conditions results in over-predicting the l_p by a factor of 3 thus demonstrating the importance of identifying and accounting for the fiber boundary conditions. The

distributions of l_p and K , shown in figure 5.6, were determined for NM fibers formed at 4 °C. All experiments were conducted at room temperature, 22 °C. The average l_p of the homogeneous fibers was $1.5 \pm 0.6 \mu\text{m}$ which corresponds to a κ_B of $0.6 \cdot 10^{-26} \pm 0.2 \cdot 10^{-26} \text{ N} \cdot \text{m}^2$, and the average axial stiffness of the 4 °C NM fibers was 5600 pN.

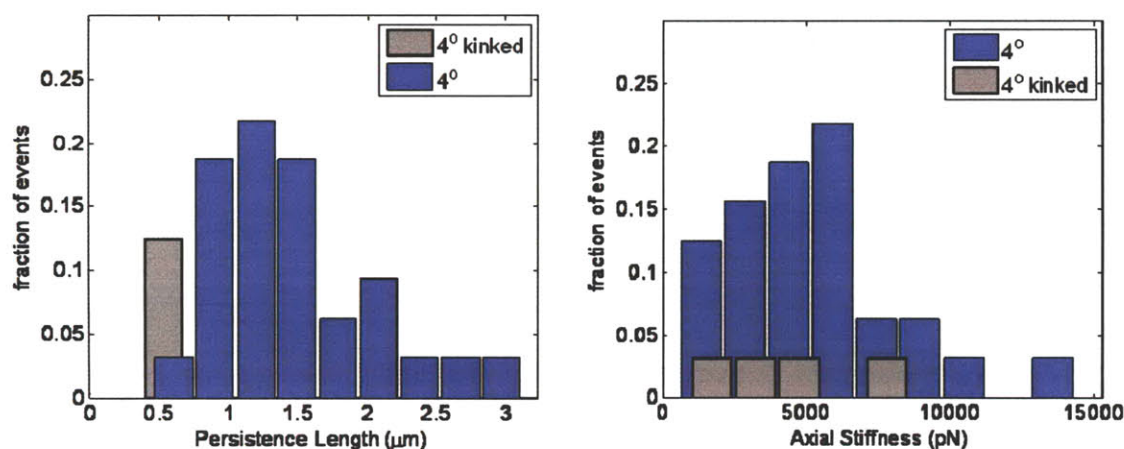


Figure 5.6 The bending stiffness and the axial stretching stiffness are determined from force-extension experiments on single fibers. The average bending stiffness is $0.6 \cdot 10^{-26} \text{ N} \cdot \text{m}^2$ which corresponds to a persistence length of $1.5 \mu\text{m}$, and the average axial stiffness is 5600 pN which for a diameter of 4.5 nm results in an elastic modulus of 0.3 GPa. Imaging revealed local inhomogeneities in fiber structure which results in kinked fibers. These fibers have a low apparent bending stiffness compared to the homogenous fibers, but the axial stiffness was similar.

Our combined force-fluorescence approach allowed for direct identification of kinked fibers. Momentarily ignoring the inhomogeneous microstructure of the kinked fibers, their force-extension behavior was similar to a homogeneous long polymer ($L_C \gg l_p$). The WLC models of equations (5.7) and (5.7a) are only appropriate for the case were $l_p \sim L_C$; for the case of $l_p \gg L_C$ the extensible Marko-Siggia model [21, 38] given in equation (5.10) is applicable and was initially fit to the kinked fiber data to determine L_C , an effective l_p and K .

$$f = \frac{k_B T}{l_p} \left[\frac{1}{4(1-r/L_c + F/K)^2} - \frac{1}{4} + \frac{r}{L_c} - f/K \right] \quad (5.10)$$

The apparent persistence length provides a means for direct comparison of the kinked fibers to homogeneous fibers. The kinked fibers exhibit an average apparent persistence length of 0.28 μm and an average axial stiffness of 4033 pN.

5.2.4 Force-extension behavior of kinked NM fibers. A model for the force-extension behavior of the kinked fibers that specifically accounts for the kinked morphology was developed. The model consists of two rods of length L_1 and L_2 connected by a hinge with a constant torsional stiffness κ_θ as shown in the inset of figure 5.5(a). When the end-to-end distance, r_h , of the fiber is increased from its initial value, r_0 , the hinge opens resulting in an increase in the internal energy, E_h , of the fiber given by:

$$E_h = \frac{\kappa_\theta}{2} (\theta - \theta_0)^2 \quad (5.11)$$

where θ is the current hinge angle, and θ_0 is the initial. Using the law of cosines, θ can be written in terms of r as:

$$\theta = \arccos \left(\frac{L_1^2 + L_2^2 - r^2}{2L_1 L_2} \right) \quad (5.12)$$

The force it takes to open the hinge can be determined by differentiating E_h with respect to r using the chain rule resulting in:

$$f_h = \frac{\partial E_h}{\partial r} = \frac{\partial E_h}{\partial \theta} \frac{\partial \theta}{\partial r} = \frac{\kappa_\theta r}{L_1 L_2} (\theta - \theta_0) \left[1 - \left(\frac{L_1^2 + L_2^2 - r^2}{2L_1 L_2} \right)^2 \right]^{-\frac{1}{2}} \quad (5.13)$$

where θ is given by equation 5.12. This equation describes the force it takes to open the hinge by a horizontal load applied at the end of the fiber assuming the rods connecting the hinge are inextensible.

In reality, when the fiber approaches its fully extended position ($r \rightarrow L_C$), the fiber can extend axially. Here we use an additive decomposition where the additional deformation due to axial extension, δ_a , is added to the extension due to opening of the hinge, δ_h . The equations of compatibility and equilibrium are:

$$\delta = \delta_h + \delta_a \quad (5.14)$$

$$f = f_h = f_a \quad (5.15)$$

A simple linear model is used for the force of axial extension given by equation (5.16) where K is the axial stiffness of the fiber and the fiber contour length, L_C , is the sum of L_1 and L_2 .

$$f_a = \frac{K}{L_C} \delta_a \quad (5.16)$$

Combining equations (5.13)-(5.16) gives equation (5.17) which describes the full force-extension behavior of an extensible fiber containing a kink.

$$f = \frac{\kappa_\theta (r_{tot} - FL_C / K)}{L_1 L_2 (1 - \cos^2 \theta)^{\frac{1}{2}}} [\theta - \theta_0] \quad (5.17)$$

where $\theta = \arccos\left(\frac{L_1^2 + L_2^2 - (r_{tot} - FL_C / K)^2}{2L_1 L_2}\right)$ when direct axial stretching is included, and

r_{tot} is the total end-to-end distance give by $r_{tot} = r_0 + \delta_h + \delta_a$. Figure 5.7 shows the impact of varying κ_θ and θ_0 on the force-extension behavior of the hinged fiber.

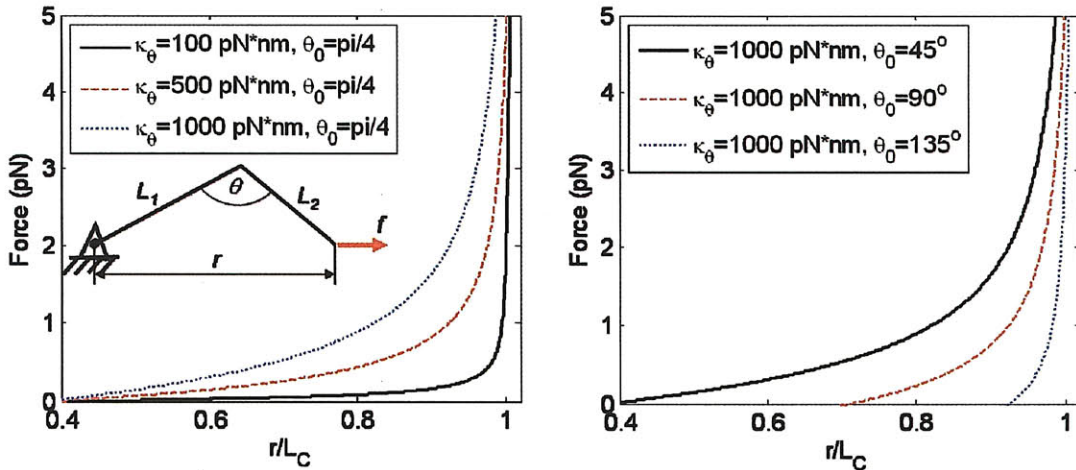


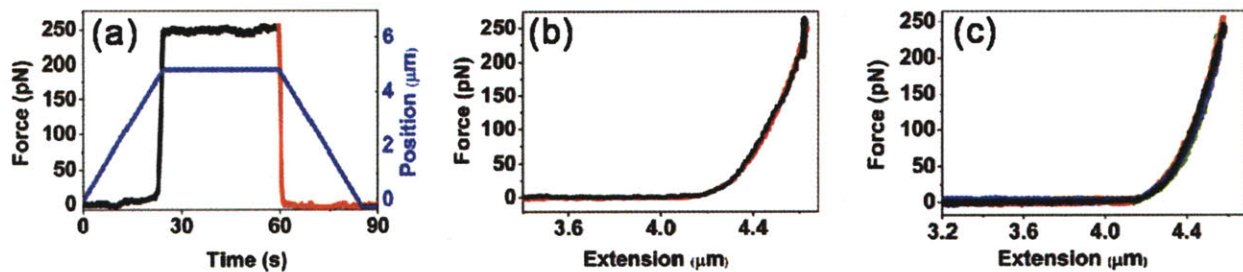
Figure 5.7 The force extension of kinked fibers is described by a mechanical model consisting of two extensible rods of lengths L_1 and L_2 connecting a hinge of angle θ with a torsional stiffness κ_θ in the geometry shown in the inset of (a). (a) shows the effects of varying κ_θ and (b) shows the effects of varying θ_0 . The contour length, $L_C = L_1 + L_2$. For these solutions, $L_1 = L_2 = 2.0 \mu\text{m}$.

For the case of a 4 °C fiber with $L_1 = 1.55 \mu\text{m}$, $L_2 = 1.10 \mu\text{m}$, and an initial kink angle $\theta_0 = 109^\circ$, the force-extension fit shown in figure 5.4 (c) gives $\kappa_\theta = 5.5 \cdot 10^{-19} \text{ N}\cdot\text{m}/\text{rad}$ and $K = 1750 \text{ pN}$. Because clear values for L_1 , L_2 , and θ_0 were difficult to obtain from images and an overall small percentage of 4 °C kinked fibers, only two force extension measurements could be made to determine torsional stiffness. The average reduced κ_θ was $5.1 \cdot 10^{-19} \text{ N}\cdot\text{m}/\text{rad}$ which is in reasonable agreement with the torsional stiffness determined from fluctuation measurements for the 4 °C kinks, and the axial stiffness is within the experimental variation. With no prior knowledge of a kink, achieving similar fits using a WLC (equation (5.10)) leads to an average l_p of $0.43 \mu\text{m}$ thus demonstrating how long rods connected by a hinge can artificially give the appearance of a flexible fiber with low bending stiffness.

5.3 MOLECULAR INTERACTIONS OF YEAST PRION PROTEINS:

With the forces typically applied by optical trapping described above, NM fibrils were stretched but no rupture or unfolding occurred. To see if we could mechanically rupture (fragment) the molecular interactions of NM proteins, we then applied force up to 250 pN, the maximum capacity of our optical tweezers. Individual tethers were pulled from the centered position to full extension (stretching phase), then held at the extended position to allow continuous exposure to high forces for a period of time (holding phase), and finally relaxed (relaxation phase) by moving the bead back to the center position. Figure 5.8(a) shows the force profile and motion of the stage for the stretching, holding, and relaxation phases of one experiment. No unfolding or rupture events were

observed in either the stretching phase or the holding phase. This was also apparent from the superimposable nature of the force-extension curves that correspond to the stretching and relaxation phases (figure 5.8(b)). Finally, individual fibrils were subject to multiple stretching-relaxation cycles and the force-extension curves from subsequent cycles were also superimposable, confirming that no rupture or unfolding had occurred (figure 5.8(c)).



Figur 5.8 (a) Fibers were subjected to extension (black), holding (black), and relaxation (red) phases by moving the piezoelectric stage (blue). (b) Extension (black) and relaxation (red) data from the loading cycle superposed indicating that no unfolding or rupture had occurred. (c) Extension and relaxation data from multiple loading cycles also superposed.

To destabilize the fibrils and thereby increase the probability of rupturing individual molecular interactions, we performed the stretching-relaxation experiments in the presence of 0.4, 0.8 or 1.2 M guanidine hydrochloride (GdnHCl). GdnHCl is a chaotropic reagent known to decrease the mechanical stability of proteins [17, 39] and fibrils that create strong prion phenotypes. Specifically, NM exhibits a cooperative unfolding transition at $D_{1/2} \sim 1.5\text{M}$ GdnHCl. GdnHCl at 0.4 and 0.8M had no effect on the stretching-relaxation behavior of the fibrils. To our surprise, at 1.2M GdnHCl, instead of fibrils simply rupturing, most trials yielded complex pulling traces characterized by sawtooth patterns during the stretching phase and sudden force drops during the

holding phase. Several examples from over a hundred similar recordings are shown in figure 5.9, with events indicated by the black arrows and the final rupture of the tethers indicated by the red arrows.

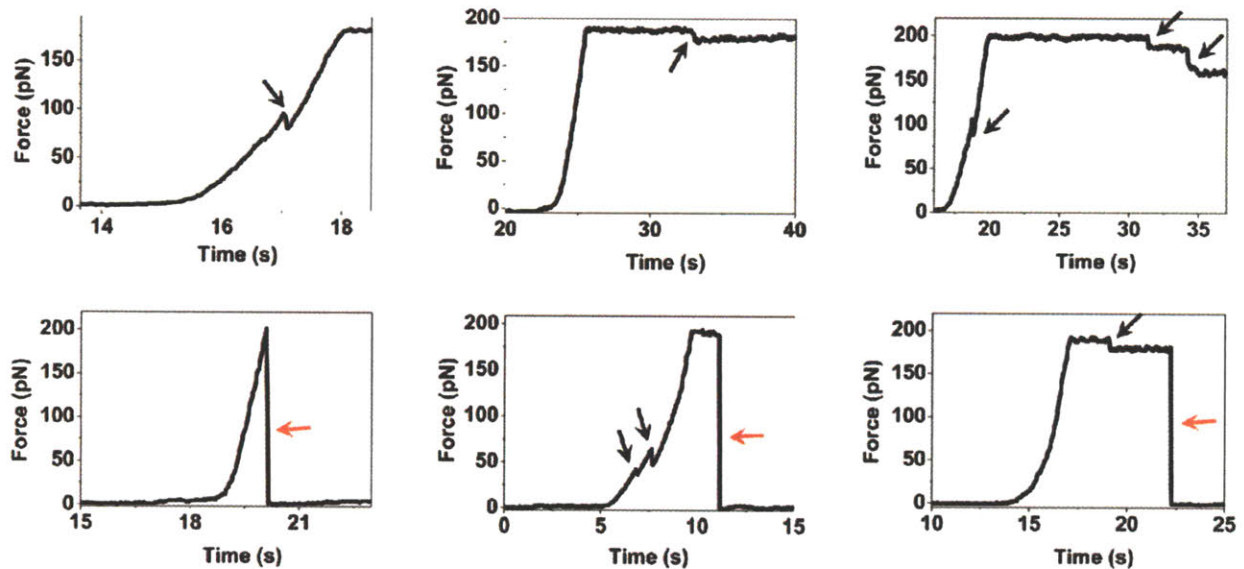


Figure 5.9 Several examples of unfolding (black arrows) and rupture events (red arrows) that occur during the extension and holding phases are shown.

Most tethered fibrils could be subjected to multiple cycles of stretching and relaxation before they ruptured. In contrast to figure 5.8(c), the force-extension curves from subsequent stretching cycles did not superimpose. Two examples are shown in figure 5.10. This was because the events causing abrupt force changes during the stretching and holding phase were only very rarely reversed in the relaxation phase or in the period between cycles. Usually loading cycles were performed in immediate succession (< 30 s between cycles); however, in some cases the bead was re-centered in between cycles requiring ~ 5 minutes and still curves did not directly superpose.

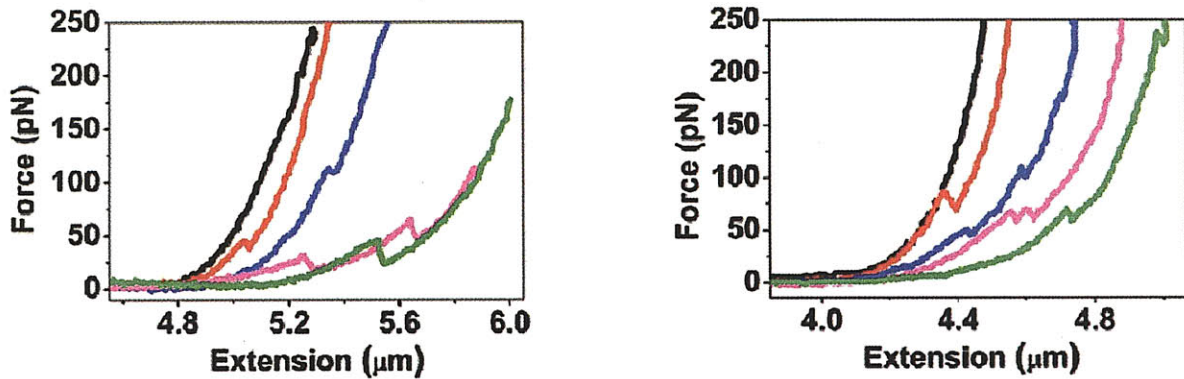


Figure 5.10 Two examples of fibers subjected to multiple loading cycles are shown. Different colors represent subsequent loading cycles. The abrupt drops in force (sawtooth features) represent unfolding events that occur during the extension phase. The holding phases which contain more unfolding events is not shown for clarity.

These sawtooth features are typical of protein unfolding events [40] leading to the conclusion that we were rupturing folding interactions of prion subunits. To confirm that these abrupt force changes were indeed due to unfolding, we first discounted several other possible explanations. First, the discontinuities in the force curves could simply reflect a stepwise release of the segments of the non-specifically bound NM protein from the glass surface. If so, the final rupture event would represent separation of the last remaining connection between the predeposited NM and the surface. To allow us to reproducibly visualize the position of rupture, fibrils were manipulated in a manner that minimized trap induced photobleaching and fluorescent images of the tethered fibrils were recorded before and after rupture. Fragments of the previously tethered fibrils could be seen, still attached to the surface, and these represented varying fractions of the initial fibril length. Figure 5.11 shows an example of a fiber fragment that is still bound to the surface after rupture. Thus, rupture was not due to detachment of fibrils

from the glass surface (or, for that matter, from the bead), but to the severing of the fibril itself at various positions along its length.

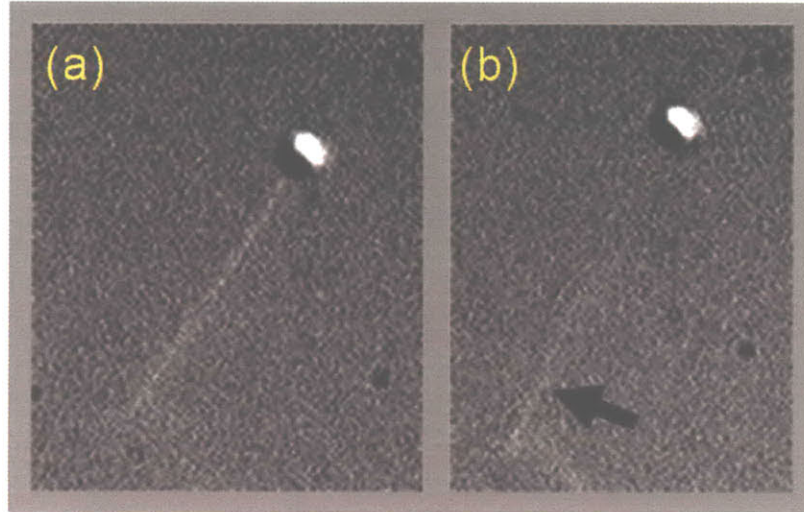


Figure 5.11 Fibers were fluorescently imaged prior to and after rupture events. (a) shows a fiber fully extended along the pulling axis before rupture. (b) After rupture a fragment of the fiber approximately half of its full length remains on the surface confirming that fiber rupture was not a result of predeposited NM monomers ripping off the surface.

Many amyloid fibrils consist of a hierarchical arrangement of laterally associated protofilaments, which frequently twist around each other up the axis of the fibril . In principle, the discontinuities in our force curves could originate from slippage of protofilaments relative to each other. However, this would require instantaneous rupture and reformation of interactions between protofilaments over a micrometer length scale which seems extremely unlikely. Moreover, protofilaments have never been observed for NM fibrils, likely because the highly charged M domain shields the amyloid core from such associations . And finally, refolding events were sometimes observed as shown in figure 5.12, arguing against slippage of protofilaments, which should be nonreversible. Thus, the unfolding of NM domains within the fibrils where noncovalent intermolecular

contacts remain intact seems the most likely explanation for the discontinuities in the force curves. If so, it follows that NM fibrils must contain at least two distinct regions with different mechanical stabilities along the fibril axis. One region has weaker interactions and several of these can be unfolded extending the length of the fibril at each step, before a stronger intermolecular contact region ruptures, severing the fibril.

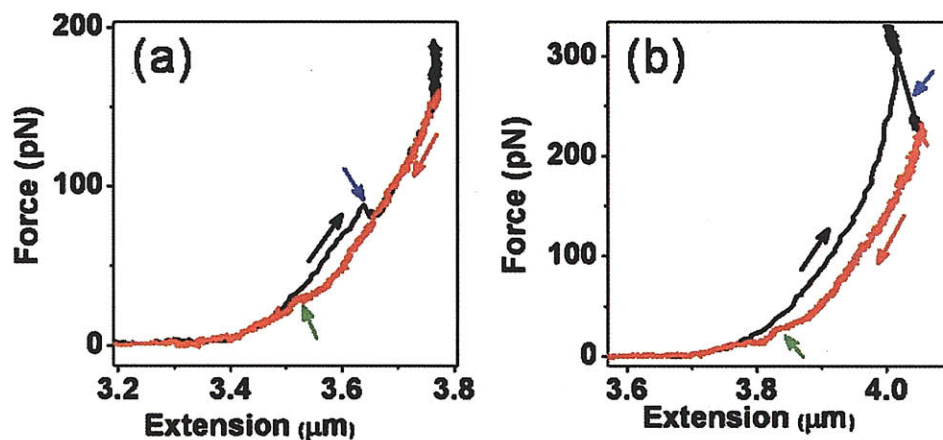


Figure 5.12 Two examples extension (black) and relaxation (red) traces are shown where unfolding and refolding occurs. (a) The unfolding indicated by the blue arrow occurs in the extension phase and no further unfolding occurs during the holding phase as indicated by the overlap of the force-extension curves at large force. The refolding event indicated by the green arrow results in the relaxation curve again overlapping with the extension curve at low forces. (b) Unfolding occurs during the holding phase resulting in hysteresis between the extension and relaxation curves. A refolding event indicated by the green arrow reduces the hysteresis between extension and relaxation.

To confirm that the complex force-extension profiles indeed result from unfolding events in the amyloid, we performed the experiments in the presence of DAPH (4,5-dianilinophthalimide) rather than GdnHCl. GdnHCl is a generic denaturant of protein structures, while DAPH specifically remodels and disrupts particular types of amyloid fibrils, including NM fibrils (29). DAPH does not affect the structure of other types of protein folds. We recorded 51 stretching-relaxation cycles from 24 tethered NM fibrils in the presence of 50 μM DAPH and observed 146 unfolding events prior to rupture. These

were remarkably similar in character to those observed in GdnHCl. The effect of DAPH was highly specific since neither unfolding nor rupture of NM fibrils was observed in the presence of staurosporine aglycone (SA) (Figure S5), a close analog of DAPH previously shown not to affect NM fibrils (29). Thus, the effect that DAPH has on the force responses of NM fibrils must be determined by structural elements within the amyloid. Taking these data together, we conclude that the discontinuities in pulling traces in response to forces applied by the optical trap reflect sequential unfolding events that culminate in rupture.

We also stretched fibrils embodying weak prion phenotypes. Prions producing weak biological phenotypes have previously been shown to be both chemically and mechanically more stable than those producing strong biological phenotypes (The weaker phenotypes are due to poorer fragmentation which produces fewer surfaces for polymerization with a net effect *in vivo* of sequestering less of the Sup35 translation function.) (1, 12, 25). In the presence of DAPH and under the identical experimental setup, only two isolated unfolding events were observed from 76 stretching-relaxation cycles collected from 16 tethered fibrils. The two tethered fibrils that showed an unfolding event were stretched multiple times afterward and no further unfolding or rupture was obtained. These NM fibrils also resisted unfolding in GdnHCl at the highest concentration that was technically feasible (1.4M) (Further increases in GdnHCl caused the polystyrene beads to stick to the glass surface). Thus, the NM fibrils that induce a weak prion phenotype are more resistant to unfolding and rupture under pulling forces. This data suggest that the many discontinuities in pulling traces with fibrils embodying

the strong prion phenotype derive from the distinct structural and biological properties defining the nature of strong prions.

We had sufficient data from strong prion fibrils to calculate the length of the region unfolding at each event. To do so, the force-extension curves in the enthalpic stretching phase were fit with a worm-like chain model in order to calculate contour length before and after each unfolding event as shown in figure 5.13(a). Figure 5.13(b) shows the linear correlation between the length of extension and the instantaneous bead displacement that occurred upon the unfolding (determined by dividing the change in force by the trap stiffness). This provided a calibration factor to calculate the length of the extension for rupture events occurring during the holding phase.

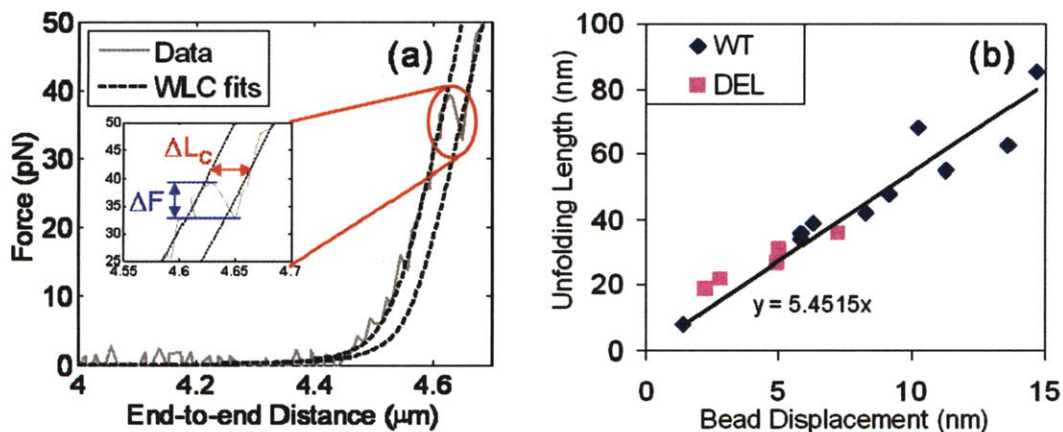


Figure 5.13 (a) A WLC model was fit to force-extension data before and after rupture events to determine the change in contour length (i.e. unfolding length), ΔL_c . The instantaneous bead displacement was found by dividing the drop in force, ΔF , by the trap stiffness. (b) A linear calibration curve was used to determine a correction factor between the unfolding length and the instantaneous bead displacement for the wild-type NM (WT) and the R Δ 2-5 NM (DEL).

Figure 5.14(a) shows the sequence of NM and the corresponding lengths of distinct subunits of the NM monomer. Figure 5.14(b) shows the unfolding length distribution for

the wild-type NM in the presence of 1.2M GdnHCl. The dominant extension units in both the stretching and holding phase were approximately 15 to 20 nm and multiples thereof. This roughly matches the length of the whole repeat region of the N domain (~9 residues per repeat x 0.34 to 0.4 nm per residue x 5 repeats = 15.5 to 18 nm), suggesting that the larger extensions from individual events could be due to simultaneous unfolding in two or three monomers. Figure 5.14(c) shows the unfolding length distribution of wild-type NM in the presence of 50 μ M DAPH. The first peak in the DAPH distribution similarly occurs at 15-20nm. Interestingly the second and third dominant peaks occurs at a slightly smaller unfolding lengths. This may be due to rearrangements in the folded structure caused by DAPH.

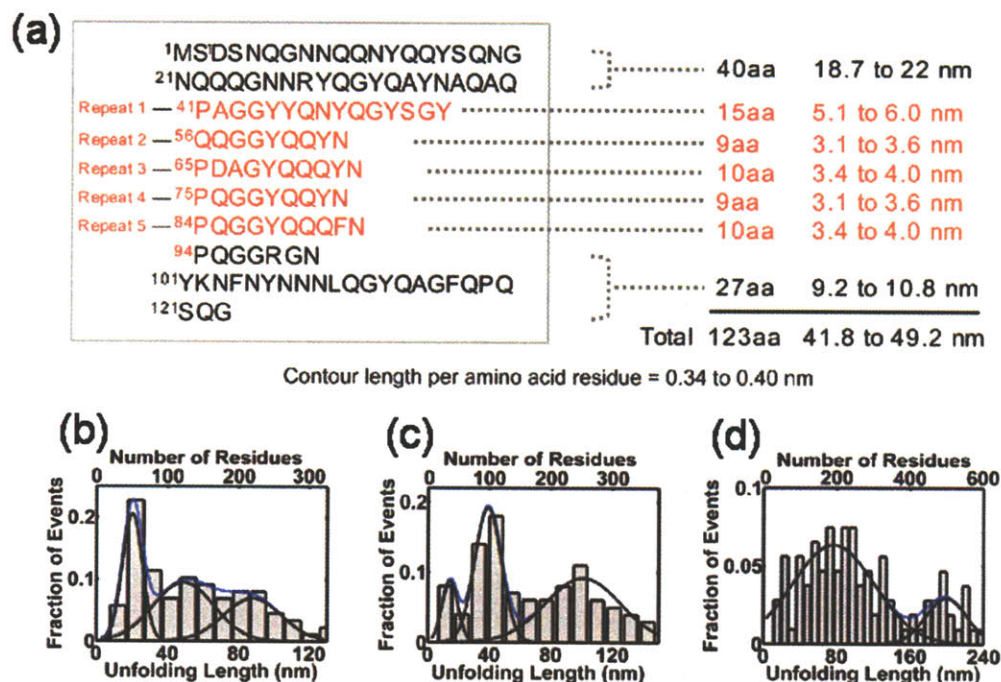


Figure 5.14 (a) The unfolding length distribution of wild-type NM in the presence of 1.2M GdnHCl. The dominant peaks occur at 15-20 nm and multiples thereof. (b) The sequence of the NM monomer is shown along with the corresponding length of distinct subunits of the NM monomer. The 15-20 nm length corresponds to the approximate length of the entire repeat region.

To test if the extension unit, 15 to 20 nm, indeed corresponds to the repeat region, we stretched an NM variant that was missing the last four repeats, referred to as R Δ 2-5. Although R Δ 2-5 alone can not induce and maintain prion phenotypes *in vivo*, R Δ 2-5 polymerization can be seeded *in vitro* by cell lysates containing strong prion elements. This produces R Δ 2-5 fibrils that were thermodynamically less stable than wild type as indicated by the melting curves in figure 5.15. The fluorescence intensity is indicative of the amount of monomer present. The wild-type NM exhibits melting temperatures of 57.8 °C and 76.8 °C for fibers reconstituted at 4 °C and 37 °C respectively, while the R Δ 2-5 fibers exhibit lower melting temperatures of 50.9 °C and 62.6 °C for fibers reconstituted at 4 °C and 37 °C respectively.

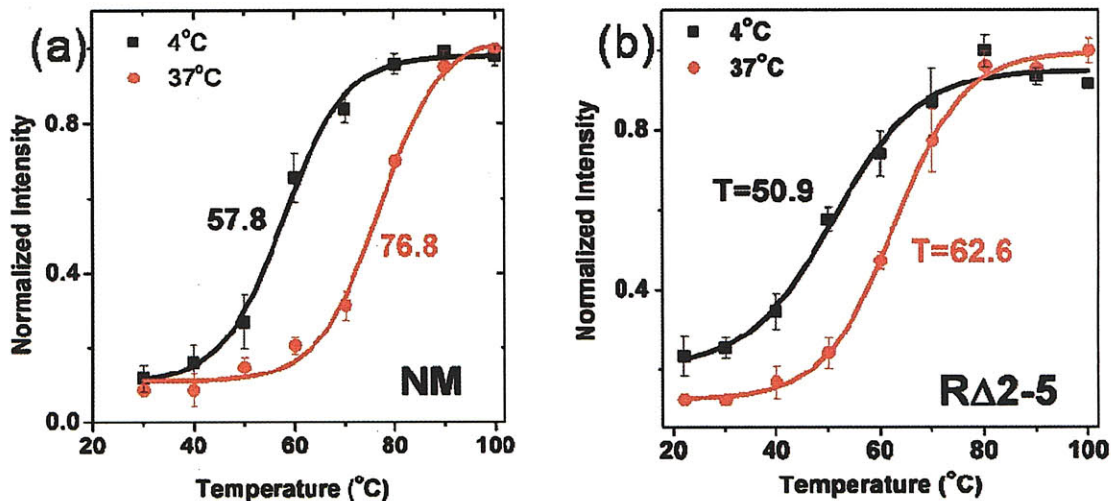


Figure 5.15 Melting curves for the wild-type NM (a) and R Δ 2-5 (b) fibers are shown. The fluorescence intensity is indicative of the amount of monomer present. The melting temperatures are shown on each plot for fibers reconstituted at 4 °C (black) and 37 °C (red)

To form tethers, we deposited wild type NM monomers on the glass surface and on the polystyrene beads as described above, anticipating that these monomers would recognize and recruit R Δ 2-5 fibrils. Formation of R Δ 2-5 fiber tethers was confirmed by

fluorescence imaging. R Δ 2-5 tethers were subjected to loading cycles as described above. Discontinuities in pulling traces were observed under normal assembly conditions, without the requirement for GdnHCl or DAPH. This result establishes that the thermodynamically less stable R Δ 2-5 fibrils are also mechanically less stable than their wild type counterparts. It also further confirms that the discontinuities in the pulling traces are due to unfolding events in the fibrils themselves and not to any property of the tethered monomers on the glass surface or the beads.

The dominant extension length of 15-20 nm for wild type NM fibrils was not observed when R Δ 2-5 fibrils were stretched (figure 5.14(d)), supporting the repeat region as the unfolding unit in the wild type fibrils. The unfolding of R Δ 2-5 fibrils gave rise to much larger and much broader distribution of extension lengths, indicating that in many cases R Δ 2-5 monomers must unfold simultaneously. The majority of these events occurred in the holding phase (constant high force regime), whereas unfolding with NM fibrils occurred equally in the stretching and holding phases. Second, many R Δ 2-5 fibrils ruptured after one unfolding event and no fibrils were able to sustain more than three unfolding events. In contrast, wild type fibrils typically sustained many unfolding events before rupture occurred (figure 5.9).

Since unfolding and rupture events with R Δ 2-5 fibrils were not complicated by the presence of the chemical modifiers, we used data obtained in the constant force regime (holding phase) to quantify the molecular interactions that underlie the mechanical stabilities of these fibrils. The lifetime of an interaction, τ , under a constant applied force,

F, can be described by Bell's equation, $\tau(F) = \tau_0 \exp(-\beta Fx^\ddagger)$ where τ_0 is the intrinsic lifetime under no load, x^\ddagger is the characteristic distance along the reaction coordinate to achieve rupture, and $\beta^{-1} = k_B T$. Rupture events showed a clear trend of a decreasing lifetime with increasing applied force. Figure 5.16(a) shows the lifetime of the intermolecular bonds where rupture occurs versus the applied force in the holding phase. Due to the large number of monomers in series contained in the fiber, the probability of rupture is much higher than for a single protein. In order to correct for this effect, the individual lifetimes of fiber were multiplied by the number of monomers. The number of monomers in a fiber was calculated using the contour length, and the length per monomer (estimated as 1.5 nm from the average of the two structural models shown in figure 5.4(a)). Figure 5.16(b) shows the rupture events Fitting the Bell model resulted in a τ_0 of 122 days and x^\ddagger of 0.13 nm after the contour length correction. This τ_0 is consistent with our observation that fibrils in flow channels lasted several weeks without any visible degradation. Unfolding events did not show any clear trend, likely due to the heterogeneous nature of the unfolding events.

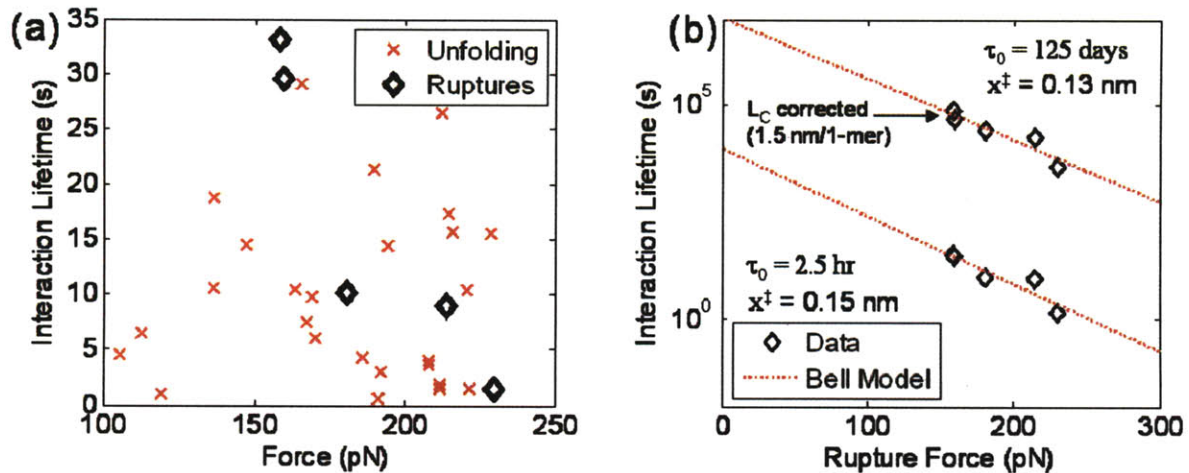


Figure 5.16 (a) shows the lifetime of folding (red x's) and intermolecular (black diamonds) interactions as a function of the force applied in the holding phase. Rupture events show a clear trend of decreasing lifetime with increasing force and therefore were fit with a Bell model to identify x^\ddagger and τ_0 . (b) shows the fitting results for the rupture events before and after the contour length correction. The contour length correction greatly increases the lifetime under zero load, τ_0 , but does not affect x^\ddagger .

5.4 DISCUSSION:

5.4.1 Physical Properties of NM Fibers. Physical characterization of the biologically relevant prion Sup35 has implications for the molecular structure, assembly, and pathological properties of amyloid fibers in addition to forward engineering and design of amyloid based nanomaterials. In this work novel experimental methods were employed to dynamically measure the physical properties of amyloid fibers in solution. The l_p of 4 °C fibers was found to be 1.5 μm reduced from force-extension measurements and 3.6 μm from a bending mode analysis of thermal fluctuations. The l_p of 37 °C fibers was found to be 7.0 μm measured by bending mode analysis. The 2.5 fold difference in l_p of 4 °C fibers as measured by thermal fluctuations versus that from force-extension is consistent with Smith et. al [7] who found a two-fold increase in the persistence length of insulin as measured by shape fluctuation analysis as compared to force spectroscopy

with AFM. Previous measurements of persistence length of amyloid fibers range from $\sim 0.3 \mu\text{m}$ [41] for fibers from terrestrial algae adhesive determined by force-extension experiments by AFM force spectroscopy, to $\sim 40 \mu\text{m}$ for insulin fibrils determined from shape analysis of surface bound fibers [7], up to a maximum of $\sim 300 \mu\text{m}$ for fibers formed from a short peptide fragment of transthyretin [19] also determined from a shape analysis of surface bound fibers. This comparison places NM fibers at the lower end of the spectrum of amyloid fiber mechanical properties. The reduced mechanical properties of Sup35 fibers suggest that they have fewer intermolecular interactions giving their axial and bending behavior and hence likely exhibit reduced stability compared to insulin, transthyretin, and A β fibers which supports the emerging hypothesis that fiber fragmentation efficiency is an important factor distinguishing prion from non-prion amyloids. The only previous measurement of l_p for Sup35 fibers reduced a persistence length of approximately $50 \mu\text{m}$ via AFM imaging of surface bound fibers [19]. However, these fibers were formed from a much smaller fragment of Sup35 (7 amino acids) than the NM fragment used in this study (253 amino acids). The smaller fragment likely adopts a non-physiological molecular structure during aggregation resulting in heightened mechanical properties. Furthermore, the surface deposition may alter the mechanical properties of the fibers. Both of our approaches, bending mode analysis by fluctuation imaging and force-extension measurement by optical trapping, have the advantage of making dynamic measurements on fibers in solution.

Our combined force-fluorescence approach enabled active measurement of the extensional stiffness of NM fibers in addition to their l_p . In general, the modulus of nano-scale fibers as measured in extension can be different from that reduced from bending data since distinct molecular level mechanisms may control these different deformations. For example, Liu et al found a factor of 3 difference in elastic moduli reduced by extensional stiffness versus bending stiffness [42]; and the steered molecular dynamics simulations of Keten et al [43] showed that amyloid fiber structures may have distinct mechanical properties in extension vs. in bending. Force-extension experiments on NM fibers assembled at 4 °C revealed a l_p of 1.5 μm and axial stiffness of K of 5600 pN. Assuming a solid cylindrical geometry and a diameter of 4.5 nm measured by AFM, we reduced elastic moduli of 0.26 GPa and 0.35 GPa from the l_p (bending) and K (extension) respectively. These values are a lower bound to the elastic modulus of NM fibers since the entire cross-section may not experience mechanical load [44]. These moduli are in good agreement suggesting that NM fibers have a structure where the same molecular interactions and deformation mechanisms govern both bending and axial mechanics.

Slight variations in the misfolded structure within a sample of fibers assembled at a given temperature result in inhomogeneous structure and physical properties. Specifically, there were distinct discontinuities in fiber morphologies resulting in either regions of static curvature or localized kinks in the morphology. The kinks could be due to competing interactions of neighboring monomers with mismatched polymorphic structures. Park et al, found that similar kinks form in amyloid fibers made from proteins

which can adopt distinct folded geometries of similar thermodynamic stability [44]. Another possibility is that the hinges form from locally unfolded regions creating flimsy domains where bending is very easy. However, this is unlikely because the measured hinge characteristic deformation energy ($\kappa_{\theta}\theta = 0.98 \cdot 10^{-19} \text{ N}\cdot\text{m}$) is large compared to $k_b T$, and the torsional stiffness ($\kappa_{\theta} = 1.02 \cdot 10^{-19} \text{ N}\cdot\text{m}/\text{rad}$) is even comparable to some actin cross-linking proteins such as Arp2/3 ($\kappa_{\theta} = 0.8\text{-}1.3 \cdot 10^{-19} \text{ N}\cdot\text{m}/\text{rad}$) [45]. The mechanical properties of fibers also showed large variations due to static inhomogeneities while the force-extension behavior of individual fibers was highly repeatable. Diameter measurements of the 4 °C fibers give significant variation with $d_4 = 4.5 \pm 0.7 \text{ nm}$ indicating that molecular interactions may occur over a cross-sectional area that varies from fiber to fiber. Assuming a solid cylindrical model, this variation in diameter would correspond to an I_p of $1.5 \pm 0.7 \mu\text{m}$ which is in excellent agreement with the standard deviation in I_p of $0.6 \mu\text{m}$ measured by force-extension indicating that the molecular interactions imparting elastic properties are similar in nature for a fiber sample, and variations in physical properties arise from deviations in misfolded geometries.

The physical differences between 4 °C and 37 °C are also due to NM polymorphism as indicated from AFM measurements of diameter which resulted in $4.5 \pm 0.7 \text{ nm}$ and $5.2 \pm 0.6 \text{ nm}$ for the 4 °C and 37 °C fibers respectively. The overlap in diameter is consistent with the overlap we see in the distribution of persistence length (see figure 5). Based on these diameters and the persistence lengths determined by the bending mode analysis of thermally fluctuating fibers, we calculated elastic moduli of $E_4 = 0.75 \text{ GPa}$ and $E_{37} = 0.80 \text{ GPa}$. These moduli are in excellent agreement indicating that the

difference in persistence length is due to the different diameters of polymorphic structures while the underlying molecular interactions providing the stiffness of the fibers are similar. Hence, prion strain diversity is conferred by variations in folded structure configurations instead of distinct molecular interactions. NM self assembly at 37 °C results in a significant fraction of fibers that have cross-links and kinks with overlapping monomers, whereas the 4 °C fiber contained none. The disparity in microstructure indicates that fibers may polymerize by distinct self-assembly pathways. In particular the 37 °C assembly pathway seems to leave fibers susceptible to inter-fiber cross-links along the length of the fiber and possibly at the ends in addition to showing increased adhesion along the length of the fiber to NM coated beads. The physical differences in the fibrous network structures (i.e. chemically cross-linked versus physically entangled) could contribute to the phenotypic diversity seen in cells infected with NM fibers.

Using combined force-fluorescence microscopy provides an accurate and thorough characterization of NM fiber physical and mechanical properties. The reduced elastic moduli range from 0.26 GPa to 0.80 GPa, which can be altered by assembly temperature, placing NM fiber mechanical properties near those of spider silk (1-10 GPa [46]). However, amyloid fibers have the distinct advantage over spider silk and several other biopolymers in their relative ease of synthetic assembly from a very wide range of proteins and organisms, here in yeast, making these fibers very attractive for a simply manufactured nanomaterial. Furthermore, many amyloid fibers including the NM fibers studied here are easily functionalized [10, 47] providing a means for interfacing with other biological or synthetic materials for applications such as biosensors, or cell

scaffolds [9]. We identified fiber assembly temperature as a new means for tuning mechanical properties and fiber structure. The fact that 37 °C fibers form inter-fiber cross-links while 4 °C fibers do not also indicates that higher level network architecture can be stabilized via fiber assembly temperature. Our measurement of torsional stiffness of the cross-links is useful for predicting mechanical properties of these network structures.

In summary, we have characterized the physical micro-structure and mechanical properties of amyloid fibers formed from the widely studied amyloidogenic N-terminal fragment of the yeast strain *saccharomyces cerevisiae* protein Sup35. We report the first experimental measurements of the extensional stiffness of amyloid fibers and of torsional stiffness of fiber kinks and cross-links. We have identified assembly temperature as a potential means to manipulate fiber physical properties, and we identified the physical consequence of amyloid fibers that are self-assembled from polymorphic misfolded proteins pointing to a structural basis for the phenotypic diversity conferred from a single prion protein, Sup35. Our results give valuable insight into the molecular aggregation process and provide useful guidance and insights for design of amyloid based nanomaterials and prion disease targets. The experimental methods we have developed are robust and can be adopted to study the structure-function relations of a wide variety of amyloid fibers and other biopolymers.

5.4.1 Molecular Interactions of Yeast Prion Proteins. Within fibrils of a single phenotypic type we discovered two regions with distinct mechanical stabilities. Failure of

one region (which evidence indicates is the repeat region) results in increased contour length; failure of the mechanically stronger region causes rupture. That a segment that comprises roughly half of the amyloid core can unfold without disrupting the intermolecular contacts and, in fact, that these contacts remain so strong that they are broken only in the presence of amyloid destabilizers under very high pulling forces, is wholly unexpected. By chemical denaturation and thermal denaturation the melting curves of these same fibrils exhibit a single cooperative unfolding transition.

A full explanation, of course must await a detailed picture of prion structure. This is inherently an extremely difficult problem, and is as yet unsolved. However, in the light of a previously proposed model the data might provide an important insight. In the beta helix-like model, two discrete sequences at the termini of the amyloid formed by the N domain are in self-contact (head-to-head and tail-to-tail) and simple geometry dictates that the beta strands at these interfaces are antiparallel to each other. The region between them, largely composed of the repeat segments, is sequestered from intermolecular interactions and consists of parallel beta strands. The two phases of transition from our mechanical data could easily derive from the distinct structural features of the inter-molecular and intra-molecular contacts. More importantly, the unfolding of two neighboring intra-molecular regions would cause an immediate topological reorientation of the intermolecular beta strands relative to the pulling force (from perpendicular to parallel). This would mean that breaking the intermolecular interface would require the shearing of beta strands (which necessitates the concerted breaking of many hydrogen bonds), rather than their stepwise unzipping that would be

expected for unfolding of the intramolecular region. Shearing beta strands requires much stronger mechanical forces than unzipping them (18, 35). The transition distance (x^\ddagger of 0.13 nm) we detected for rupturing prion fibers is strikingly similar to previously determined beta strand shearing transitions. The mechanical properties of β -helical proteins have recently been the subject of computational simulations. These have yielded a persistent length on the order of a few micrometers, comparable with our measurements and predicted a reorientation of the beta strands after partial unfolding. Remarkably then, even if the intermolecular strands have similar chemical stability to the intramolecular strands, the unfolding of the latter, followed by reorientation, would strongly increase the fibrils mechanical stability.

An increasing number of functional amyloids have been identified in recent years and many of their functions rely on their mechanical properties. For example, the formation of amyloids in biofilms provides a remarkably strong mechanism of adhesive in many organisms. The method we have developed should be readily applicable to these proteins and will facilitate our understanding of their functions, enhance our ability to control them, and accelerate the application of protein-based nanostructures for the fabrication of new materials and devices.

5.5 Appendix 5A: EXPERIMENTAL METHODS

5.5.1 Protein Purification and Labeling. Wild type NM or NM with a single cysteine mutation at amino acid position 184 were cloned in the pNOTAG expression constructs (with no exogenous N- or C-terminal purification tags or epitopes). Proteins were purified as described in [48]. NM monomers with a single cysteine mutation were labeled with either fluorescent dye or biotin following the manufacture protocols. In short, NM cysteine mutants (100 μ M) were incubated in 6 M GdnHCl with 2mM Alexa Fluor 555 C2 maleimide (Invitrogen) or 2mM Maleimide-PEO2-Biotin (Thermo Fisher Scientific, Rockford, IL) overnight at 4°C and purified using desalting columns.

5.5.2 Fluorescence Imaging of Morphology. Fibers were reconstituted *in vitro* from purified NM protein at 4 °C or 37 °C in 1xCRBB buffer (5mM potassium phosphate, 150mM NaCl and 5mM TCEP). 50% of the monomers used in reconstituted fibers were fluorescently labeled with Alexa555. To provide a uniform form of NM fibrils with defined structural and biological properties, we seeded the assembly reaction at 4°C by crude lysates of yeast cells with a strong [PSI+] phenotype, while seeding the reaction at 37°C by crude lysates of yeast cells with a weak [PSI+] phenotype. The preformed fibers were then sandwiched in between two 20 x 40 mm PEG (5000 MW – Laysan Bio.) coated coverslips at a concentration of ~ 10-100 nM. A volume of ~1 μ l resulting in a sample height of ~ 100 nm was used in order to constrain fiber fluctuations to a 2D imaging plane. Fibers were visualized with a Nikon TE2000 microscope using a 1.45 TIRF objective using epifluorescence excitation with a 532 nm laser. Images were recorded on a back-thinned EMCCD camera (ANDOR).

5.5.3 Fluorescence Imaging of Thermal Fluctuations. Dynamic thermal fluctuations of the fiber shape were monitored using a similar sample geometry with a series of 250-300 frames recorded at ~ 5 Hz. For the bending mode analysis, the filament in each image of the sequence was skeletonized, smoothed, and the tangent angle, ϕ , was calculated as a function of arc length, s , by fitting a cubic spline to the skeletonized fiber. A fourier series was fit to the s - ϕ waveform and the variations, σ_j^2 , in the amplitude coefficients a_j were computed for each mode j . Following the approach of Gittes et al [29] which is summarized in section 2 of the Supplemental Information, the bending stiffness, κ_B , was calculated using equation (5.18).

$$\sigma_j^2 = \frac{k_b T}{\kappa_B} k_n^2 \quad (5.18)$$

where the wave number k_n is defined as $L_C/n\pi$. In general, the first mode was not well resolved due to the long time it took for the 1st mode to fluctuate, and the higher modes (usually > 7) were not resolved due to the resolution of the fluorescence measurement (~ 500 nm). We therefore used a simultaneous fit of modes 2-8 that appeared to follow a linear trend with a slope of 2 on a log-log plot of σ_j^2 vs k_n (See supplemental figure 2) to determine κ_B , and then calculated l_p from the equation $l_p = \kappa_B/k_b T$.

The torsional stiffness of the hinge domains was determined using identical sample geometry and image processing as described previously. The hinge angle was

determined by manually fitting lines to the skeletonized fiber and then visually confirmed using the fluorescence image (see figure 5(c)). The fluctuations in hinge angle were then related to the hinge torsional stiffness using the equation $k_b T = \kappa_\theta \langle \theta^2 \rangle$ [31, 32].

5.5.4 Force-extension with Fluorescent Imaging. A tethered fiber assay was developed in order to perform force-extension experiments on single amyloid fibers. Experiments were carried out in a flow chamber made of a glass cover slip attached to a glass microscope slide via double-sided sticky tape to create a channel of approximately 10-15 μl in volume. Individual His-tagged NM monomers were flown into the channel at 0.5 μM and incubated for 15 min to allow for non-specific adsorption to the glass cover slip surface. 5 mg/ml Casein (Sigma-Aldrich) was then flown into the channel and incubated for ~ 40 min to cover the remaining exposed cover slip surface and prevent further non-specific interactions with the glass. Preformed fibers with 50 % fluorescently labeled NM monomers were flown into the chamber at a concentration of 0.5 μM and incubated for 30 minutes. These fibers attached to the NM monomer on the surface via NM self-recognition. When no NM monomers were deposited on the surface we found < 1 fiber per field of view ($\sim 15 \times 15$ mm) as opposed to ~ 5 fibers per field of view when NM monomers were present on the surface. 800 nm streptavidin coated polystyrene beads (Spherotech) were coated with both biotinylated NM monomers and Alexa488 fluorescent markers (Invitrogen) by incubating 10 μl of pre-washed beads at 1% w/v with 500 μl of 5 μM biotinylated NM and 0.2 μM Alexa488 for 40 minutes at room temperature, 22 $^\circ\text{C}$. These NM coated beads were then washed and flown into the flow channel and incubated overnight to allow beads to attach to free

fiber ends again via self-recognition. Slides were washed with 200 μl of assembly buffer between incubation steps, and after the final bead incubation slides were washed with 400 μl of assembly buffer to remove any free fibers and beads from the flow channel. This protocol resulted in fibers tethered to the cover slip surface at one end and an 800 nm polystyrene bead at the other end.

Beads were initially centered over the cover slip attachment point where they experienced negligible load due to the fiber and then subjected to position and stiffness (equipartition method) calibrations as described in chapter 1. Force-extension experiments were then performed using the bead and cover slip as handles by holding the bead in the stationary optical trap and moving the cover slip attachment point via a piezoelectric sample stage. Prior to each pulling experiment, the tethered fiber and bead were fluorescently imaged to confirm the single fiber assay and to identify fiber microstructure. For each fiber 4 unloading and 4 loading curves were collected – 2 in the x-direction and 2 in the y-direction yielding 8 force-extension curves.

To determine fiber morphology and boundary condition fibers were fluorescently imaged during deformation using the same fluorescence excitation as previously described. However, fluorescence and excitation lasers were cycled out of phase at 50 kHz with a 10 % duty cycle lag time in between to allow excited electrons to return to their ground state. In the case of the pinned boundary condition, all 8 were fit to equations (5.7)-(5.9) to determine l_p , L_C , and K by minimizing the sum-squared error between the model prediction and the data. The resulting parameters were averaged to obtain

representative mechanical properties for each fiber. In general, the force-extension behavior was highly repeatable for loading and unloading in all directions for pinned boundary conditions.

Because clamped fibers showed direction dependent mechanical response, only the two force-extension curves (loading and unloading) in the direction of the surface attachment point were used to be consistent with the assumptions of the WLC model, and the data were fit to equation (5.7a)-(5.9). If the fiber was determined to have a hinge, the apparent persistence length was determined using equation (5.10). When fitting the hinged fibers to equation (5.17), the geometrical parameters, L_1 , L_2 , and θ_0 were determined from the fluorescent images taken prior to the force-extension experiments.

5.5.5 Unfolding and Rupture of Prion Molecular Interactions. A similar force-extension assay was used to probe the misfolding and aggregation interactions of NM proteins. However, an optical trap capable of exerting forces up to 250 pN was used in an attempt to rupture fibers. A schematic of the trap layout is shown in Chapter 1 (figure 1.10). The capacity of the trap to achieve 250 pN was confirmed using the force extension behavior of the amyloid fibers as an internal control. Fibers were subjected to force extension as described in section 5.5.4. A WLC model was fit to the data for low forces (< 50 pN corresponding to a bead displacement of < 50 nm where the trap is linear) to extract l_p , L_C , and K . These parameters were used to predict the force applied to the bead by the fiber at larger bead displacements. This enabled characterization of

the trapping force as function of bead displacements up to ~ 300 nm (limit of the detection region). Figure 5.17 shows one representative curve confirming that the trap is capable of applying forces up to ~ 250 pN.

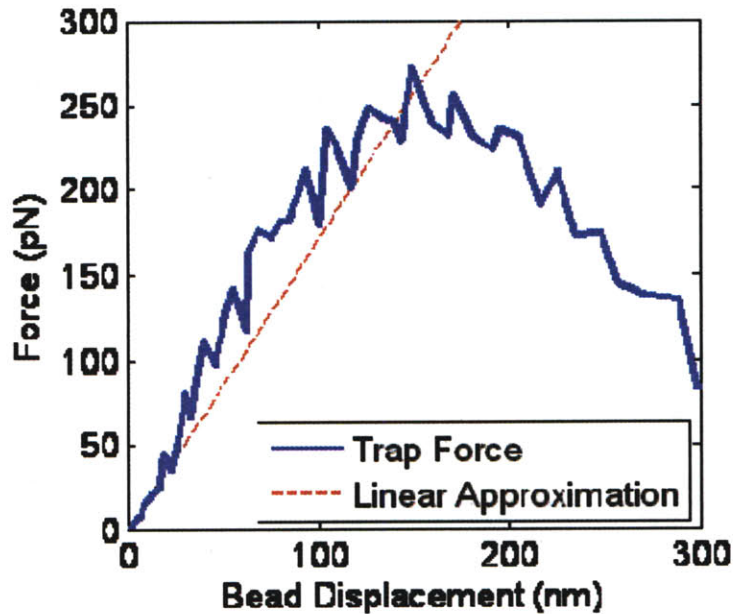


Figure 5.17 The trap force as a function of bead position was determined using the WLC force-extension behavior of amyloid fibers to predict trap forces at bead displacements greater than 50 nm. The linear spring approximation using the trap stiffness is also shown.

Beads were trapped using the primary branch of the laser trap (see figure 1.10) and centered over the surface attachment point and then subjected to a position calibration. The primary branch of the laser trap passes through two AODs (one for each axis) which are employed for the position calibration. These AODs result in ~50% power loss. In order to avoid this power loss, the bead was exchanged between the primary trap branch and the secondary trap branch (previously aligned with the primary branch) which has minimal power losses. Since both the primary and secondary branch come from the same laser source, they diameter, shape, and mode of the laser should be

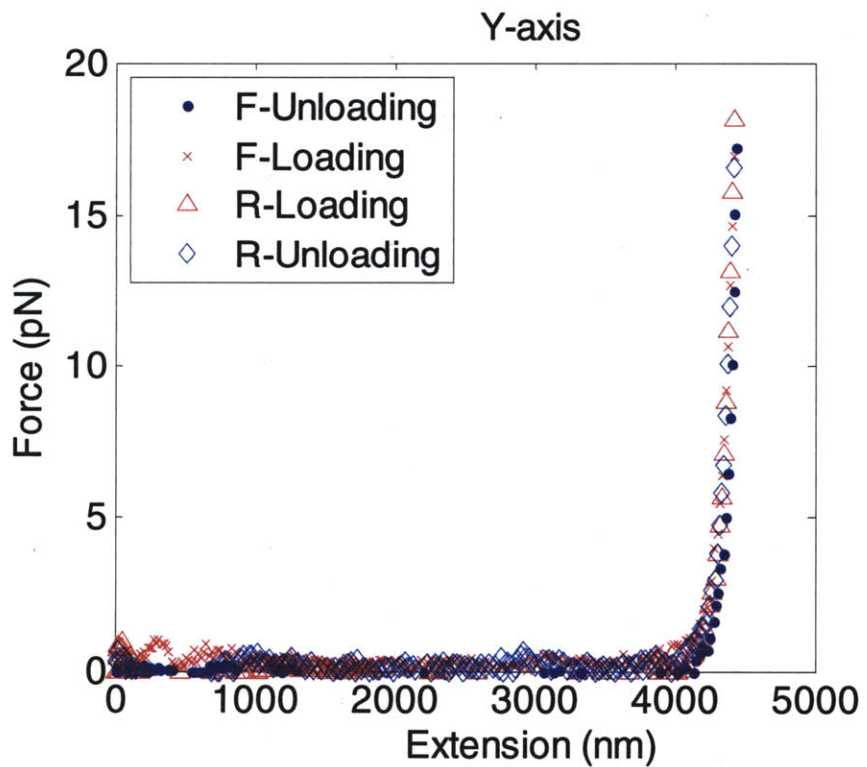
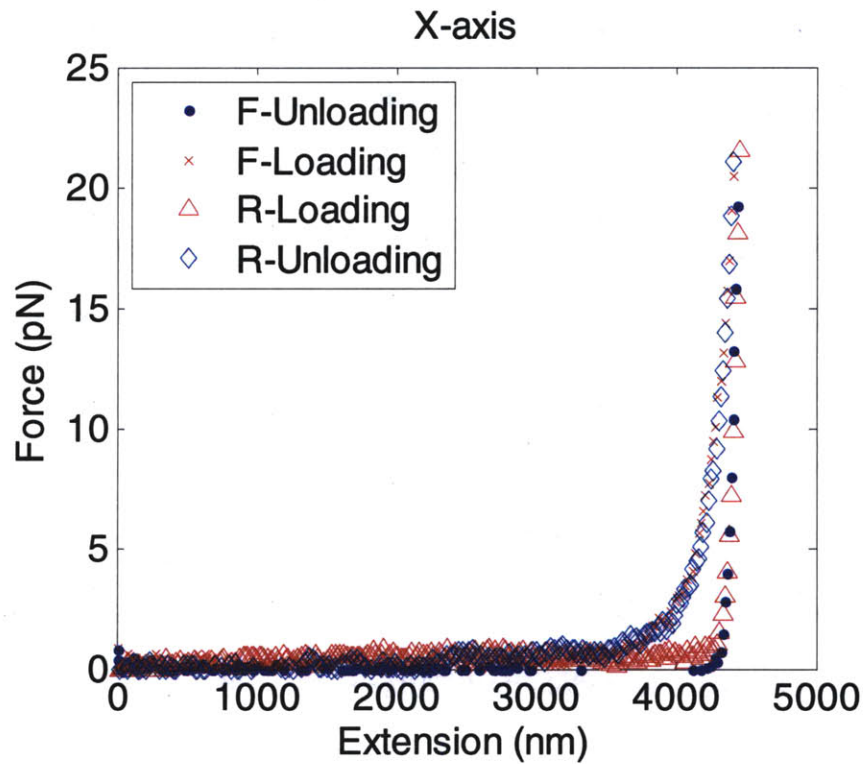
equivalent. The secondary trap branch was then subjected to a stiffness calibration and was used for subsequent force extension experiments.

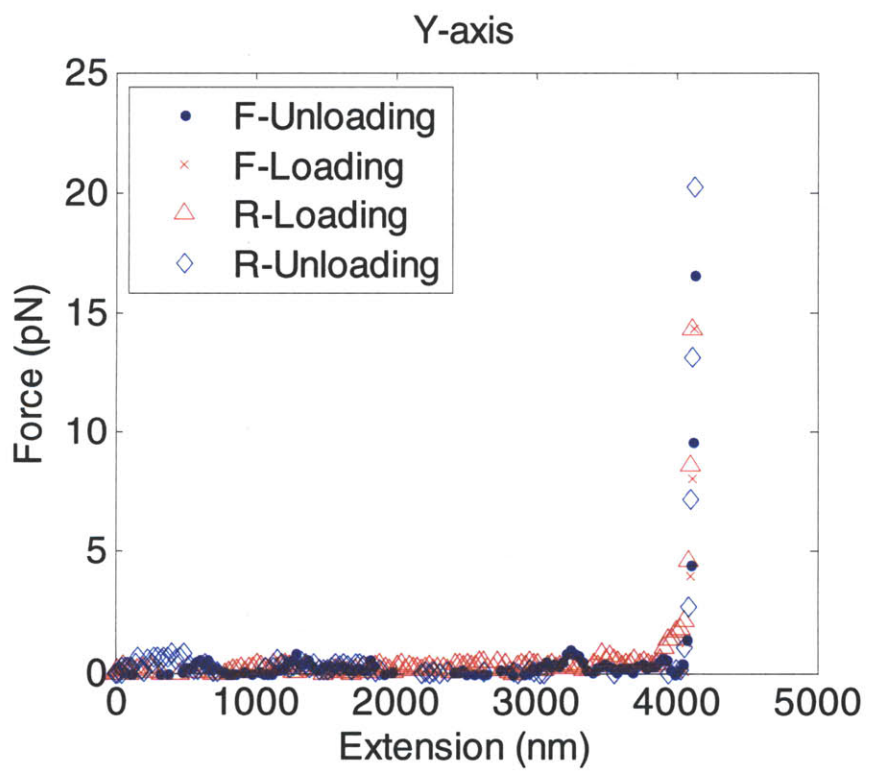
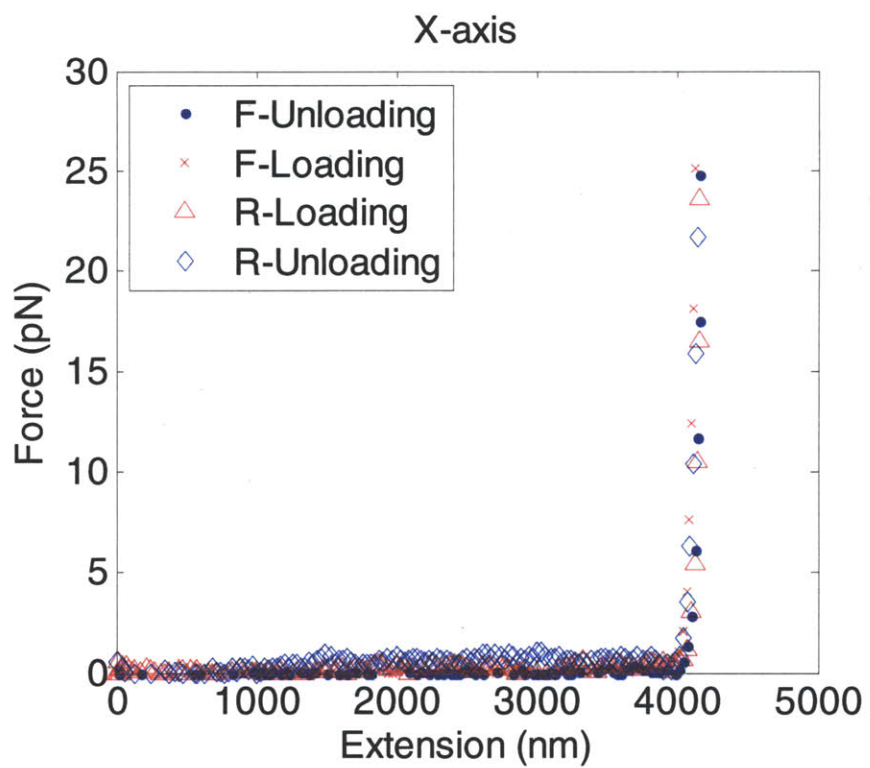
5.5.6 Imaging of Fibers after Rupture Events. The loading-unloading protocol was adjusted when attempting to image fragments of the fiber remaining on the surface after rupture. In order to avoid trap accelerated photobleaching, the centering process was forgone. The bead was trapped and the microscope stage was moved to align the fiber along the pulling direction near its fully extended length. The fiber was briefly exposed to fluorescence excitation in order to image its fully extended length. The fiber was then extended by moving the piezoelectric stage in small incremental distances until a significant force on the bead was detected. The fiber extension was held at that position until a rupture event was detected. After rupture, the fiber was again exposed to fluorescence excitation in order to image the fragment remaining on the surface.

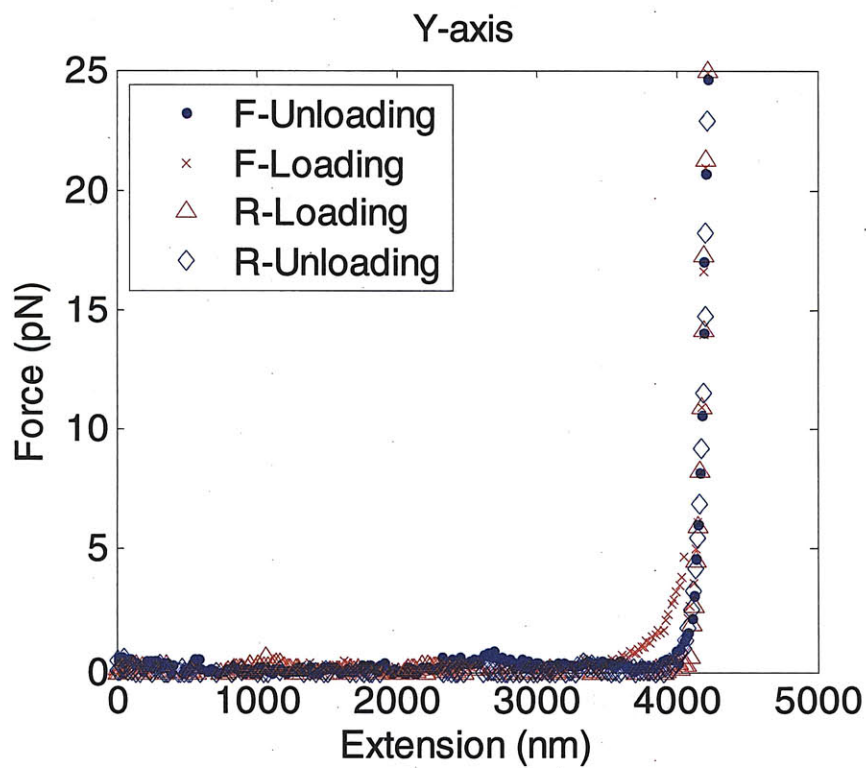
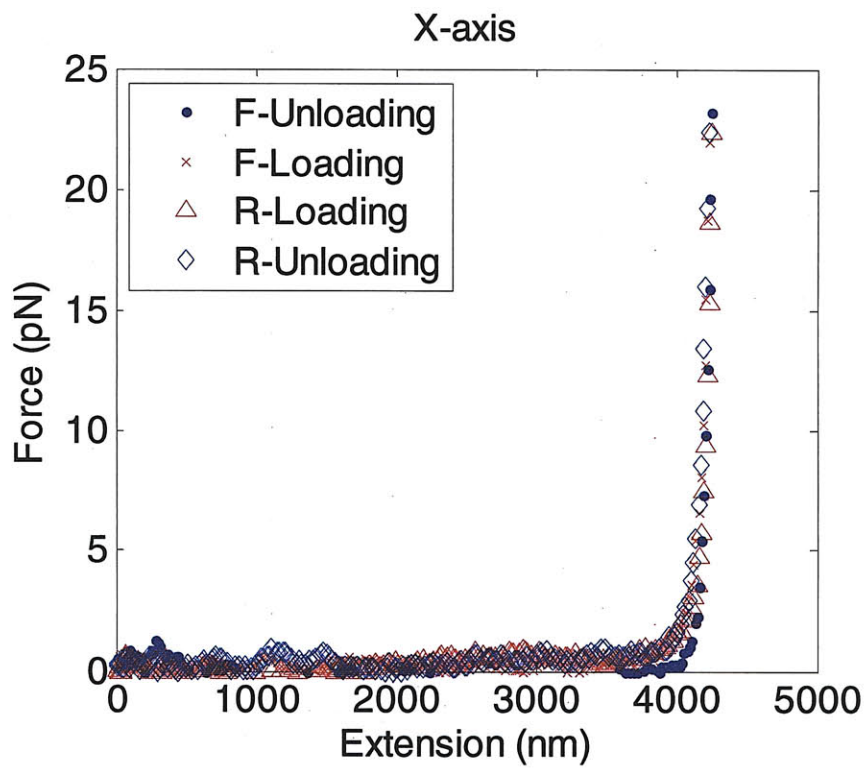
5.5.7 Melting Curves of NM and R Δ 2-5 Fibers. Aliquots of fibril solution were mixed with protein loading buffer (containing 2% SDS) and then incubated at indicated temperature (ranging from 30 to 100oC) for 15mins. The samples were then loaded and run on 10%SDS-PAGE gel. While monomer ran into the gel, oligomers and fibers were retained in the loading well. The gel was stained by Coomassie blue. The intensities of the monomer bands were quantified and normalized to the band intensity of pre-assembled protein solution.

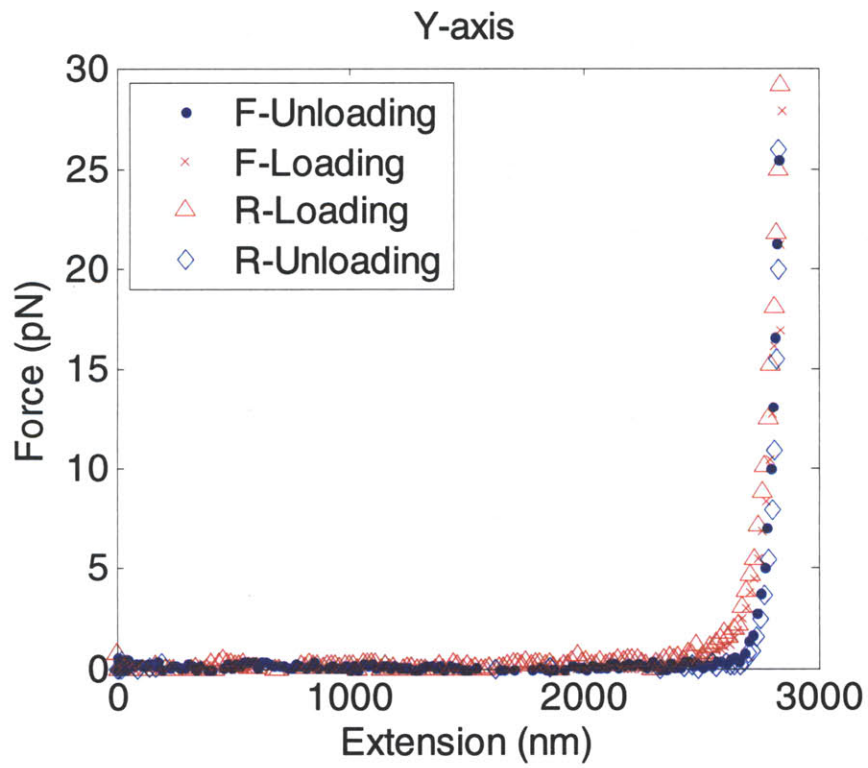
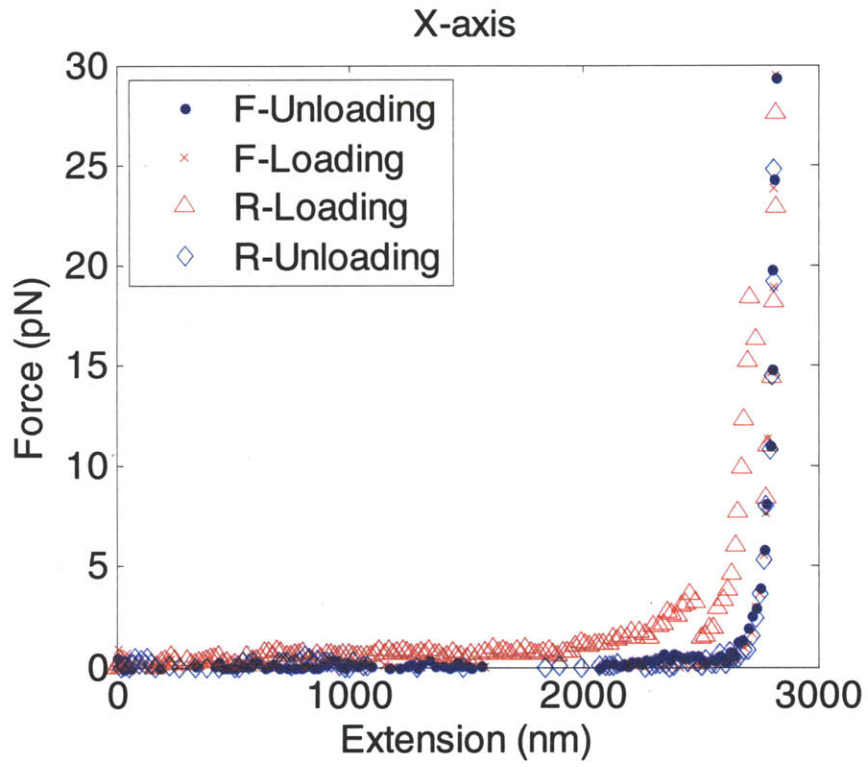
5.6 Appendix 5B: Sample Amyloid Fiber Data Curves

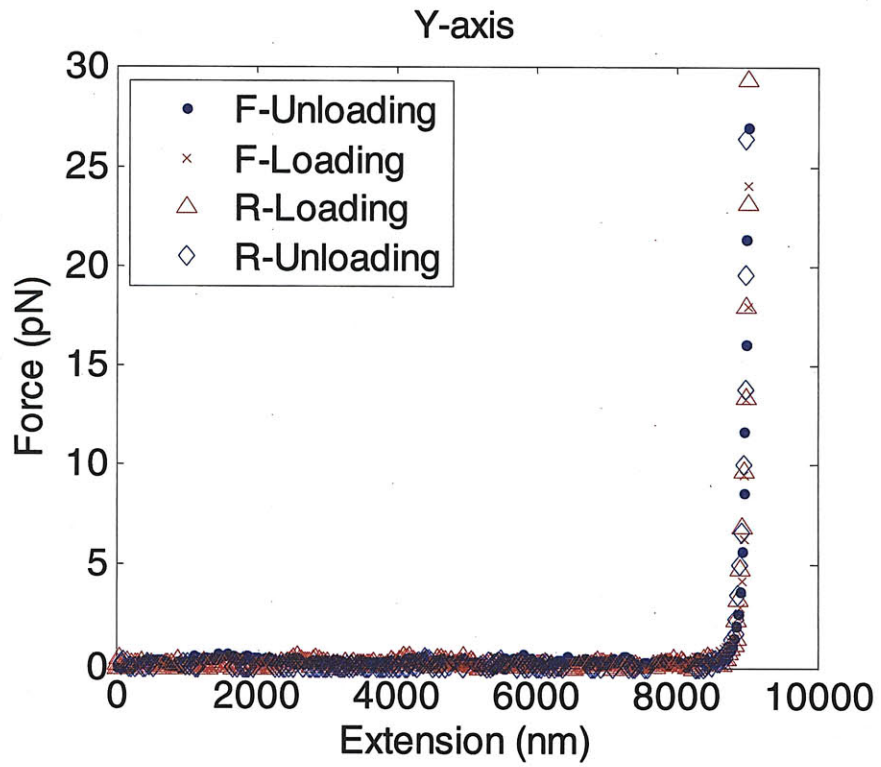
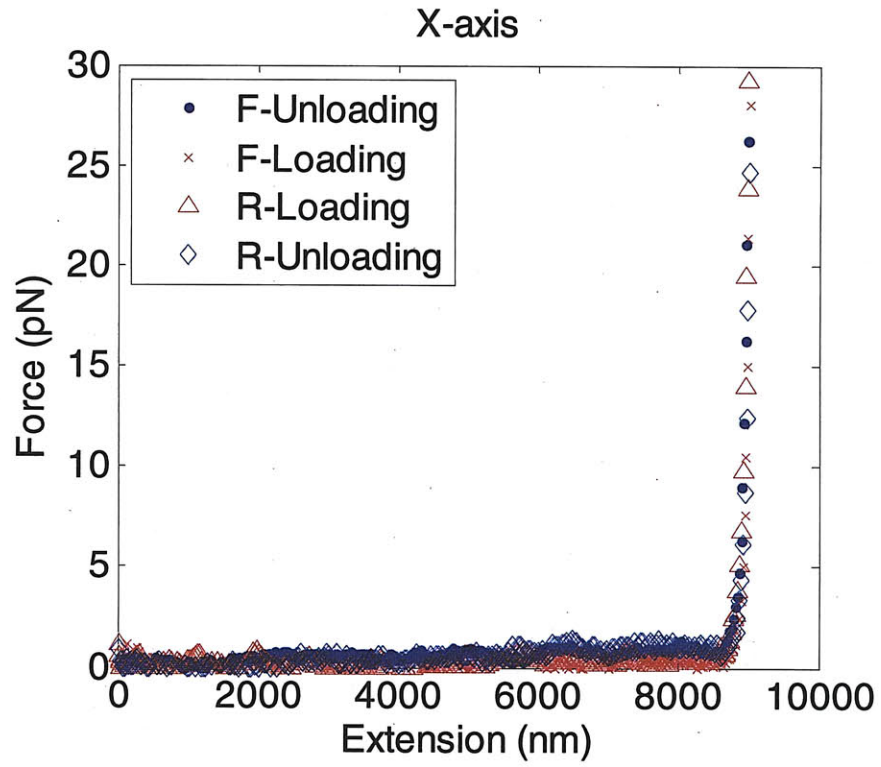
5.6.1 Force-extension Curves.

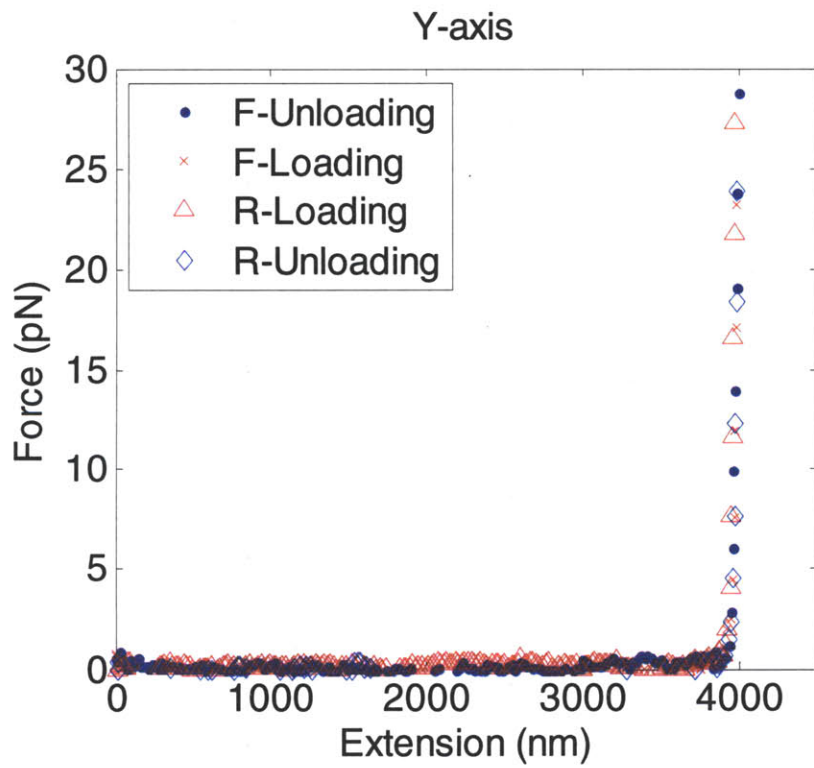
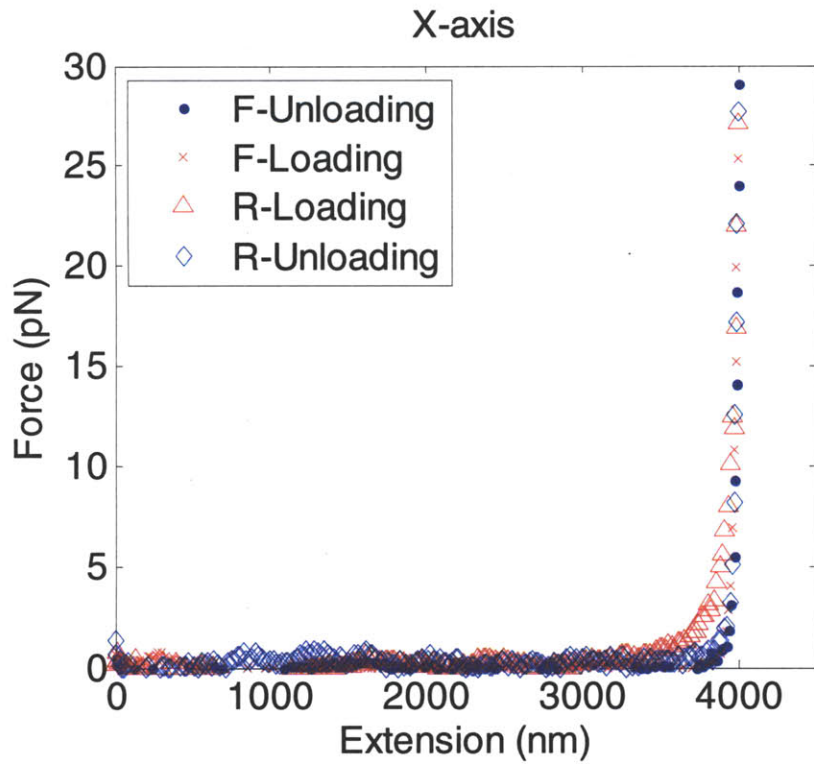


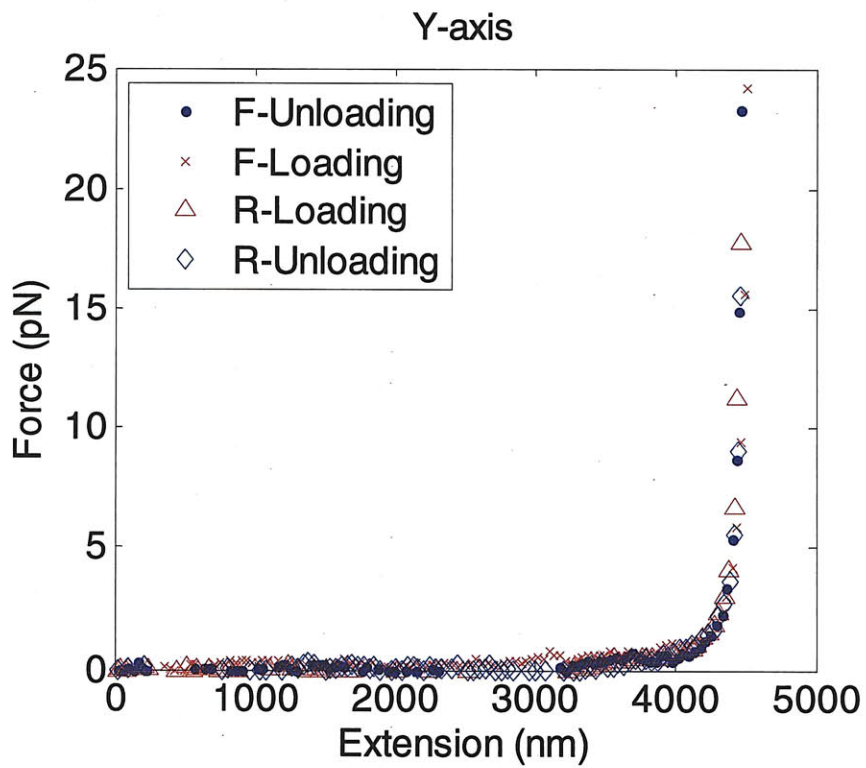
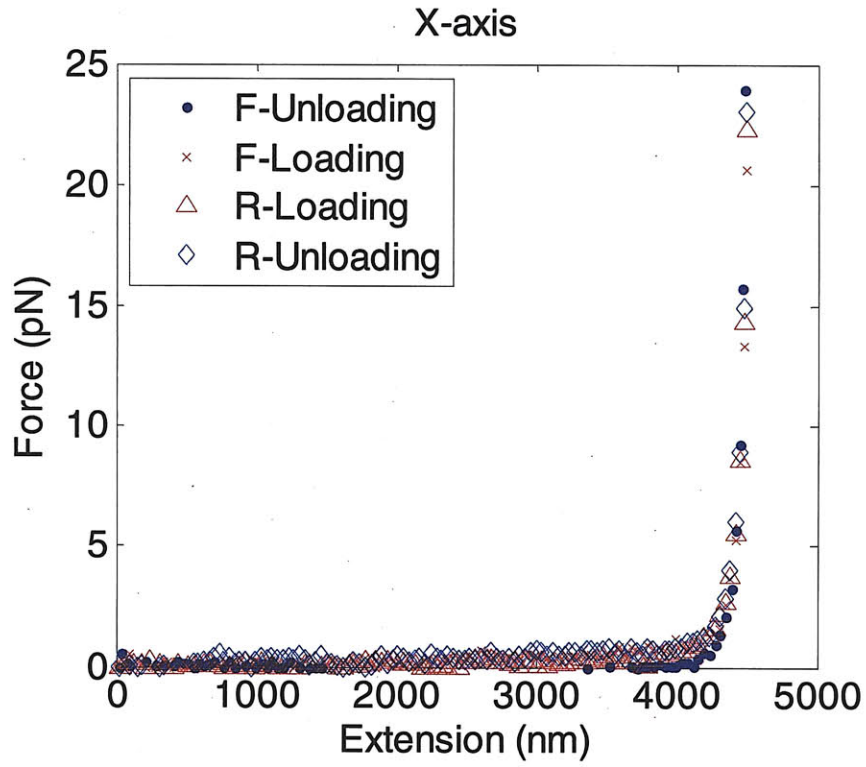


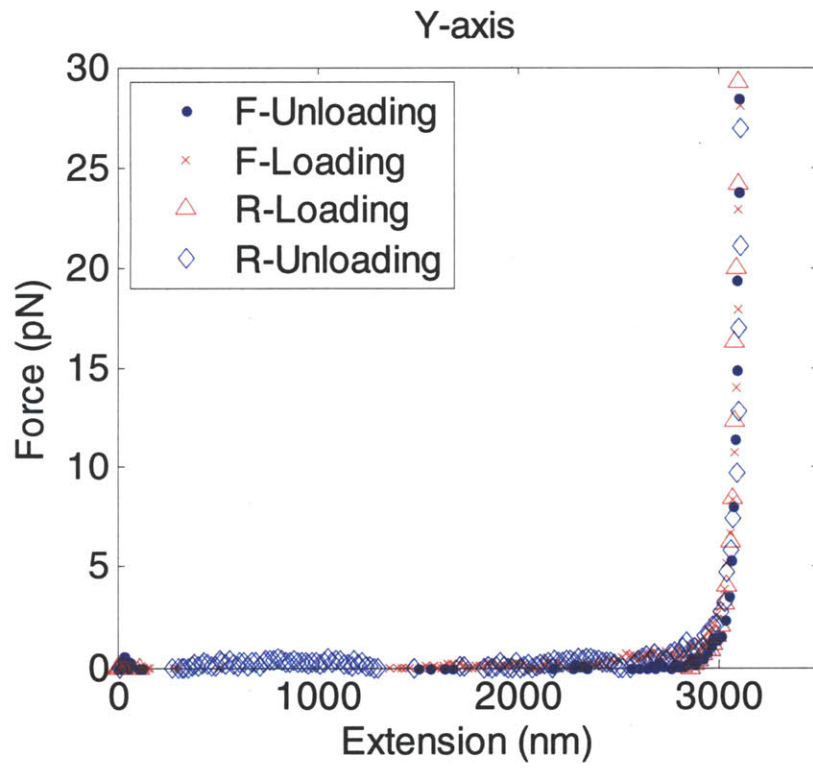
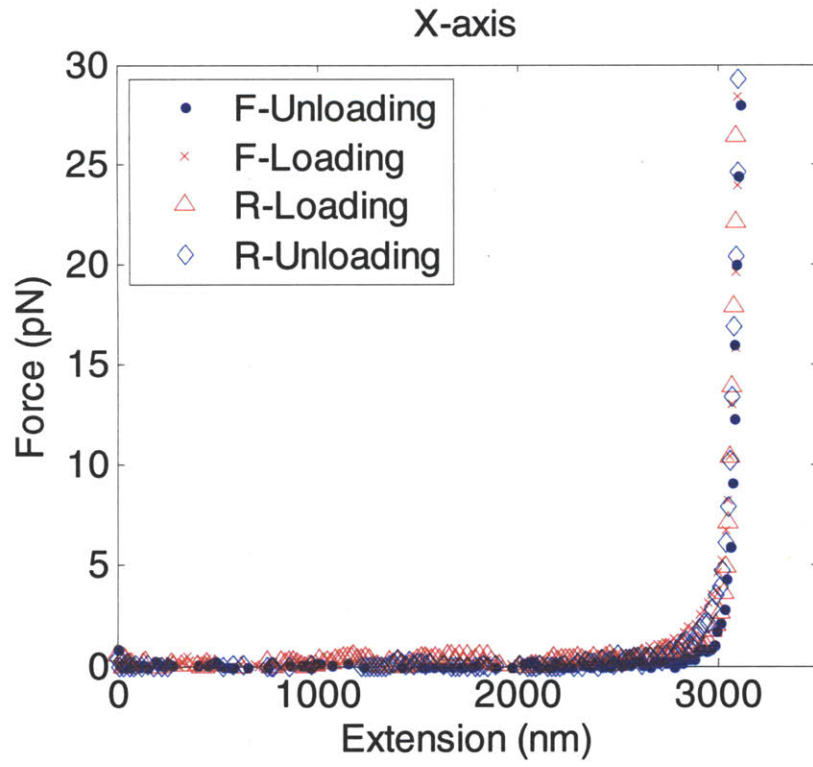


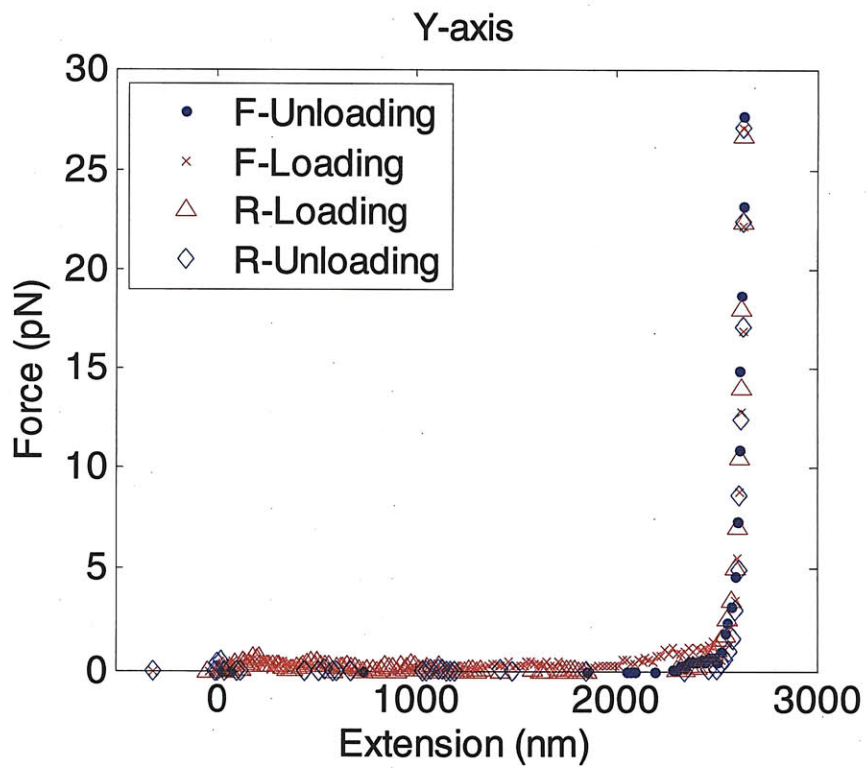
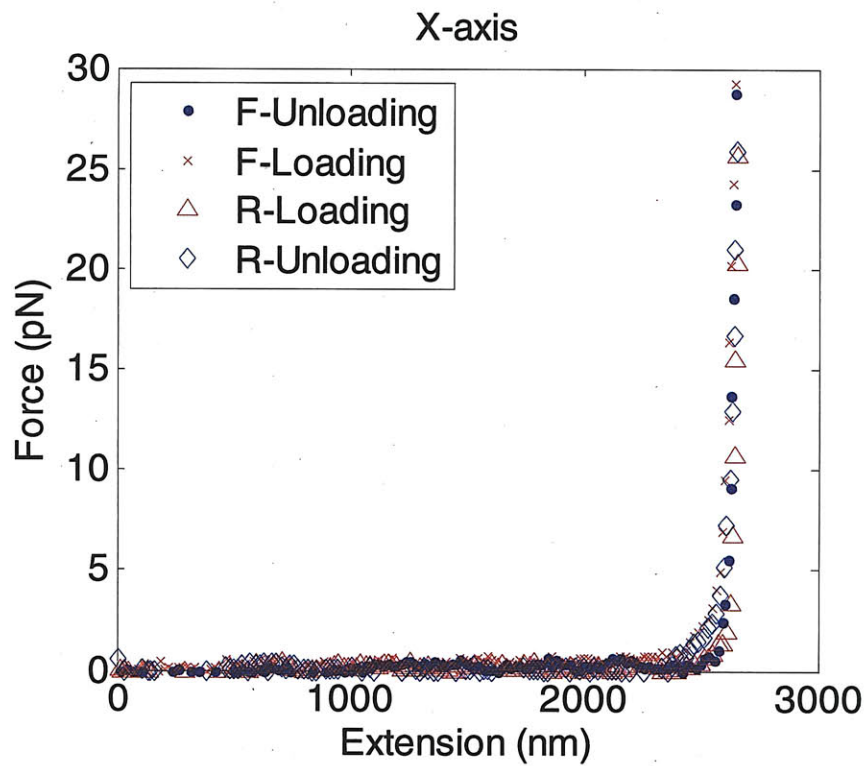


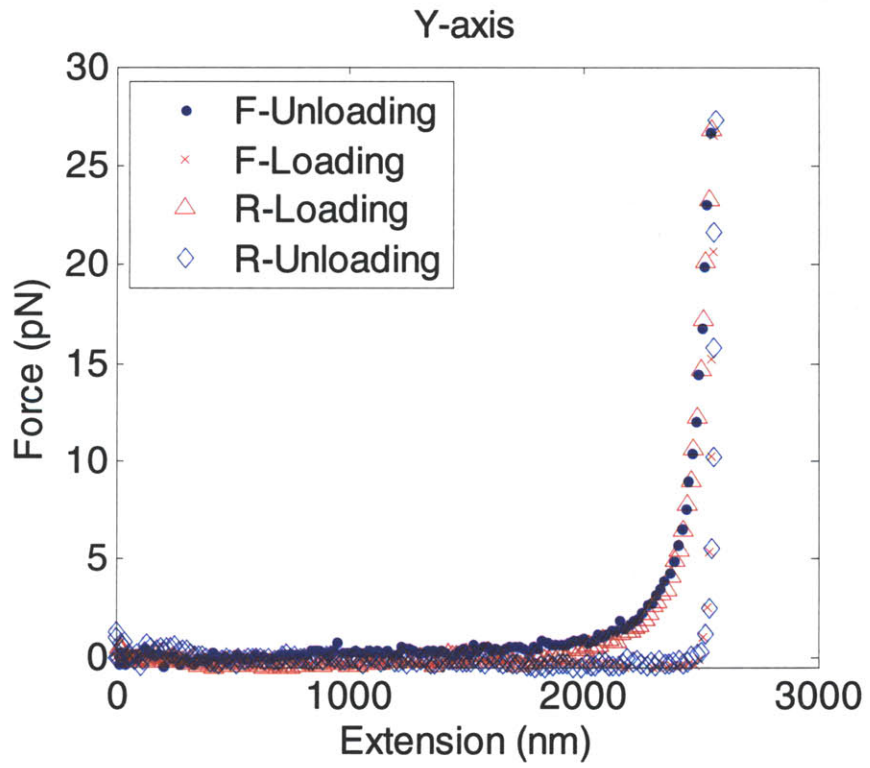
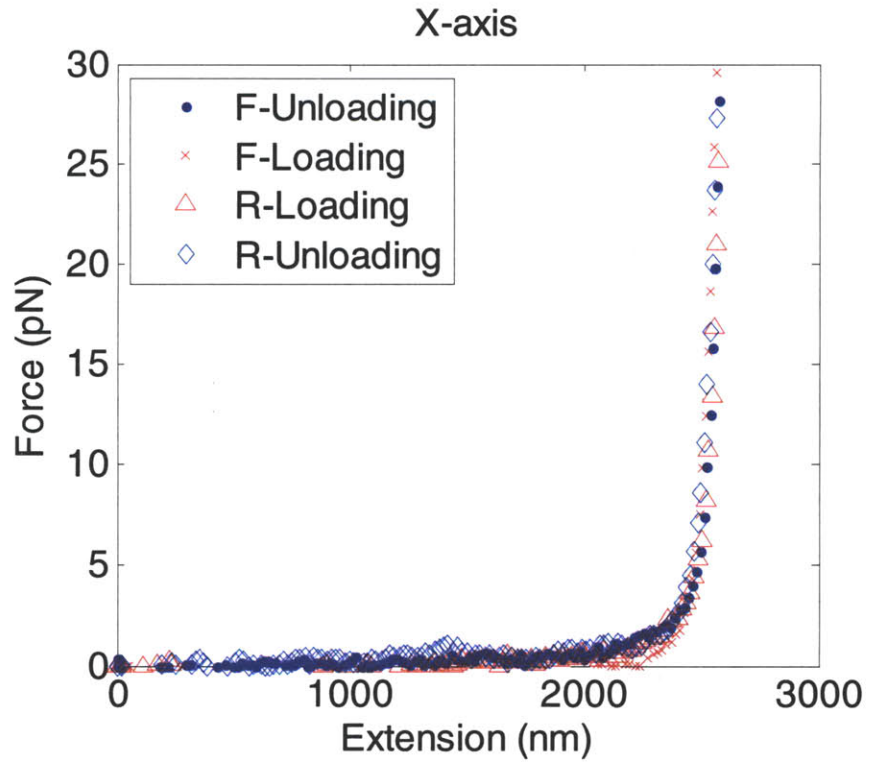




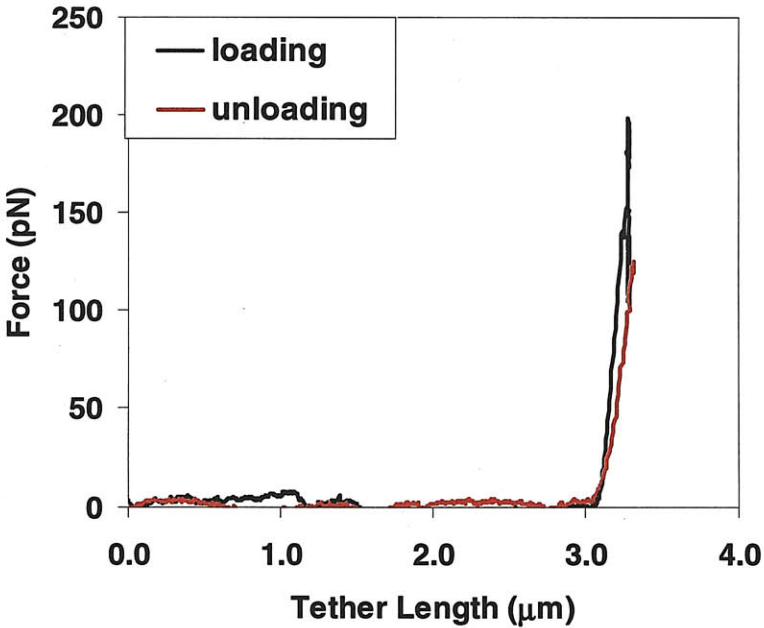
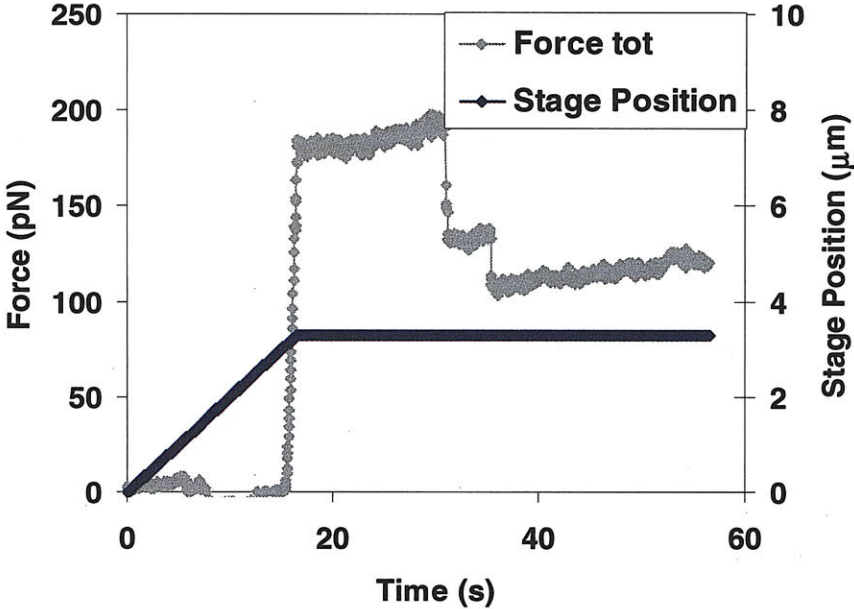


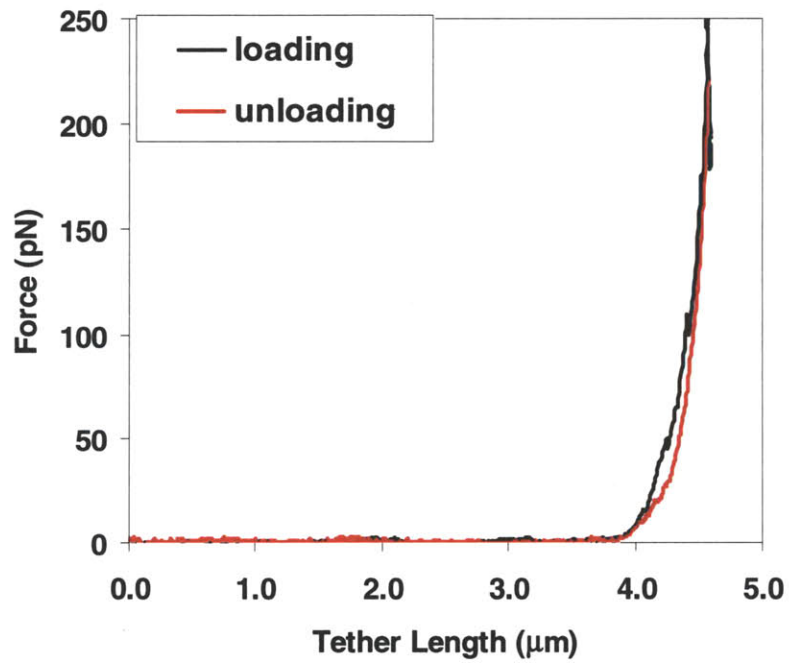
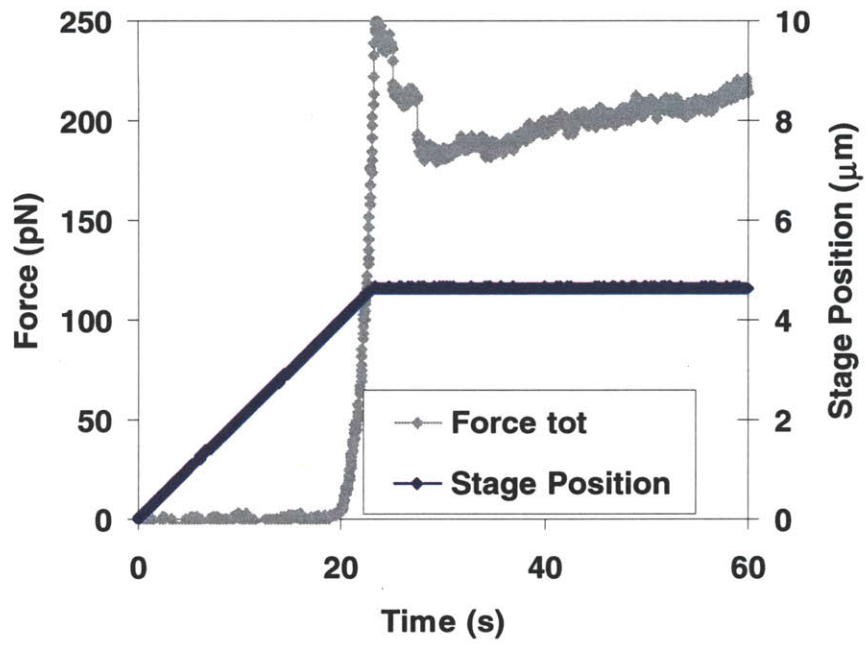


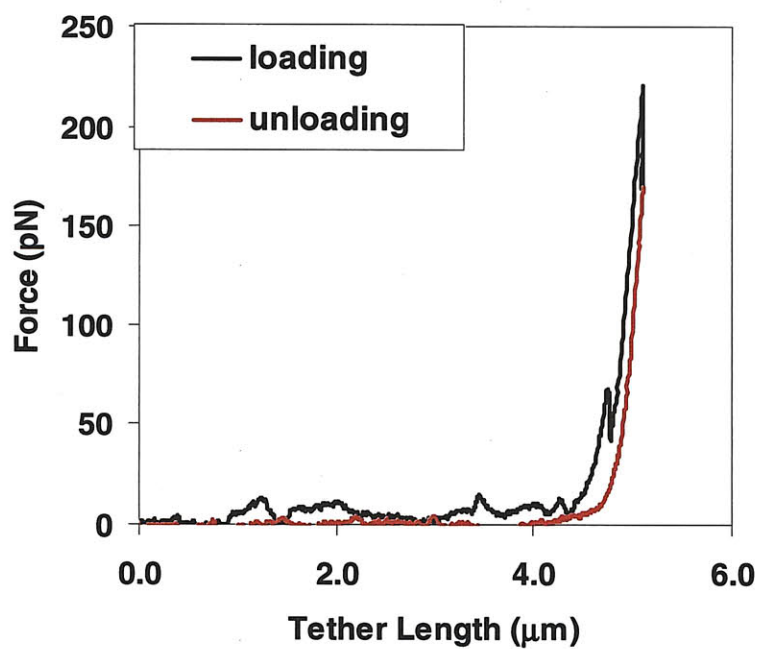
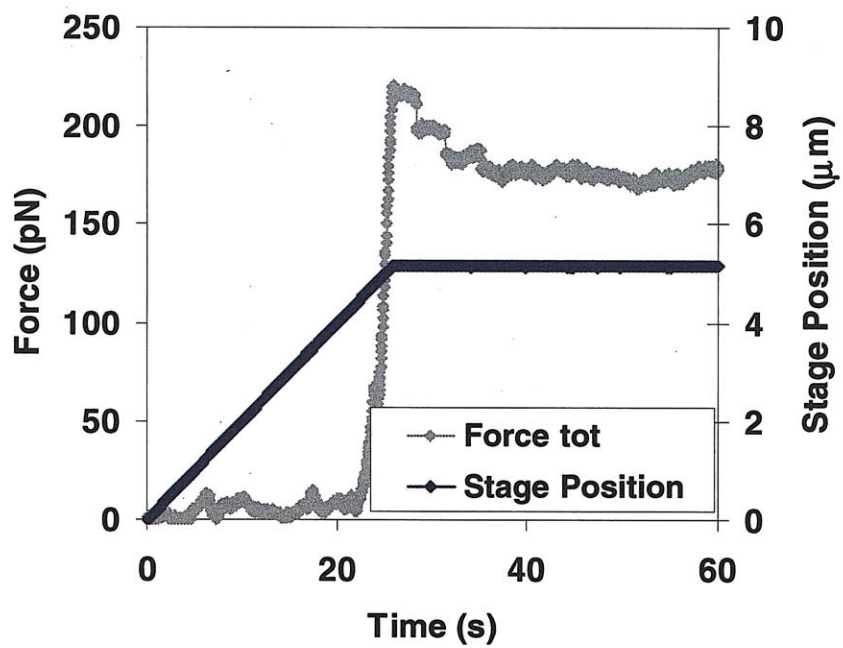


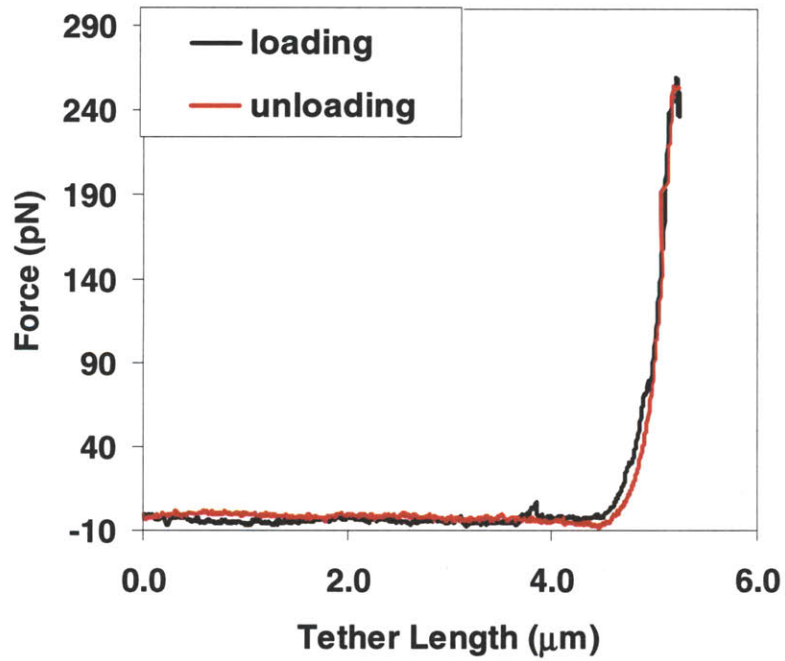
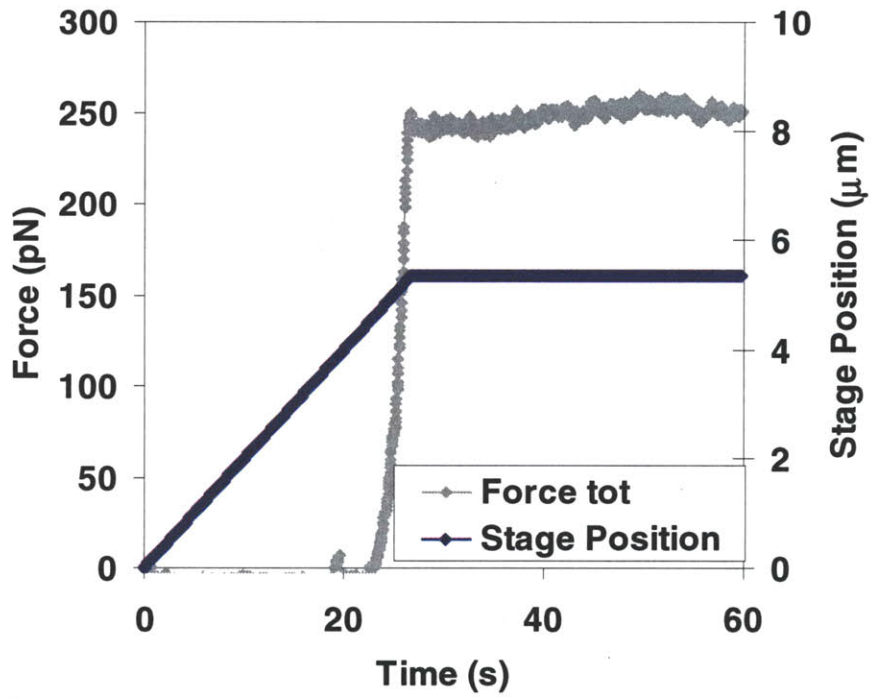


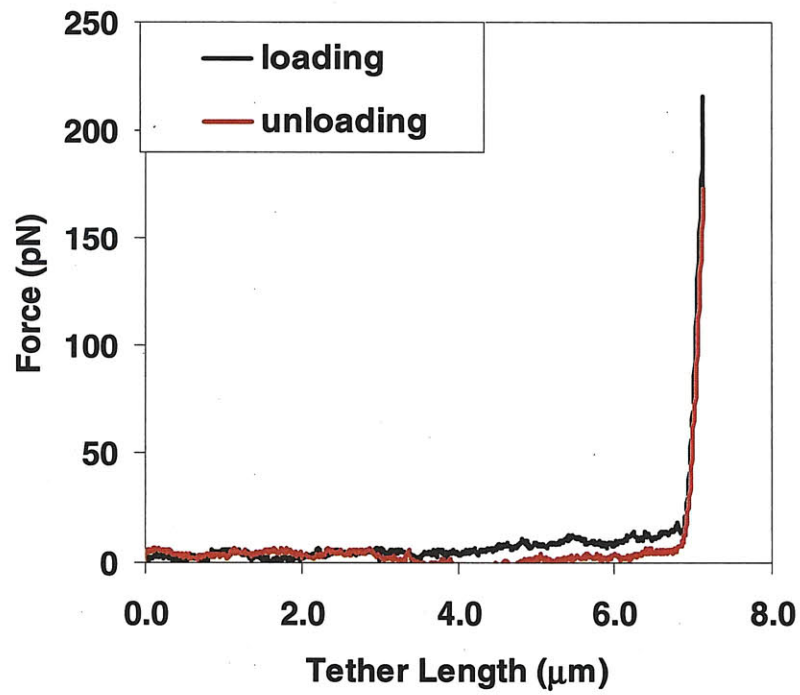
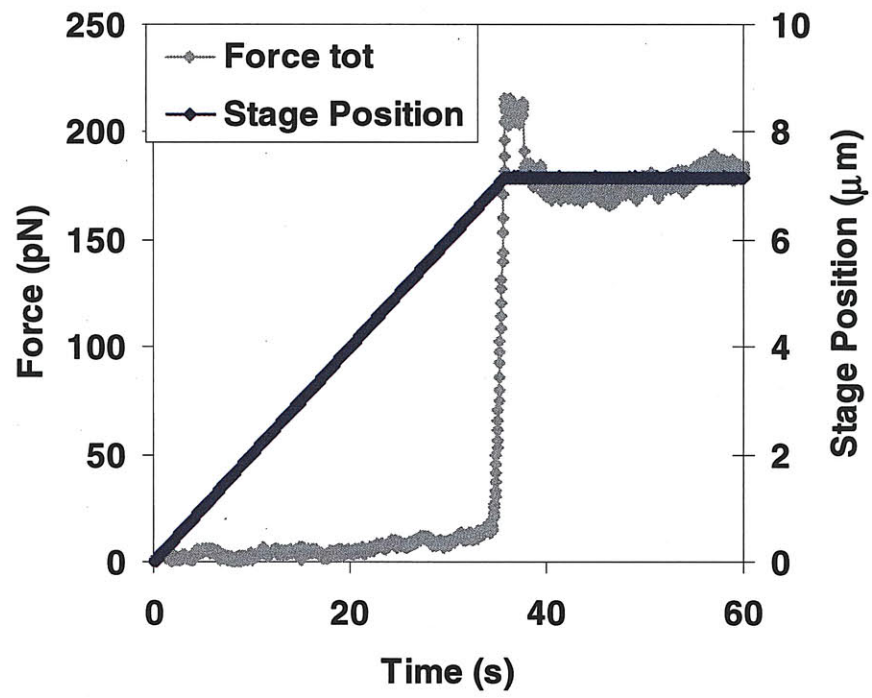
5.6.2 High Force Unfolding and Rupture Curves.











5.7 REFERENCES:

- [1] Hammer, N. D., Wang, X., McGuffie, B. A. and Chapman, M. R., 2008. "Amyloids: Friend or foe?" *J Alzheimers Dis.* **13**: p. 407-419.
- [2] Koo, E. H., Lansbury, P. T. and Kelly, J. W., 1999. "Amyloid diseases: Abnormal protein aggregation in neurodegeneration". *P Natl Acad Sci USA.* **96**: p. 9989-9990.
- [3] Dobson, C. M., 1999. "Protein misfolding, evolution and disease". *Trends Biochem Sci.* **24**: p. 329-332.
- [4] Dobson, C. M., 2001. "The structural basis of protein folding and its links with human disease". *Philos T Roy Soc B.* **356**: p. 133-145.
- [5] Glover, J. R., Kowal, A. S., Schirmer, E. C., Patino, M. M., Liu, J. J. and Lindquist, S., 1997. "Self-seeded fibers formed by Sup35, the protein determinant of [PSI+], a heritable prion-like factor of *S-cerevisiae*". *Cell.* **89**: p. 811-819.
- [6] MacPhee, C. E. and Dobson, C. M., 2000. "Formation of mixed fibrils demonstrates the generic nature and potential utility of amyloid nanostructures". *J Am Chem Soc.* **122**: p. 12707-12713.
- [7] Smith, J. F., Knowles, T. P. J., Dobson, C. M., MacPhee, C. E. and Welland, M. E., 2006. "Characterization of the nanoscale properties of individual amyloid fibrils". *P Natl Acad Sci USA.* **103**: p. 15806-15811.
- [8] Scheibel, T., Parthasarathy, R., Sawicki, G., Lin, X. M., Jaeger, H. and Lindquist, S. L., 2003. "Conducting nanowires built by controlled self-assembly of amyloid fibers and selective metal deposition". *P Natl Acad Sci USA.* **100**: p. 4527-4532.
- [9] Gras, S. L., Tickler, A. K., Squires, A. M., Devlin, G. L., Horton, M. A., Dobson, C. M. and MacPhee, C. E., 2008. "Functionalised amyloid fibrils for roles in cell adhesion". *Biomaterials.* **29**: p. 1553-1562.
- [10] Baxa, U., Speransky, V., Steven, A. C. and Wickner, R. B., 2002. "Mechanism of inactivation on prion conversion of the *Saccharomyces cerevisiae* Ure2 protein". *P Natl Acad Sci USA.* **99**: p. 5253-5260.
- [11] Prusiner, S. B., 1997. "Prion diseases and the BSE crisis". *Science.* **278**: p. 245-251.
- [12] True, H. L. and Lindquist, S. L., 2000. "A yeast prion provides a mechanism for genetic variation and phenotypic diversity". *Nature.* **407**: p. 477-483.
- [13] True, H. L., Berlin, I. and Lindquist, S. L., 2004. "Epigenetic regulation of translation reveals hidden genetic variation to produce complex traits". *Nature.* **431**: p. 184-187.
- [14] Tyedmers, J., Madariaga, M. L. and Lindquist, S., 2008. "Prion Switching in Response to Environmental Stress". *Plos Biol.* **6**: p. 2605-2613.
- [15] Shorter, J. and Lindquist, S., 2005. "Prions as adaptive conduits of memory and inheritance". *Nat Rev Genet.* **6**: p. 435-450.
- [16] Eaglestone, S. S., Cox, B. S. and Tuite, M. F., 1999. "Translation termination efficiency can be regulated in *Saccharomyces cerevisiae* by environmental stress through a prion-mediated mechanism". *Embo J.* **18**: p. 1974-1981.
- [17] Krishnan, R. and Lindquist, S. L., 2005. "Structural insights into a yeast prion illuminate nucleation and strain diversity". *Nature.* **435**: p. 765-772.
- [18] Tanaka, M., Collins, S. R., Toyama, B. H. and Weissman, J. S., 2006. "The physical basis of how prion conformations determine strain phenotypes". *Nature.* **442**: p. 585-589.

- [19] Knowles, T. P., Fitzpatrick, A. W., Meehan, S., Mott, H. R., Vendruscolo, M., Dobson, C. M. and Welland, M. E., 2007. "Role of intermolecular forces in defining material properties of protein nanofibrils". *Science*. **318**: p. 1900-1903.
- [20] Petkova, A. T., Leapman, R. D., Guo, Z. H., Yau, W. M., Mattson, M. P. and Tycko, R., 2005. "Self-propagating, molecular-level polymorphism in Alzheimer's beta-amyloid fibrils". *Science*. **307**: p. 262-265.
- [21] Wang, M. D., Yin, H., Landick, R., Gelles, J. and Block, S. M., 1996. "Stretching DNA with optical tweezers." *Biophys J*. **70**: p. Sup63-Sup63.
- [22] Baumann, C. G., Smith, S. B., Bloomfield, V. A. and Bustamante, C., 1997. "Ionic effects on the elasticity of single DNA molecules". *P Natl Acad Sci USA*. **94**: p. 6185-6190.
- [23] Wen, J. D., Manosas, M., Li, P. T. X., Smith, S. B., Bustamante, C., Ritort, F. and Tinoco, I., 2007. "Force unfolding kinetics of RNA using optical tweezers. I. Effects of experimental variables on measured results". *Biophys J*. **92**: p. 2996-3009.
- [24] Khalil, A. S., Ferrer, J. M., Brau, R. R., Kottmann, S. T., Noren, C. J., Lang, M. J. and Belcher, A. M., 2007. "Single M13 bacteriophage tethering and stretching". *P Natl Acad Sci USA*. **104**: p. 4892-4897.
- [25] Robertson, A., Castro, C. E., Lang, M. J. and Matsudaira, P., 2009. "Role of scruin in the formation of crosslinked actin filament bundles". In preparation.
- [26] Arai, Y., Yasuda, R., Akashi, K., Harada, Y., Miyata, H., Kinoshita, K. and Itoh, H., 1999. "Tying a molecular knot with optical tweezers". *Nature*. **399**: p. 446-448.
- [27] Brau, R. R., Tarsa, P. B., Ferrer, J. M., Lee, P. and Lang, M. J., 2006. "Interlaced optical force-fluorescence measurements for single molecule biophysics". *Biophys J*. **91**: p. 1069-1077.
- [28] Tarsa, P. B., Brau, R. R., Barch, M., Ferrer, J. M., Freyzon, Y., Matsudaira, P. and Lang, M. J., 2007. "Detecting force-induced molecular transitions with fluorescence resonant energy transfer". *Angew Chem Int Edit*. **46**: p. 1999-2001.
- [29] Gittes, F., Mickey, B., Nettleton, J. and Howard, J., 1993. "Flexural Rigidity of Microtubules and Actin-Filaments Measured from Thermal Fluctuations in Shape". *J Cell Biol*. **120**: p. 923-934.
- [30] Ott, A., Magnasco, M., Simon, A. and Libchaber, A., 1993. "Measurement of the Persistence Length of Polymerized Actin Using Fluorescence Microscopy". *Phys Rev E*. **48**: p. R1642-R1645.
- [31] Hua, W., Chung, J. and Gelles, J., 2002. "Distinguishing inchworm and hand-over-hand processive kinesin movement by neck rotation measurements". *Science*. **295**: p. 844-848.
- [32] Hunt, A. J. and Howard, J., 1993. "Kinesin Swivels to Permit Microtubule Movement in Any Direction". *P Natl Acad Sci USA*. **90**: p. 11653-11657.
- [33] Shewmaker, F., Wickner, R. B. and Tycko, R., 2006. "Amyloid of the prion domain of Sup35p has an in-register parallel beta-sheet structure". *P Natl Acad Sci USA*. **103**: p. 19754-19759.
- [34] Palmer, J. S. and Boyce, M. C., 2008. "Constitutive modeling of the stress-strain behavior of F-actin filament networks". *Acta Biomater*. **4**: p. 597-612.
- [35] Mackintosh, F. C., Kas, J. and Janmey, P. A., 1995. "Elasticity of Semiflexible Biopolymer Networks". *Phys Rev Lett*. **75**: p. 4425-4428.
- [36] Palmer, J. S., Castro, C. E., Arslan, M. and Boyce, M. C., 2009, *Constitutive Models for the Force-extension Behavior of Biological Filaments (Proceedings of the IUTAM Symposium on Cellular, Molecular, and Tissue Mechanics)*, Springer, New York, NY.

- [37] Palmer, J. S., 2008. "Microstructurally-based constitutive models of cytoskeletal networks for simulation of the biomechanical response of biological cells". PhD Thesis.
- [38] Marko, J. F. and Siggia, E. D., 1995. "Stretching DNA". *Macromolecules*. **28**: p. 8759-8770.
- [39] Cao, Y. and Li, H., 2008. "How do chemical denaturants affect the mechanical folding and unfolding of proteins?" *J Mol Biol*. **375**: p. 316-324.
- [40] Oberhauser, A. F., Hansma, P. K., Carrion-Vazquez, M. and Fernandez, J. M., 2001. "Stepwise unfolding of titin under force-clamp atomic force microscopy". *P Natl Acad Sci USA*. **98**: p. 468-472.
- [41] Mostaert, A. S., Higgins, M. J., Fukuma, T., Rindi, F. and Jarvis, S. P., 2006. "Nanoscale mechanical characterisation of amyloid fibrils discovered in a natural adhesive". *J Biol Phys*. **32**: p. 393-401.
- [42] Liu, X. M. and Pollack, G. H., 2002. "Mechanics of F-actin characterized with microfabricated cantilevers". *Biophys J*. **83**: p. 2705-2715.
- [43] Keten, S. and Buehler, M. J., 2008. "Large deformation and fracture mechanics of a beta-helical protein nanotube: Atomistic and continuum modeling". *Comput Method Appl M*. **197**: p. 3203-3214.
- [44] Park, J., Kahng, B., Kamm, R. D. and Hwang, W., 2006. "Atomistic simulation approach to a continuum description of self-assembled beta-sheet filaments". *Biophys J*. **90**: p. 2510-2524.
- [45] Blanchoin, L., Amann, K. J., Higgs, H. N., Marchand, J. B., Kaiser, D. A. and Pollard, T. D., 2000. "Direct observation of dendritic actin filament networks nucleated by Arp2/3 complex and WASP/Scar proteins". *Nature*. **404**: p. 1007-1011.
- [46] Vollrath, F. and Knight, D. P., 2001. "Liquid crystalline spinning of spider silk". *Nature*. **410**: p. 541-548.
- [47] Gras, S. L., Squires, A. M., Dobson, C. M. and MacPhee, C. E., 2006. "Functionalised fibrils for bio-nanotechnology". 2006 International Conference on Nanoscience and Nanotechnology, Vols 1 and 2: p. 265-267
724.
- [48] Serio, T. R., Cashikar, A. G., Moslehi, J. J., Kowal, A. S. and Lindquist, S. L., 1999. "Yeast prion [psi(+)] and its determinant, Sup35p". *Methods in Enzymology*. **309**: p. 649-673.